Universidade de Brasília
Instituto de Geociências
Programa de Pós-Graduação em Geociências Aplicadas

RECURSOS HÍDRICOS DO ALTIPLANO ANDINO: CONTRIBUIÇÃO DO SENSORIAMENTO REMOTO

Frédéric Christophe Satgé

Tese de Doutorado

Orientador:
Professor Dr. Jérémie Garnier

Comissão examinadora:
Professora Dra. Tati de Almeida - IG/UnB - Examinadora Interna
Professor Dr. Walter Collischon - IPH/UFRGS - Examinador Externo
Dra. Evlyn Márcia Leão de Morães Novo - INPE - Examinadora Externa

Brasília, 2017

Agradecimentos

Primeiro, quero agradecer a Marie-Paule Bonnet por confiar em mim desde o estágio de mestrado até hoje me transmitindo a sua paixão pelo trabalho de pesquisa. Agradeço particularmente ao professor Jérémie Garnier por confiar em mim e me dar a oportunidade de realizar o doutorado nas melhores condições possíveis.

Sou grato às instituições onde este trabalho foi desenvolvido – Universidade de Brasília (UnB), o Instituto de Hidrologia e Hidráulica (IHH) de La Paz, o laboratório Géosciences Environnement Toulouse (GET), a *Maison de la Télédétection*, onde incluo todos os pesquisadores e funcionários, por todo o apoio administrativo, técnico e científico e pelo ambiente propício para o estudo.

Agradeço a Franck Timouk por sua grande ajuda no desenvolvimento da missão de trabalho no campo; a Ramiro Pillco Zola e Jorge Molina por me receberem em La Paz quando foi necessário e pelas suas colaborações nos trabalhos de campo; a Raul Espinoza por sua colaboração em trabalhos de campo e compartilhamento de conhecimento; ao professor Henrique Lacer Roig por emprestar material específico necessário para minha pesquisa, compartilhar seu conhecimento e ajuda no campo.

Agradeço ao SENAMHI (Serviço Nacional de Meteorologia y Hidrologia) da Bolívia por compartilhar os dados hidrometeorológicos disponíveis na Bolívia, indispensáveis para o desenvolvimento deste trabalho.

Agradeço a Frédérique Seyler, Stéphane Calmant, Marielle Gosset, pelos comentários construtivos durante o processo de revisão dos artigos científicos relacionados a esta tese.

Agradeço ao Conselho Nacional de Desenvolvimento Científico e Tecnológico (CNPq) pela bolsa de doutorado e também à UnB, ao IRD (*Institut de Recherche pour le Développement*) e ao CNES (*Centre National d'Etudes Spatial*).

Agradeço aos diferentes amigos encontrados durante o doutorado e particularmente Sébastien Pinel, Diogo Olivetti e Henrique Bernini por trocar ideias de trabalho que contribuíram com o avanço do meu projeto de doutorado.

Agradeço particularmente a Eudes Bomfim por sua amizade e grande ajuda desde a minha chegada no Brasil até hoje.

Finalmente, agradeço à minha família pelo apoio ao longo desse período.

Muito obrigado a todos.

Resumo

Recursos Hídricos do Altiplano Andino: Contribuição do Sensoriamento Remoto.

Autor: Frédéric Christophe Satgé
Orientador: Jérémie Garnier

Localizado a uma elevação média de 4.000 m, o sistema endorreico do Altiplano (190.000 km^2), é delimitada pelas serras andinas com picos de mais de 6.000 m de altitude. A bacia inclui ecossistemas icônicos, como o lago Titicaca, o lago Poopó e os desertos de sal de Coipasa e de Uyuni na parte sul da bacia. Os recursos hídricos do Altiplano, estão sob pressão climática com um aumento de temperatura de 0,15 a 0,25 °C por década que contribuiu a diminuição de 43% da superfície dos glaciares entre 1981 e 2014. Além dos fatores climáticos, fatores antrópicos, tais como, as atividades agrícolas e industriais são conhecidas por contribuir na diminuição do recurso hídrico, mas não foram quantificadas na região. Nesse contexto, o monitoramento hidrometeorológico deve ajudar a prevenir e antecipar os diferentes impactos ocasionados pelas mudanças climáticas e pelas práticas agrícolas. No entanto, devido ao contexto geopolítico, dificuldades econômicas e de acesso, a bacia sofre de escassez de infraestrutura meteorológica, e assim, poucos dados estão disponíveis. Assim, os dados de sensoriamento remoto fornecem uma excelente alternativa para observar o comportamento hidrometeorológica regional. A primeira etapa do doutorado foi dedicada à avaliação de grupos de dados de sensoriamento remoto primordiais na hidrologia como (i) modelo digital de elevação (MDE) (descrições topográficas e caracterização do escoamento), (ii) estimativas de precipitações (entrada de água), (iii) estimativas da evapotranspiração (saída de água) e (iiii) imagens do visível (variação espaço-temporal da superfície dos lagos. Finalmente, foi realizado no lago Poopó o uso integrado dos dados previamente avaliados e validados para entender a seca completa do lago de dezembro 2015 em base (i) a variabilidade climática e (ii) o desenvolvimento agrícola na região. O estudo permitiu observar que o lago já secou duas vezes em 1994 e 1995. Por entanto esses eventos foram associados a fortes anomalias negativas de precipitações em quanto a seca de 2015 foi associada a fortes anomalias positivas de precipitações. O estudo revelou também um aumento significativo da evapotranspiração real (ETr) de aproximadamente 13%, independentemente da variabilidade climática. Esse aumento da ETr foi registrado nas zonas agrícolas sugerindo assim o papel significativo da agricultara no processo de desertificação da região. De fato devido ao aumento do preço da *Chenopodium Quinoa* (quinoa) no mercado externo, a superfície ocupada pelas plantações passou de 10.000 para 50.000 ha entre 1980 e 2011. O uso de métodos de irrigação aumentou a disponibilidade de água para a evaporação e diminui a quantidade das águas superficial e subterrânea. Este trabalho pioneiro no Altiplano, permite demonstrar a grande potencialidade da integração de dados de sensoriamento remoto em regiões áridas remotas para seguir e entender as problemáticas socioambiental relacionadas a pressões antrópicas e climáticas.

Palavras-chaves: Altiplano, recursos hídricos, variações climáticas, agricultura, sensoriamento remoto, modelo de elevação, precipitação, evaporação, Landsat, lago Poopó.

Abstract

Water Resources of the Andean Altiplano: Remote Sensing Contribution.

Author: Frédéric Christophe Satgé
Advisor: Jérémie Garnier

Located at an average elevation of 4000 m, the Altiplano (190.000 km^2) is an endoreic system delimited by the Andean mountains with peaks higher than 6000 m. The basin includes iconic ecosystems such as Lake Titicaca, Lake Poopó and the salt deserts of Coipasa and Uyuni in the southern part of the basin. The water resource of the Altiplano is under climatic pressure with a temperature increase of 0.15°C and 0.25°C per decade, which decreased the glacier surface by 43% between 1981-2014. In addition to climatic variability, anthropic factors, such as agriculture and industrial activities, is known to contribute to the water resource decrease but remains unquantified in the region. In this context, hydro-meteorological monitoring should help to prevent and anticipate the different impacts of climate change and agricultural practices. However, given the geopolitical context, economic and access problems few stations are available. Therefore, remote sensing data provide an alternative to observe regional hydro-meteorological behavior. The first stage of the PhD was dedicated to the assessment of remote sensing data useful in hydrology such as (i) digital elevation model (topographic description, flows characterization), (ii) precipitation (water input), (iii) evapotranspiration (water output) and (iiii) visible images (water superficial dynamic) which is the first study of such remote sensing data potential over the region. Finally, an integrated use of the evaluated/validated remote sensing data was carried out to understand the lake Poopó drought of December 2015 considering (i) climate variability and (ii) agriculture increase. The study highlighted that the lake already drought in 1994 and 1995. However, these droughts events were associated to strong rainfall anomalies while the 2015 one was associated to positive rainfall anomalies. The study also highlighted an increase of real evapotranspiration (ETr) of approximately 13% independently to climate variability in the region. The ETr increase was observed over cropped areas suggesting a significate influence of agriculture to the regional desertification process. Indeed, between 1980 and 2011, quinoa's cultivated area increased from 10.000 to 50.000 ha, related to the increase of quinoa's price. The use of irrigation method increased the availability of water for evapotranspiration and, therefore, decreased the amount of water in the surface and underground reservoir. This work, a pioneer in the Altiplano, demonstrates the great potential of the integration of remote sensing data in remote arid regions subject to anthropic and climate pressures

Keywords: Altiplano, water resource, climate variability, agriculture, remote sensing, digital elevation model, rainfall, evapotranspiration, Landsat, lake Poopó.

Sumario

Lista de figuras e tabelas

Lista de Siglas e Abreviações

ASTER	Advanced Spaceborne Thermal Emission Reflection
Adj	Adjusted
ALOS	Advanced Land Observing Satellite
AW3D30	ALOS World 3D-30
AWEI	Automated Water Ratio Index
CHRS	Center de Hidrometeorology e Remote Sensing
CMORPH	Climate prediction center MORPHing
CNES	Centre National d'Etudes Spatiale
CNPq	Conselho Nacional de Desenvolvimento Científico e
CPC	Climate Prediction Center
CREST	Core Research for Evolutional Science and Technology
Etp	Evapotranspiração Potencial
Etr	Evapotranspiração Real
FAR	Fals Alarm Ratio
FSR	False Slope Ratio
GCLC	GlobCover Land Cover
GDEM	Globlal Digital Elevation Model
GET	Géosciences Environnement Toulouse
GLAS	Geoscience Laser Altimeter System
GPCP	Global Precipitation Climatology Project
GPM	Global Precipitation Measurement
GRACE	Gravity Recovery And Climate Experiment
GSMaP	Global Satellite Mapping of Precipitation
ICESat	Ice Cloud and Land Elevation Satellite
IHH	Instituto de Hidrologia y Hidráulica
IMERG	Integrated Multi-satellitE Retrievals for GPM
IPCC	Intergovernmental Panel on Climate Change
IRD	Institut de Recherche pour le Développement
ITCZ	Inter Tropical Convergence Zone
JAXA	Japan Aerospace Exploration Agency
JST	Japan Science and Technology
LSWI	Land Surface Water Index
MDE	Modelos de Elevação do Terreno
METI	Ministry of Economy, Trade, and Industry
MNDWI	Modified NDWI
MOD16	MODIS Global Evapotranspiration Project
MSWEP	Multi-Source Weighted-Ensemble Precipitation
NASA	National Aeronautics and Space Administration

NBR	Normalized Burn Ratio
NDVI	Normalized Difference Vegetation Index
NDWI	Normalized Difference Water Index
NGA	National Geospatial-Intelligence Agency
NRCSS	Natural Resources Conservation Service Soils
PER	Pontos de Elevação de Referencia
PERSIANN	Precipitation Estimation from remotely Sensed Information using Artificial Neural Networks
PERSIANN-CDR	PERSIANN-Climate Data Record
PMM	Precipitation Measuring Mission
POD	Probability of Detection
PR	Precipitation Radar
PRISM	Panchromatic Remote-sensing Instrument for Stero Mapping
RT	Real Time
SENAMHI	Serviço Nacional de Meteorologia e Hidrologia da Bolívia e do Peru
SOTERLAC	Soil and Terrain digital database for Latin America and the Caribbean
SRE	Satellite Rainfall Estimate
SRTM	Shuttle Radar Topographic Mission
TDPS	Titicaca Desaguadero Poopó Salar
TMI	TRMM Microwave Imager
TMPA	TRMM Mulstisatelite Precipitation Analysis
TRMM	Tropical Rainfall Measuring Mission
UnB	Universidade de Brasilia
USDA	United States Department of Agriculture
USGS	United States Geological Survey
VIRS	Visible Infrared Radiometer
VR	Vetor Regional
WRB	World Reference Base
WRI	Water Ratio Index

I. Introdução

1. Contexto geral: os recursos hídricos no mundo

A água é um recurso essencial à manutenção dos organismos vivos do planeta e sua importância é irrefutável. No entanto, os recursos hídricos doces estão enfrentando pressões antrópicas sem precedentes e poderiam ser ainda mais ameaçados devido às mudanças do clima (Wheater e Gober, 2015). Atividades antrópicas que resultam em uma mudança de ocupação de terras em larga escala, a crescente urbanização, armazenamento ou retirada de água para uso industrial, agrícola ou doméstico ameaçam diretamente os sistemas aquáticos (Hering et al., 2011). Além de afetar a quantidade de água, atividades antrópicas conduzem a degradação de sua qualidade, podendo torna-la imprópria para alguns usos fundamentais tais como uso doméstico ou agrícola (Vörösmarty et al., 2010).

Devido ao aumento da população mundial e ao desenvolvimento econômico, a demanda de água é crescente. Durante o século 20, a população mundial triplicou, e neste mesmo período o uso de água foi multiplicado por seis. Enquanto o consumo doméstico cresceu 10 % e o uso industrial 20%, o uso agrícola cresceu 70% para responder à demanda alimentar (Vision, Word Water Concil, 2000). Assim, no último século, o uso de água para fins agrícolas (principalmente pelas práticas de irrigação) representa o maior consumo de água, contabilizando 90% do consumo das águas frescas no mundo, sendo 40 e 60% extraída dos reservatórios subterrâneos e superficiais respectivamente (Giordano, 2009; Siebert et al., 2010).

Devido às conexões entre os reservatórios de águas subterrâneas e superficiais, através de processos hidrológicos, a exploração desequilibrada de um desses dois reservatórios pode afetar o outro, e assim, afetar drasticamente os recursos hídricos regionalmente. Neste contexto, diversas normas e políticas de gestão foram estabelecidas pelas autoridades competentes para tentar manter o equilíbrio entre o uso e a renovação de recursos hídricos. Porém, vários exemplos, tais como, a seca dos lagos Chad (Lemoalle et al., 2012; Ndehedehe et al., 2016) Eyre e Urmia e os mares Morto e Aral (Precoda, 1991; Small et al., 2001; Rokni et al., 2014) e o rebaixamento em vários metros do aquífero continental na Tunísia (Abidi, B. & Ben Baccar, B., 2001) ilustram falhas e a necessidade de melhorar o modelo de uso de recursos hídricos, de forma a não comprometer a qualidade do meio ambiente e da vida humana (Wheater e Gober, 2015).

Em várias regiões do mundo, o acesso à água já está restrito, com uma demanda superior à disponibilidade (Figura 1a). Com foco nos rios e tendo em conta vários estressores, incluindo distúrbios da cobertura do solo e poluição da água, (Vörösmarty et al., 2010) concluem que “mais de 80% da população mundial está exposta a altos níveis de ameaça à segurança da água. Investimentos maciços em tecnologia de água permitem que os países ricos compensem altos níveis de estresse sem remediar suas causas subjacentes, enquanto os países menos ricos continuam vulneráveis". Foram registrados nos últimos anos importantes esgotamentos de reservatórios subterrâneos com relação direta com o uso antrópico (Rodell et al., 2009; Scanlon et al., 2012; Voss et al., 2013; van Steenbergen et al., 2015; Long et al., 2016). Atualmente, 1.7 bilhão de pessoas vivem em áreas onde os recursos hídricos subterrâneos e/ou os ecossistemas dependentes das águas subterrâneas estão sob ameaça (Gleeson et al., 2012). A recente escassez de água em alguns estados do Brasil, um pais com altos índices pluviométricos, também pode ilustrar os desafios atuais.

As mudanças climáticas representam uma pressão adicional sobre os recursos hídricos, tendendo a acentuar os impactos das alterações antrópicas antes descritas. Hanasaki et al., (2013a, 2013b) estimam que aproximadamente 50% da população mundial estará vivendo sob estresse hídrico severo até 2071-2100. As variações climáticas têm impacto direto nos dois principais componentes do balanço hídrico: a evapotranspiração e a precipitação. As variações climáticas observadas nos últimos anos causam o aumento da evapotranspiração regional, associado a uma diminuição quantitativa das precipitações e ao aumento de eventos climáticos extremos (Trenberth, 2011).

Adicionalmente, as variações climáticas são principalmente caracterizadas pelo aumento da temperatura global, estimado em 0.85 °C por década, entre 1880 e 2012, pelo *Intergovernmental Panel on Climate Change* (IPCC) (IPCC, 2014). Esse aumento de temperatura afeta drasticamente o ciclo da água contribuindo com a diminuição dos recursos e, caso mais visível, o derretimento de geleiras. Em determinadas regiões, essas geleiras constituem reservatórios de água, e assim, possuem um papel crítico no balanço hídrico. Esses reservatórios se recarregam nas estações úmidas e liberam água para o sistema nos períodos de seca, mantendo uma vazão de base maior nos rios. Nos últimos anos, observou-se a diminuição da superfície recoberta por neves e geleiras relacionada diretamente ao aumento global de temperatura (Rabatel et al., 2013; Rangecroft et al., 2013; López-Moreno et al., 2014; Vicente-Serrano et al., 2015). O derretimento de geleiras está associado a um aumento geral da vazão dos rios (Mark e Mckenzie, 2007), a qual fica limitada no tempo de acordo com a massa de gelo armazenado (Mark et al., 2005; Mark e Mckenzie, 2007). A partir de um certo tamanho e volume de gelo armazenado nas geleiras, a vazão de base do rio diminui consideravelmente (Huss et al., 2009; Lambrecht e Mayer, 2009). Esse fenômeno é ainda mais marcado nos períodos de seca, nos quais a contribuição do fluxo de base é máxima, enquanto a contribuição da chuva é mínima. Em longo prazo, a diminuição/desaparição das geleiras resultará em uma diminuição de entrada de água nos sistemas hidrológicos, alterando o equilíbrio do balanço hídrico e ameaçando os diferentes usos de água, tal como, abastecimento público, agricultura ou produção de energia hidroelétrica.

Em alguns contextos e regiões, as instituições governamentais tendem a minimizar os efeitos da agricultura e/ou das mudanças climáticas por razões econômicas ou geopolíticas. Porem, há já evidências científicas que indicam que esses efeitos podem ter consequências irreversíveis (e.g. o desastre do mar Aral: Precoda, 1991; Small et al., 2001). As principais alterações dos recursos hídricos, resultantes da agricultura se baseiam (i) na mudança da cobertura, a qual acelera o processo de evapotranspiração, (ii) no uso da irrigação, o qual facilita a disponibilização de água para o processo de evapotranspiração e (iii) no efeito da cobertura vegetal, por seu processo de absorção da água proveniente da precipitação, o que diminui a contribuição das precipitações para o processo de recarrega dos reservatórios superficiais e subterrâneos. Simultaneamente, pode-se esperar uma relação entre variações climáticas e os efeitos das práticas agrícolas nas regiões áridas. Existe uma tendência em aumentar os processos de irrigação para compensar, tanto o aumento da evaporação associado ao aquecimento global, quanto a diminuição no padrão de precipitação. Portanto, pode-se sugerir uma forte relação entre variações climáticas e uso agrícola no tocante à pressão exercida sobre os recursos hídricos em muitas zonas que se encontram em risco de desertificação.

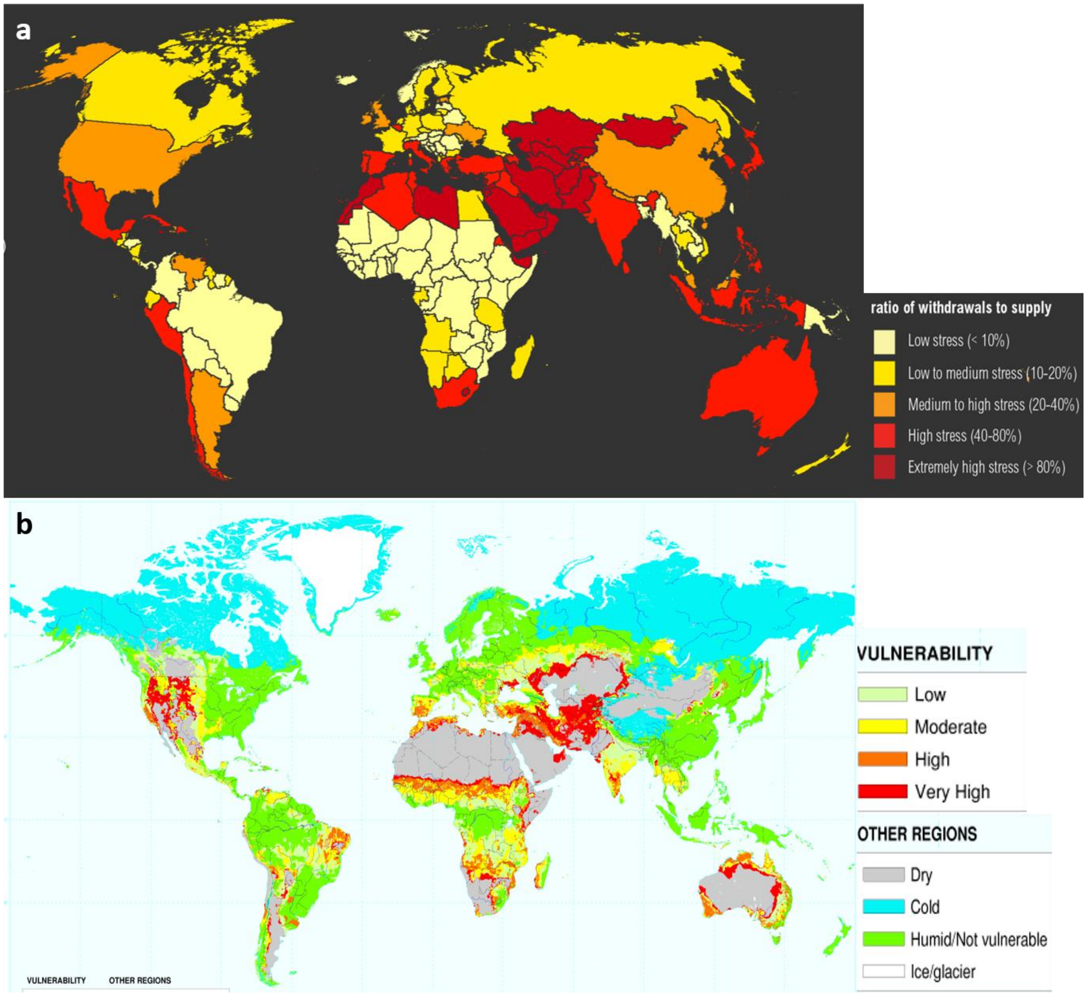

Figure 1. Mapa de estresse hídrico no mundo com base na razão de uso e da disponibilidade (a) e vulnerabilidade ao processo de desertificação no mundo (b). Estes mapas foram adaptados dos mapas estabelecidos por Gassert et al., 2013 (a) e pelo USDA-NRCSS (United States Department of Agriculture-Natural Resources Conservation Service Soils).

2. O Recurso Hídrico no Altiplano

Na bacia do Altiplano, localizada no Platô Andino Sul-Americano (Bolívia, Peru, Chile), convergem mudanças climáticas e antrópicas e problemas sociais e econômicos a elas relacionados. Devido ao seu contexto regional árido, i.e. com valores de precipitação e evapotranspiração muito próximos, a região do Altiplano está potencialmente ameaçada pelas mudanças previamente descritas. Portanto, uma alteração mínima no regime climático e/ou no uso dos recursos hídricos pode alterar de maneira significativa o equilíbrio hidrometeorológico regional que levem a consequências ambientais e sociais drásticas.

Entre 1965 e 2012 o aumento da temperatura foi estimado entre 0.15 e 0.25°C por década (Seiler et al., 2013; López-Moreno et al., 2015). Esse aumento contribuiu com a diminuição da cobertura de gelo em aproximadamente 43% entre 1981 e 2014 (Cook et al., 2016). Algumas geleiras já desapareceram, como o glaciar de Chacaltaya em 2009 (Rabatel et al., 2013; Soruco et al., 2015) e outras podem desaparecer em um futuro próximo, afetando os recursos hídricos principalmente durante a estação seca (Bradley et al., 2006; Frans et al., 2015). Tais efeitos já são observados na parte boliviana da bacia do Altiplano. Entre novembro de 2016 e março de 2017, pela primeira vez, metade da população da cidade de La Paz, capital da Bolívia (2 milhões de habitantes), teve acesso restrito a água devido à diminuição rápida das reservas de água da cidade alimentada principalmente pelo derretimento de geleiras (Painter, 2007). A vazão na saída da geleira Zongo, nas proximidades da cidade de La Paz, foi modelada por Frans et al., (2015) no período entre 1987 e 2100, cujo resultado indicou a tendência nítida à diminuição, prevendo o risco recorrente de escassez de água para as populações num futuro próximo. Por outro lado, de acordo com diferentes modelos globais de circulação climática, nenhuma modificação significativa no regime de precipitação foi evidenciada (Seth et al., 2010; Seiler et al., 2013; Valdivia et al., 2010, 2013).

Embora apresente altitude elevada, altas temperaturas, pouca precipitação e solo arenoso com baixa disponibilidade de nutrientes, a região do Altiplano é uma zona agrícola muito importante, somando um quarto da população agrícola boliviana (Vacher, 1998). Juntamente com a batata, a quinoa é o cultivo mais importante na região. A quinoa é um cereal Andino tradicional com alto valor nutricional, o qual pode crescer em solo pobre e condições climáticas desfavoráveis. Bolivianos e peruanos usaram esse cultivo por mais de 7.000 anos (Cusicanqui et al., 2013). De 1980 a 2011, a superfície ocupada pelo cultivo de quinoa passou de 38.800 a 70.000 ha (Cusicanqui et al., 2013) e a produção de 34.000 a 84.000 toneladas de 2009 a 2014 (Canedo et al., 2016). Essa mudança foi incentivada pelo aumento da demanda de quinoa pelo mercado externo, ilustrada na multiplicação do preço por quatro de 1989 a 2011. Inicialmente, as áreas cultivadas no Altiplano eram localizadas nas vertentes das montanhas (vulcões), enquanto regiões mais planas eram usadas para pastagem de lhamas. Nas últimas décadas, o cultivo foi expandido para regiões planas em detrimento das estepes nativas. Essa mudança exigiu o uso de métodos mais modernos e mecanizados em detrimento dos antigos métodos antigos manuais. Assim, o uso de sistema mecanizados para lavoura, semeadura e irrigação se tornou cada vez mais comun. Tais mudanças de cobertura e de técnicas tendem a aumentar o processo erosivo dos solos e a evapotranspiração, acelerando o processo de desertificação da região (Jacobsen, 2011, 2012). Neste contexto e no das mudanças antrópicas e climáticas regionais, a situação hídrica na parte sul do altiplano é crítica e representa uma ameaça ecológica e social pondo em risco o bem estar e sobrevivência das populações locais. A desertificação da região, potencialmente irreversível, pode comprometer a ocupação humana, as suas atividades e a produção de quinoa, que representa a principal fonte alimentar e de renda das comunidades regionais do Altiplano (Jacobsen, 2011). No ano de 2016, a atividade agropecuária ocupou o segundo lugar nas atividades econômicas, contribuindo com 11,2% do PIB boliviano (INE, 2017). Portanto, a desertificação da região ameaça a economia nacional.

Na região, devido à riqueza mineral do subsolo, a atividade industrial é essencialmente baseada em extração mineral. Além de participar no aumento da evaporação, os processos erosivos em áreas de lavra e o processo de drenagem ácida das minas, associado a exploração dos sulfetos de metais (cobre, prata, estanho e zinco) e do ouro, conduz à acidificação das águas e liberação de metais que podem afetar os ecossistemas. Na região de Oruro (parte central do Altiplano, Bolívia), por exemplo, concentrações elevadas de metais tais como As e Hg foram encontradas nos efluentes e rios da região assim como nos sedimentos e peixes do lago Uru-Uru e Poopó (Jorge e Daza Pelaez, 2014; Alanoca et al., 2016). Além disso, outras atividades industriais, como a exploração do lítio dos salares, podem afetar os ciclos dos elementos e liberar contaminantes no meio ambiente. De fato, o salar (deserto de sal) de Uyuni, com uma superfície de 12.500 km^2, é uma das maiores reservas potenciais de lítio do mundo. O *United States Geological Survey* (USGS) estima as reservas mundiais em aproximadamente 33 milhões de toneladas, sendo 9 milhões de toneladas a salmoura do salar de Uyuni. Em função da utilização crescente do Li (baterias e outras aplicações tecnológicas), o preço do carbonato de lítio foi multiplicado por três entre 2003 e 2010. O governo boliviano está concluindo um acordo com empresas mineiras chinesas e alemãs para exploração prevista a partir de 2018. A extração requer bombeamento intenso nas salmouras e a sua evaporação em bacia de decantação artificial de vários quilômetros quadrados. Tal atividade tem potencial para agrava ainda mais o desequilíbrio do balanço hídrico regional pelo aumento da evaporação local e alteração dos escoamentos subterrâneos. Além disso o setor de mineração pode afetar a qualidade das águas.

Finalmente, o contexto geopolítico da bacia hidrológica do Altiplano contribui para aumentar a pressão sobre os recursos hídricos na região. A maior parte da bacia se encontra na Bolívia porem os principais rios, em termos de vazão, nascem no Peru e no Chile. Por consequência, o uso e a retirada de água no Peru e no Chile tem impacto na parte boliviana da bacia, com redução da vazão dos rios transfonteiriços (Moran 2009; Molina Carpio et al. 2012; Urquidi Barrau 2012) e, potencialmente, na contaminação do recurso.

3. Objetivos

A luz de um contexto socioambiental delicado e das diversas pressões exercidas nos recursos hídricos dessa região frágil, torna-se necessário entender melhor o funcionamento hidrometeorológico do Altiplano.

A observação da variação quantitativa dos recursos hídricos ao longo do tempo permite definir a tendência evolutiva geral dos recursos e assim prever eventuais riscos futuros para o equilíbro do sistema considerado. Essas observações são feitas por medição direta do recurso hídrico com base em medições piezométricas, níveis de lagos e vazão dos rios. Porém, essas medições, sendo pontuais no tempo e no espaço, não permitem entender as variações observadas na escala da bacia como um todo. Para entender as variações medidas pontualmente no espaço é necessário representar o balanço hidrometeorológico regional, representando todas as entradas e saídas de água do sistema e as relações existentes entre elas. Dessa forma, com base nas observações coletadas ao longo do tempo, é possível entender a variação quantitativa observada pontualmente em relação às mudanças climatológicas e/ou ao uso de água em escala regional. Em bacias de grande escala como a do Altiplano, essa abordagem é ainda mais importante pois as variações medidas em um determinado ponto podem ser consequentes de mudanças ocorrendo em vastas áreas, em escala nacional, ou em outros países vizinhos devido ao contexto internacional da bacia.

Nesse contexto, o objetivo geral do trabalho de tese consistiu no desenvolvimento de uma nova metodologia para estudo do processo de desertificação do Altiplano. O estudo foi desenvolvido na bacia do lago Poopó com o intuito de fornecer um primeiro diagnóstico dos impactos relacionados às mudanças climáticas e antrópicas na seca completa do lago Poopó em dezembro 2015. Devido a sua localização na parte sul da bacia, as suas variações traduzem mudanças climatológicas e antrópicas ocorrendo em escala de bacia (à montante). Portanto, o lago representa uma estação de controle do estado hidroclimatológico global da região. Suas variações podem ser confrontadas com a variabilidade espaço-temporal climatológica e de uso para entender os fatores dominantes na desertificação regional e na seca do lago Poopó. Com base nessas análises será possível apoiar os gestores e propor uma gestão mais razoável dos recursos hídricos, afim de proteger o abastecimento doméstico e as diversas atividades que dele dependem.

Para efetuar o presente estudo, foi necessário ter acesso a dados hidrometeorológicos, tais como níveis de lençóis freáticos, vazão e pluviometria e evapotranspiração (atuais e antigas), tudo isso distribuído ao longo do espaço e do tempo. O Serviço Nacional de Meteorologia e Hidrologia da Bolívia e do Peru (SENAMHI) mantém uma rede de estações hidrometeorológicas. O contexto internacional e as tensões geopolíticas relacionadas ao conflito do uso de águas na região prejudicaram a coleta de dados hidrológicos e meteorológicos. Ao longo do tempo a quantidade e repartição espacial das estações variou consideravelmente, devido a problemas de manutenção, ao contexto econômico regional e à mudança de objetivos gerais de monitoramento. Além disso, devido às dificuldades de acesso no altiplano, a distribuição espacial dos dados não é homogênea. A porção norte da bacia (mais povoada e de fácil acesso) conta com mais estações e series mais continuas em comparação a parte sul e oeste da bacia (menos povoadas e de difícil acesso). Desta forma, existe escassez de dados e por vezes falta de continuidade no monitoramento de base da bacia.

Nesse contexto, o primeiro objetivo específico consistiu em aumentar a cobertura espacial e paramétrica da rede de monitoramento disponibilizada pelo SENAMHI. Com este intuito, 5 estações meteorológicas complementares foram instaladas. Além de medir os parâmetros meteorológicos clássicos (vento, precipitação, temperatura, umidade do ar, radiação solar), as estações incluem sensores de umidade do solo e sensores necessários para a representação do balanço radiativo (parâmetros não medidos pelas estações da rede nacional). Adicionalmente, foram realizados trabalhos de campo objetivando a coleta de parâmetros complementares primordiais para a conclusão deste projeto de doutorado (dados espectro-radiômetros e observação visual) a fim de avaliar e validar modelos de correções atmosféricas e índices de separação água/solo para a estimação da superfície dos corpos de água da região. Devido à ausência de intercâmbio de dados entre Peru e Bolívia, um trabalho de revisão bibliográfica permitiu coletar os dados previamente publicados e disponíveis na parte peruana da bacia. Finalmente, foi desenvolvido um trabalho de consolidação dos dados *in situ* disponíveis por meio de análise da incerteza nas séries temporais das estações meteorológicas, a fim de descartar as estações sujeitas a erros consideráveis de medições.

Face às limitações da rede hidrometeorológica regional, propôs-se como segundo objetivo dessa pesquisa avaliar a aplicação de dados de sensoriamento remoto na estimativa de parâmetros prioritários à representação do balanço hidrológico, visto que contam com uma cobertura quase mundial, alta frequência de aquisição e o acesso fácil e livre por internet. Assim sendo, foram avaliados os seguintes parâmetros para compor a base de dados da bacia do Altiplano, fundamentais a seu balanço hidrológico:

- Modelo Digital de Elevação do Terreno, i.e. MDE (topografia e caracterização do escoamento superficial)
- Precipitação (principal entrada de água)
- Evapotranspiração (principal saída de água)
- Imagens multiespectrais (variações espaciotemporais dos níveis dos lagos)

De fato, para cada um dos grupos dos dados mencionados, diferentes produtos e metodologias estão disponíveis. De acordo com a região de interesse e dos objetivos do trabalho, um produto (MDE, precipitação, evapotranspiração) ou uma metodologia de processamento (imagem multiespectral) pode ser mais adequada que outra o que dificulta a escolha do produto e/ou da metodologia.

Finalmente, a nova metodologia de estudo do processo de desertificação da região do Altiplano foi desenvolvida com base no banco de dados de sensoriamento remoto previamente realizado, o qual permitirá avaliar o potencial desses dados como alternativa ao dado de estação *in situ*.

Para concluir, com o objetivo de realizar este estudo, o meu trabalho de doutorado se articulou entorno das seguintes perguntas:

- Quais dos MDEs disponíveis descreve melhor a topografia regional? Quais são os principais componentes de erro dos MDEs que controlam a acurácia dos MDEs e como avaliar esses erros? Qual erro é o mais importante no contexto hidrológico?
- Qual dos produtos das estimativas de chuva descreve melhor o padrão regional? Qual é a influência da topografia, da variação de emissividade e do clima nas estimativas no espaço e no tempo?

- E possível medir a evapotranspiração com precisão com base nos dados de sensoriamento remoto?
- Como corrigir os efeitos atmosféricos nas imagens Landsat? Como estimar a variação de superfície do lago Poopó, ao longo do tempo, com um erro mínimo a partir de uma imagem Landsat?
- Como usar de maneira integrada os diferentes dados para identificar o papel da variabilidade climática e da atividade humana na seca do lago Poopó com base em dados de sensoriamento remoto?

4. Organização do trabalho

Após a apresentação da bacia do altiplano e das suas principais características, esta tese de doutorado está organizada em 3 capítulos distintos apresentando, respectivamente, os estudos realizados sobre os MDEs, as estimativas das precipitações e o estudo da flutuação do lago Poopó o qual inclui também um estudo de avaliação da potencialidade das imagens Landsat e das estimativas de evapotranspiração de sensoriamento remoto (Figura 2). Este estudo de doutorado resultou em cinco publicações internacionais e um artigo ainda em revisão, assim eu decidi redigir o manuscrito na forma de artigos. Cada capitulo é organizado entorno de uma introdução em português e de um artigo escolhido para ilustrar o trabalho realizado. As introduções apresentam o quadro do estudo, os matérias e métodos utilizados, assim como, os principais resultados obtidos.

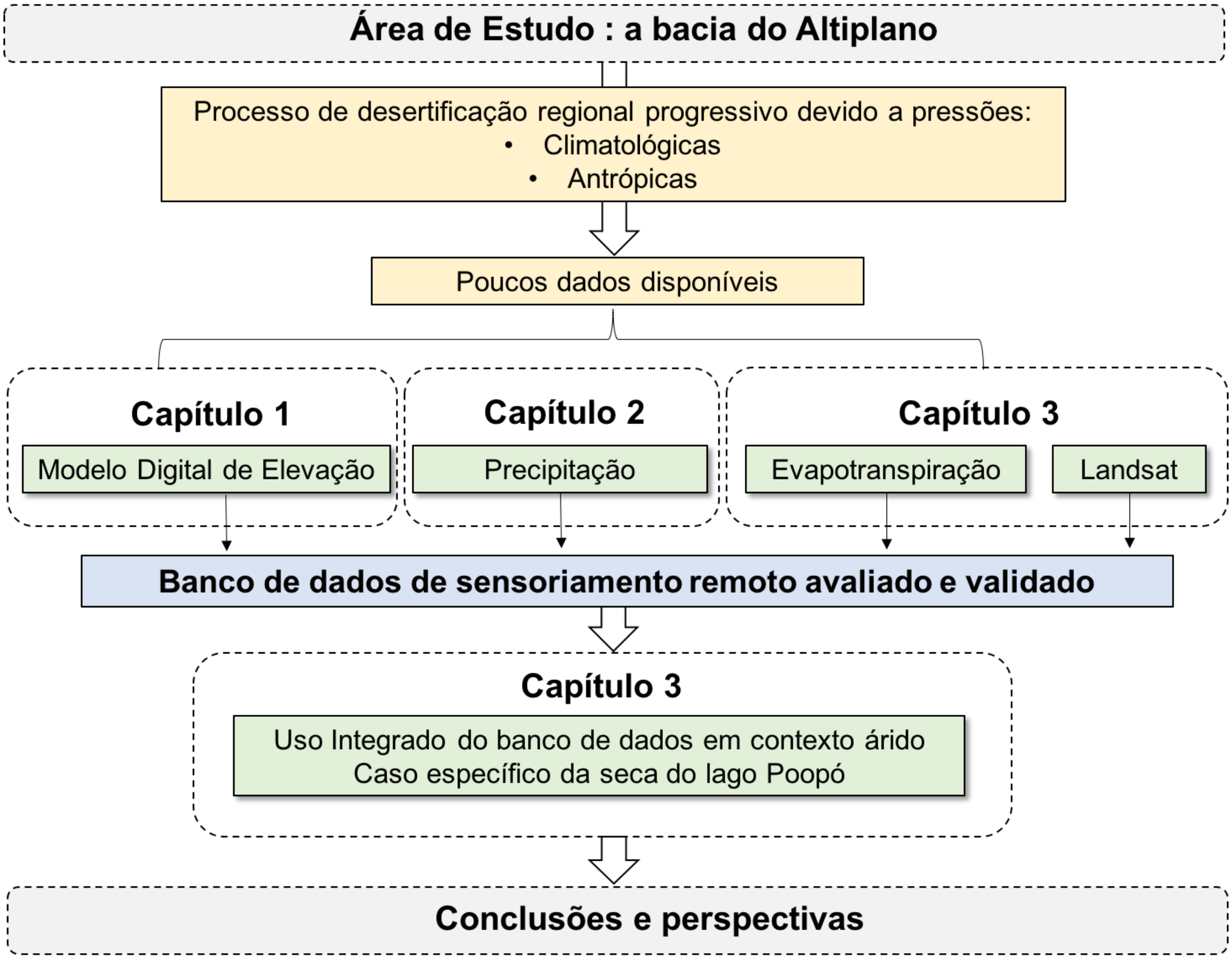

Figura 2. Organograma ilustrativo da estruturação do trabalho

II. Área de estudo: a Bacia do Altiplano

A bacia do Altiplano se encontra localizada entre as latitudes 14° e 20° sul, dividida entre o Peru (27%), a Bolívia (69%) e o Chile (4%) (Figura 3). O altiplano é uma região muito plana, com declividade média de 5° e uma elevação média de 4.000 m variando entre 3.500 m a 6.500 m (Figura 3). As elevações menores estão localizadas na parte sul e na planície do rio Desaguadero. Este rio conecta superficialmente o lago Titicaca ao norte com o lago Uru-Uru e Poopó no centro da bacia. Relevos altos se encontram nas duas Cordilheiras (Ocidental e Real) que marcam os limites das bacias nas partes oeste e leste (Figura 3). Os Salares de Coipasa e de Uyuni ocupam a parte sul da bacia. Com uma superfície total de aproximadamente 192.000 km^2, ela é considerada a maior bacia endorreica de altitude do mundo. Por possuir grandes unidades, a Bacia do Altiplano é chamada de sistema TDPS (Titicaca, Desaguadero, Poopó e Salar) (Figura 3).

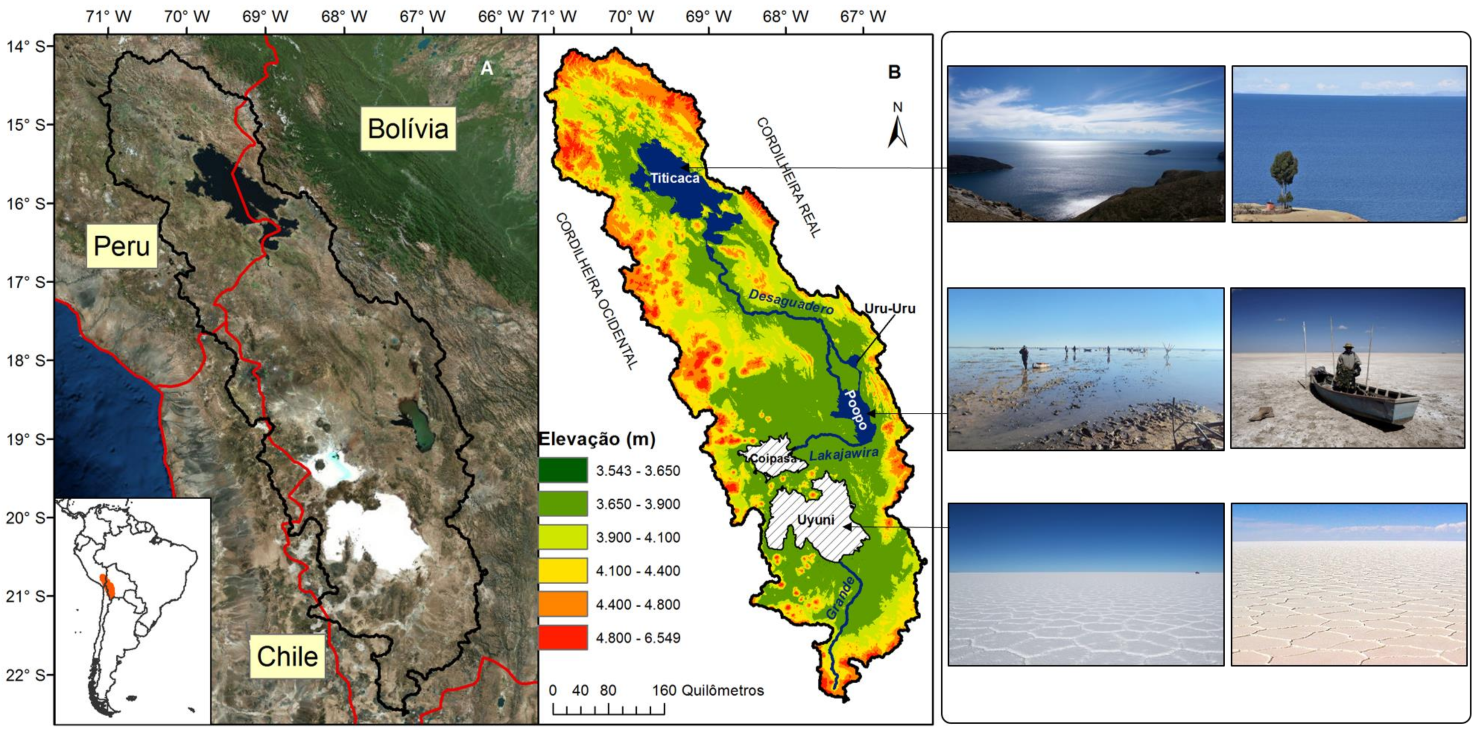

Figura 3. Área de estudo: Sistema TDPS (Titicaca, Desaguadero, Poopó, Salar) com fotos referentes aos lagos Titicaca, Poopó e ao deserto de sal de Uyuni.

Com uma superfície de aproximadamente 8.400 km^2 e profundidade média de 107 m, o lago Titicaca é o maior lago de água doce da América do Sul (Figura 4). Também é um dos maiores lagos de altitude do mundo. As precipitações e as vazões contribuem com 50 % dos aportes de água do lago (Kessler e Monheim, 1966; Richerson, 1977; Carmouze et al., 1977;

Carmouze e Aquize, 1981; Lozada, 1985; Roche et al., 1992). A bacia do Lago Titicaca (56.270 km^2) pode ser dividida em sub-bacias das quais 5 contribuem com 66.6 % da entrada de água (Figura 4 A). Contribuindo com 28 %, o rio Ramis constitui sua principal fonte de água do Lago, enquanto os rios Coata, Llave, Huancané y Suches contribuem com 16,4, 12,6, 6,5 e 2,8 %, respectivamente (Carmouze e Aquize, 1981). O lago Titicaca é composto de duas unidades: O lago maior (7.131 km^2) e o lago menor (1.426 km^2) conectado pelo estuário de Tiquina (Boulange e Aquize Jaen, 1981). As saídas de água do lago Titicaca são feitas em 90 % por evaporação. Estima-se que as infiltrações no lençol freático contribuam com 2 a 10% das saídas de água do lago (Kessler e Monheim, 1966; Carmouze et al., 1977; Carmouze e Aquize, 1981; Lozada, 1985; Roche et al., 1992).

O rio Desaguadero nasce no extremo sul do lago Titicaca e deságua no Lago Poopó depois de percorrer uma distância de 300 km (Figura 4). A sua bacia tem uma superfície de aproximadamente 30.000 km^2. O rio Desaguadero recebe água de diferentes afluentes. O aporte maior é feito pelo rio Mauri, a Oeste, com uma vazão média de 18,7 m^3.s^{-1} (Molina Carpio et al., 2012) (Figura 4B). No entanto, a vazão na entrada do rio Desaguadero está relacionada ao nível do lago Titicaca: quanto mais alto é o nível do lago Titicaca, maior é a vazão do rio Desaguadero (Pillco e Bengtsson, 2010). A vazão do rio tem uma forte variabilidade sazonal, com valores maiores na estação chuvosa (de dezembro a março). Na entrada do lago Poopó a vazão média do Desaguadero é de 66 m^3.s^{-1} na estação chuvosa (Pillco e Bengtsson, 2010).

No Centro da bacia, próximo aos lagos Uru-Uru e Poopó, o Desaguadero se divide em dois braços. Um braço desce pelo oeste até o lago Poopó e o outro braço desce pelo leste formando o lago Uru-Uru, conectado pelo Sul ao lago Poopó (Figura 4). O lago Uru-Uru, menor, tem uma superfície de 280 km^2 e profundidade média de 0,75 m. Esse lago seca anualmente na estação seca. A bacia do lago Poopó tem uma superfície de 15.000 km^2. O lago Poopó é o segundo maior lago do sistema TDPS. Devido ao contexto muito plano da região, o lago Poopó tem uma superfície variando entre 3.000 km^2 no seu máximo, até a metade desse valor na estação seca (Pillco et al., 2007). É um lago pouco profundo com uma profundidade média de 1,08 m. Vários rios temporários contribuem com 10 % da entrada de água do Lago Poopó (Figura 4C). A maior entrada é feita pelo rio Desaguadeiro, o qual contribui com mais de 60% do total da entrada. O lago tem uma exutório na parte extrema sul na direção dos salares de Coipasa pelo rio Lakajawira (Figure 1). Porem nos últimos 50 anos o rio Lakajawira levo água apenas um ano.

Para o rio Lakajawira entrar em água o nível do lago tem que suficientemente elevado para pode se contribuir aos aportes de água do salar de Coispasa pelo rio Lakajawira devido ao contexto geomorfológico (Figura 5). Portanto, o lago Poopó pode ser considerado como o ponto terminal de uma bacia formado pelas bacias do lago Titicaca, do rio Desaguadero e do lago Poopó chamada de sistema chamada de bacia TDP (Ticaca, Desaguadero, Poopó) (Figura 5).

No período Tauca (-26.000 a -15.000 anos), um lago maior e homônimo se estendia na zona dos Salares de Uyuni e Coipasa assim como a do lago Poopó, chegando próximo ao lago Titicaca (Figura 5). Com o tempo, o lago começou a secar e se separou em três bacias: A do sistema TDP e as dos Salares de Coipasa e Uyuni (Argollo e Mourguiart, 2000; Fritz et al., 2004) (Figura 4 e 5). Os Salares se preenchem de água de dezembro a março na estação de chuva formando lagos temporários muito rasos com água ultras salina.

Não existe comunicação hidrológica entre a bacia do salar de Uyuni e o resto do sistema. O principal rio da bacia do salar de Uyuni é o rio Grande, cuja vazão é temporária. Este rio se enche de água na estação úmida, durante a qual o salar se transforma em um lago temporário muito raso (<50 cm) de água ultras salina.

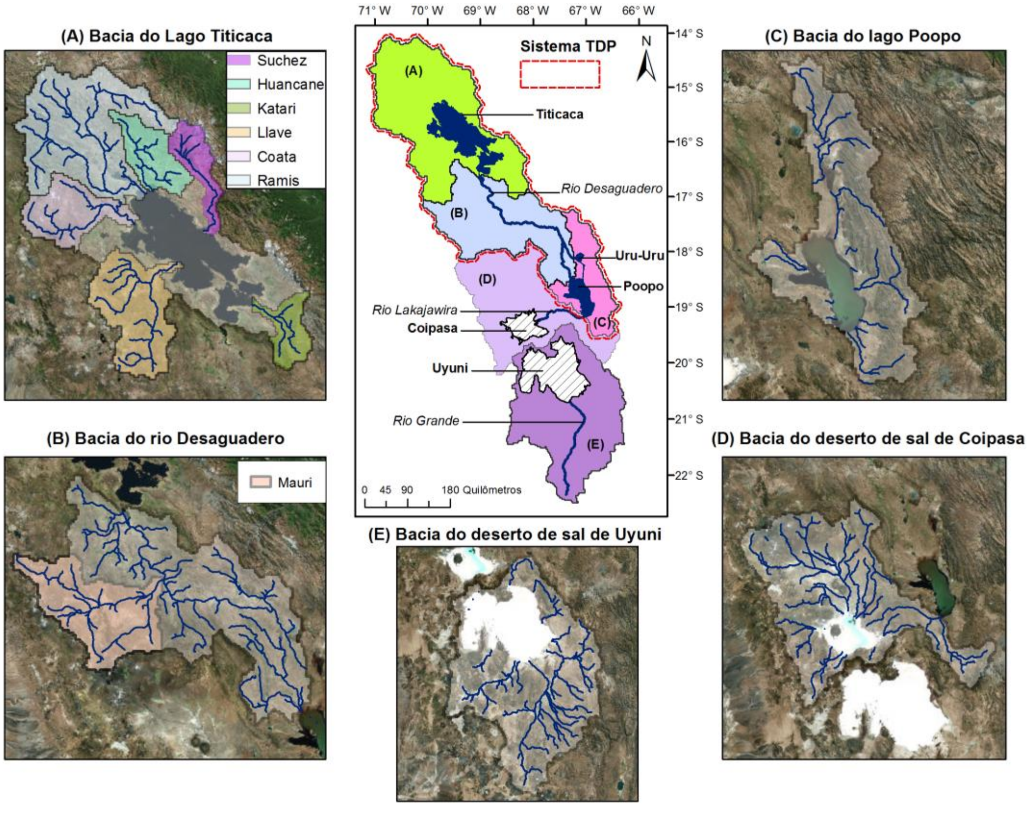
(A) Bacia do Lago Titicaca

(B) Bacia do rio Desaguadero

(C) Bacia do lago Poopo

(D) Bacia do deserto de sal de Coipasa

(E) Bacia do deserto de sal de Uyuni

Figura 4. Hidrologia do Altiplano com as principais bacias.

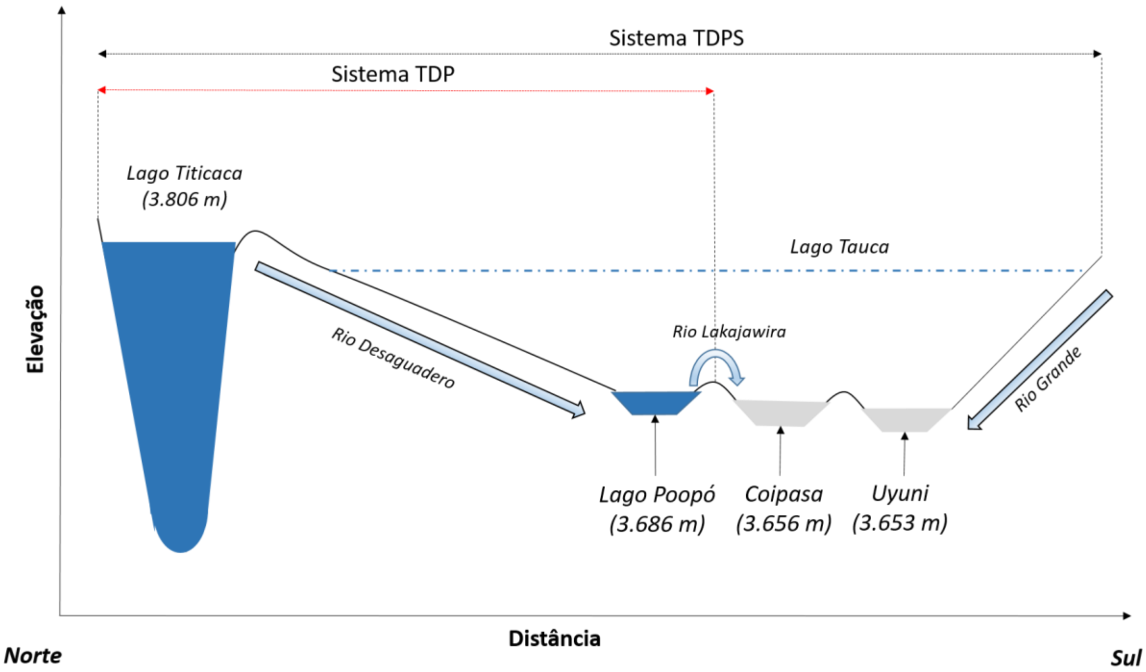

Figura 5. Seção esquematizada Norte-Sul do Altiplano representando o contexto endorreico regional. As dimensões espaciais não respeitadas (modificado de Fornari et al., 2001).

O clima no Altiplano é semiárido e está relacionado com a circulação do ar. As principais entradas de umidade ocorrem na porção nordeste, provenientes da região Amazônica (Vuille et al., 1998; Garreaud et al., 2003). Devido ao alto relevo da região, próximo a 800 m acima do nível do mar, e à inversão de temperatura, a umidade da zona pacífica não chega à região do Altiplano (; Rutllant e Ulriksen, 1979; Garreaud et al., 2003). Em consequência, as precipitações apresentam um forte gradiente norte-sul que varia de 1.100 mm.ano^{-1}, na porção norte, a 200 mm.ano^{-1}, no sul (Garreaud et al., 2003; Pillco et al., 2007) (Figura 6B). Portanto, o padrão de precipitação é o mesmo em toda a bacia hidrográfica com uma estação úmida de dezembro a março, representando uma contribuição anual de 81% no norte e 51% no sul (Guyot e Gumiel, 1990; Garreaud et al., 2003) (Figura 7). No restante do ano, os ventos Leste-Oeste da região, juntamente com o deslocamento da zona de Convergência Intertropical (*Inter Tropical Convergence Zone* - ITCZ) na parte norte da América do Sul, não permitem as entradas úmidas da região amazônica (Vuille, 1999). As médias de evapotranspiração potencial e real (ETp e ETr) foram estimadas em 1,500 e 520 mm.ano^{-1} respectivamente (Roche et al., 1992; Satgé et al., 2017a) (Figura 6 A e B). A zona norte, mais úmida, apresenta um potencial evaporativo baixo em comparação com a zona árida sul. Porém, similarmente, a disponibilidade de água é maior na porção norte que na porção sul. Portanto, a ETr segue o padrão regional inverso das precipitações, aumentando de norte para sul, enquanto as precipitações diminuem. Sazonalmente, a ETr (ETp) segue o mesmo padrão que as precipitações, com valor máximo no verão (outubro a março) e valor mínimo no inverno (abril-setembro) (Figura 7). Consequentemente, o verão corresponde a um período de estresse hídrico com uma taxa evapotranspirativa maior que as precipitações enquanto o inverno corresponde a uma recarga do estoque hídrico (Figura 7).

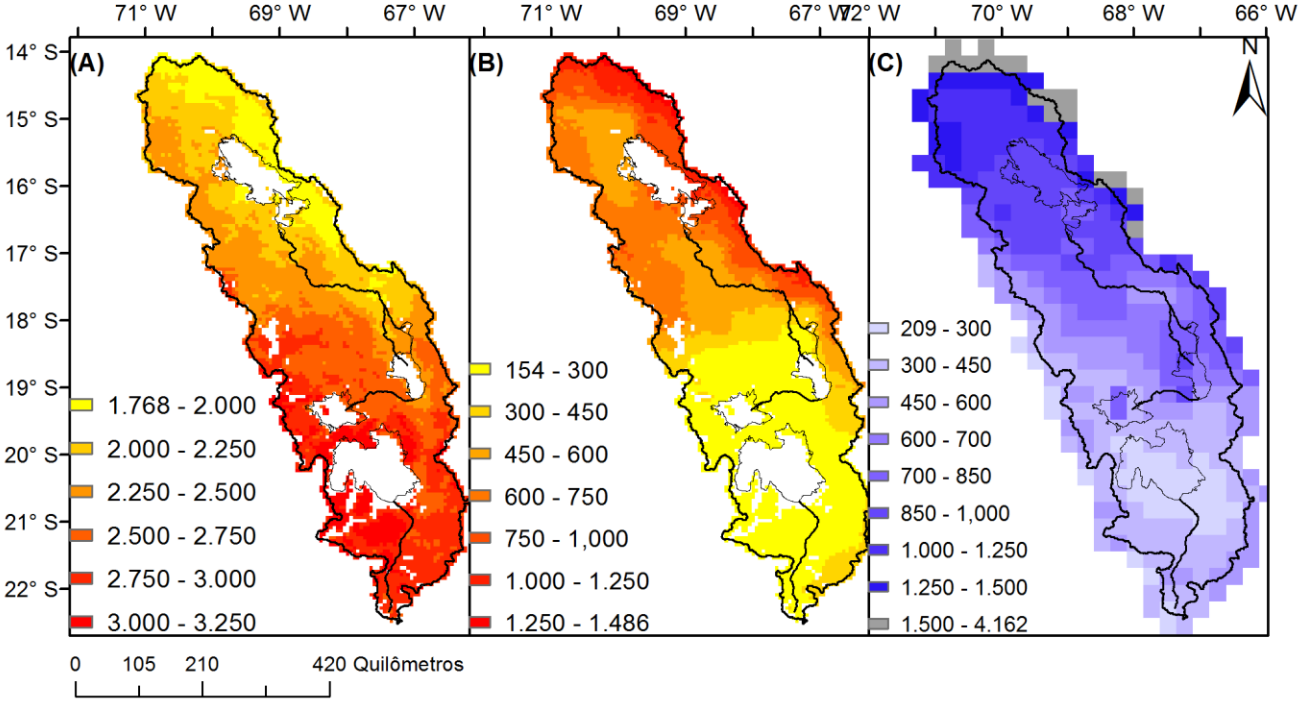

Figura 6. Evapotranspiração Potencial e Real anual média em mm derivada do MOD16 para o período 2000-2015 (A-B) e precipitação anual média em mm derivada do TMPA para o período 1998-2015 (C).

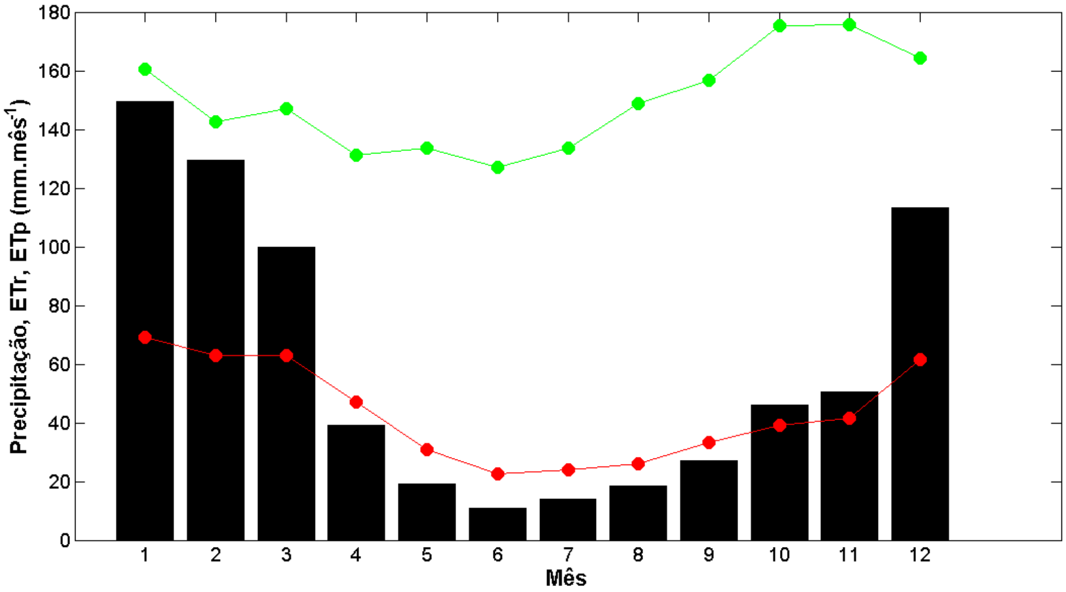

Figura 7. Precipitação (barra preta) e evapotranspiração potencial e real mensal média na escala regional extraído de TMPA e MOD16 para o período entre 2002 e 2010 (linhas verde e vermelha).

A população do Altiplano foi estimada em mais de 3 milhões de pessoas divididas entre Peru (48%) e Bolívia (52%). Composta principalmente por povos indígenas com baixa renda, estima-se que apenas 20% da população tenha acesso à água tratada (sistema de abastecimento público) e tratamento de esgoto sanitário. As atividades agrícolas, pecuária e mineral representam as principais atividades econômicas da população do Altiplano. De acordo com a classificação de ocupação do solo, apresentada em *GlobCover Land Cover* (GCLC) (Bicheron et al., 2008), a região pode ser considerada como deserta na parte sul, com dominância de vegetação rasteira, e semideserta na parte norte, com presença de vegetação um pouco mais densa do tipo urze (Figura 8A). De acordo a classificação do solo *Soil and Terrain Database for Latin America and the Caribbean* (SOTERLAC) (Koos Dijkshoorn, Jan Huting e Tempel, 2005), os solos dominantes na região são classificados como *cambisols leptosol* e *regisol (classificação World Reference Base: WRB)* (Figura 8B). Esses solos são jovens, rasos, com presencia de cascalhos e materiais grossos no horizons A e B, devido à geologia (rochas sedimentares do quaternário) e ao clima.

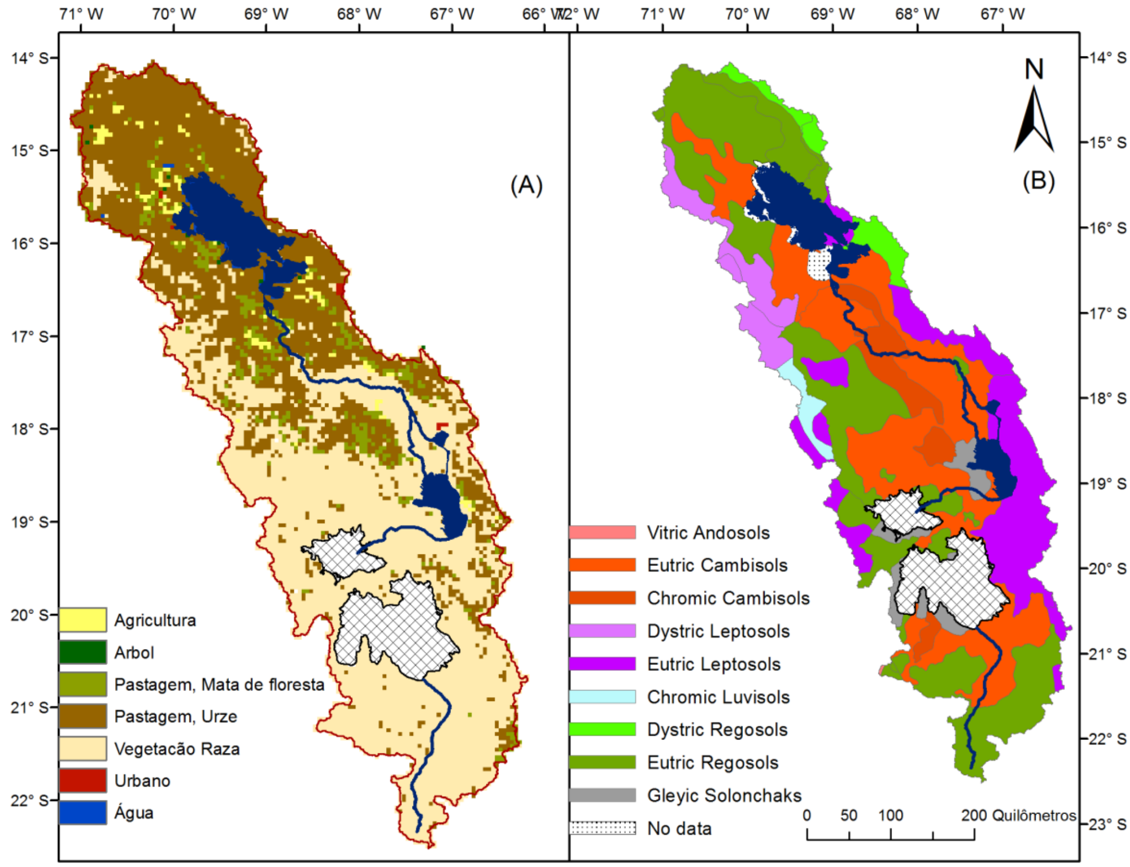

Figura 8. (A) Mapa de ocupação do solo (fonte: Global Land Cover Map) e (B) Mapa dos principais solos da região (fonte: SOTERLAC).

III. Capítulo 1

Modelo Digital de Elevação - MDE

A informação topográfica é fundamental à hidrologia, visto que a partir dela pode gerar a declividade, variável fundamental para a extração da rede de drenagem e limite da bacia hidrográfica. Nas áreas isoladas, como o Altiplano, a falta de mapas topográficos de qualidade torna os MDEs derivados de dados de SR a melhor fonte de informação topográfica regional. Vários MDEs estão disponíveis gratuitamente:

- O MDE mais conhecido e mais utilizado atualmente é o *Shutlle Radar Topographic Mission* (SRTM), produto da *National Aeronautics Space Administration* (NASA) e *National Geospatial-Intelligence Agency* (NGA). O SRTM foi gerado a partir de imagens de radar (SIR-C) e dual X-band, radar de abertura sintética (X-SAR) adquirido no dia 11 de fevereiro de 2000. Várias versões do SRTM foram liberadas ao longo do tempo. As últimas versões são o SRTM-v4 e o SRTM-GL1 (disponibilizado em novembro de 2014) com resolução espacial de 90 e 30 m, respectivamente.
- O *Advanced Spaceborne Thermal Emission and Reflection Globlal Digital Elevation Model* (ASTER GDEM) é um produto do *Ministry of Economy, Trade, and Industry* (METI) do Japão e da NASA. Cerca de 1.2 milhão de cenas de dados estereoscópicos foram coletadas pelo radiômetro ASTER a bordo do satélite Terra da NASA e foram utilizados para desenvolver um MDE conhecido como GDEM versão 1 (GDEM-v1). A segunda versão (GDEM-v2) foi desenvolvida incluindo 260.000 cenas estereoscópicas adicionais em relação à primeira versão.
- O MDE *Advanced Land Observing Satellite* (ALOS) *World 3D-30* (AW3D30) é um produto da *Japan Aerospace eXploration Agency* (JAXA). Para gerar o MDE AW3D30 foram utilizadas um total de aproximadamente 1 milhão de imagens estereoscópicas, adquiridas entre 2006 e 2011 pelo *Panchromatic Remote-sensing Instrument for Stero Mapping* (PRISM), a bordo do ALOS. O AW3D30 é o MDE mais acurado da região e foi disponibilizado em maio de 2016.

MDEs	Resolução espacial	Dados usados	Ano de disponibilização
SRTM-v4	90 m	Radar	2008
SRTM-GL1	30 m	Radar	2014
GDEM-v2	30 m	Visível	2014
AW3D30	30 m	Pancromática	2016

Tabela 1. Modelos Digitais de Elevações utilizados.

Os dados e algoritmos utilizados para a geração dos MDEs variam em função do produto considerado (Tabela 1). Como consequência, as estimativas de elevação variam entre os MDEs. Nesse contexto, vários estudos de avaliação da acurácia dos MDEs foram feitos no mundo todo. Os autores comparam as elevações a Pontos de Elevação de Referência (PERs), derivados de medições de GPS ou altímetros, com as elevações estimadas pelos MDEs. Esse tipo de estudo permite avaliar o erro vertical dos MDEs. De acordo com esses estudos, o MDE com o menor erro vertical é considerado como o MDE mais acurado. Porém, o erro dos MDEs não se limita ao erro vertical. Existe outro tipo de erro conhecido como erro relativo. O erro relativo mede o erro na diferença de elevação entre *píxels* da rede dos MDEs (por exemplo: no MDE um determinado *pixel* pode ser mais o menos elevado em comparação aos *pixels* vizinhos em quanto é o caso contrario que deveria ser observado). De acordo com a definição feita do erro relativo, um MDE pode sobre-estimar ou subestimar a declividade existente entre os elementos do MDE e, em alguns casos, os MDEs podem errar na orientação da declividade. Portanto, o erro relativo controla a descrição do esquema topográfico feito pelos MDEs. Alguns autores comparam elementos hidrológicos de referências (rede, bacia) com os mesmos derivados de differentes MDEs para ter uma aproximação do erro relativo. Os autores consideram que o MDE que consegue melhor representar os elementos hidrológicos de referência é o MDE com o menor erro relativo, já que os elementos hidrológicos dependem da topografia. Porém, essa metodologia é válida somente em escala regional (bacia), e não permite quantificar diretamente o erro relativo. Até hoje, nenhum estudo quantificou diretamente o erro relativo dos MDEs. Contudo, em geociências, os MDEs são principalmente usados para descrever o esquema topográfico controlando os processos hidrológicos e geológicos e nesse fim a escolha do MDE deveria ser feita com base no erro relativo e não no erro vertical pois é o erro relativo que informa sobre o potencial dos MDEs para representação do esquema topográfico.

Considerando o exposto acima, nesta tese de doutorado os MDEs SRTM-GL1, SRTM-v4, GDEM-v2 e AW3D30 foram avaliados na região do Altiplano com base em aproximadamente 160.000 PERs derivados dos dados altimétricos do *Geoscience Laser Altimeter System* (GLAS), a bordo do *Ice Cloud and Land Elevation Satellite* (ICESat), denominado como ICESat/GLAS a partir desse ponto do texto. O trabalho levou à publicação de 3 artigos em revistas internacionais.

O primeiro artigo "*Accuracy assessment of SRTM v4 and GDEM v2 over the Altiplano watershed using ICESat GLAS data*" publicado na revista "*International Journal of Remote Sensing*" tem foco no erro vertical dos MDEs disponíveis no momento do estudo: o SRTM-v4 e GDEM-v2 (Anexo 1: Satgé et al., 2015). O erro vertical foi medido em escala global e em diferentes classes de ocupação do solo e de declividade, considerando o desvio padrão, o erro médio quadrático e o erro médio absoluto. Os resultados mostram uma grande relação entre o erro vertical e valores de declividades. Os MDEs têm um erro vertical menor nas zonas planas, aumentando de acordo com o aumento da declividade. Por outro lado, o tipo de ocupação do solo não afeta o erro vertical dos MDEs na região estudada.

O segundo artigo "*Absolute and relative height-pixel accuracy of SRTM-GL1 over the South American Andean plateau*", publicado na revista "*Journal of Photogrametry and Remote Sensing*", tem maior foco na avaliação do erro relativo dos MDEs. O artigo descreve uma nova metodologia para quantificar o erro relativo dos MDEs (Satgé et al., 2016b). A metodologia está baseada na comparação de aproximadamente 265.000 valores de declividades derivadas dos PERs com as derivadas dos MDEs. A metodologia, que inclui um novo índice conhecido como *False Slope Ratio* (FSR), foi descrita e aplicada aos MDEs SRTM-v4, GDEM-v2 e ao novo SRTM-GL1 disponibilizado a partir de setembro de 2014. O erro relativo e vertical foi calculado para cada um dos MDEs para as mesmas classes de declividades usadas no primeiro estudo. Classes de ocupação do solo não foram consideradas, já que não houve uma influência na potencialidade dos MDEs na região, como foi mostrado no primeiro artigo (Satgé et al., 2015). Os resultados mostram a complementaridade das avaliações vertical e relativa dos MDEs. O erro relativo diminui de acordo com o valor de declividade, enquanto o erro vertical aumenta. Portanto, a consideração de um ou do outro tipo de erro leva a conclusões diferentes. Similarmente, o MDE com o menor erro vertical apresenta o maior erro relativo. Um MDE pode ser acurado pontualmente (baixo erro vertical) e, no entanto, apresentar uma descrição topográfica menos acurada do que um MDE com maior erro vertical. Finalmente, foram realizadas comparações entre uma rede de referência com as redes derivadas dos MDEs. Os resultados mostram que os MDEs com menor erro relativo são os MDEs que representam melhor a rede hidrológica de referência. De maneira geral, a metodologia proposta pode ser facilmente adaptada a outras regiões e oferece grandes perspectivas na avaliação dos MDEs para uma visão completa das suas potencialidades.

O terceiro artigo, "*ALOS World 3D-30m absolute and relative height pixel accuracy over a barren region and hydrological conditioning potential*", em revisão a ser publicado no periódico "*Journal of Hydrology*", foca na avaliação do erro vertical e relativo do MDE AW3D30, disponibilizado desde maio de 2016 (anexo 2). Considerando os erros vertical e relativo medidos no segundo artigo, o SRTM-GL1 é o MDE mais acurado da região, e foi considerado neste estudo por comparação. Os erros foram calculados para as diferentes classes de declividade previamente usadas para cada MDE, antes e depois da calibração hidrológica. Os resultados mostram que o MDE AW3D30 apresenta o menor erro vertical e relativo, tanto antes quanto depois da calibração hidrológica. É importante notar que a calibração hidrológica considerada melhora a extração da rede hidrológica a partir dos MDEs. No entanto, esta aumenta o erro vertical e relativo introduzindo, localmente, um erro na orientação e quantificação das declividades. Assim, tal calibração deve ser usada com precaução nos estudos em que os resultados são controlados por valores de declividade (erosão, movimento de terreno ou precisam de alta precisão nas estimativas pontuais de elevação (georeferenciamento).

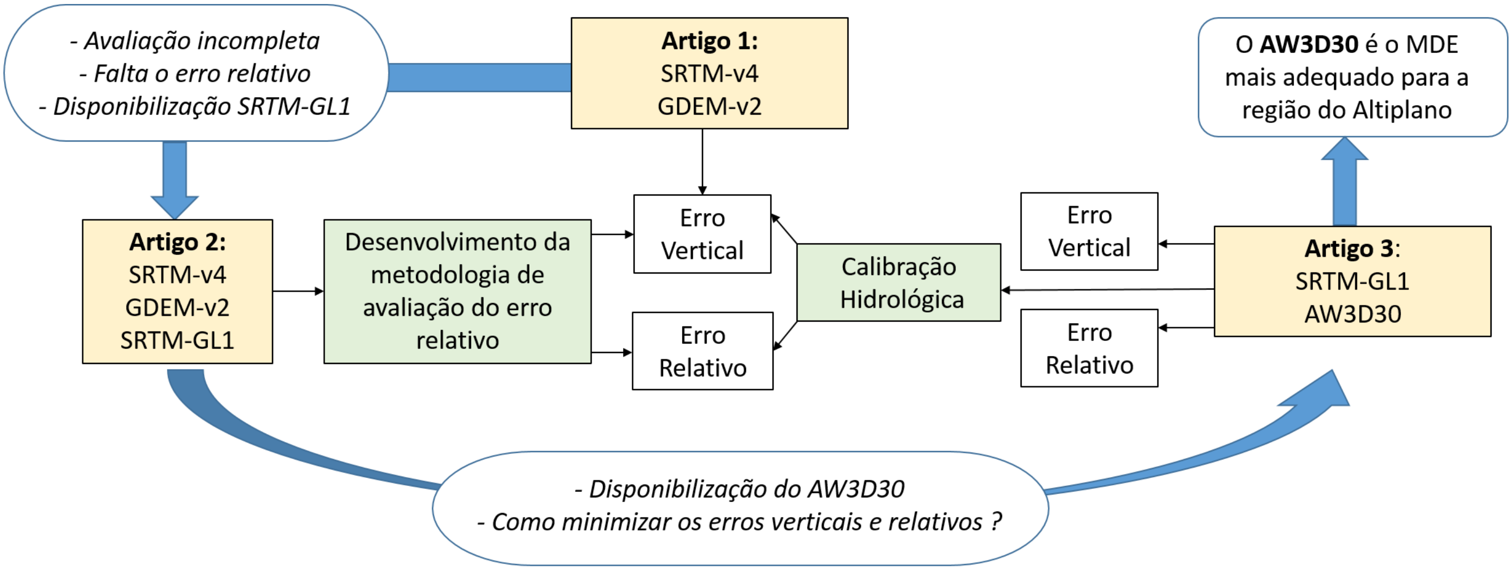

Figure 9. Esquema de síntese do trabalho nos MDEs realizado no quadro deste doutorado.

A Figura 9 esquematiza a dinâmica dos trabalhos no âmbito do doutorado e as interconexões e complementaridade existentes entre os diferentes estudos e publicações. O segundo artigo, que introduz a nova metodologia de avaliação do erro relativo junto à avaliação do erro relativo e absoluto dos MDEs SRTM-v4, SRTM-GL1 e GDEM-v2, é apresentado para ilustrar o capítulo. Os demais artigos se encontram disponíveis anexos neste doutorado.

Absolute and relative height-pixel accuracy of SRTM-GL1 over the South American Andean Plateau

---

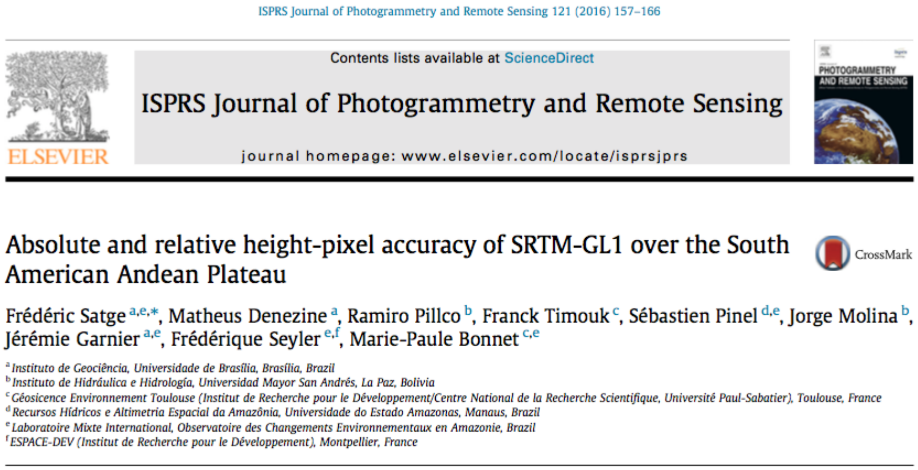

ISPRS Journal of Photogrammetry and Remote Sensing 121 (2016) 157–166

Contents lists available at ScienceDirect

ISPRS Journal of Photogrammetry and Remote Sensing

journal homepage: www.elsevier.com/locate/isprsjprs

Absolute and relative height-pixel accuracy of SRTM-GL1 over the South American Andean Plateau

Frédéric Satge [a,e,*], Matheus Denezine [a], Ramiro Pillco [b], Franck Timouk [c], Sébastien Pinel [d,e], Jorge Molina [b], Jérémie Garnier [a,e], Frédérique Seyler [e,f], Marie-Paule Bonnet [c,e]

[a] *Instituto de Geociência, Universidade de Brasília, Brasília, Brazil*
[b] *Instituto de Hidráulica e Hidrología, Universidad Mayor San Andrés, La Paz, Bolivia*
[c] *Géosicence Environnement Toulouse (Institut de Recherche pour le Développement/Centre National de la Recherche Scientifique, Université Paul-Sabatier), Toulouse, France*
[d] *Recursos Hídricos e Altimetria Espacial da Amazônia, Universidade do Estado Amazonas, Manaus, Brazil*
[e] *Laboratoire Mixte International, Observatoire des Changements Environnementaux en Amazonie, Brazil*
[f] *ESPACE-DEV (Institut de Recherche pour le Développement), Montpellier, France*

Abstract

Previously available only over the Continental United States (CONUS), the 1 arc-second mesh size SRTM-GL1 (Shuttle Radar Topographic Mission – Global 1) product has been freely available worldwide since November 2014. With a relatively high spatial resolution, this digital elevation model (DEM) provides valuable topographic information over remote regions. SRTM-GL1 is assessed for the first time over the South American Andean Plateau in terms of both the absolute and relative vertical point-to-point accuracies at the regional scale and for different slope classes. For comparison, SRTM-v4 and GDEM-v2 Global DEM version 2 (GDEM-v2) generated by ASTER (Advanced Spaceborne Thermal Emission and Reflection Radiometer) are also considered. A total of approximately 160,000 ICESat/GLAS (Ice, Cloud and Land Elevation Satellite/Geoscience Laser Altimeter System) data are used as ground reference measurements. Relative error is often neglected in DEM assessments due to the lack of reference data. A new methodology is proposed to assess the relative accuracies of SRTM-GL1, SRTM-v4 and GDEM-v2 based on a comparison with ICESat/GLAS measurements. Slope value derived from DEMs and ICESat/GLAS measurements at approximately 265,000 ICESat/GLAS point pairs are compared using quantitative and categorical statistic analysis with introducing a new index: the False Slope Ratio (FSR). Additionally, a reference hydrological network is derived from Google Earth and compared with river networks derived from the DEMs to assess each DEM's potential for hydrological applications over the region. In terms of the absolute vertical accuracy on a global scale, GDEM-v2 is the most accurate DEM, while SRTM-GL1 is more accurate than SRTM-v4. However, a simple bias correction makes SRTM-GL1 the most accurate DEM over the region in terms of vertical accuracy. The relative accuracy results generally did not corroborate the absolute vertical accuracy. GDEM-v2 presents the lowest statistical results based on the relative accuracy, while SRTM-GL1 is the most accurate. Vertical accuracy and relative accuracy are two independent components that must be jointly considered when assessing a DEM's potential. DEM accuracies increased with slope. In terms of hydrological potential, SRTM products are more accurate than GDEM-v2. However, the DEMs exhibit river extraction limitations over the region due to the low regional slope gradient.

Keywords: Digital Elevation Model, SRTM, accuracy, South America, Andean Plateau

1. Introduction

Digital elevation models (DEMs) are widely used around the world to represent topographic features used in many hydrological and geomorphological studies. A variety of DEMs are now freely available. Numerous studies have used inter-comparison techniques to determine the most accurate DEM in a certain region. Most of these studies compare elevation accuracies between available DEMs. Accurate ground control points (GCPs) derived from global positioning systems (GPS) (Athmania and Achour, 2014; Hirt et al., 2010; Zhao et al., 2010) or high quality altimetry measurements (Carabajal, 2011; Enble et al., 2012; Satgé et al., 2015; Zhao et al., 2010) are used as ground references to compute the elevation errors of the DEMs. A large GCP data set allows for comparisons of different land uses and/or slope classes (Carabajal et al., 2010; Carabajal, 2011; Enble et al., 2012; Satgé et al., 2015), providing insight regarding a DEMs elevation accuracy. If the GCP data set is large enough, such an approach is suitable for assessing the absolute vertical accuracy (Li and Wong, 2010). Moreover, recurrent errors can be documented and elevation corrections can be made by researchers to reduce a DEMs vertical error (Arefi and Reinartz, 2011; Satgé et al., 2015; Zhao et al., 2011; Pinel et al., 2015). However, these studies have generally focused on elevation accuracy and have not considered the errors of the eight neighboring pixels. For a specific pixel, the elevation can be higher or lower than those of the neighboring pixels. As a result, a false Earth Superficial Shape (here after call ESS) can be observed in some DEMs. Thus, the elevation of DEM can be accurate while not necessarily providing the most accurate ESS (El Hage et al., 2012). The absolute vertical accuracy and ESS description are complementary, as they are relevant for different purposes. The elevation accuracy is required for orthorectification, while the shape quality is used for geomorphology and hydrology applications (El Hage et al., 2012). However, most studies have focused on the elevation accuracy.

Hydrological processes, such as hydrological network mapping or watershed delineation, strongly rely on the ESS because it drives surface flows (Wechsler, 2006). These features can be numerically retrieved from the DEM through successive computational steps, such as via the D8 algorithms (Jenson and Domingue, 1988; O'Callaghan and David M. Mark, 1991), which were scripted in GIS software (ArcGIS and GRASS). Algorithms rely on the point-to-point elevation relationships in DEMs; thus, inconsistencies in DEM-derived features depend on DEM ESS representation and provide indirect information about a DEM's relative accuracy. In this context, assuming the algorithm used is free of errors, some studies compared hydrological features derived from DEMs with reference features, providing indirect information about a DEM's relative accuracy.

Reference data can be obtained from different sources, such as national or international water services (Vogt et al., 2003), high-accuracy DEMs (Li and Wong, 2010) or high-resolution imagery (El Hage et al., 2012; Metz et al., 2011; Paz and Collischonn, 2007). Researchers generally utilize reference hydrological networks (RHNs) and DEM-derived hydrological networks (DHNs). Polygon buffers are generated from the RHN. The percentage of the DHN within the buffer is computed to assess the DHN's degree of confidence (Bothale et al., 2013; Vogt et al., 2003). The distance or overlap between the RHN and DHN (Le Coz et al., 2009; Rahman et al., 2010), correctness (Cr) and figure of merit (FM) are also used by some researchers (Bothale et al., 2013; Li and Wong, 2010). Reference and DEM-derived watersheds can also be compared based on size, area or mean slope (Bothale et al., 2013). The better the match between the derived features and reference, the better the relative accuracy of the DEM is.

Previously available for the continental United States (CONUS) at no charge, SRTM-GL1 data are now available at a global scale (60° N to 56° S). With an improved resolution of 30 m, this data set is expected to provide more detailed elevation analyses than the previous 90 m SRTM products. Few studies have assessed the SRTM-GL1 accuracy. Some have focused on absolute vertical accuracy using altimetry data (Carabajal and Harding, 2006). Other studies have assessed the data set's potential for hydrological studies (Dowling et al., 2011; Li and Wong 2010). Recently, two studies assessed both the vertical accuracy and hydrological potential (Jarihani et al., 2015; Pinel et al., 2015). Even if the derived hydrological features provide a high relative accuracy, they are often limited to a large scale (watershed scale). Moreover, reference hydrological data are often missing over remote regions or are of poor quality, limiting the use of such a methodology.

We proposed the use of ICESat altimetry data to assess the relative accuracy of DEMs at a finer spatial scale. The methodology was applied to SRTM-GL1, SRTM-v4 and GDEM-v2 data sets over the South American Andean Plateau. The SRTM-GL1 accuracy was assessed in terms of the absolute vertical accuracy, as the vertical and relative accuracies are complementary. The results were compared with those previously observed for SRTM-v4 and GDEM-v2 data sets over the same region. Finally, a standard GIS algorithm was used to extract hydrological networks from all the DEMs. The derived hydrological networks were compared with a reference hydrological network derived from Google Earth (GE) to assess the DEM efficiencies in the context of hydrological modelling.

2. Study area and Data sets

2.1 Study area

The Altiplano watershed is an endorheic system located between the latitudes of 22° S and 14° S and longitudes of 71° and 66° W. The watershed encompasses a total area of approximately 192,390 km2. The Altiplano watershed is shared by three countries: Bolivia (70 %), Peru (26 %) and Chile (4 %). The climate of this region is semi-arid with low precipitation. Approximately 82.7 % of precipitation occurs during the 5 rainy months, while the total amounts vary between the north (approximately 715 mm year−1) and south (170 mm year−1) (Satgé et al., 2016a). The Altiplano can be considered a desert region where barren areas and shrub cover are predominant. Urbanized areas, water bodies and salt areas account for 0.1 %, 3.5 % and 5.3 % of the entire area, respectively (Satgé et al. 2015). The elevation of the region varies between 3500 and 6500 m, with a mean elevation of 4000 m. The region includes the Titicaca Desaguadero Poopó Salar (TDPS) system, which is composed of Lake Titicaca, the Desaguadero River, Poopó Lake and the Coipasa Salt Pan (or Salar) Basin. The lowest elevations are mainly located in the southern portion of the region and in the floodplain of the Desaguadero River. This river serves as a connection between Lake Titicaca in the north and the Uru-Uru and Poopó lakes in the central portion of the basin. The Altiplano Plateau is a flat region with a mean slope of approximately 5°. High relief areas are found in two cordilleras (Occidental and Royal) that form the western and eastern borders of the watershed. In addition, our study area includes Uyuni Salar, which is located south of the TDPS system but is not part of the same watershed (Figure 1).

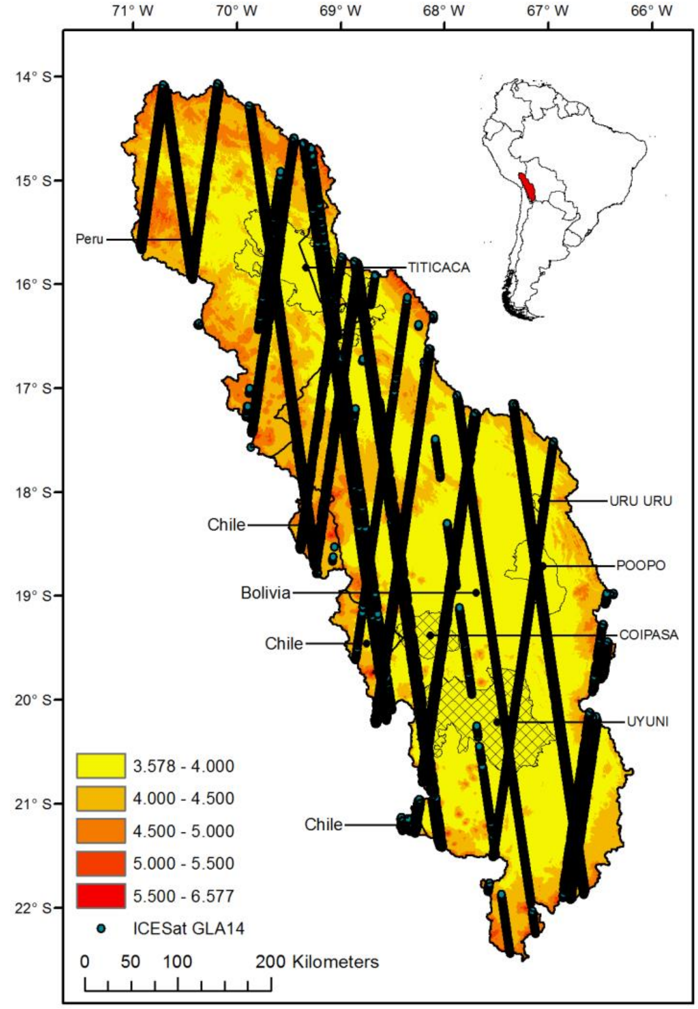

Figure 1. SRTM-GL1 DEM of the study area with GCP locations

2.2 Data sets

2.2.1 DEMs

This study focused on the newly released SRTM Global 1 arc-second DEM (SRTM-GL1). The data set is a joint product of the National Geospatial-Intelligence Agency (NGA) and the National Aeronautics and Space Administration (NASA). Data were collected over 11 days in February 2000 using dual spaceborne imaging radar (SIR-C) and dual X-band synthetic aperture radar (X-SAR). The SRTM-GL1 data features a resolution of 1 arc-second (30 m near the equator) and spans 60° N to 56° S. Previously, the native 1 arcsecond (arcsec) version (SRTM-GL1) was available for free over the CONUS, while the mesh size was limited to 3 arcsec outside CONUS. The SRTM-GL1 data have been freely available for Europe, South America and Africa since November 2014. They can be downloaded at NASA´s Earth Observing System Data and Information System (EOSDIS) website (http://reverb.echo.nasa.gov/). Data are delivered as 1° by 1° tiles referenced to the World Geodetic System 84 (WGS84) ellipsoid and Earth Gravitational Model 1996 (EGM96) geoid. 33 SRTM-GL1 tiles were required to cover the study area. The 1 arcsec Global Digital Elevation Model version 2 (GDEM-v2) from NASA and and the latest 3 arcsec SRTM version (SRTM-v4) data sets were also utilized for comparison. GDEM-v2 was jointly developed by the Ministry of Economy, Trade, and Industry (METI) of Japan and NASA using stereoscopic data collected by the advanced spaceborne thermal emission and reflection radiometer (ASTER) aboard the NASATerra spacecraft (ASTER GDEM Validation Team: USGS/EROS METI/ERSDAC NASA/LPDAAC 2009). The elevation accuracies of SRTM-v4 and GDEM-v2 products were previously assessed over the same study area (Satgé et al., 2015). For more information about SRTM-v4 and GDEM-v2, please refer to Satgé et al. (2015). All DEMs (SRTM-GL1, v4 and GDEM-v2) are referenced to the WGS84 ellipsoid and EGM96 geoid.

2.2.2 ICESat/GLAS

The ICESat/GLAS data were produced by NASA. The data were collected between 12 January 2003 and 11 October 2009 by the geoscience laser altimeter system (GLAS) aboard the Ice Cloud and Land Elevation Satellite (ICESat). The footprint size is approximately 70 m, with one elevation measurement every 172 m and inter-track spacing of 30 km (near the equator). The altimeter measures the two-way travel time of a pulse that is reflected by the ground. GLA14 v33 Global Land-Surface Altimeter data were used, as they are specifically suited for land-surface elevation studies. The data are referenced to the TOPEX/Poseidon ellipsoid and EGM96 geoid and can be downloaded through the NASA website (NASA 2014b). The National Snow and Ice Data Center (NSIDC) provides an IDL routine for reading ICESat/GLAS data and for extracting information in a readable array format with the latitude, longitude, elevation and geoid of each measured point. Thus, this script was used in this study. The ICESat/GLAS vertical accuracy at the global scale is approximately 15 cm under good conditions (Zwally et al., 2002). The SRTM-v4 absolute accuracy is 8.8 m based on the mean absolute error on the Andean Plateau (Satgé et al., 2015). Because SRTM-v4 is derived from SRTM-GL1, ICESat/GLAS data are accurate enough to be used as GCPs for assessing SRTM-GL1.

2.2.3 Google Earth

GE is a free software product that was released by Google in 2005. It provides an easy interface for observing the Earth's surface using high-resolution images. Most of the images used by GE are from Digital Globe QuickBird (2.65 m spatial resolution); however, many images are being actively replaced by SPOT (2.5 m spatial resolution) and higher resolution imagery (Mohammed et al., 2013). Where high resolution images are not available, GE uses LandSat imagery (30 m spatial resolution) (Potere, 2008). Thus, GE provides a valuable tool for validating land cover information across the world with a high degree of reliability (Baker et al., 2001). Before being used by GE, images are processed via geometric corrections and orthorectifications, which can modify their original horizontal accuracies. However, GE does not provide such information. In this context, various studies have assessed the horizontal accuracy of GE. A 1.63 m RMSE was found over Texas (Benker et al., 2011) by comparing traced positions extracted from GE with high-precision (<1 m) field measurements. Using GCPs derived from a rural cadastral database, a 5 m RMSE value was found for the positional accuracy in northeastern Mexico (Paredes-Hernández et al., 2013). More recently, an RMSE value of 2.18 m RMSE was determined in Riyadh, Saudi Arabia (Farah and Algarni, 2014) and an RMSE value of 1.59 m was found in Khartoum, Sudan (Mohammed et al., 2013) using GPS measurements as reference data. Finally, a 10.58 m RMSE value was found over Cairo by extracting coordinates from a georeferenced GE scene instead of by direct extraction from GE (Ragheb, 2015).

In remote regions such as the Altiplano, such a high positional accuracy makes GE the most widely available free tool for accurately detecting reference hydrological networks via visual inspection. Most rivers of the region are a few meters wide (<10 m). Thus, detecting rivers from LandSat imagery, as demonstrated by (Paz and Collischonn, 2007), can be difficult because the spatial image resolution is often lower than the river size. With a 2.5 meters spatial resolution image available over the Andean Plateau, an accurate manually digitized hydrological network is attainable using GE. Finally, the GE-derived network was referenced to the same positioning system as the DEMs (WGS84 ellipsoid) using ArcGIS.

3. Methods

3.3 DEM data preprocessing and GPC selection

The first preprocessing step referenced all of the data to the same ellipsoid and geoid systems. The NSIDC-provided IDL tool called 'IDL Ellipsoid Conversion' was used to convert the GLA14 latitude and elevation array from Topex/Poseidon (T/P) to WGS84 (http://nsidc.org/data/icesat /tools.html). Then, EGM96 was computed using the interpolation program available on the NGA website (http://earth-info.nga.mil/GandG/wgs84/gravitymod/egm96/egm96.html) at each ICESat/GLAS measurement location. This result was subtracted from the GLA14 elevation to obtain the GLA14 value referenced to the SRTM-GL1 system (WGS84/EGM96). GCPs were selected according to a quality control analysis based on several flags provided by NSDIC, ensuring the best possible accuracy over the study area (Satgé et al., 2015). A total of 157,254 GCPs were available for this study. The SRTM-GL1 data elevations were computed for all GLA14 points using a two-dimensional linear interpolation tool available in Matlab. Finally, the slopes were computed using the ArcGIS Spatial Analyst tool at each GCP location based on SRTM-v4. For each pixel including a GCP, the elevation difference was computed between it and its neighbors. Then, the maximum change in elevation was used to compute the slope at the GCP location.

3.4 Elevation Accuracy

We assessed SRTM-GL1 elevation accuracy by comparing its elevation with the GCP elevations based on the mean error (ME), standard deviation (STD) and root mean square error (RMSE) (equations 1 through 3).

$$(1)\ ME = \frac{\sum_{i=1}^{i=n}(x_i - y_i)}{n}$$

$$(2)\ STD = \sqrt{\frac{1}{n-1}\sum_{i=1}^{i=n}[(x_i - y_i) - ME]^2}$$

$$(3)\ RMSE = \sqrt{\frac{\sum_{i=1}^{i=n}[(x_i - y_i)^2]}{n}}$$

$$(4)\ MAE = \frac{\sum_{i=1}^{i=n}(|x_i - y_i|)}{n}$$

Where n is the number of values, x is the GCP value (meters), y is the DEM value (meters) and ME is the mean error.

We first computed those statistical parameters on a regional scale using the entire GCP data set. Then, different slope classes were considered. The slope classes used in this study are the same as those used in Satgé et al. (2015) to allow for comparison between SRTM-GL1 results and the results previously found for SRTM-v4 and GDEM-v2. The slopes are based on the histogram distribution of 0°-2°, 2°-5°, 5°-10°, 10°-20° and >20° and correspond to 55 %, 16 %, 14 %, 13 % and 2 % of the GCP data set, respectively. ME, STD and RMSE values were computed for each SRTM-GL1 class. The slope value at each GCP location was derived from SRTM-v4. The slopes derived from SRTM-GL1 differ from those computed from SRTM-v4, with an absolute mean error of 0.9º (STD=7º). Thus, different results may be observed due to the SRTM-GL1 slope. However, as the assessment is based on slope classes, the difference is not large enough to influence our analysis. Indeed, results obtained from slope classes based on SRTM-v4 and GL1 values exhibit good agreement. Hereafter, we present results based on the SRTM-v4 slope values. Slopes derived from GDEM-v2 were not considered based on the low relative accuracy determined in this study.

Land-cover classes were found to not impact the DEM elevation accuracies over the Altiplano. DEM accuracies remained stable when vegetation cover types with different heights were analyzed (Satgé et al. 2015). Thus, we do not include land-cover classes in our analysis.

Note that no significant horizontal shift was found between SRTM-v4 and either GDEM-v2 or GCP data sets (Satgé et al., 2015). As SRTM-v4 is derived from SRTM-GL1, it is assumed that SRTM-GL1 does not present a significant horizontal shift with respect to other DEMs and GCPs.

3.5 Relative accuracy

On a DEM matrix, point elevation could be higher or lower than its neighboring points (Figure 2). Here, relative accuracy term is used to refer to the point-to-point elevation relationship and how well the point-to-point elevation relationship observed in DEMs match with GCPs one. Slope value between neighboring is function of the point-to-point elevation relationship and thus can be used to quantify DEMs relative accuracy. Thus, slopes between GCPs are computed for all point pairs in the region using all DEMs and GCPs. Close slope value between DEMs and GCPs mean good relative accuracy while far slope value means low relative accuracy. Because the mesh size of the DEMs is 90 m, we only consider the slopes computed between points separated by at least 100 m. A maximum distance threshold value between point pairs was arbitrarily fixed at 500 m. We assume that slopes above this threshold value are more representative of the regional shape than the DEM's relative accuracy. To account for the global absolute vertical accuracy of ICESat (15 cm), we only consider slopes retrieved from GCPs with elevation differences greater than or equal to 1 m. In summary, only GCPs point horizontally distant from 100 to 500m with an absolute elevation difference superior to 1m were considered. According to this selection procedure, a data set of 263,535 slope values was used to compare DEMs and GCPs. Unlike the elevation, the slopes are not expected to be only positive over the study region. Thus, ME is expected to be insignificant, with values close to 0. In addition, the RMSE should yield similar results as the STD. In this context, MAE (equation 4) was preferred to ME for quantifying the relative DEM accuracy jointly with STD. % MAE and % STD were computed by dividing MAE and STD by reference mean absolute values obtained from GCPs, which were computed at the global scale for all slope classes. A total of 128,413, 59,591, 45,465, 28,302 and 3617 slope measurements were available for the 0°-2°, 2°-5°, 5°-10°, 10°-20° and >20° classes, respectively.

Finally, we used a statistical analysis to evaluate each DEM's relative accuracy. Slope is considered a discrete value with only two options: positive or negative value. Two outcomes are possible: (a) DEMs and GCPs report the same slope trend or (b) DEMs and GCPs report different slope trends (Figure 2).

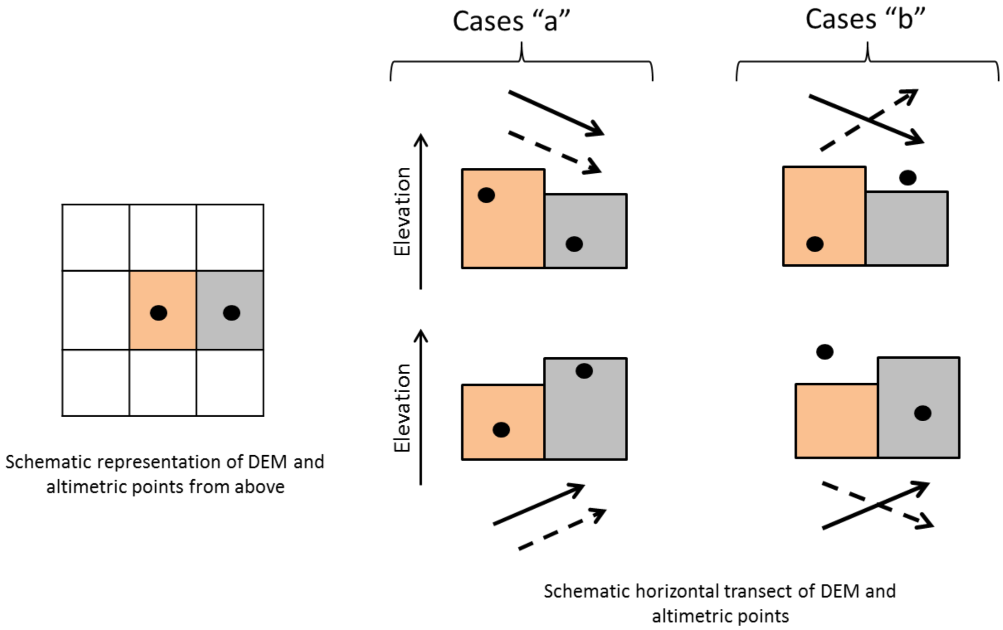

Figure 2. Categorical statistic approach. Black points represent GCPs, black and dotted arrow represent the slope orientation from DEM and GCPs, respectively.

According to this characterization, the False Slope Ratio (FSR) can be computed:

$$FSR = \frac{B}{A + B} \times 100$$

Where A and B are the total number of observed cases “a” and “b”, respectively.

Values vary from 0 to 100, with a perfect score of 0. FSR was first computed for all DEMs considering the reference data and slope classes separately.

3.6 Hydrological application

DHNs were computed from all DEMs using the Arc Hydro tool in ArcGIS 10.2 (Maidment, 2002). This tool is based on the D8 algorithm. Arc Hydro is commonly used for hydrological analyses. We do not consider enhanced algorithms or methodologies because they seek to overcome local DEM errors and improve hydrological feature extraction. Our procedure included 4 major steps that were applied successively. All sinks were first filled using the ‘fill sink’ function to ensure flow continuity across the study area. To account for the endorheic regional context, lakes, salt areas and the associated flood plains were masked in each DEM. Using the filled DEMs, the ‘flow direction’ function was applied to define the direction of the steepest descent in each cell. The result is used by the 'flow accumulation' function, which defines the number of accumulated upstream cells for each cell. Finally, the hydrological network was extracted using the 'stream definition' function, which defines rivers based on a threshold value for the contributing area. The number of extracted rivers varies with the threshold value. Thus, a larger threshold reduces the number of sufficiently small streams, while a smaller threshold may create some stream features that do not actually exist. In this study, a fixed threshold value of 23.5 km2 was used to extract rivers. Finally, Strahler classification (Strahler, 1952) was used to select third-order or higher rivers, denoting significant rivers. All other rivers were excluded from the analysis.

The RHN was manually digitalized from GE. We only digitalized rivers included in at least one DHN. To ensure significant comparisons, artifact rivers in DHNs were used in the analysis and the length of each river extracted from the GE and DEM data sets was limited to the maximum length of the corresponding river among all DHNs (Figure 3).

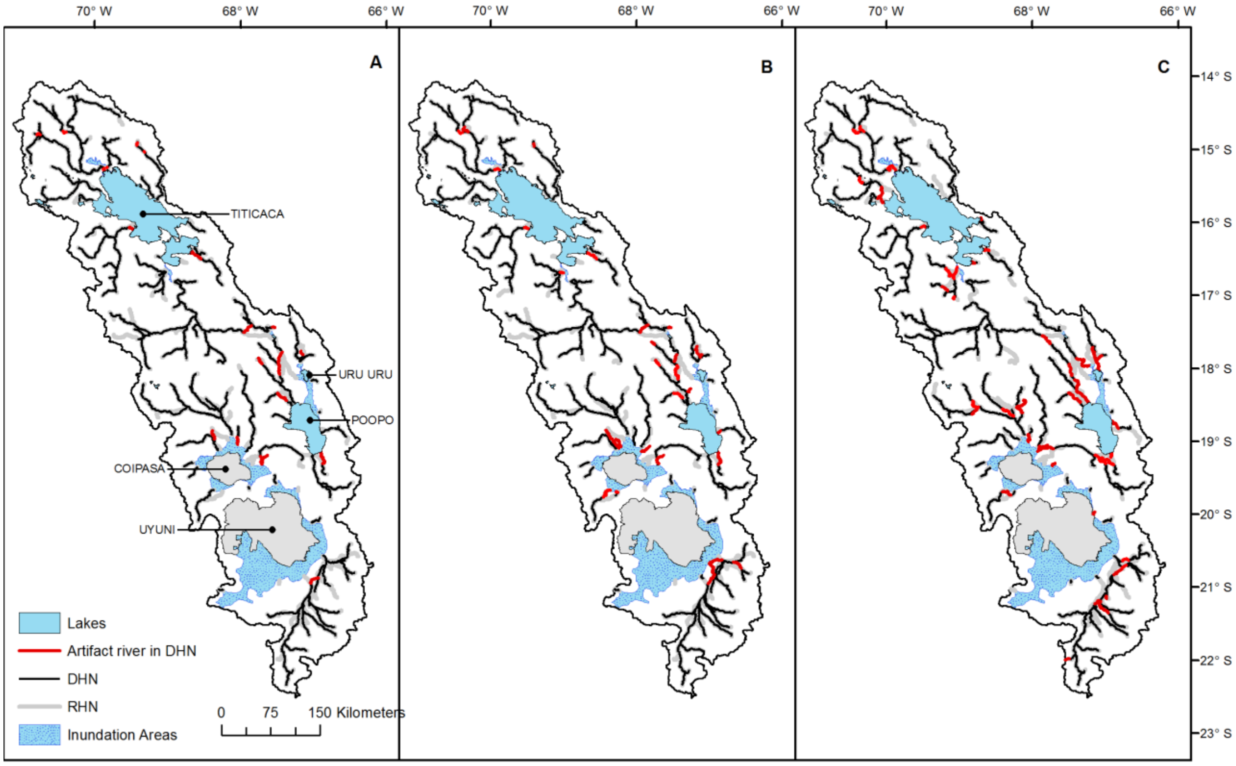

Figure 3. DHNs vs RHN for (A) SRTM-GL1, (B) SRTM-v4 and (C) GDEM-v2

First, a visual comparison was conducted to highlight obvious discrepancies between the DHNs and RHN (Figure 3). Second, the DHNs and RHN were converted to grids to compute correctness (Cr) and figure of merit (FM) indices (equations 5 and 6). These indices were used to assess the similarity between the RHN and DHNs (Li and Wong 2010; Pontius et al. 2008). A pixel size of 100 m was used to account for the 90 m mesh size of the SRTM-v4 data and the global positioning accuracy of GE, which is approximately 10 m according to the literature. Cr indicates the proportion of RHN correctly represented by the DHNs. FM indicates how well the DHNs can replicate the RHN.

$$(5)\ C_r = \frac{N_{A\cap B}}{N_B}$$

$$(6)\ FM = \frac{N_{A\cap B}}{N_{A\cup B}}$$

Where N_B is the number of cells representing the RHN, $N_{A\cap B}$ is the number of DHN cells overlapping RHN cells and $N_{A\cup B}$ is the sum of all DHN and RHN cells. A cell size of 100 m was used to compute both Cr and FM for all DHNs.

4. Results and Discussion

4.1 Elevation Accuracy

On a regional scale, a negative bias of 7 m is observed in both SRTM-v4 and GL1 (Table 1; Figure 4), while a positive bias of 0.8 m is observed for GDEM-v2. SRTM-GL1 presents a higher bias than GDEM-v2; however, its error is less dispersed and it has a lower STD value. GDEM-v2 has a lower RMSE than SRTM products due to a lower ME (Table 1).

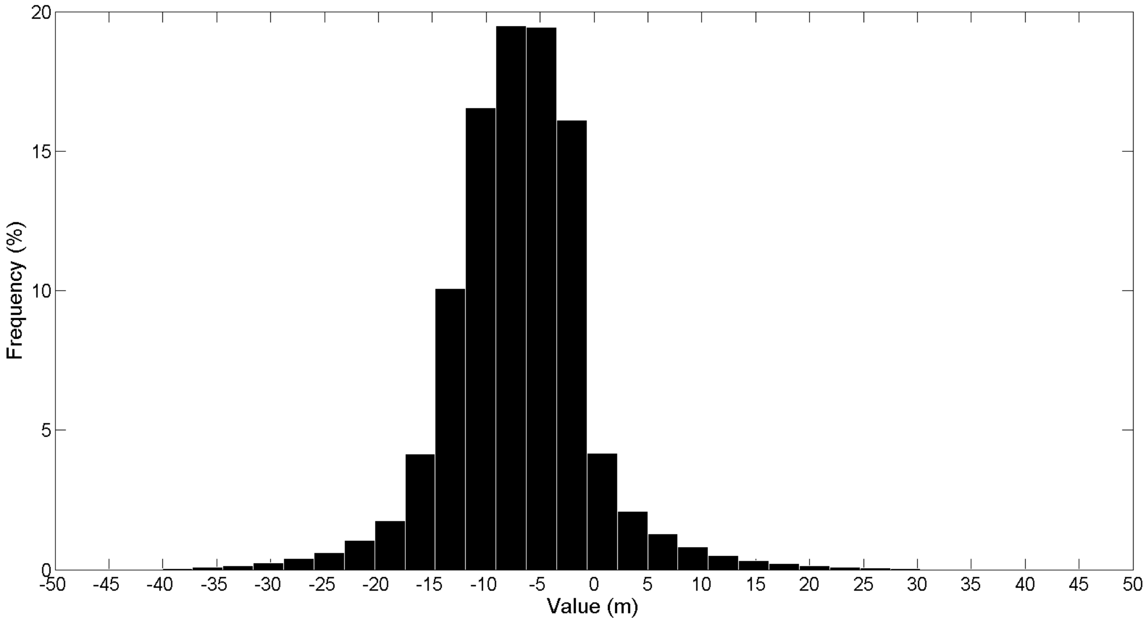

Figure 4. Error distribution of SRTM-GL1

Considering slope classes, SRTM-v4 and SRTM-GL1 exhibit the same ME, STD and RMSE values for mean slope values lower than 2° (Table 1). Differences increase with mean slope value, likely due to the aggregation process associated with shifting from a 1- to 3 arc-second mesh size. In flat areas, this procedure does not impact the elevation accuracy, as the elevation variations from pixel to pixel are low. In mountainous regions, elevation changes between points can be large based on the aggregation of 9 pixels in close proximity. Additionally, errors are introduced by the linear interpolation method used to retrieve DEM elevations at each GCP location. Linear interpolations are expected to be more significant at a lower mesh size, such as SRTM-GL1, than at a higher mesh size, such as SRTM-v4. Generally, SRTM-GL1 provides a more accurate estimation of elevation than SRTM-v4 for regions with mean slopes larger than 2°. When compared to GDEM-v2, SRTM-GL1 exhibits higher absolute error but lower STD. Above slopes of 10°, SRTM-GL1 exhibits lower RMSE than GDEM-v2. In the case of GDEM-v2, STD and RMSE values are equal for all classes. This is because the GDEM-v2 distribution error is approximately 0. In this case, the mean error tends to 0 and the STD and RMSE equations become equal. This is not observed for SRTM products because of negative bias, which results in mean error values smaller than 0.

On a global scale, the results depend on the representativeness of study area GCPs. For example, the study area has a mean slope of 5.4° based on SRTM-v4 values; however, the GCP data set has a mean slope of 4.2°. Thus, the regional-scale results are slightly influenced by low slope areas. In this context, the different mean slope classes of DEMs must be assessed to provide more robust and representative results.

A simple bias correction of 7m in the SRTM-GL1 data set enhanced its elevation accuracy and decreased the ME and RMSE values by approximately 100 % and 30 %, respectively (Table 1). STD does not change, as the error distribution is based on the new ME. After bias correction, SRTM-GL1 is the most accurate DEM in terms of elevation estimation.

		ME (m)			STD (m)			RMSE (m)		
SLOPE (°)	Number of GCPs	GDEM-v2	SRTM-v4	SRTM-GL1	GDEM-v2	SRTM-v4	SRTM-GL1	GDEM-v2	SRTM-v4	SRTM-GL1
0-2	86,595	0.8	-7.0	-7.0	6.6	4.1	4.1	6.6	8.1	8.1
2-5	24,583	0.0	-7.5	-7.5	8	6.8	5.7	8	10.2	9.4
5-10	22,143	0.7	-7.0	-7.1	10.2	10.5	7.8	10.2	12.6	10.5
10-20	20,144	1.2	-6.6	-6.7	13.8	15.6	11.1	13.9	16.9	12.9
>20	3789	2.6	-4.1	-5.4	18	20.7	14.9	18.2	21.1	15.9
TOTAL	1,57,224	0.8	-7.0	-7.0 (-0.02)	9.0	8.6	6.6 (6.6)	9.0	11.1	9.7 (6.6)

Table 1. Computed ME, STD and RMSE values for GDEM-v2, SRTM-v4 and SRTM-GL1 based on an absolute vertical accuracy assessment considering different slope classes. Values in parentheses were obtained after bias removal.

4.2 Relative accuracy

On a global scale, SRTM-GL1 is more accurate than GDEM-v2 and SRTM-v4 based on % MAE and % STD values. The GDEM-v2 and SRTM-v4 statistical results are similar. In contrast to the absolute vertical accuracy, the relative accuracy increased with the mean slope for all DEMs, decreasing the % MAE and % STD values. SRTM-GL1 presents the lowest % MAE and % STD values for all considered slope classes. Over flat regions, all DEMs exhibit poor accuracy, with % MAE values close to 100 % and % STD values close to 200 %. GDEM-v2 provided the best results in these regions, which should be treated differently in future DEM generations to improve the local relative accuracy.

For all DEMs, statistical results for the 10°-20° and >20° classes are similar, with slopes greater than 10° exhibiting the highest accuracies. SRTM-v4 exhibits the lowest statistical results for slopes larger than 10° followed by SRTM-GL1 and GDEM-v2. In those steep regions, elevation variations are common over small distances. With a mesh size 3 times larger than other products, SRTM-v4 elevation data cannot capture these variations as well as GDEM-v2 or SRTM-GL1 data.

		MAE (%)			STD (%)		
SLOPE (°)	Number of measurements	GDEM-v2	SRTM-v4	SRTM-GL1	GDEM-v2	SRTM-v4	SRTM-GL1
0-2	128413	131.0	90.3	84.3	207.1	171.8	150.8
2-5	59591	54.4	49.7	41.6	78.7	73.8	62.9
5-10	45465	32.1	32.2	26.3	45.2	44.9	37.6
10-20	28302	22.4	25.1	19.8	31.5	34.7	27.8
>20	3617	23.6	29.7	23.2	30.8	36.8	29.2
TOTAL	263535	41.7	38.2	32.1	66.2	66.2	54.9

Table 2. Computed MAE and STD values for GDEM-v2, SRTM-v4 and SRTM-GL1 based on a relative accuracy assessment considering different slope classes

FSR values confirm the % MAE and % STD results. On a global scale, SRTM-GL1 exhibits lower FSR values than SRTM-v4 and GDEM-v2 (Figure 5). FSR values decreased with increasing slope, and SRTM-GL1 exhibits the lowest FSR value for all classes. Over flat regions, GDEM-v2 poorly represents the local topography, with an FSR value close to 25 %. Conversely, SRTM products provide reasonable results, with FSR values of 5.9 % and 3.2 % for SRTM-v4 and GL1, respectively. Even if these products are subject to slope quantification uncertainties based on high % MAE and % STD values (Table 2), they reasonably represent the ESS over flat regions with relative low FSR values (Figure 5). In regions with slopes greater than 2°, the topographic variation of SRTM-GL1 is good based on an FSR value below 0.66 %. However, the product still exhibits high % MAE and % STD values.

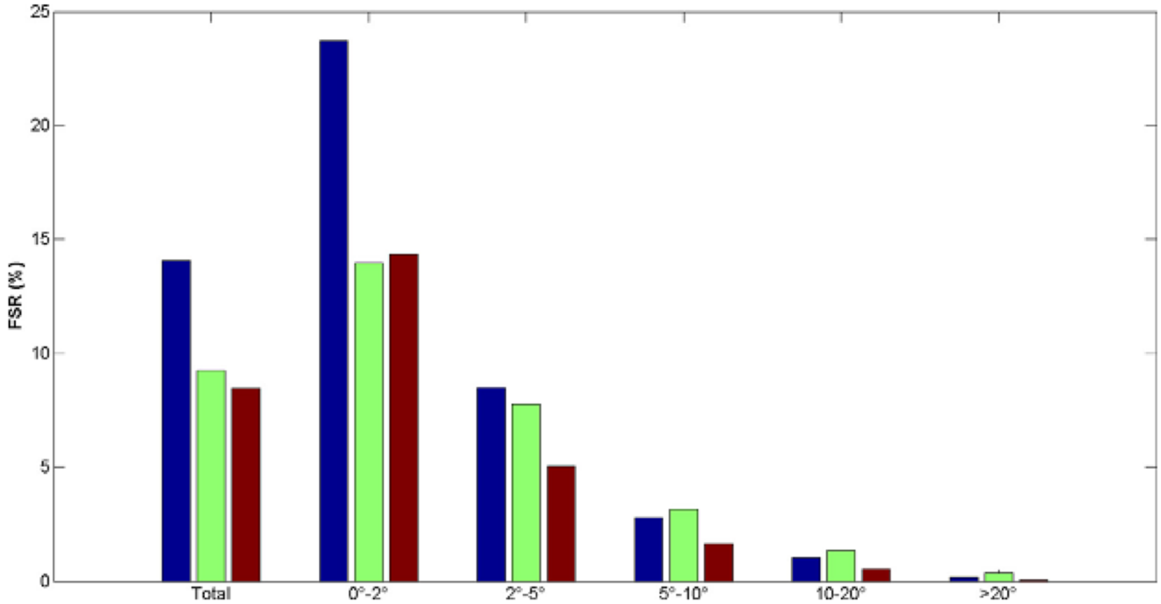

Figure 5. FSR values for GDEM-v2 (blue), SRTM-v4 (green) and SRTM-GL1 (red) on a global scale and for different slope classes

This analysis emphasized the importance of considering both continuous and categorical statistical analyses when assessing a DEM's relative accuracy. Continuous statistics illustrates a DEM's ability to quantify relative elevation variations in space, especially over flat regions. However, these statistics cannot assess a DEM's relative accuracy. Categorical statistics show that, even if the relative accuracy is not well quantified, the ESS can be satisfactory for SRTM products based on low FSR values.

4.3 Hydrological application

From a visual inspection point of view, all DEMs captured the regional RHN tendencies in terms of global positioning and direction (Figure 3). Similarities are more evident in the northern part of the study near Lake Titicaca. The topographic features are more prominent and the mean slope values are higher in this area compared to the southern and central parts of the study area. For all DEMs, DHN artifact rivers are mainly located in the central and southern parts of the study area, with GDEM-v2 exhibiting the highest proportion of artifacts.

Three main recurrent deficiencies are illustrated in Figure 6. In the central plain, DHNs deviate from the Desaguadero River, which is the most important river in the watershed. All SRTM products derived northward flow directions through a Desaguadero tributary, which joins the Desaguadero River some 50 km downstream (Figure 6A). GDEM-v2 effectively separates the

Desaguadero from this tributary but deviates from the Desaguadero further south near another tributary. This tributary is well identified by SRTM products and joins the Desaguadero River some 70 km later according to RHN. The Desaguadero River plain is a very flat region with a mean slope lower than 2°. These areas exhibited low relative accuracies, which likely explain these variations (Tables 1 and 2; Figure 5). Deficiencies over flat regions have been previously noted (Getirana et al., 2009; Rezak et al., 2012). In such low gradient regions, rivers often split into multiple channels, which merge again some kilometers later (Figure 6B). DEMs cannot reproduce those features, which are identified as a single river channel. The Uyuni and Coipasa salt areas and Poopó Lake correspond to other very flat regions (Figure 1). In these regions, local rivers are dry the majority of the year, with periodic runoff occurring during the rainfall season. Such conditions tend to displace river beds over time. Thus, these rivers become less accurately located if DEMs are not updated.

GDEM-v2 displays considerable inconsistencies in "urbanized" areas where it tends to misidentify roads as streams (Figure 6C). This generally occurs in relatively flat regions and could be due to the lower elevations of roads compared to the surrounding land. These observations clearly limit the use of GDEM-v2 in some parts of the watershed.

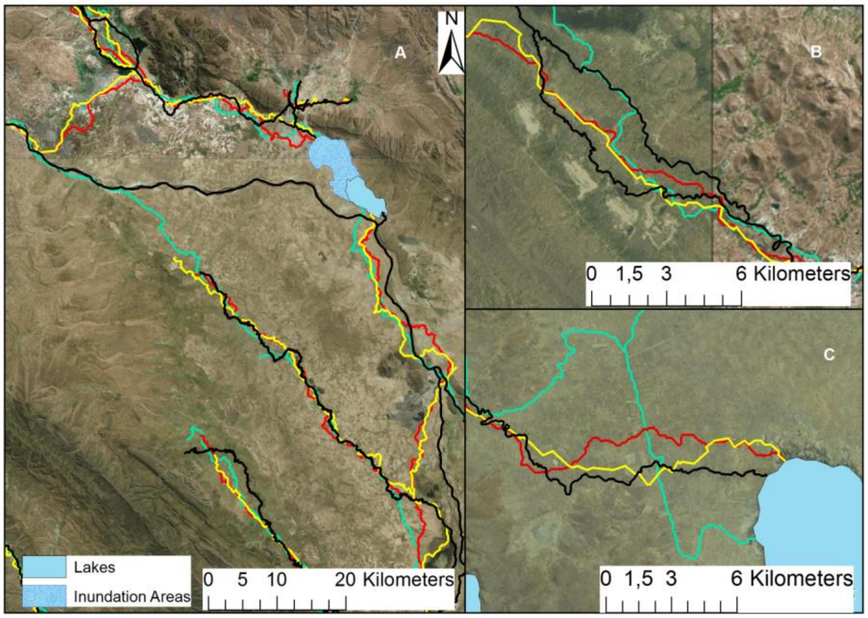

Figure 6. DHN deficiencies over flat regions. (A) Desaguadero River example, (B) river duplication example and (C) urbanized area example. Black lines represent the RHN. Red, yellow and green lines represent SRTM-GL1, SRTM-v4 and GDEM-v2, respectively.

Finally, using a pixel size of 100m, Cr values of 0.26, 0.25 and 0.18 and FM values of 0.17, 0.16 and 0.11 were found for SRTM-GL1, SRTM-v4 and GDEM-v2, respectively. Higher values of Cr and FM associated with SRTM products suggest that those products can better reproduce the regional river network compared to GDEM-v2. This confirms visual observations and previous results related to the relative accuracy. DEMs with lower relative errors are the most suitable for hydrological applications, such as river network extraction. Low values of Cr and FM are associated with low gradient portions of the region. In addition, the DEM algorithm does not adequately reproduce river channel divisions induced by low regional gradients (Figure 5C). Thus, DEMs should be hydrologically conditioned (Jarihani et al., 2015; Pinel et al., 2015) before they are used for hydrological studies. These results must be interpreted with caution, as the dates of GE images used to define the RHN do not match those of the DEMs. Therefore, some of the uncertainty may be attributed to this temporal inconsistency. However, the comparison between DHNs is still valuable.

5. Conclusion

The quality of the newly released, free SRTM-GL1 data set was assessed for the first time based on both the vertical and relative accuracies over the South American Andean Plateau. This study was conducted in a relatively barren region. Because vegetation interferes with optical photogrammetry and short wavelength radar interferometry used in DEM processing, different results may be observed over vegetated areas. In terms of elevation estimations on the regional scale, SRTM-GL1 performed better than SRTM-v4 based on STD and RMSE values that were 23 % and 13 % lower, respectively, compared to ICESat/GLAS GCPs. In addition, GDEM-v2 is more accurate than SRTM-GL1 based on lower ME and RMSE values. A simple bias removal considerably enhances the SRTM-GL1 elevation estimation, making it the most accurate over the region in terms of absolute vertical accuracy. We assessed the relative accuracies of multiple DEMs, including SRTM-GL1, SRTM-v4 and GDEM-v2. Compared to SRTM-v4, SRTM-GL1 provided a better relative accuracy, reducing % MAE and % STD by 16 % and 17 %, respectively. GDEM-v2 and SRTM-GL1 provided the least and the most accurate vertical accuracies, respectively, for all slope classes. A complementary categorical statistical analysis based on FSR index values confirms this trend. The analysis shows that SRTM-GL1 reasonably represents the ESS trend (low FSR) but failed to accurately quantify it (low % MAE and % STD). An interesting result notes the independence between vertical and relative accuracy. GDEM-v2 is the most accurate in terms of elevation accuracy but exhibited a poor relative accuracy. Thus, assessing DEMs using only a vertical elevation approach cannot provide complete insight into a DEM's potential. Future studies must consider both the vertical and relatively accuracies of DEMs to produce more consistent results.

The comparison between the DHNs and RHN shows the limitations of DEMs for hydrological purposes over the region. On a regional scale, SRTM-GL1 provides the best river network extraction. GDEM-v2 exhibits substantial local inadequacies over flat and urbanized areas, resulting in the detection of more artifact rivers. Hydrological conditioning based on an accurate reference river network, as proposed by Pinel et al. (2015), is recommended to enhance river positioning.

Additionally, this study shows the usefulness of the reference data set used. GE is useful for retrieving RHNs in remote regions without defined networks and in areas with small river sizes, as these may not be detected by free imagery data, such as MODIS or Landsat. ICESat/GLAS data can be used to effectively assess vertical accuracies as shown in this study, which utilized a large (160,000 points) data set and produced an accurate statistical analysis. The methodology proposed to assess the relative error benefits the large number of ICESat/GLAS data from which close to 265,000 local slope value were derived for the analyze. Comparisons were conducted over a large slope range, making this study the most comprehensive DEMs relative error assessment to date.

Studies requiring accurate ESS descriptions, such as hydrological and geomorphological analyses, should utilize SRTM-GL1 over SRTM-v4 and GDEM-v2, as it presents the best vertical and relative height-pixel accuracies among the freely available DEMs.

Acknowledgments

This work was supported by the Centre National d'Etudes Spatiales (CNES) in the framework of the HASM project (Hydrology of Altiplano: from Spatial to Modeling). The first author thanks the IRD (Institut de Recherche pour le Développement) and CAPES (Coordenação de Aperfeiçoamento de Pessoal de Nível Superior) Brazil for their financial support.

References

Arefi, H., Reinartz, P., 2011. Accuracy Enhancement of ASTER Global Digital Elevation Models Using ICESat Data. Remote Sens. 3, 1323–1343. doi:10.3390/rs3071323

Athmania, D., Achour, H., 2014. External validation of the ASTER GDEM2, GMTED2010 and CGIAR-CSI- SRTM v4.1 free access digital elevation models (DEMs) in Tunisia and Algeria. Remote Sens. 6, 4600–4620. doi:10.3390/rs6054600

Baker, P. a, Rigsby, C. a, Seltzer, G.O., Fritz, S.C., Lowenstein, T.K., Bacher, N.P., Veliz, C., 2001. Tropical climate changes at millennial and orbital timescales on the Bolivian Altiplano. Nature 409, 698–701. doi:10.1038/35055524

Benker, S.C., Langford, R.P., Pavlis, T.L., 2011. Positional accuracy of the Google Earth terrain model derived from stratigraphic unconformities in the Big Bend region, Texas, USA. Geocarto Int. 26, 291–303. doi:10.1080/10106049.2011.568125

Billemont, S., 2010. Validation of ASTER GDEM over Tibet.

Bothale, R.V., Joshi, A.K., Krishnamurthy, Y.V.N., 2013. Cartosat-1 derived DEM (CartoDEM) towards Parameter Estimation of Microwatersheds and Comparison with ALTM DEM. J Indian Soc Remote Sens 41, 487–495. doi:10.1007/s12524-012-0258-8

Carabajal, C.., Harding, D.J., Boyc, J.-P., Danielson, J.J., Geschd, D.., Suchdeo, V.P., 2011. Evaluation of the Global Multi-Resolution Terrain Elevation Data 2010 (GMTED2010) Using ICESat Geodetic Control, in: SPIE. pp. 1–13. doi:10.1117/12.912776

Carabajal, C.C., 2011. ASTER GLOBAL DEM VERSION 2.0 EVALUATION USING ICESat GEODETIC GROUND CONTROL.

El Hage, M., Simonetto, E., Faour, G., Polidori, L., 2012. EVALUATION OF ELEVATION, SLOPE AND STREAM NETWORK QUALITY OF SPOT DEMS, in: ISPRS Annals of Photogrammetry, Remote Sensing and Spatial Information Sciences. pp. 63–67. doi:10.5194/isprsannals-I-2-63-2012

Enble, F., Heinzel, J., Koch, B., 2012. EVALUATING HEIGHT DIFFERENCES BETWEEN GLOBAL DIGITAL SURFACE MODELS AND ICESAT HEIGHTS AT FOOTPRINT GEOLOCATION, in: GIS Ostrava 2012 - Surface Models for Geosciences.

Farah, A., Algarni, D., 2014. Positional Accuracy Assessment of Googleearth in Riyadh. Artif. Satell. 49, 8–13. doi:10.2478/arsa-2014-0008

Getirana, A.C. V., Bonnet, M.-P., Rotunno Filho, O.C., Mansur, W.J., 2009. Improving hydrological information acquisition from DEM processing in floodplains. Hydrol. Process. 23, 502–514. doi:10.1002/hyp.7167

Hirt, C., Filmer, M.S., Featherstone, W.E., 2010. Comparison and validation of the recent freely available ASTER-GDEM ver1, SRTM ver4.1 and GEODATA DEM-9S ver3 digital elevation models over Australia. Aust. J. Earth Sci. 57, 337–347. doi:10.1080/08120091003677553

Jarihani, A.A., Callow, J.N., McVicar, T.R., Van Niel, T.G., Larsen, J.R., 2015. Satellite-derived Digital Elevation Model (DEM) selection, preparation and correction for hydrodynamic modelling in large, low-gradient and data-sparse catchments. J. Hydrol. 524, 489–506. doi:10.1016/j.jhydrol.2015.02.049

Jenson, S.K., Domingue, J.O., 1988. Extracting Topographic Structure from Digital Elevation Data for Geographic Information System Analysis. Photogramm. Eng. Remote Sensing 54, 1593–1600.

Le Coz, M., Delclaux, F., Genthon, P., Favreau, G., 2009. Assessment of Digital Elevation Model (DEM) aggregation methods for hydrological modeling: Lake Chad basin, Africa. Comput. Geosci. 35, 1661–1670. doi:10.1016/j.cageo.2008.07.009

Li, J., Wong, D.W.S., 2010. Computers , Environment and Urban Systems Effects of DEM sources on hydrologic applications. Comput. Environ. Urban Syst. 34, 251–261. doi:10.1016/j.compenvurbsys.2009.11.002

Maidment, D.R., 2002. Arc Hydro: GIS for Water Resources, Volume 1.

Metz, M., Mitasova, H., Harmon, R.S., 2011. Efficient extraction of drainage networks from massive , radar-based elevation models with least cost path search. Hydrol. Earth Syst. Sci. 667–678. doi:10.5194/hess-15-667-2011

Mohammed, N.Z., Ghazi, A., Mustafa, H.E., 2013. Positional accuracy testing of Google Earth. Int. J. Multidiscip. Sci. Eng. 4, 6–9.

O’Callaghan, J.F., David M. Mark, 1991. On the extraction of channel networks from digital elevation data. Comput. vision, Graph. image Process. 5, 81–100.

Paredes-Hernández, C.U., Salinas-Castillo, W.E., Guevara-Cortina, F., Martínez-Becerra, X., 2013. Horizontal positional accuracy of Google Earth’s imagery over rural areas: a study case in Tamaulipas, Mexico. Bol. Ciencias Geod. 19, 588–601. doi:http://dx.doi.org/10.1590/S1982-21702013000400005

Paz, A.R., Collischonn, W., 2007. River reach length and slope estimates for large-scale hydrological models based on a relatively high-resolution digital elevation model. J. Hydrol. 343, 127–139. doi:10.1016/j.jhydrol.2007.06.006

Pinel, S., Bonnet, M.-P., Santos Da Silva, J., Moreira, D., Calmant, S., Satgé, F., Seyler, F., J-P Schumann, G., Koch, M., Thenkabail, P.S., 2015. Correction of Interferometric and Vegetation Biases in the SRTMGL1 Spaceborne DEM with Hydrological Conditioning towards Improved Hydrodynamics Modeling in the Amazon Basin. Remote Sens. Remote Sens 7, 16108–16130. doi:10.3390/rs71215822

Potere, D., 2008. Horizontal positional accuracy of google earth’s high-resolution imagery archive. Sensors 8, 7973–7981. doi:10.3390/s8127973

Ragheb, A.E., 2015. Enhancement of Google Earth Positional Accuracy. Int. J. Eng. Res. Techmology 4, 627–630.

Rahman, M.M., Arya, D.S., Goel, N.K., 2010. Limitation of 90 m SRTM DEM in drainage network delineation using D8 method-a case study in flat terrain of Bangladesh. Appl. Geomatics 2, 49–58. doi:10.1007/s12518-010-0020-2

Rezak, S., Laborde, J.-P., Errih, M., 2012. Validation d’un modèle numérique de terrain adapté à la modélisation hydrologique régionale sur l'Algérie du Nord. Hydrol. Sci. J. 57, 928–941. doi:10.1080/02626667.2012.685742

Satgé, F., Bonnet, M.-P., Gosset, M., Molina, J., Hernan Yuque Lima, W., Pillco Zolá, R., Timouk, F., Garnier, J., 2016. Assessment of satellite rainfall products over the Andean plateau. Atmos. Res. 167, 1–14. doi:10.1016/j.atmosres.2015.07.012

Satgé, F., Bonnet, M.P., Timouk, F., Calmant, S., Pillco, R., Molina, J., Lavado-Casimiro, W., Arsen, A., Crétaux, J.F., Garnier, J., 2015. Accuracy assessment of SRTM v4 and ASTER GDEM v2 over the Altiplano watershed using ICESat/GLAS data. Int. J. Remote Sens. 36, 465–488. doi:10.1080/01431161.2014.999166

Strahler, A.N., 1952. HYPSOMETRIC (AREA-ALTITUDE) ANALYSIS OF EROSIONAL TOPOGRAPHY. Geol. Soc. Am. Bull. 63, 1117. doi:10.1130/0016-7606(1952)63[1117:HAAOET]2.0.CO;2

Vogt, J. V., Colombo, R., Bertolo, F., 2003. Deriving drainage networks and catchment boundaries : a new methodology combining digital elevation data and environmental characteristics. Geomorphology 53, 281–298. doi:10.1016/S0169-555X(02)00319-7

Wechsler, S., 2006. Uncertainties associated with digital elevation models for hydrologic applications: a review. Hydrol. Earth Syst. Sci. Discuss. 3, 2343–2384. doi:10.5194/hessd-3-2343-2006

Zhao, G., Xue, H., Ling, F., 2010. Assessment of ASTER GDEM Performance by Comparing with SRTM and ICESat / GLAS Data in Central China, in: 18th International Conference on Geoinformatics. Beijing. doi:10.1109/GEOINFORMATICS.2010.5567970

Zhao, S., Cheng, W., Zhou, C., Chen, X., Zhang, S., Zhou, Z., Liu, H., Chai, H., 2011. Accuracy assessment of the ASTER GDEM and SRTM3 DEM: an example in the Loess Plateau and North China Plain of China. Int. J. Remote Sens. 32, 8081–8093. doi:10.1080/01431161.2010.532176

Zwally, H.J., Schutz, B., Abdalati, W., Abshire, J., Bentley, C., Brenner, A., Bufton, J., Dezio, J., Hancock, D., Harding, D., Herring, T., Minster, B., Quinn, K., Palm, S., Spinhirne, J., Thomas, R., 2002. ICESat's laser measurements of polar ice, atmosphere, ocean, and land. J. Geodyn. 34, 405–445. doi:10.1016/S0264-3707(02)00042-X

IV. Capítulo 2

Estimativas de Chuva por Sensoriamento Remoto

As precipitações, sendo a maior entrada de água nos sistemas hidrológicos, representam um parâmetro primordial nos estudos dos recursos hídricos. Na região do altiplano, a alta variabilidade espacial e temporal das precipitações dificulta a sua estimativa com precisão. As precipitações podem variar consideravelmente, em distâncias muito curtas, tornando a medição por pluviômetro não representativa das áreas vizinhas e assim, obsoleta para estudos regionais. A alternativa é a constituição de uma rede densa de pluviômetros localizados de tal forma que as precipitações medidas pontualmente por eles possam ser compiladas para a representação do padrão regional. Porém, em regiões como o Altiplano, poucas estações pluviométricas estão disponíveis devido ao contexto geomorfológico e econômico. De fato, a rede nacional do SENAMHI inclui poucas estações, principalmente localizadas nas zonas povoadas mais acessíveis. Portanto, a maior concentração de pluviômetros está localizada na região do lago Titicaca e Poopó. Ao mesmo tempo, devido à escassez de recursos, o número de estações e a manutenção limitada ao longo do tempo, não é possível ter uma rede e séries temporais diárias, mensais ou até mesmo anuais de qualidade.

Com aproximadamente 20 anos de monitoramento, as estimativas de chuva por satélites (SRE: *Satelite Rainfall Estimation*) aparecem como uma ferramente alternativa promissora. As estimativas das precipitações em escala quase-global permitem analisar as variações pluviométricas no espaço e no tempo e, potencialmente, avaliar tendências associadas às mudanças climáticas. A primeira geração de SREs foi lançada em 1997 pela colaboração entre a NASA e a JAXA com o intuito de monitorar e estudar as precipitações tropicais (*Tropical Rainfall Measuring Mission* (TRMM)). Um satélite homônimo, o TRMM, embarcou 3 sensores úteis nas estimativas de chuva: *Precipitation Radar* (PR), TRMM *Microwave Imager* (TMI), *Visible Infrared Radiometer* (VIRS). Os dados do satélite TRMM são usados em conjunto com os dados de micro-ondas passivas e dados infravermelhos, a bordo de outros satélites para gerar a primeira geração de SREs, incluindo:

- TRMM *Mulstisatelite Precipitation Analysis* (TMPA), produto da NASA.
- *Climate prediction center MORPHing* (CMORPH), produto do NOAA/Climate Prediction Center (NOAA/CPC).
- *Precipitation Estimation from Remotely Sensed Information using Artificial Neural Networks* (PERSIANN), produto do *Center of Hidrometeorology and Remote Sensing* (CHRS).

- *Global Satellite Mapping of Precipitation* (GSMaP), produto do *Core Research for Evolutional Science and Technology* (CREST) patrocinado pelo *Japan Science and Technology* (JST) e promovido pela equipe de ciências *Precipitation Measuring Mission* (PMM) da JAXA.

TMPA, CMORPH, PERSIANN e GSMaP estão disponíveis numa versão feita unicamente a partir de dados de satélites, chamada de versão *Real-Time* (RT) e em uma versão ajustada (*Adjusted*: Adj) a partir de precipitações derivadas de pluviômetros, principalmente do *Global Precipitation Climatology Project* (GPCP) o do *Climate Prediction Center* (CPC).

A segunda geração de SREs teve início em fevereiro de 2014 com o lançamento do satélite *Global Precipitation Measurement Core Observatory* (GPM), com o objetivo de dar continuidade à aquisição de dados após o término do funcionamento do sensor TMI do TRMM. O GPM inclui o primeiro radar de precipitações de dupla-frequência operando nas bandas Ku (13 GHz) e Ka (35 GHz), juntamente com o primeiro radiômetro de micro-ondas de varredura cônica de 885 km de largura conical e treze canais de frequência distribuídos entre 10 e 183 GHz. O principal potencial dos novos sensores reside na possibilidade de medir com melhor precisão as chuvas de baixa intensidade. Portanto, a nova geração de SREs é de grande interesse nas regiões áridas tais como o Altiplano. Dois SREs se baseiam no uso dos dados do GPM em conjunto com dados de outros satélites:

- *Integrated Multi-satellite Retrievals for GPM* (GPM), produto da NASA.
- GSMaP-v6, como nova versão do GSMaP da primeira geração.

Assim como os SREs de primeira geração, o IMERG e o GSMaP-v6 estão disponíveis nas versões usando unicamente dados dos satélites e nas versões ajustada a partir de dados de precipitações do GPCC para o IMERG e do CPC para o GSMaP-v6.

Os SREs de primeira e segunda geração usam dados de micro-ondas passivas e de sensores de radiação infravermelha para a estimativa de precipitação. De maneira geral, as anomalias de valores de temperatura (infravermelhos) e emissividades (micro-ondas passivas) são usada para identificar no espaço e no tempo as células chuvosas como também as precipitações derivadas delas. A limitação da metodologia reside na capacidade de transposição/adaptação aos diferentes processos de precipitações e ocupação do solo. Por tanto, há anomalias "naturais" de temperatura e emissividade associadas à topografia, presença de corpo de água e de neve. Essas anomalias podem ser mal interpretadas pelos algoritmos na detecção/quantificação das precipitações e assim levar a perda ou a falsa detecção de evento chuvoso e por consequência introduzir erros nas estimativas feitas a partir dos SREs. Cada SREs usa um conjunto de dados e algoritmos próprios. Portanto, um SRE pode ser mais adequado para estimativas de chuva em certa região enquanto outro SREs seria mais adaptado em outra região. Nesse contexto, vários estudos avaliam os diferentes SREs disponíveis em diferentes regiões do mundo para quantificar o erro e limite dos SREs. Tais informações são primordiais para usuários potenciais como também para o desenvolvimento de metodologia de correção das estimativas e melhoria dos futuros SREs.

Na região do Altiplano, não foram realizados trabalhos anteriores ao presente estudo de avaliação do erro nas estimativas feita pelos SREs. A região conta com altas variações topográficas e de emissividade devido à presença das cordilheiras, dos desertos de sal de Uyuni e Coipasa e dos lagos Titicaca e Poopó, os quais podem alterar significativamente as medições feitas pelos SREs (Figura 3). Nesse contexto, torna-se primordial avaliar a potencialidade dos produtos antes de seu uso. Ambos SREs de primeira e segunda geração foram avaliados por comparação direta das estimativas derivadas dos SREs com as obtidas a partir da rede de pluviômetros do SENAMHI. As comparações foram feitas em escala anual, mensal e diária. Esse trabalho levou à publicação de dois artigos em revistas internacionais.

O primeiro artigo, "*Assessment of satellite rainfall products over the Andean plateau*", publicado na revista "*Atmospheric research*", avalia o erro das estimativas de chuva dos SREs de primeira geração nas versões RT e Adj (Satgé et al., 2016a). Foram realizadas comparações das estimativas dos SREs com valores de 57 pluviômetros na região do Altiplano em escala anual, mensal e diária, no período entre 2005 e 2007. A análise é feita em escala global considerando todos os *píxels,* incluindo pelo menos um pluviômetro, e por cada *píxel* individualmente, para observar a variação espacial do erro nas medições dos SREs. Uma análise adicional foi realizada considerando os *píxels* localizados na margem do lago Titicaca de modo a observar sua inluencia sobre as estimativas dos SREs. Portanto, devido a características próprias (superfície de 8.400 km^2 e profundidade média de 110 m), o lago poderia ter uma influência significativa nas medições devido à forte anomalia de emissividade e temperatura que ele ocasiona regionalmente. As comparações, em escalas de tempo anuais e mensais, foram feitas considerando o coeficiente de correlação, o erro médio e o erro médio quadrático. Em uma escala diária, uma análise estatística categórica foi desenvolvida para observar a potencialidade dos SREs na separação dos dias chuvosos e não chuvosos. A análise se baseia nos índices *False Alarm Ratio* (FAR) e *Probability Of Detection* (POD). Os resultados mostram que o produto TMPA-Adj v7 tem a maior acurácia nos passos de tempo considerados (diário, mensal e anual). TMPA-Adj v7 é suficientemente acurado para ser utilizado para o monitoramento das tendências pluviométricas regionais do Altiplano nos passos de tempo mensal e anual. Em escala diária de tempo, todos os produtos conseguem separar dias chuvosos dos dias sem chuva mas erram consideravelmente na quantificação. A análise diária deve ser considerada com cuidado devido à baixa representatividade entre as medições pontuais dos pluviômetros e as medições do SREs com tamanho de *píxel* de 100 km^2 (0.1°) a 625 km^2 (0.25°). Os SREs são mais acurados na região mais úmida, parte norte do Altiplano, em comparação com a parte sul árida. Finalmente, o Lago Titicaca influencia as medições dos SREs. Como esperado, observa-se uma subestimativa das precipitações na região do lago Titicaca devido à anomalia de temperatura no lago. De maneira geral, este estudo evidencia a potencialidade do TMPA-Adj v7 para os estudos hidroclimatológicos no passo de tempo mensal e anual na região. Também se observou uma relação entre intensidade de chuva e acurácia dos SREs com erro menor observado na zona úmida.

O segundo artigo, "*Comparative assessment of the latest GPM mission's spatially enhanced satellite rainfall products over the main Bolivian watersheds*", publicado na revista "*Remote Sensing*", possui foco nos dois SREs da segunda geração, o IMERG e o GSMaP-v6 disponibilizados a partir de 2015 (Anexo 3: Satgé et al., 2017b). As avaliações foram feitas no passo de tempo anual, mensal e diário nas 3 principais bacias Bolivianas (Altiplano, La Plata e Amazona) por comparação com 247 pluviômetros. Em vista dos resultados obtidos e publicados no primeiro artigo (melhor potencialidade dos SREs em contexto úmido do que árido), as estações secas e úmidas foram consideradas separadamente. Essa análise tem como objetivo avaliar dentro de cada região definida, a acurácia dos SREs considerando as variações das intensidades de chuva observadas entre estação seca e chuvosa. A variação topográfica é conhecida por influenciar as medições dos SREs, ocorrendo de maneira geral, um erro maior nas zonas montanhosas do que nas planícies. Nesse contexto, os *píxels* foram classificados em diferentes classes de declividade para observar a distribuição do erro em função da variação topográfica. Nesta nova análise, o TMPA-Adj v7 está mantido a fim de observar se os produtos IMERG e GSMaP-v6 apresentam acurácia semelhante. Os resultados mostram que na região do Altiplano o IMERG é mais acurado do que o TMPA-Adj v7 para todos os passos de tempo considerados. Na estação chuvosa, as estimativas são mais acuradas do que na estação seca. O IMERG permite a continuidade do monitoramento das estimativas de chuva, começado com os SREs de primeira geração, com acurácia suficiente para estudo hidroclimatológico na região do Altiplano.

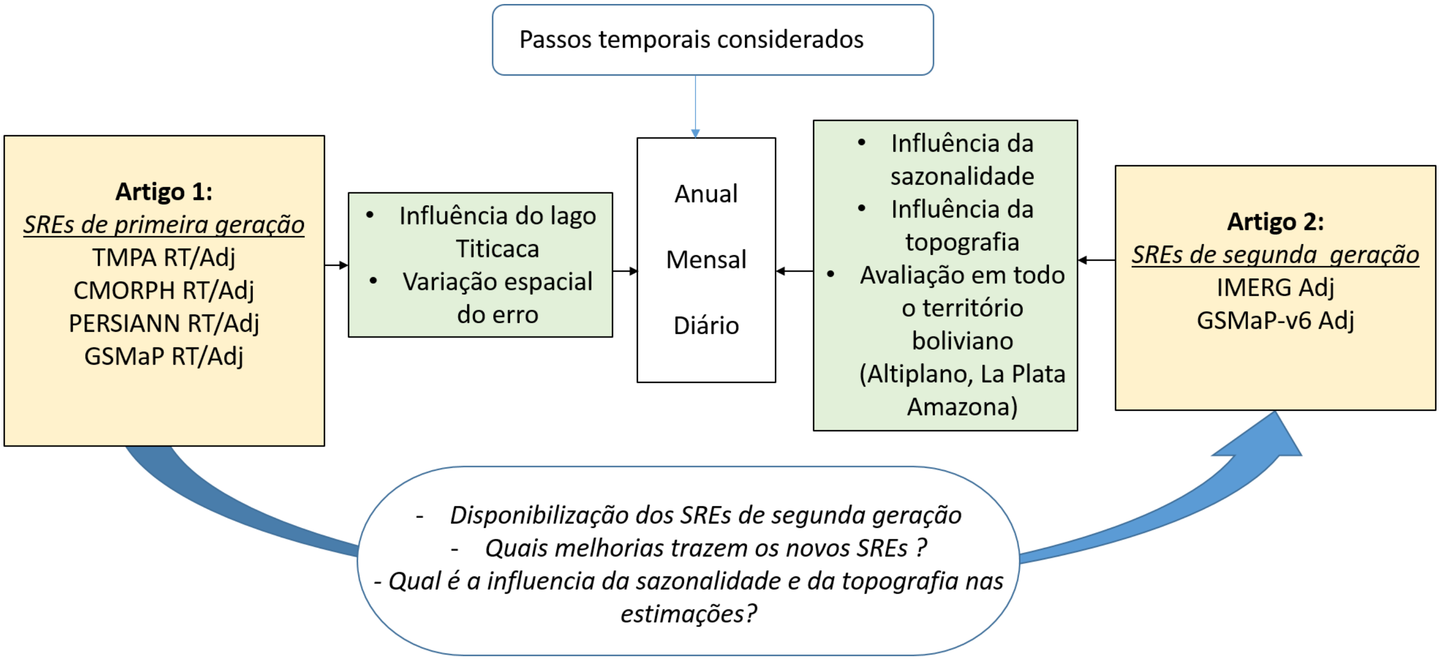

Figure 10. Quadro esquemático que sintetiza o trabalho realizado nos SREs neste doutorado.

A Figura 10 esquematiza a dinâmica, as interconexões e a complementaridade existente entre os dois artigos. O primeiro artigo é apresentado como exemplo neste capítulo. O segundo artigo está disponível nos anexos.

Assessment of satellite rainfall products over the Andean plateau

Contents lists available at ScienceDirect

Atmospheric Research

journal homepage: www.elsevier.com/locate/atmos

Assessment of satellite rainfall products over the Andean plateau

Frédéric Satgé [a], Marie-Paule Bonnet [b], Marielle Gosset [b], Jorge Molina [c], Wilson Hernan Yuque Lima [c], Ramiro Pillco Zolá [c], Franck Timouk [b], Jérémie Garnier [a]

[a] Instituto de Geociência, Universidade de Brasília, Brasília, Brazil
[b] Géosciences Environnement Toulouse (Institut de Recherche pour le Développement/Centre National de la Recherche Scientifique, Université Paul Sabatier), Toulouse, France
[c] Instituto de Hidráulica e Hidrología, Universidad Mayor de San Andrés, La Paz, Bolivia

Abstract

Nine satellite rainfall estimations (SREs) were evaluated for the first time over the South American Andean plateau watershed by comparison with rain gauge data acquired between 2005 and 2007. The comparisons were carried out at the annual, monthly and daily time steps. All SREs reproduce the salient pattern of the annual rain field, with a marked north-south gradient and a lighter east-west gradient. However, the intensity of the gradient differs among SREs: it is well marked in the Tropical Rainfall Measuring Mission (TRMM) Multisatellite Precipitation Analysis 3B42 (TMPA-3B42), Precipitation Estimation from remotely Sensed Information using Artificial Neural Networks (PERSIANN) and Global Satellite Mapping of Precipitation (GSMaP) products, and it is smoothed out in the Climate prediction center MORPHing (CMORPH) products. Another interesting difference among products is the contrast in rainfall amounts between the water surfaces (Lake Titicaca) and the surrounding land. Some products (TMPA-3B42, PERSIANN and GSMaP) show a contradictory rainfall deficit over Lake Titicaca, which may be due to the emissivity contrast between the lake and the surrounding lands and warm rain cloud processes. An analysis differentiating coastal Lake Titicaca from inland pixels confirmed this trend. The raw or Real Time (RT) products have strong biases over the study region. These biases are strongly positive for PERSIANN (above 90%), moderately positive for TMPA-3B42 (28%), strongly negative for CMORPH (-42%) and moderately negative for GSMaP (-18%). The biases are associated with a deformation of the rain rate frequency distribution: GSMaP underestimates the proportion of rainfall events for all rain rates; CMORPH overestimates the proportion of rain rates below 2 mm.day^{-1}; and the other products tend to overestimate the proportion of moderate to high rain rates. These biases are greatly reduced by the gauge adjustment in the TMPA-3B42, PERSIANN and CMORPH products, whereas a negative bias becomes positive for GSMaP. TMPA-3B42 Adjusted (Adj) version 7 demonstrates the best overall agreement with gauges in terms of correlation, rain rate distribution and bias. However, PERSIANN-Adj's bias in the southern part of the domain is very low.

Keywords: Satellite Rainfall Estimation, Assessment, Andean Plateau

1. Introduction

Precipitation affects many economic activities, such as agriculture, industry, transport and tourism. It is also a key variable for improving water resource management and flood or drought forecasting, as well as for hydrological research or climatology. For all these applications, accurate rainfall estimation is required worldwide, but in many regions, rain gauge coverage is sparse. This is particularly true in remote regions such as the Andean plateau in South America where ground gauges are unevenly distributed; they are mainly located close to cities or communities to facilitate maintenance operations. Consequently, some areas in the Andean plateau are relatively well monitored, but a large number of areas are not monitored at all. In a region where rainfall is highly variable, extrapolating from a sparse and unevenly distributed rain gauge network leads to inaccuracies (Li and Heap, 2008*;* Scheel et al., 2011*)*. Moreover, in the Andean plateau, most of the rain gauge data are still collected manually. Collecting and digitizing the information introduces uncertainties in the time series and delays the availability of data. Rainfall data availability is even more complicated in trans-boundary watersheds like the Andean plateau, which is shared by three countries, because of potential water use conflicts. With global spatial coverage, good spatio-temporal resolution and online availability, Satellite Rainfall Estimates (SREs) represent an attractive alternative solution.

SREs are based on a combination of data from different Passive Micro-Wave (PMW) and Infra-Red (IR) radiometers on board Low Earth-Orbiting (LEO) and Geosynchronous (GEO) satellites, respectively. Depending on the region and rainfall regimes, the biases introduced by each type of sensor may impact the final combined product. Due to the irregular sampling of LEOs and the limited number of overpasses, short rainfall events are not well captured by PMWs (Tian et al., 2009*;* Gebregiorgis and Hossain, 2013). This can explain the reduced accuracy of some SREs (TMPA-3B42-RT and Adj v6, CMORPH) in arid regions or during the dry season when short rainfall events are predominant (Prakash et al., 2014; Shen et al., 2010; Yang and Luo, 2014; Gao and Liu, 2013). Researchers also agree that rain/no rain classification based on cloud top IR temperature may fail in mountainous regions (Dinku et al., 2010, 2007; Hirpa et al., 2010; Li et al., 2013 Gebregiorgis and Hossain, 2013). The threshold used might be too low to identify orographic warm clouds as rain. PMWs may also introduce errors in mountainous regions because snow and ice surfaces may be interpreted as rainy clouds (Dinku et al. 2010). SREs tend to underestimate precipitation over large water bodies (Paiva et al., 2011; Tian et al., 2007; Katiraie-Boroujerdy et al., 2013). Tian et al. (2007) attribute this inconsistency to a misinterpretation of the PMWs' emissivity over water surfaces. Paiva et al. (2011), working in the Amazon basin, attributed the underestimation of rainfall over the river to the river breeze effect that locally reduced rainfall amounts. Products like Tropical Rainfall Measuring Mission (TRMM) Multisatellite Precipitation Analysis 3B42 (TMPA-3B42; hereafter called TMPA), Climate prediction center MORPHing (CMORPH) and Global Satellite Mapping of Precipitation (GSMaP) rely heavily on the instant rain retrieval data derived from the PMW information from LEOs. Due to the insufficient number of overpasses from LEOs, IR data are used to fill in the gaps between the PMW estimates. Precipitation Estimation from Remotely Sensed Information using Artificial Neural Networks (PERSIANN) uses a different approach. The rainfall amount is first estimated through IR data, and the PMW information is used to improve the accuracy of the estimate. These four combined products have versions based only on PMW and IR data available with a short delay (and referred to as RT for real time or RAW hereafter) and Adjusted versions that ingest rain gauge information to reduce the biases are available with longer delays (they are referred to as Adj hereafter).

To our knowledge, there are only 2 published works on the performance of SREs over the Andean plateau. The first (Heidinger et al., 2012) focused on a correction methodology for TMPA-Adj v6. Their method improves TMPA-Adj v6 agreement with rain gauge daily data but is strongly dependent on the availability of rain gauges. The second paper assessed TMPA-RT v7, Modern-Era Retrospective Analysis for Research and Applications (MERRA), Climate Forecast System Reanalysis and Reforecast (CFSR) and a combined scheme product (CoSch) using both rain gauges and TMPA-RT v7 rainfall estimation over the Bolivian Altiplano watershed part on a coarse scale (0.5°) and daily basis (Blacutt et al., 2015). Over the studied period (1999-2009), CoSch outperformed the other SREs in terms of categorical statistics, STD, RMSE, bias and correlation, followed by TMPA-RT v7, CFSR and MERRA. For the rainy season, TMPA-RT v7 outperformed the other SREs in terms of STD, RMSE and bias, and its categorical statistics are very close to CoSch's. As only three rain gauges were used, these results have to be considered as preliminary, and comparison with a denser rain gauge network is still needed to assess TMPA-RT v7 performance over the Andean plateau. Apart from Salio et al. (2014) over South America, Buarque et al. (2011) in the Amazon and Dinku et al. (2010) in the Colombian Andes, who included CMORPH in their study, only the TMPA products have been assessed over South America (Collischonn et al., 2008; Getirana et al., 2011; De Paiva et al., 2013; Su et al., 2008; Vila et al., 2009; Condom et al., 2010; Zulkafli et al., 2014; Ochoa et al., 2014; Scheel et al., 2011), and SRE intercomparison is not available for the Andean plateau. This is one reason for the present work. It should also be noted that no common conclusion could be drawn from the various SRE inter-comparison studies that have been carried out around the world. Even if focusing only on the four PMW-IR combined products cited above (TMPA, CMORPH, PERSIANN and GSMaP), the conclusions of the inter-comparison exercise vary among studies, and no product outperforms the others in all conditions. When considering CMORPH, PERSIANN-RT and TMPA-Adj v6, TMPA-Adj v6 was found more suitable to describe both daily and monthly precipitation over China with better categorical statistical results and both lower bias and higher correlation (Yang and Luo, 2014). Considering the same SREs, TMPA-Adj v6 was found to best reproduce some hydrological features (annual amounts over catchment, spatial distribution patterns, seasonality, number of rainy days per year, timing and volume of heavy rainfall events) in 4 African watersheds (Thiemig et al., 2012). CMORPH was found to perform better at a daily time step in terms of categorical statistics than TMPA-Adj and RT v5 in the mountainous areas of South America (Dinku et al., 2010) and to present lower bias for monthly and 10-day time steps in Africa (Dinku et al., 2007). Considering seasonal bias, PERSIANN-RT was more accurate than CMORPH and TMPA-RT in northwest Ethiopia (Romilly and Gebremichael, 2010). On the contrary, in West Africa, many authors (Gosset et al., 2013; Casse et al., 2015) found that PERSIANN-RT has by far the strongest bias compared to the two other RT products. The results for SRE quality can also vary in the same study area so that no particular SRE is found to be outperform the others in detecting daily rainfall (Gebregiorgis and Hossain, 2013) or determining seasonal and spatial monthly rainfall characteristics (Asadullah et al., 2008). The latter authors have suggested combining all SREs to optimize rainfall estimations. In comparison with other SREs, GSMaP is less documented. Over the continental United States, GSMaP-RAW v4 was found to successfully capture the seasonal spatial pattern of precipitation, and its global performance was similar to CMORPH, PERSIANN-RT and TMPA-Adj v5 (Tian et al., 2010). In China, TMPA-Adj v7 outperformed CMORPH and GSMaP-RAW v5 in terms of continuous and categorical statistics on a daily basis (Qin et al., 2014).

Our study compares nine of the most commonly used SREs with rain gauges over the Andean plateau. The objective is to determine which products have the best agreement with rain gauges, with foreseeable applications in the field of hydrology. Both real-time (or short release delay) and post-adjusted products are evaluated, as their scope of applications is complementary: RT or RAW products are necessary for some operational applications such as flood forecasting, while post-adjusted (i.e., supposedly unbiased) products are preferable for process studies or hydro-climatology purposes. Comparing both RT and adjusted versions against rain gauges is also necessary, as some studies have suggested that the adjustment may increase uncertainties in some areas (Bitew and Gebremichael, 2011); however, most studies have found that adjustment improves the products (Gourley et al., 2010; Shen et al., 2010; Dinku et al., 2010; Gosset et al., 2013; Gao and Liu, 2013; Chen et al., 2013). This is also an opportunity to verify how TMPA-Adj v7 and v6 compare over the Andean Plateau. This is the first comparison of the PERSIANN and GSMaP products against rain gauges in South America. In arid conditions similar to those of the Andean Plateau, Katiraie-Boroujerdy et al. (2013) found that TMPA-Adj v6 and PERSIANN-Adj behaved similarly in Iran. Because CMORPH has been found to perform well over mountainous areas (Dinku et al., 2007, 2010), the new CMORPH-RAW and its adjusted version, CMORPH-Adj, are tested in our study.

Trapped between high relief, with lake and salt areas accounting for close to 10% of the total area (Satgé et al., 2015), the arid region of the Altiplano presents all the typical features for which SREs suffer strong uncertainties. Assessing the behavior of nine commonly used SREs in this region is therefore instructive. This study is a step towards using SREs over the Andean plateau for hydrological applications. The evaluation is focused on rainfall characteristics that are important for assessing the water budget over the region and for understanding processes: rainfall spatial variability, seasonal variability, monthly correlations, biases and the detection and distribution of daily rainfall. Given the limited number of rain gauges in the study area, small spatial temporal features are not assessed.

2. Study Area

The Altiplano watershed is an endoreic system located between latitude 22°S and 14°S and longitude 71°W and 66°W. Three countries contribute to this area: Bolivia (70%), Peru (26%) and Chile (4%). The total area is approximately 192 000 km^2. Elevations range between 3500 m and 6500 m, with a mean elevation of 4000 m. The region includes the TDPS system, composed of Lake Titicaca, the Desaguadero River, Lake Poopó and the Coipasa salt pan (or salar) basins (Figure 1). The lowest elevations are mainly located in the southern part and in the Desaguadero River plain. This river makes the surficial connection between Lake Titicaca in the north and Uru-Uru and Poopó Lakes in the central part of the basin. The Altiplano Plateau is a very flat region with a mean slope value of approximately 5°. High and accidented reliefs are located in the two cordilleras (Occidental and Royal) that mark the western and eastern borders of the watershed, respectively. Our study area also includes the Uyuni Salar, located to the south of the TDPS system but which does not belong to the same watershed. The climate is semi-arid and closely related to the upper-air circulation. Wet conditions are due to an easterly zonal flow coming from the lowlands of the Amazonian watershed (Vuille et al., 1998; Garreaud, 1999). Because of the coastal topographic and the persistent temperature inversion close to 800 m above sea level, wet pacific conditions cannot reach the Altiplano regions (Rutllant and Ulriksen, 1979; Garreaud et al., 2003). As a consequence, an east-west gradient in precipitation is observed as well as a very marked north-south gradient, with rainfall decreasing from 1100 mm/year to less than 200 mm/year in the southern part (Garreaud et al., 2003; Pillco et al., 2007). There are two marked seasons over the area. The austral summer wet season is 5 months long (November to March) and receives more than 70% of the total annual rainfall amount (Garreaud et al., 2003). The rest of the year is the dry season, with prevailing westerly winds that prevent moisture entrance from the east (Vuille, 1999).

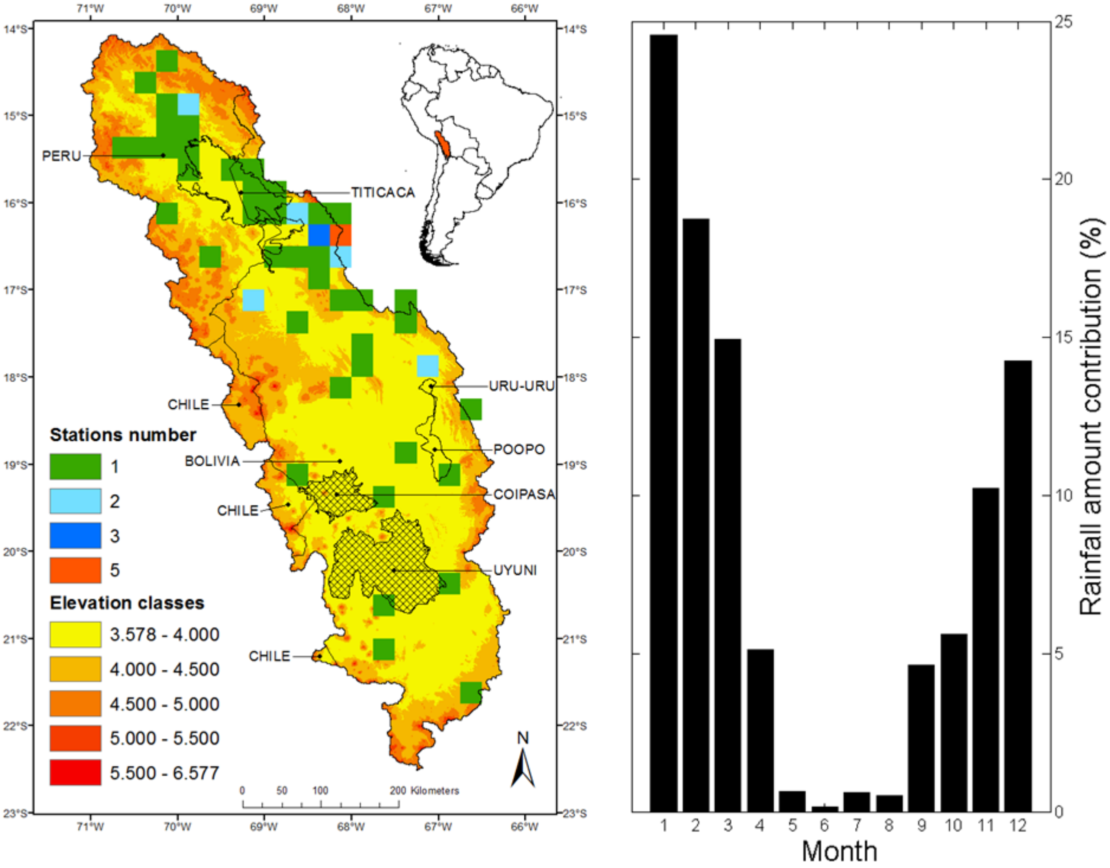

Figure 1. Study area with the number of rain gauges included in studied pixels (left) and monthly rainfall contribution (right)

3. Data Sets

3.1 Rain gauges

The Servicios Nacional de Meteorología e Hidrología from Bolivia and Peru (SENAMHI) are in charge of the meteorological network. Apart from SENAMHI, the Instituto de Hidrología y Hidráulica (IHH) of the University of San Andres in La Paz, supported by the Swedish International Development Cooperation (SIDA) operates some meteorological stations around Lake Poopó and the Institut de Recherche pour le développement (IRD) around Lakes Poopó and Titicaca. SENAMHI from both Bolivia and Peru, IHH and IRD information is available on a daily basis. A total of 176 stations are available from the 1960 – 2012 periods, but the number has considerably decreased between the 1960s and the present. For the 2005-2007 period and after quality control, 59 stations were available for this study.

3.2 Satellite Rainfall Estimates

The Tropical Rainfall Measuring Mission (TRMM) is a collaboration between the National Aeronautics and Space Administration (NASA) and the Japan Aerospace Exploration Agency (JAXA) to study tropical rainfall. TMPA is one of the regular gridded products derived from this mission. As a first step, four PMW radiometers named TRMM Microwave Imager (TMI), Special Sensor Microwave/Imager (SSM/I), Advanced Microwave Scanning Radiometer-EOS (AMSR-E) and Advanced Microwave Sounding Unit-B (AMSU-B) on board four LEO satellites named TRMM, Defense Meteorological Satellite Program (DMSP), Aqua mission and National Oceanic and Atmospheric Administration (NOAA) are used to estimate the rainfall rates at the time of overpass of these satellites in each grid cell (Huffman et al., 2007). The sparse sampling of LEOs results in significant gaps between PMW overpasses. IR data from Geosynchronous Earth Orbit (GEO) satellites (GOES-8, GOES-10, GMS-5, Meteosat-5 and Meteosat-7) were merged into half-hourly 4*4 km pixels by the Climate Prediction Center (CPC) of the National Weather Service/NOAA (Huffman et al., 2010; Janowiak et al., 2001) and are used to fill the gaps (CPC-IR hereafter). TMPA-RT is the result of these two steps and is available 6 hours after observations. TMPA-Adj is derived from a TMPA-RT calibration with monthly gauge-based data. Prior to March 2005, data were provided on a 1° scale by the Global Precipitation Climatology Centre (GPCC). After 2005, the Climate Assessment and Monitoring System (CAMS) product with a finer 0.5° resolution developed by CPC was used. TMPA-RT is first rescaled from its 0.25º / 3-hourly spatio-temporal resolution to the same as the gauge-based product (GPCP or CAMS). Both products are compared at the monthly scale, and the product ratio is calculated. A correction (multiplicative) is then applied to the TMPA-RT at the 3-hourly original time step to produce TMPA-Adj. TMPA v6 ended on July 2011 with the beginning of a new version (TMPA v7). The latter has been reprocessed for the whole TRMM mission period. Changes in the v7 algorithm are described in Huffman et al. (2010) and Huffman and Bolvin (2014). Improvements are expected because the RT version includes two additional PMW observations, the Special Sensor Microwave Imager/Sounder (SSMIS) and Micro-wave Humidity Sounder (MHS), along with two additional IR data information sources, the Meteorological Operational satellite program (MetOp) and the 0.07° Grisat-B1 (Table 1). Inconsistencies in

AMSU-B are removed using a single calibration to reprocess it instead of the two different calibration periods used for the v6 process. TMPA-RT v7, TMPA-Adj v7 and v6 are evaluated.

CMORPH is a product of the NOAA/Climate Prediction Center (NOAA/CPC). Rainfall estimates are derived from PMW radiometers (AMSU-B, SSM/I, TMI and AMSR-E). PMW rainfall estimates are propagated in space and time using motion vectors (Joyce et al., 2004) derived from CPC-IR data. Linear interpolation is performed between rainfall features propagated forward in time from the previous microwave estimate and those that have been propagated backward in time from the following microwave estimate (this part of the technique is referred to as 'morphing'). The first version (CMORPH v0.x) used an evolving algorithm with different inputs, leading to substantial inhomogeneity between 2003 and 2006. To overcome this problem and ensure better homogeneity, a new version (CMORPH v1) was generated by reprocessing data with the use of a fixed algorithm and homogeneous inputs (NOAA, 2012). CMORPH v1 (called CMORPH hereafter) substitutes the old version and covers the entire period from January 1st 1998 to the present. There is a satellite only-based estimation (CMORPH-RAW) and a bias corrected version (CMORPH-Adj). CMORPH-Adj is derived from the RAW version using two different Reference Data Sets (RDS): the CPC unified gauge analysis over land and the pentad GPCP over the ocean. Probability Density Functions (PDFs) of both CMORPH-RAW and RDS are computed, and the coefficient correction match CMORPH-RAW PDF with RDS is applied to remove the bias (Xie et al., 2011). Both CMORPH-RAW and CMORH-Adj are used in this study.

PERSIANN is a product of the Center for Hydrometeorology and Remote Sensing (CHRS). PERSIANN methodology to compute estimated rainfall differs from TMPA and CMORPH methodologies. Instead of using PMW rainfall estimation as a basis, PERSIANN uses CPC-IR data. Rainfall rates are estimated using a neural network technique described by Hsu et al. (1997) and Sorooshian et al. (2000). Rainfall computed through PMWs (TMI, AMSU-B and SSM/I) is used in a second step to adjust the neural network parameters and increase the accuracy of the rainfall estimates. There is a near real-time version (PERSIANN-RT) based on satellite only and an adjusted version (PERSIANN-Adj) using Global Precipitation Climatology Project data (version 2.1) from GPCC at a 2.5° monthly scale. To obtain PERSIANN-Adj, PERSIANN-RT is aggregated to the same 2.5° monthly scale as GPCP data so that a ratio can be computed between PERSIANN-RT and GPCP. Then, this ratio is used to compute PERSIANN-Adj. Both PERSIANN-RT and PERSIANN-Adj are used in this study.

All SREs used in this study were acquired on a 0.25° and a 3-hourly spatial and temporal resolution. All of them are freely available on the internet.

The GSMaP project is sponsored by the Japan Science and Technology (JST) agency under the Core Research for Evolutional Science and Technology (CREST) framework. GSMaP activities are promoted by the Japan Aerospace Exploration Agency (JAXA) Precipitation Measuring Mission (PMM) science team. GSMaP uses a combination of PMW and IR sensors (Table 1) (GSMaP, 2012). The PMW sensors used include TMI, AMSR-E, SSM/I and SSMIS on board the DMSP satellite; AMSU-A/-B on board the NOAA satellite; and MHS on board MetOp satellites. The algorithms used to retrieve the rainfall rate from PMWs utilize brightness temperature and are based on Aonashi and Liu (2000). Over the ocean, the algorithm developed by Shige et al. (2009) is used. For more information, please refer to GSMaP (2012). IR data from GEO satellites (MTSAT; meteosat-7/-8; GOES-11/-12) merged with a 4 km spatial resolution are used to increase the temporal and spatial resolution. To do so, a Kalman filter refines PMW rainfall estimation propagation by using the atmospheric moving vector derived from two successive IR images (Ushio et al. 2009).

Three versions of GSMaP rainfall products exist: GSMaP-NRT (GSMaP near Real Time), GSMaP-Std (GSMaP Standard, called GSMaP-RAW hereafter) and GSMaP-Adj (GSMaP Adjusted). Both GSMaP-NRT and RAW use only satellite information to retrieve rainfall rates. Due to the very short delay between a rain event and public data availability, the GSMaP-NRT product differs from GSMaP-RAW in terms of input datasets and algorithms (GSMaP, 2012). GSMaP-Adj is derived from a gauge adjustment performed on GSMaP-RAW using a daily CPC global rain gauge data set with a 0.5° spatial resolution (Mega et al., 2014). We considered version 5 of GSMaP-RAW and Adj. GSMaP-NRT was not assessed, as it is no longer available for the considered period. Both GSMaPs were acquired on a 0.1°and a 1-hourly spatial and temporal resolution. Both are freely available on internet.

SREs	PMW	IR	Main algorithm references
PERSIANN-RT	AMSU-B; SSM/I; TMI	CPC-IR	Hsu et al., 1997 / Sorooshian et al., 2000
PERSIANN-Adj	AMSU-B; SSM/I; TMI	CPC-IR	Hsu et al., 1997 / Sorooshian et al., 2000
CMORPH-RAW	AMSU-B; SSM/I; TMI; AMSR-E	CPC-IR	Joyce et al., 2004 / Xie et al., 2011
CMORPH-Adj	AMSU-B; SSM/I; TMI; AMSR-E	CPC-IR	Joyce et al., 2004 / Xie et al., 2011
TMPA-RT v7	AMSU-B; SSM/I; TMI; AMSR-E; SSMIS; MHS	CPC-IR; MetOp; Grisat-B1	Huffman et al., 2010 / Huffman and Bolvin 2014
TMPA-Adj v7	AMSU-B; SSM/I; TMI; AMSR-E; SSMIS; MHS	CPC-IR; MetOp; Grisat-B1	Huffman et al., 2010 / Huffman and Bolvin 2014
TMPA-Adj v6	AMSU-B; SSM/I; TMI; AMSR-E	CPC-IR	Huffman et al., 2007
GSMaP-RAW	TMI; AMSR-E; SSM/I; SSMIS; AMSU-A; AMSU-B; MHS	MTSAT; meteosat -7/-8 ; GOES -11/-12	GSMaP., 2012; Ushio et al 2009;
GSMaP-Adj	TMI; AMSR-E; SSM/I; SSMIS; AMSU-A; AMSU-B; MHS	MTSAT; meteosat -7/-8 ; GOES -11/-12	GSMaP., 2012; Ushio et al 2009; Mega et al., 2014

Table 1. PMW and IR data used by SREs for rainfall retrievals

4. Methodology

4.1 Rain gauge data processing

The quality of the rain gauge data was assessed using the Regional Vector Method (RVM) (Vauchel, 2005; Villar et al., 2009). RVM is based on the hypothesis that the inter-annual variability of rainfall amounts for gauges located in the same climatic zone should have some consistency given that they experience the same rainfall regime.

Data from 159 stations with at least 5 continuous years available during the 1960-2012 period were analyzed. The data were classified into 8 regional groups. Only 123 stations had a homogeneous series for the period 1990-2012 and only 72 for the period 2002-2010. There is indeed a decrease in the number of stations in operation, especially since the 1990's. Data from stations with a homogeneous annual series were subsequently analyzed at the monthly scale, and consistency with other stations from the same regional climate group was verified. A total of 59 quality-controlled stations were selected for the 2005-2007 period. These stations are distributed on 48 SRE resolution (0.25°) pixels (Figure 1) and 54 SRE resolution (0.1°) pixels (*Anexo 4*, Figure S1). Data were not interpolated because interpolation from a sparse and uneven rain gauge network could generate unrealistic estimations (Li and Heap, 2008; Scheel et al., 2011). For pixels with more than 1 rain gauge, the data were averaged to produce a single mean value per day and per pixel. According to the GPCC database (http://kunden.dwd.de/GPCC/Visualizer), only 2 gauges situated southeast and west of Lake Titicaca were included in the GPCC product for the region and period of interest. Therefore, our reference data set can be considered mostly independent from the GPCC data used to adjust some of the SREs.

The SRE daily accumulations are computed from 12:00 to 12:00 UTC to match the 8:00 to 8:00 local time of the gauge data in Bolivia. The native 0.25° spatial resolution is kept for TMPA, CMORPH and PERSIANN products along with 0.1° for GSMaP products.

4.2 Comparison methodology

This study aims to assess each SRE in its native spatial resolution. However, GSMaP products present a finer spatial resolution (0.1°) in comparison with all other SREs assessed in this study (0.25°). This does not allow direct comparison between SREs in their native spatial resolution. Thus, to simplify interpretation of the results, the methodology is applied with a 0.25° SRE pixel resolution (TMPAs; PERSIANNs and CMORPHs). Then, according to the same methodology, GSMaP products were treated separately, and the results are available in the *Anexo 4*.

The SRE-gauge comparisons are carried out only for the 5 months of the rainy season (November – March) to avoid spurious correlations due to the seasonal cycle. These 5 months were found to contribute to 82.7% of total rainfall amount for the period 2005-2007 (Figure 1).

Some daily values are missing in the SRE or rain gauge time series. When one estimate is missing on one day for a pixel, then this day is excluded from this pixel's series for all SREs and the rain gauge. The mean seasonal rainfall (for the November-March season only) for the period 2005-2007 and for each pixel was computed and plotted (Figure 2). Statistical scores were computed considering the pixels and years for which at least 80% of the daily data were available (Buarque et al., 2011). The mean Root Mean Square Error (RMSE), Bias (Equation) and Correlation Coefficient (CC) were computed considering all pixels and all years; additionally, the 10 coastal Lake Titicaca pixels and all other inland pixels were separated to highlight some potential deficiencies in SRE estimations over this lake.

$$bias = \frac{\sum_{i=1}^{n}(P_{SRE_i} - P_{G_i})}{\sum_{i=1}^{n} P_{G_i}} \times 100$$

$$RMSE = \frac{\sqrt{\frac{\sum_{i=1}^{n}(P_{SRE_i} - P_{G_i})^2}{N}}}{\frac{\sum_{i=1}^{n} P_{SRE_i}}{N}} \times 100$$

where N is the length of the series and includes the rainfall total (monthly or yearly) from all available pixels; $P_{G\,i}$ is the gauge precipitation for the considered month or years i; and $P_{SRE\,i}$ is the SRE precipitation for the considered month or year i.

At the monthly scale, the same selection procedure as for the annual step was used for each pixel. We built our database by selecting months with more than 80% of the common daily rainfall for all SREs and corresponding rain gauges. Thus, each pixel has between 13 and 15 months for the 2005-2007 period, with a total of 716 months for the 48 pixels. The mean value of the 716 monthly RMSE, bias and CC total amounts was first computed to assess SREs at the regional scale (Table 3). As for the seasonal scale, we also analyzed the 10 coastal Lake Titicaca pixels separately from all other inland pixels (Table 3). Finally, RMSE, bias and CC were computed for each pixel to analyze the spatial variability of the performance for the whole period 2005-2007 (Figure 5 to 7).

We considered CC as significant if its value was equal or greater than 0.7 (Condom et al., 2010), RMSE as acceptable if it was less than or equal to 50% (Adeyewa and Nakamura, 2003; Condom et al., 2010) and bias as acceptable when -10% <= bias <=10% (Brown, 2006; Yang and Luo, 2014).

Figure 4 displays the Cumulative Distribution Function (CDF), which indicates how well the SREs reproduce rainfall distribution, an important consideration for hydrology.

We used categorical statistics to evaluate the products at the daily time step; rainfall amounts are considered as discrete values with only two observable cases --rainy day or not. A rainy day is considered to be precipitation greater than or equal to a prescribed threshold ($mm.day^{-1}$). Four cases are possible (Table 2): both SRE and rain gauge report a rain event (a), only SRE reports a rain event (b), only rain gauge reports a rain event (c) or neither SRE nor rain gauge report a rain event (d).

According to this characterization, two statistical parameters can be computed: the Probability of Detection (POD) and the False Alarm Ratio (FAR). (Scheel et al., 2011; Katiraie-Boroujerdy et al., 2013; Prakash et al., 2014; Ochoa et al., 2014).

$$POD = \frac{a}{(a + c)}$$

POD is an indicator of the SRE's ability to correctly forecasts rain events. Values vary from 0 to 1, with 1 as a perfect score.

$$FAR = \frac{b}{(a + b)}$$

FAR is an indicator of how often SREs detect a rain event when it does not occur. Values vary from 0 to 1, with 0 as a perfect score.

SRE rainfall is a mean estimation of an area of approximately 625 km^2 (100 km^2 for GSMaPs). A single rain gauge can be representative of such an area at monthly and annual scales but not at the daily scale. In the hypothesis where SREs perfectly represent rain patterns, a rain event detected by the rain gauge will automatically be detected by the SREs. However, because of high rainfall spatial variation in tropical areas and a larger area represented by SREs than by rain gauges, a rain event detected by the SREs will not always be detected by a rain gauge. This feature will increase the occurrence of "b" (Table 2) and will consequently have an impact on FAR computation and interpretation. To limit the impact of gauge representativity error, POD and FAR were only computed for pixels that include at least 2 rain gauges. All indices were computed for several thresholds: 0, 2, 5, 10, and 15 mm.day^{-1} (Li et al., 2013; Su et al., 2008; Ochoa et al., 2014). Based on rain gauge measurements, these classes respectively regroup 100%, 54.6%, 26.3%, 7.7% and 2% of rainfall events and account for 100%, 90%, 64.7%, 28.9% and 10.4% of the rainfall amount over the considered period (Figure 8A and B). For both SREs and rain gauges, the percentage of rain event occurrence for each threshold and the total amount of rainfall for each class are shown in Figure 8A and B, respectively.

		Rain gauge	
		Rain	No rain
SRE	Rain	*a*	*b*
	No Rain	*c*	*d*

Table 2. Contingency table used to define categorical scores for the verification of SREs against gauge data.

5. Results and discussions

5.1 Rainy season scale

Figure 2 presents the spatial distribution of the mean seasonal (November-March) cumulative rainfall for each SRE. All SREs reproduce the typical regional north-south rainfall pattern (Garreaud et al., 2003; Pillco et al., 2007) and the less marked east-west gradient. These gradients are most pronounced for the PERSIANN products.

Another salient feature of the mean annual rainfields is the difference between rainfall over land and over the large water surfaces: Lakes Titicaca and Poopó. Interestingly, these land-lake contrasts are very different among SREs. A decrease in rainfall amount is observed over Lake Titicaca for all SREs except for CMORPH-RAW and Adj. Unfortunately, the rain gauges are located on the lakeshore and do not provide information about the rainfall pattern over the lake. However, the analysis of Lake Titicaca pixels confirms this underestimation trend with lower statistical criteria (see below). The observed SRE decrease over the lake contradicts the higher rainfall amount previously observed (Roche et al., 1992) based on an isohyet map including a rain gauge located on Taquili island in the northwest part of Lake Titicaca that registers the highest annual rainfall amount. According to these authors, the high water content of Lake Titicaca allows more solar radiation absorption and results in higher temperatures for the lake water than for the surrounding land. Crossing the lake, air masses pick up lake moisture while their temperature increases and permits their ascension. This convection increases rainfall above the lake (Roche et al., 1992). This strong land-water contrast (in radiation absorption, temperature and humidity) is a potential source of error for PMW rainfall retrieval (Ferraro et al., 1998; Levizzani et al., 2002) and could explain why some products underestimate rainfall over Lake Titicaca. Moreover, warm rain processes rely on higher temperature clouds, which can be misidentified as a non-rainy day by IR data. As a result, rainfall events can be lost by SREs, thus underestimating the rainfall amount over Lake Titicaca. An extended water surface such as Lake Titicaca should most likely be treated with caution by algorithms, in the same way coast lines are (Adler et al. 1993). SRE behavior is different over Lake Poopó. Both CMORPH products and TMPA-RT enhance rainfall over this lake. This contrasting SRE behavior over the two lakes may be attributed to their size difference. Lake Poopó's mean depth is only 1.5 m (Zolá and Bengtsson, 2010), and the water and air temperature are typically similar over its surface. Because of its low depth, solar absorption is low over Lake Poopó, and the water temperature is close to the temperature of the surrounding land, with a resulting small emissivity contrast. Given the considerable extent of salt areas and their different emissivity features, these areas should influence SREs. However, over the Andean plateau, these salt areas do not seem to impact SREs.

A wet region of few pixels appears in the southeastern Andean part of Lake Titicaca. Northeast wet winds are deviated to these mountain regions (Roche et al., 1992). However, this zone must be considered with caution because it has permanent ice cover, which SREs can confuse with precipitation (Dinku et al., 2007). Northward rainfall is known to occur less because of high-elevation mountains that prevent moisture entrance. TMPA products present some pixel inconsistencies most likely caused by snow and ice cover. The slightly higher rainfall zone detected by TMPA-Adj v7 in the northwestern part of the watershed agrees with previous isohyet maps (Roche et al., 1992).

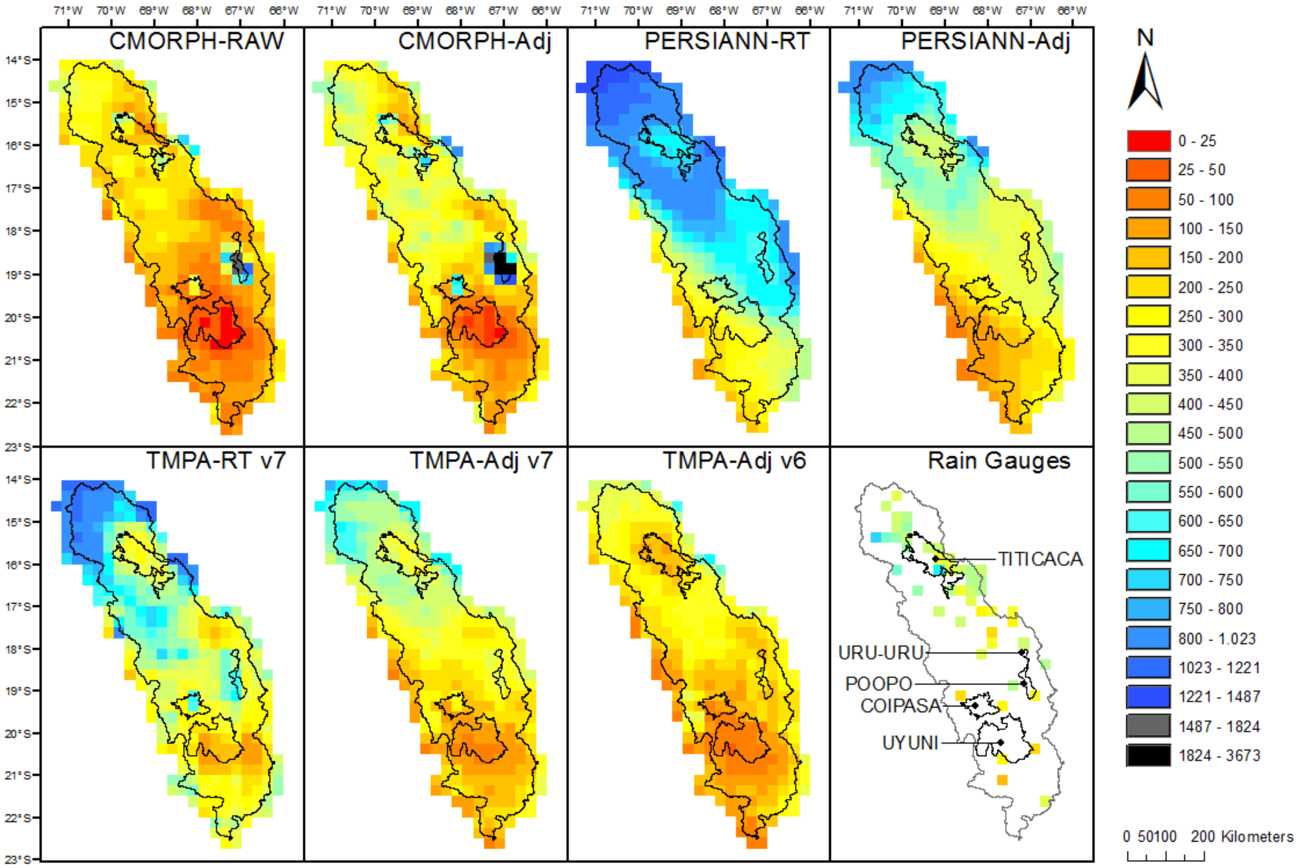

Figure 2. Annual rainfall pattern for all SREs and rain gauges measurements. Rainfall amounts are in mm.

In addition to spatial variability, the absolute value of rainfall differs among SREs. TMPA-Adj v7 is the closest to rain gauge estimates, as confirmed below.

The RMSE, bias and CC calculated using all pixels as well as the November-March rainfall over the 2005-2007 period for the seven SREs are shown in Table 3. Despite the small number of gauges available in the region for the adjustment, all Adjs versions present better statistical scores than their RT versions. PERSIANN-RT overestimates rainfall by 94.2%, and the calibration conducted on PERSIANN-Adj reduces the bias to 22%. TMPA-RT v7 overestimation (bias=28.2%) is completely canceled by the adjustment, and TMPA-Adj v7 presents a small negative bias of -4.2%. CMORPH-RAW tends to underestimate precipitation (negative bias of -42.7%), and this is well corrected in CMORPH-Adj (-13%). The adjustment effects are clear in Figure 3, with Adj values fitting better with gauge measurement than RT values over the whole study period. Unlike the other products, the adjustment reduces the CC in the case of CMORPH. The low CC of CMORPH products appears related to the strong overestimation of rainfall over

Lake Poopó, which is further enhanced by adjustment (Figure 2, Table 3). This feature is highlighted by more outlier values in CMORPH-Adj than CMORPH-RAW products (Figure 3). The improvement of TMPA-Adj v7 over v6 is clear from Figures 2 and 3; the spatial patterns are much improved, and all scores are higher. To sum up, at the season scale, TMPA-RT v7, TMPA-Adj v7 and v6 and PERSIANN-Adj present RMSE values below 50%. Only TMPA-Adj v7 has a suitable bias value (≤10%). All SREs have a CC below 0.7. The best CC value is 0.62 for TMPA-Adj v7. Bias values are higher for coastal pixels than inland pixels for all SREs (Table 3) and thus confirm the underestimation tendency of SREs over Lake Titicaca (Figure 2). Additionally, coastal pixels are poorly or uncorrelated with gauge measurement for all SREs except for CMORPH products, which are least affected by Lake Titicaca. RMSE variations between coastal and inland pixels remain slight, except for TMPA-Adj v6, with an increment of more than 50% from inland to coastal pixels. TMPA-Adj v7 could be used at the seasonal scale for inland regions, as it fits all previously defined quality criteria (absolute bias ≤10%, RMSE ≤50% and CC ≥0.7) with a bias of -1.5%, a RMSE of 26% and a CC of 0.72.

	RMSE (%)			Bias (%)			CC		
	All	Inland	Coastal	All	Inland	Coastal	All	Inland	Coastal
PERSIANN-RT	58.9	60.3	52.2	94.2	100.5	71.8	0.37	0.47	-0.11
PERSIAN-Adj	33.5	33.8	32	22	25.6	8.9	0.55	0.65	-0.13
TMPA-RT v7	43	43.1	39.8	28.2	38.3	-8.3	0.49	0.64	-0.11
TMPA-Adj v7	29.4	26	40.9	-4.2	-1.5	-14.3	0.62	0.72	0.1
TMPA-Adj v6	76.4	63.1	138.8	-35.2	-29.9	-54	0.27	0.4	-0.16
CMORPH-RAW	100.9	101.2	99.9	-42.7	-42.2	-44.5	0.28	0.27	0.34
CMORPH-Adj	67.6	70.6	52.3	-13.3	-10,8	-22.6	0.19	0.16	0.43

Table 3. Seasonal Bias, RMSE and CC for each SREs on the global scale and considering coastal and inland pixels

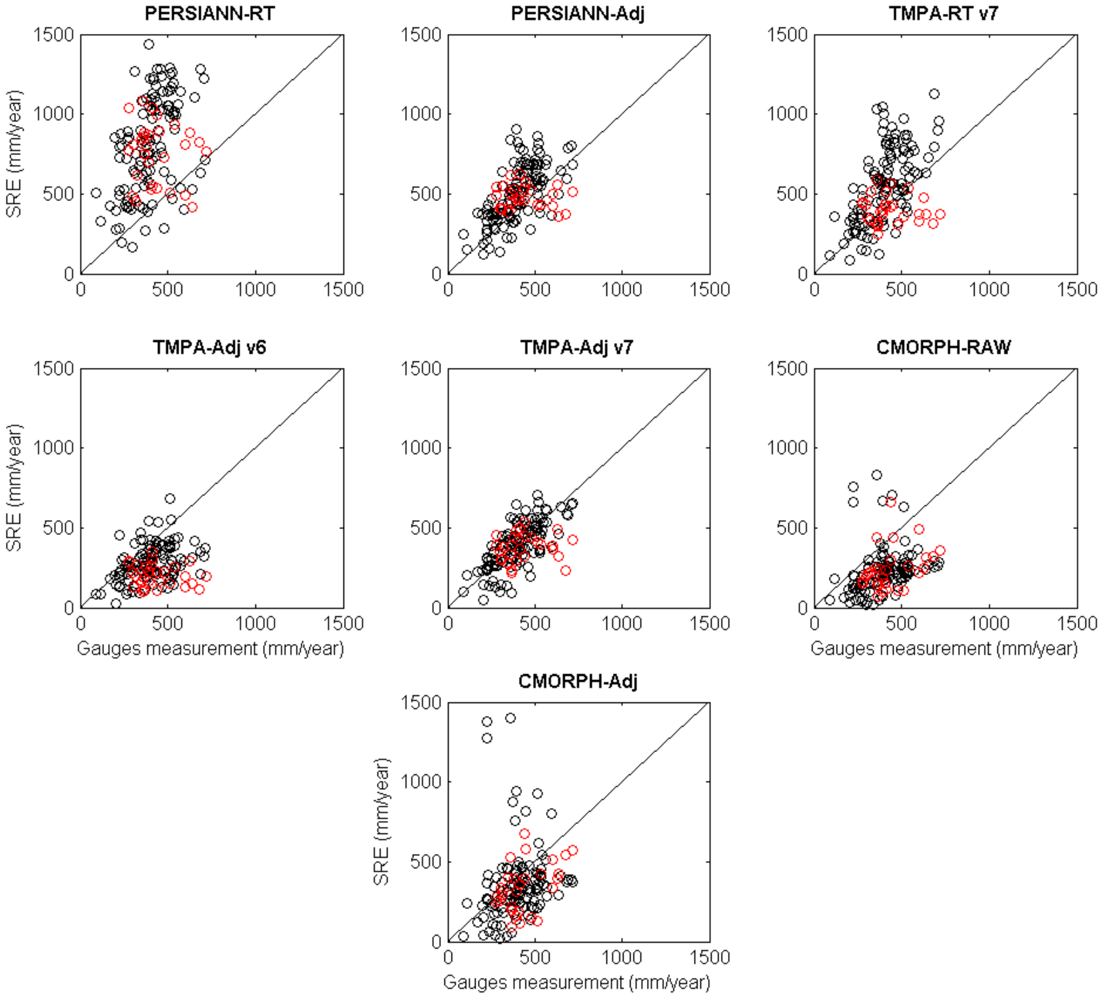

Figure 3. Scatter plots of SREs versus Rain gauges with Inland pixel values in black and coastal pixel in red.

5.2 Monthly scale

Table 3 displays the bias, RMSE and CC values at the monthly scale. TMPA-Adj v7 has the best scores overall. With a bias of -4.3%, a RMSE of 48.7% and a CC of 0.68, this product fits the quality criteria set in the “Methodology” section (absolute bias ≤10%, RMSE ≤50% and CC ≥0.7). PERSIANN-Adj can be considered 'second best', with performance close to the prescribed quality criteria. All other SREs are far from the prescribed quality criteria. For the seasonal scale, Lake Titicaca coastal pixels present a lower bias and correlation than inland pixels for all SREs except CMORPH products. The results confirm the rainfall underestimation over Lake Titicaca for those SREs at the monthly scale. When considering only inland pixels, TMPA-Adj v7 fits all quality criteria, with a bias of -1.4%, a RMSE of 43.8% and a CC of 0.74.

	RMSE (%)			Bias (%)			CC		
	All	Inland	Coastal	All	Inland	Coastal	All	Inland	Coastal
PERSIANN-RT	67.7	68.9	61.7	93.8	100.5	70.03	0.39	0.44	0.19
PERSIANN-Adj	46.5	45.4	50.9	21.9	25.7	8.64	0.63	0.68	0.48
TMPA-RT	63.5	61.6	72.3	28.0	38.4	-8.59	0.43	0.49	0.27
TMPA-Adj v7	48.7	43.8	65.3	-4.3	-1.4	-14.39	0.68	0.74	0.48
TMPA-Adj v6	99.1	84.0	170.6	-35.3	-29.9	-53.93	0.53	0.60	0.34
CMORPH-RAW	138.4	138.9	136.3	-42.7	-42.1	-44.71	0,21	0.19	0.28
CMORPH-Adj	88.4	90.9	76.8	-13.4	-10.7	-22.74	0.33	0.30	0.53

Table 4. Monthly Bias, RMSE and CC for each SREs on the global scale considering and considering coastal and inland pixels

Figure 4 analyzes the Cumulative Distribution Functions (CDFs) of the monthly rainfall rates. It confirms that TMPA-Adj v7 is the closest to rain gauge observations. Despite its relatively low bias and satisfactory CC, PERSIANN-Adj does not reproduce well the observed CDF and tends to overestimate the proportion of moderate to high monthly rainfall rates. A similar tendency to overestimate the proportion of high monthly rainfall is found for TMPA-RT, and this problem is extreme for PERSIANN-RT. On the contrary, CMORPH-RAW and Adj tend to overestimate the relative proportion of low monthly rainfall.

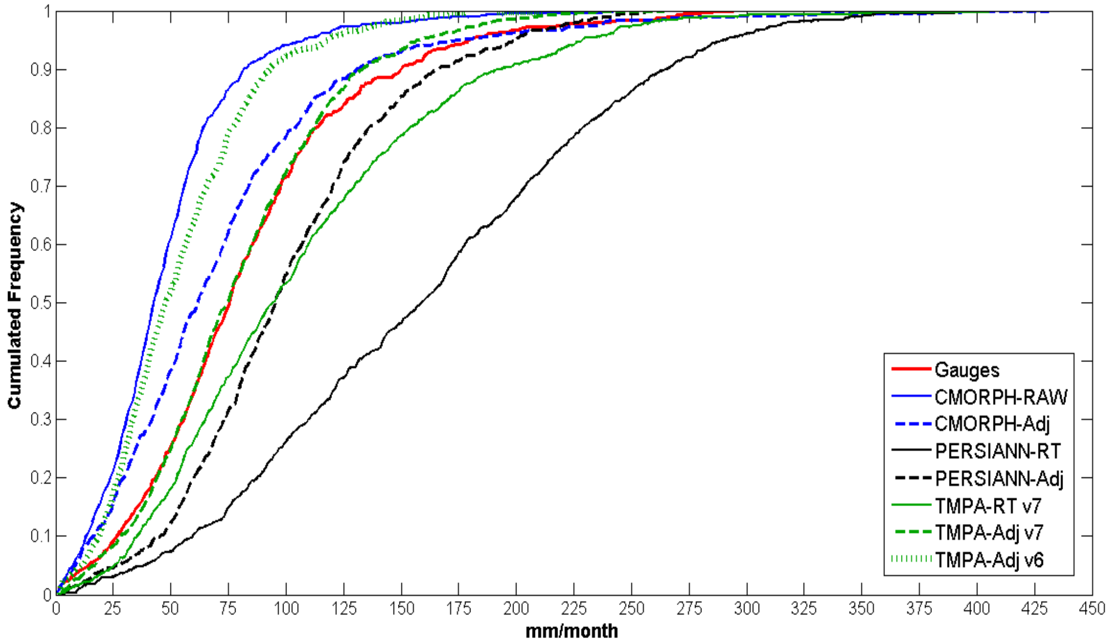

Figure 4. CDF for SREs and rain gauges with a 1 mm.month^{-1} increment.

Figure 5 presents the mean monthly bias computed for each of the 48 pixels and for all considered SREs. These maps confirm the trend shown in Table 3 and Figure 4. Over the entire study area, PERSIANN-RT overestimates rainfall with a high positive bias, while CMORPH-RAW underestimates rainfall with a high negative bias. PERSIANN-Adj and CMORPH-Adj present lower overall biases, although with some differences inside the domain and only a few pixels where the bias falls below +/- 10%. For TMPA products, the adjustment on v7 reduces the bias in the northern part of the domain, especially over the Lake Titicaca region, with many pixels reaching an absolute bias level below 10%. Again, the improvement over v6 is obvious. In the northern part of the domain, TMPA-Adj v7 biases are low and better than any other SRE. In the southern half of the domain, the bias appears lower and more uniform spatially for PERSIAN-Adj than for TMPA-Adj v7. This is also confirmed by the monthly rainfall CDF for the southern half (not shown), where PERSIANN-Adj is closer to the gauge than TMPA-Adj v7.

Figure 6 displays the RMSE spatial pattern. Regarding bias, CMORPH-RAW, Adj and TMPA-Adj v6 show high RMSE values, especially in pixels located around Lake Titicaca and the southern part. Both PERSIANN-Adj and TMPA-Adj v7 have a majority of pixels with a RMSE below 50%. Similar to the bias results, PERSIANN-Adj seems to be closer to the gauge series in the southern half of the domain.

Figure 7 displays the CC maps. As expected from Table 3, CMORPH-RAW presents the worst results, with a negative CC for several pixels. These results are much improved for CMORPH-Adj. A single negative CC pixel remains south of Lake Poopó, where CMORPH-Adj was found to significantly overestimate total rainfall. PERSIANN-Adj and TMPA-Adj v7 present high CC values, and many pixels reach a CC value better than or equal to the quality threshold value of 0.7. TMPA-Adj v7 presents a better CC value than TMPA-Adj v6 for the whole watershed. As for bias and RMSE, PERSIANN-Adj CC values are close to TMPA-Adj v7 in the southern part and are slightly worse in the northern half.

Figures 5 to 7 confirm the positive effects of gauge adjustment on TMPA v7 and PERSIANN. The improvement of PERSIANN-Adj over PERSIANN-RT agrees with the results found over Iran in a similar arid context (Katiraie-Boroujerdy et al., 2013). A similar conclusion for TMPA-Adj v7 versus its RT version was also found over the continental United States and West Africa (Chen et al., 2013; Gosset et al., 2013). The new TMPA-Adj v7 gives better rainfall estimation than TMPA-Adj v6 over the Andean Plateau, as found in other pacific Andean regions (Zulkafli et al., 2014; Ochoa et al., 2014) and China (Chen et al., 2013). The first CMORPH version was found to outperform TMPA products in mountainous areas (Dinku et al., 2007, 2010). Here, we find poor statistical results at the monthly scale for CMORPH-RAW in the Andean plateau. However, our set of rain gauges is mostly located in the flat central plain. CMORPH-Adj is closer to the gauges but still suffers from serious deficiencies, especially on Lake Poopó. In the southern half of the domain, PERSIANN-Adj has slightly lower biases and RMSE than TMPA-Adj v7 and a similar CC value. However, given the fewer gauges available in this part of the domain, any conclusion should be drawn with caution. If these differences were confirmed, one could recommend the use of PERSIANN-Adj in the southern half and TMPA-Adj v7 in northern half.

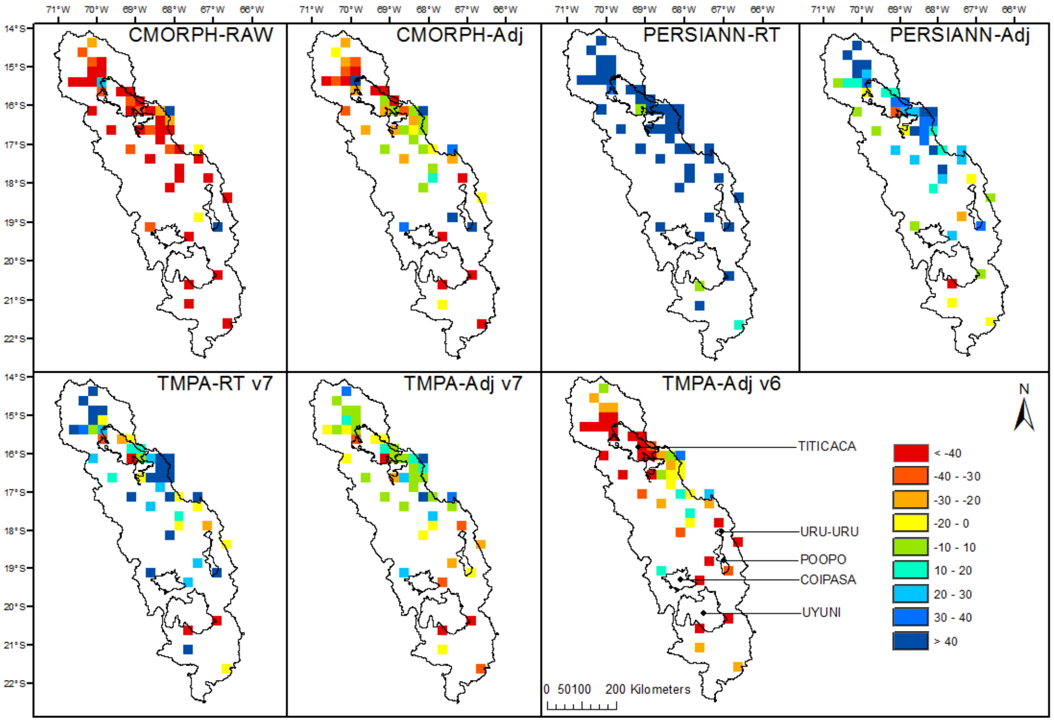

Figure 5. Spatial pattern of the mean monthly bias between SREs and rain gauges for the whole 2005-2007 period.

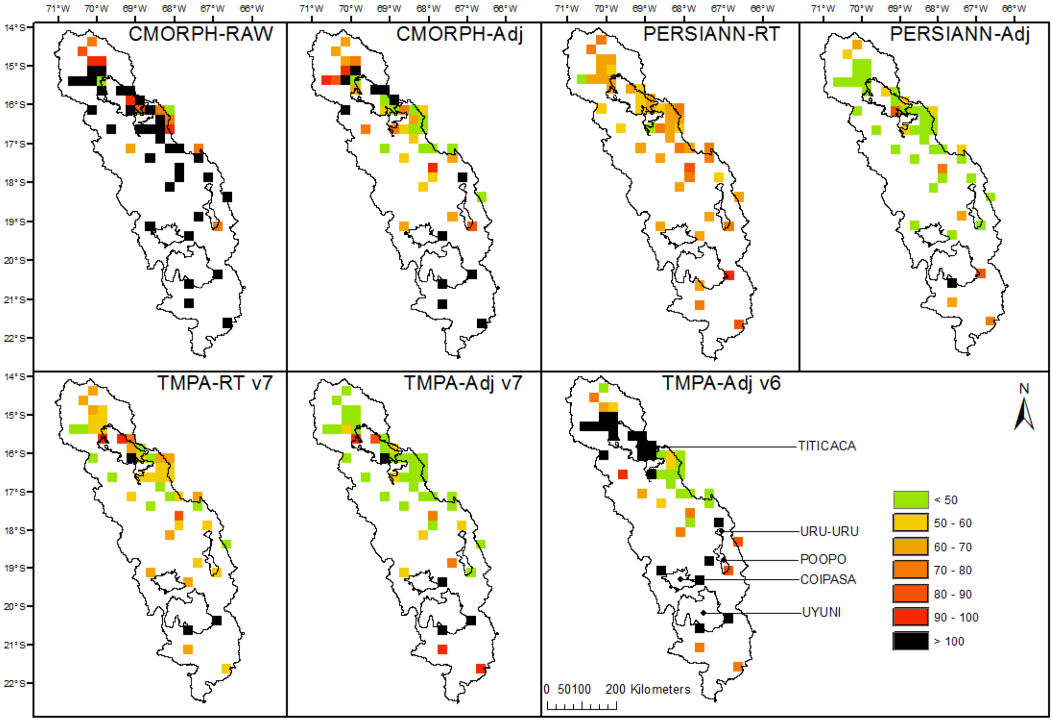

Figure 6. Spatial pattern of RMSE between rain gauges and SREs monthly precipitation for the 2005-2007 period.

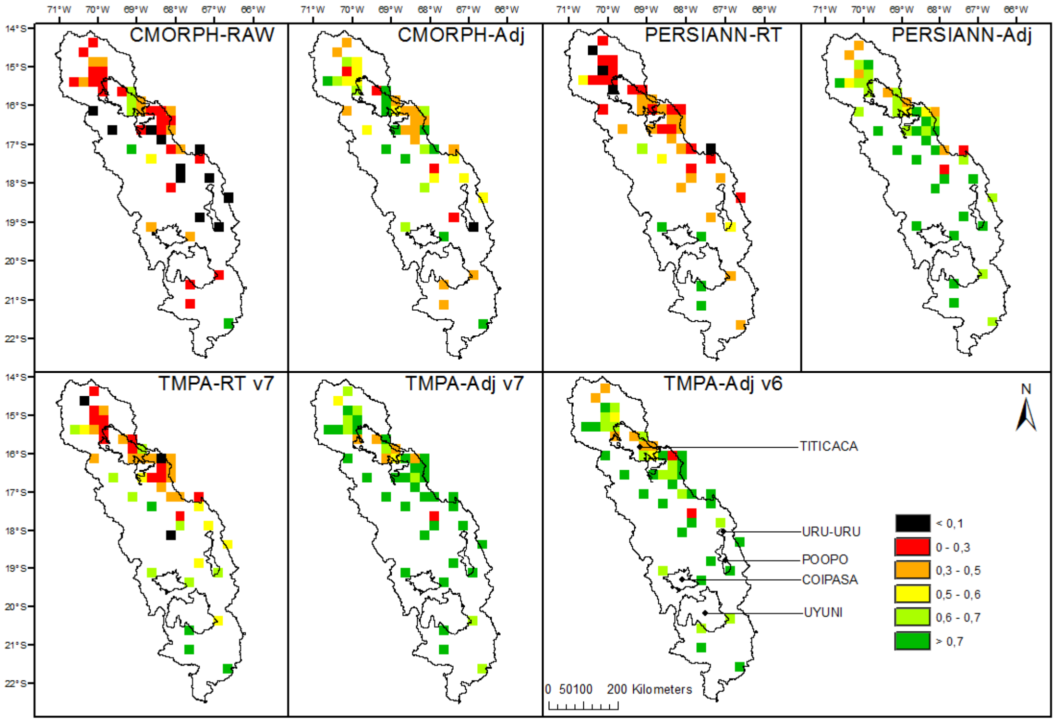

Figure 7. The spatial pattern of CC between rain gauges and SREs monthly precipitation for the whole 2005-2007 period.

5.3 Daily scale

The sparseness of the available gauge network limits the diagnostics that can be provided at the daily time step. Given the spatial variability of the daily rainfall amounts, a single gauge is not perfectly representative of the mean areal rainfall over a 0.25° pixel. At the daily time step, this sampling uncertainty is higher than at the monthly or seasonal time step. Nevertheless, the consistency between the gauge and the SREs can be analyzed, at least for the pixels where at least 2 gauges are available (see Figure 1).

Figure 8A and 8B analyze the SREs in terms of daily rainfall distribution. Because hydrological processes are generally nonlinear, they react not only to rainfall accumulation but also to the way rainfall is distributed within the basin and in time. From a hydrological point of view, only daily rainfall events superior to evapotranspiration contribute to superficial and sub-superficial runoff. Previously, evapotranspiration values ranging from 3.4 to 5.8 mm.day^{-1} were found on the Altiplano (Garcia et al., 2004; Geerts et al., 2006). A realistic distribution of daily rain rates, especially rain rates above 5 mm.day^{-1}, is therefore an important consideration for the hydrological applications of SREs.

Both CMORPH products –and, even more so, CMORPH-RAW- underestimate the proportion of daily rainfall above 2 mm.day^{-1} (Figure 8A). This explains their strong negative bias (Figure 8B) despite a relatively high POD (Figure 8C) of rainfall above 0 mm.day^{-1}. The POD decreases sharply from 2 mm.day^{-1} onwards. On the contrary, PERSIANN-RT and, to a lesser extent, PERSIANN-Adj and TMPA-RT overestimate the proportion of rainfall rates above 2 mm.day^{-1}. Figure 8B shows that most of the positive bias in these three products is incurred by rain rates in the range of 2 to 15 mm.day^{-1}. TMPA-Adj v7 is the SRE that best renders the distribution of daily rainfall rates, even if a small positive bias is incurred by rain rates above 10 mm.day^{-1}.

All SREs (except TMPA-Adj v6) have a good ability to detect when a day is rainy (above 0 mm.day^{-1}) and when the overall FAR (threshold 0 mm.day^{-1}) is low. However, the categorical statistics degrade for all products for higher daily rainfall rates, as previously found in other studies (Li et al., 2013; Ochoa et al., 2014). Some of this degradation may be due to the uncertainty on the reference itself and the gauge spatial representativeness issue. More analysis with a denser gauge network would be necessary to analyze the daily rainfall time series and investigate further these differences. By considering coarser pixel size with only one rain gauge over the same region, Blacutt et al. (2015) found a very high value of FAR for the same rainy season (0.63) for TMPA-RT v7 and for a 0 mm.day^{-1} in comparison with our result (0.17). By averaging daily rainfall event occurrence on a watershed scale, Ochoa et al. (2014) found slightly better POD and FAR values in the Pacific Andean region.

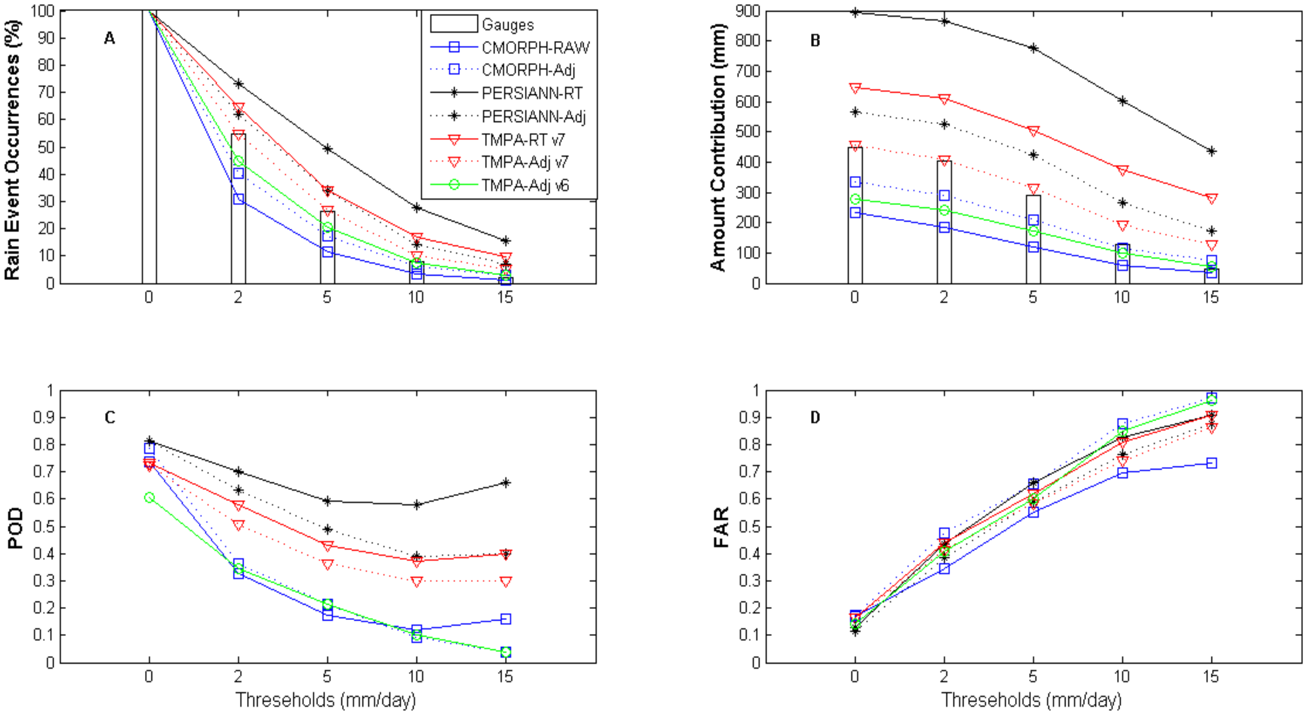

Figure 8. Rain event occurrences (A) and total amount contribution (B) for all SREs and rain gauges measurement for different thresholds values and for the whole 2005- 2007 period. Categorical statistic (POD, FAR) for all SREs based on both same thresholds values and period (C,D).

6. Conclusion

The Andean plateau is one of many tropical regions where SREs are needed for water studies to compensate for the deficit in rain gauges. Unfortunately, this rain gauge deficit also means that SRE validation in these regions is limited. In the present work, a total of 59 gauges spread over 48 0.25° and 54 0.1°resolution satellite pixels were used to analyze several SREs over a 3-year period. Although limited, this is the most comprehensive satellite-ground rainfall comparison available thus far over South America regions. The TMPA (RT, Adj v7 and v6), PERSIANN (RT and Adj), CMORPH (RAW and Adj) and GSMaP (RAW and Adj) products were compared to the gauges at the season (rainiest 5 months) and monthly scale; some analysis was also conducted at the daily scale on a limited number of pixels. Despite the limited coverage and scarcity of the ground reference, some consistent features emerged from the analysis:

- All SREs reproduce the salient pattern of the annual rain field: a marked north-south gradient and a lighter east-west gradient. However, the intensity of the gradient differs among SREs; it is well marked in the TMPA, PERSIANN and GSMaP products and smoothed out in the CMORPH products.
- Another interesting difference among products is the contrast in rainfall between the water surfaces (Lakes Titicaca and Poopó) and the surrounding land. Some products (PERSIANN; TMPA and GSMaP) show a rainfall deficit over Lake Titicaca, which seems to contradict the literature and may be due to the emissivity contrast between the lake and the surrounding lands and warm rain cloud processes. There is currently no rainfall measurement over the lakes to validate the rainfall pattern. However, a first approach was attempted to separate inland and Lake Titicaca coastal pixels. Rainfall underestimation over Lake Titicaca was confirmed for PERSIANN, TMPA and GSMaP, with a lower CC and bias for coastal pixels at both the seasonal and monthly scale.
- The RAW (or RT) products have strong biases over the studied region. Theses biases are strongly positive for PERSIANN (above 90%), moderately positive for TMPA (28%), strongly negative for CMORPH (-42%) and moderately negative for GSMaP-RAW (-18%). They are associated with a deformation of the rain rate frequency distribution: CMORPH overestimates the proportion of rain rates below 2 mm.day^{-1}; GSMaP-RAW underestimates the proportion of all rain rates, and the other products tend to overestimate the proportion of moderate to high rain rates. These biases are much reduced by gauge adjustment in all four products. TMPA-Adj v7 shows the best overall agreement with gauges in terms of correlation (spatial and temporal, at the monthly scale), rain rate distribution and bias. The agreement is even better when considering only inland pixels, as it fits all the quality criteria for both the seasonal and monthly scale. However, PERSIANN-Adj bias and RMSE in the southern part of the domain are lower.

These results imply that some of the tested SREs (namely TMPA-Adj v7 and PERSIANN-Adj) can be used over the region when monthly to annual rainfall estimates are needed, e.g., hydro-climatological and agro-climatological studies or water budget assessment at the season/regional scale. For hydrological applications that require a good representation of the daily rainfall rate frequency distribution, TMPA-Adj v7 seems the most suitable. For hydrological prediction needing SREs available in real-time or with a short delay, a bias correction or compensation (Casse et al., 2015; Thiemig et al., 2013) technique would be required given the observed biases in the non-adjusted products.

Complementary work is planned based on a regional and integrative approach. The hydrological water budget and its variability will be assessed using complementary satellite data, such as Gravity Recovery and Climate Experience (GRACE) data, soil humidity content derived from Soil Moisture Ocean Salinity (SMOS) and MOD16 evapotranspiration products, to check consistency. Additionally, hydrological modelling using SREs as rainfall inputs and comparisons with observed discharge or soil moisture would complement the hydrological assessment of SREs while avoiding direct comparison with a scarce gauge network and the subsequent gauge spatial representativeness problem.

Acknowledgments

This work was supported by the Centre National d’Etudes Spatiales (CNES) in the framework of the HASM project (Hydrology of Altiplano: from Spatial to Modeling). The first author is grateful to the SENAMHI and IHH for the release of their rainfall information and to the IRD (Institut de Recherche pour le Développement) and CAPES (Coordenação de Aperfeiçoamento de Pessoal de Nível Superior) Brazil for their financial support. The authors are also thankful for the two anonymous reviewers for their constructive reviews that enhanced this work.

References

Adeyewa, Z. D., and K. Nakamura, 2003: Validation of TRMM Radar Rainfall Data over Major Climatic Regions in Africa. J. Appl. Meteorol., 42, 331–347, doi:10.1175/1520-0450(2003)042<0331:VOTRRD>2.0.CO;2.

Adler, R. F., A. J. Negri, P. R. Keehn, and I. M. Hakkarinen, 1993: Estimation of monthly rainfall over Japan and surrounding waters from a combination of low-orbit microwave and geosynchronous IR data. doi:10.1175/1520-0450(1993)032<0335:EOMROJ>2.0.CO;2.

Aonashi, K., Liu, G., 2000. Passive Microwave Precipitation Retrievals Using TMI during the Baiu Period of 1998. Part I: Algorithm Description and Validation. J. Appl. Meteorol. 39, 2024–2037. doi:10.1175/1520-0450(2000)039<2024:PMPRUT>2.0.CO;2

Asadullah, A., N. McINTYRE, and M. Kigobe, 2008: Evaluation of five satellite products for estimation of rainfall over Uganda / Evaluation de cinq produits satellitaires pour l’estimation des précipitations en Ouganda. Hydrol. Sci. J., 53, 1137–1150, doi:10.1623/hysj.53.6.1137. http://www.tandfonline.com/doi/abs/10.1623/hysj.53.6.1137 (Accessed November 3, 2014).

Bitew, M. M., and M. Gebremichael, 2011: Assessment of satellite rainfall products for streamflow simulation in medium watersheds of the Ethiopian highlands. Hydrol. Earth Syst. Sci., 15, 1147–1155, doi:10.5194/hess-15-1147-2011. http://www.hydrol-earth-syst-sci.net/15/1147/2011/ (Accessed April 24, 2013).

Blacutt, L. A., D. L. Herdies, L. G. G. de Gonçalves, D. A. Vila, and M. Andrade, 2015: Precipitation comparison for the CFSR, MERRA, TRMM3B42 and Combined Scheme datasets in Bolivia. Atmos. Res., doi:10.1016/j.atmosres.2015.02.002. http://www.sciencedirect.com/science/article/pii/S0169809515000435 (Accessed March 12, 2015).

Brown, J. E. M., 2006: An analysis of the performance of hybrid infrared and microwave satellite precipitation algorithms over India and adjacent regions. Remote Sens. Environ., 101, 63–81, doi:10.1016/j.rse.2005.12.005. http://www.sciencedirect.com/science/article/pii/S0034425705004086 (Accessed November 4, 2014).

Buarque, D. C., R. C. D. de Paiva, R. T. Clarke, and C. A. B. Mendes, 2011: A comparison of Amazon rainfall characteristics derived from TRMM, CMORPH and the Brazilian national rain gauge network. J. Geophys. Res., 116, 1–12, doi:10.1029/2011JD016060. http://www.agu.org/pubs/crossref/2011/2011JD016060.shtml (Accessed August 15, 2012).

Casse, C., M. Gosset, C. Peugeot, V. Pedinotti, a. Boone, B. a. Tanimoun, and B. Decharme, 2015: Potential of satellite rainfall products to predict Niger River flood events in Niamey. Atmos. Res., doi:10.1016/j.atmosres.2015.01.010. http://linkinghub.elsevier.com/retrieve/pii/S0169809515000277.

Chen, S., and Coauthors, 2013: Evaluation of the successive V6 and V7 TRMM multisatellite precipitation analysis over the Continental United States. Water Resour. Res., 49, 8174–8186, doi:10.1002/2012WR012795. http://doi.wiley.com/10.1002/2012WR012795 (Accessed November 3, 2014).

Collischonn, B., W. Collischonn, and C. E. M. Tucci, 2008: Daily hydrological modeling in the Amazon basin using TRMM rainfall estimates. J. Hydrol., 360, 207–216, doi:10.1016/j.jhydrol.2008.07.032. http://linkinghub.elsevier.com/retrieve/pii/S0022169408003806 (Accessed March 17, 2013).

Condom, T., P. Rau, and J. C. Espinoza, 2010: Correction of TRMM 3B43 monthly precipitation data over the mountainous areas of Peru during the period 1998-2007. Hydrol. Process., 25, 1924–1933, doi:10.1002/hyp.7949. http://doi.wiley.com/10.1002/hyp.7949 (Accessed October 30, 2014).

Dinku, T., P. Ceccato, E. Grover-Kopec, M. Lemma, S. J. Connor, and C. F. Ropelewski, 2007: Validation of satellite rainfall products over East Africa's complex topography. Int. J. Remote Sens., 28, 1503–1526, doi:10.1080/01431160600954688. http://www.tandfonline.com/doi/abs/10.1080/01431160600954688 (Accessed August 8, 2012).

Dinku, T., S. J. Connor, and P. Ceccato, 2010: Satellite Rainfall Applications for Surface Hydrology. Satellite Rainfall Applications for Surface Hydrology, M. Gebremichael and F. Hossain, Eds., Springer Netherlands, Dordrecht, 193–204 http://www.springerlink.com/index/10.1007/978-90-481-2915-7 (Accessed August 6, 2012).

Ferraro, R. R., E. A. Smith, W. Berg, and G. J. Huffman, 1998: A Screening Methodology for

Passive Microwave Precipitation Retrieval Algorithms. J. Atmos. Sci., 55, 1583–1600, doi:10.1175/1520-0469(1998)055<1583:ASMFPM>2.0.CO;2.

Gao, Y. C., and M. F. Liu, 2013: Evaluation of high-resolution satellite precipitation products using rain gauge observations over the Tibetan Plateau. Hydrol. Earth Syst. Sci., 17, 837–849, doi:10.5194/hess-17-837-2013. http://www.hydrol-earth-syst-sci.net/17/837/2013/ (Accessed March 2, 2013).

Garcia, M., D. Raes, R. Allen, and C. Herbas, 2004: Dynamics of reference evapotranspiration in the Bolivian highlands (Altiplano). Agric. For. Meteorol., 125, 67–82, doi:10.1016/j.agrformet.2004.03.005. http://www.sciencedirect.com/science/article/pii/S0168192304000681 (Accessed November 4, 2014).

Garreaud, R., 1999: Multiscale Analysis of the Summertime Precipitation over the Central Andes. Mon. Weather Rev., 127, 901–921, doi:10.1175/1520-0493(1999)127<0901:MAOTSP>2.0.CO;2. http://journals.ametsoc.org/doi/abs/10.1175/1520-0493(1999)127%3C0901:MAOTSP%3E2.0.CO;2 (Accessed November 3, 2014).

Garreaud, R., M. Vuille, and A. C. Clement, 2003: The climate of the Altiplano: observed current conditions and mechanisms of past changes. Palaeogeogr. Palaeoclimatol. Palaeoecol., 194, 5–22, doi:10.1016/S0031-0182(03)00269-4. http://linkinghub.elsevier.com/retrieve/pii/S0031018203002694 (Accessed April 9, 2013).

Gebregiorgis, A. S., and F. Hossain, 2013: Understanding the Dependence of Satellite Rainfall Uncertainty on Topography and Climate for Hydrologic Model Simulation. IEEE Trans. Geosci. Remote Sens., 51, 704–718, doi:10.1109/TGRS.2012.2196282. http://ieeexplore.ieee.org/lpdocs/epic03/wrapper.htm?arnumber=6203572.

Geerts, S., D. Raes, M. Garcia, C. Del Castillo, and W. Buytaert, 2006: Agro-climatic suitability mapping for crop production in the Bolivian Altiplano: A case study for quinoa. Agric. For. Meteorol., 139, 399–412, doi:10.1016/j.agrformet.2006.08.018. http://www.sciencedirect.com/science/article/pii/S0168192306002395 (Accessed November 4, 2014).

Getirana, a. C. V., J. C. V. Espinoza, J. Ronchail, and O. C. Rotunno Filho, 2011: Assessment of different precipitation datasets and their impacts on the water balance of the Negro River basin. J. Hydrol., 404, 304–322, doi:10.1016/j.jhydrol.2011.04.037. http://linkinghub.elsevier.com/retrieve/pii/S0022169411003003 (Accessed November 3, 2014).

Gosset, M., J. Viarre, G. Quantin, and M. Alcoba, 2013: Evaluation of several rainfall products used for hydrological applications over West Africa using two high-resolution gauge networks. Q. J. R. Meteorol. Soc., 139, 923–940, doi:10.1002/qj.2130. http://doi.wiley.com/10.1002/qj.2130 (Accessed October 10, 2014).

Gourley, J. J., Y. Hong, Z. L. Flamig, L. Li, and J. Wang, 2010: Intercomparison of Rainfall Estimates from Radar, Satellite, Gauge, and Combinations for a Season of Record Rainfall. J. Appl. Meteorol. Climatol., 49, 437–452, doi:10.1175/2009JAMC2302.1. http://journals.ametsoc.org/doi/abs/10.1175/2009JAMC2302.1 (Accessed September 13, 2012).

GSMaP, 2012. User's guide for Global Satellite Mapping of Precipitation Microwave-IR Combined Product (GSMaP_MVK) Version 5.

Heidinger, H., C. Yarlequé, A. Posadas, and R. Quiroz, 2012: TRMM rainfall correction over the Andean Plateau using wavelet multi-resolution analysis. Int. J. Remote Sens., 33, 4583–4602, doi:10.1080/01431161.2011.652315. http://www.tandfonline.com/doi/abs/10.1080/01431161.2011.652315 (Accessed October 22, 2014).

Hirpa, F. a., M. Gebremichael, and T. Hopson, 2010: Evaluation of High-Resolution Satellite Precipitation Products over Very Complex Terrain in Ethiopia. J. Appl. Meteorol. Climatol., 49, 1044–1051, doi:10.1175/2009JAMC2298.1. http://journals.ametsoc.org/doi/abs/10.1175/2009JAMC2298.1 (Accessed March 6, 2013).

Hsu, K., X. Gao, S. Sorooshian, and H. V. Gupta, 1997: Precipitation Estimation from Remotely Sensed Information Using Artificial Neural Networks. J. Appl. Meteorol., 36, 1176–1190, doi:10.1175/1520-0450(1997)036<1176:PEFRSI>2.0.CO;2. http://journals.ametsoc.org/doi/abs/10.1175/1520-0450(1997)036%3C1176%3APEFRSI%3E2.0.CO%3B2 (Accessed October 29, 2014).

Huffman, G. J., and Coauthors, 2007: The TRMM Multisatellite Precipitation Analysis (TMPA): Quasi-Global, Multiyear, Combined-Sensor Precipitation Estimates at Fine Scales. J. Hydrometeorol., 8, 38–55, doi:10.1175/JHM560.1. http://journals.ametsoc.org/doi/abs/10.1175/JHM560.1 (Accessed July 11, 2014).

Huffman, G.J., Adler, R.F., Bolvin, D.T., Nelkin, E.J., 2010. The TRMM Multi-satellite Precipitation Analysis (TMPA). Satell. Rainfall Appl. Surf. Hydrol. 3–22. doi:10.1007/978-90-481-2915-7_1

Huffman, G.J., Bolvin, D.T., 2014. TRMM and Other Data Precipitation Data Set Documentation. Lab. for Atmos., NASA Goddard Space Flight Cent. and Sci. Syst. and Appl. [Available at: http://precip.gsfc.na- sa.gov/pub/trmmdocs/3B42_3B43_doc.pdf]

Janowiak, J.E., Joyce, R.J., Yarosh, Y., 2001. A real-time global half-hourly pixel-resolution infrared dataset and its applications. Bull. Am. Meteorol. Soc. 82, 205–217. doi:10.1175/1520-0477(2001)082<0205:ARTGHH>2.3.CO;2

Joyce, R. J., J. E. Janowiak, P. A. Arkin, and P. Xie, 2004: CMORPH : A Method that Produces Global Precipitation Estimates from Passive Microwave and Infrared Data at High Spatial and Temporal Resolution. J. Hydrometeorol., 5, 487–803, doi:10.1175/1525-7541(2004)005<0487:CAMTPG>2.0.CO;2.

Katiraie-Boroujerdy, P.-S., N. Nasrollahi, K. Hsu, and S. Sorooshian, 2013: Evaluation of satellite-based precipitation estimation over Iran. J. Arid Environ., 97, 205–219, doi:10.1016/j.jaridenv.2013.05.013. http://www.sciencedirect.com/science/article/pii/S0140196313001092 (Accessed November 4, 2014).

Levizzani, V., R. Amorati, and F. Meneguzzo, 2002: A review of satellite-based rainfall estimation methods. http://www.geomin.unibo.it/hydro/music/reports/d6.1_satellite rainfall overview.pdf.

Li, J., and A. D.Heap, 2008: Spatial Interpolation Methods: A Review for Environmental Scientists. http://www.ga.gov.au/corporate_data/68229/Rec2008_023.pdf (Accessed

November 4, 2014).

Li, X., Q. Zhang, and C.-Y. Xu, 2013: Assessing the performance of satellite-based precipitation products and its dependence on topography over Poyang Lake basin. Theor. Appl. Climatol., 115, 713–729, doi:10.1007/s00704-013-0917-x. http://link.springer.com/10.1007/s00704-013-0917-x (Accessed November 3, 2014).

Mega, T., Tomoo, U., Kubota, T., Kachi, M., Aonashi, K., Shige, S., 2014. Gauge Adjusted Global Satellite Mapping of Precipitation - GSMaP _ Gauge product - 0–3.

NOAA., 2012 : ftp://ftp.cpc.ncep.noaa.gov/precip/CMORPH_V1.0/CMORPH_V1.0_README.txt

Ochoa, a., L. Pineda, P. Crespo, and P. Willems, 2014: Evaluation of TRMM 3B42 precipitation estimates and WRF retrospective precipitation simulation over the Pacific–Andean region of Ecuador and Peru. Hydrol. Earth Syst. Sci., 18, 3179–3193, doi:10.5194/hess-18-3179-2014. http://www.hydrol-earth-syst-sci.net/18/3179/2014/ (Accessed November 11, 2014).

Paiva, R. C. D., D. C. Buarque, R. T. Clarke, W. Collischonn, and D. G. Allasia, 2011: Reduced precipitation over large water bodies in the Brazilian Amazon shown from TRMM data. Geophys. Res. Lett., 38, 2–6, doi:10.1029/2010GL045277. http://www.agu.org/pubs/crossref/2011/2010GL045277.shtml (Accessed September 13, 2012).

De Paiva, R. C. D., D. C. Buarque, W. Collischonn, M. P. Bonnet, F. Frappart, S. Calmant, and C. A. Bulhões Mendes, 2013: Large-scale hydrologic and hydrodynamic modeling of the Amazon River basin. Water Resour. Res., 49, 1226–1243, doi:10.1002/wrcr.20067.

Pillco, R., C. B. Uvo, and L. Bengtsson, 2007: Precipitation variability and regionalization over the Southern Altiplano , Bolivia. Int. J. Climatol., 149–164.

Prakash, S., V. Sathiyamoorthy, C. Mahesh, and R. M. Gairola, 2014: An evaluation of high-resolution multisatellite rainfall products over the Indian monsoon region. Int. J. Remote Sens., 35, 3018–3035, doi:10.1080/01431161.2014.894661. http://www.tandfonline.com/doi/abs/10.1080/01431161.2014.894661 (Accessed November 3, 2014).

Qin, Y., Chen, Z., Shen, Y., Zhang, S., Shi, R., 2014. Evaluation of Satellite Rainfall Estimates over the Chinese Mainland. Remote Sens. 6, 11649–11672. doi:10.3390/rs61111649

Roche, M. A., J. Bourges, J. Cortes, and R. Mattos, 1992: Climatología e hidrología de la cuenca del lago Titicaca. C. Dejoux and A. Iltis, Eds. Springer Netherlands, Boston. El Lago Titicaca, Sintesis del conocimiento limnologico actual. ORSTOM – HISBOL, La Paz, Bolivia, pp. 83–104

Romilly, T. G., and M. Gebremichael, 2010: Evaluation of satellite rainfall estimates over Ethiopian river basins. Hydrol. Earth Syst. Sci. Discuss., 7, 7669–7694, doi:10.5194/hessd-7-7669-2010. http://www.hydrol-earth-syst-sci-discuss.net/7/7669/2010/ (Accessed September 13, 2012).

Rutllant, J., and P. Ulriksen, 1979: ARID DYNAMICS PART OF THE EXTREMELY OF CHILE : The Antofagasta Field Experiment. Bound. Layer Meteorol., 17, 41–55, doi:10.1007/BF00121936.

Salio, P., M. P. Hobouchian, Y. García Skabar, and D. Vila, 2014: Evaluation of high-resolution satellite precipitation estimates over southern South America using a dense rain gauge network. Atmos. Res., doi:10.1016/j.atmosres.2014.11.017. http://www.sciencedirect.com/science/article/pii/S0169809514004219 (Accessed March 12, 2015).

Satgé, F., and Coauthors, 2015: International Journal of Remote Accuracy assessment of SRTM v4 and ASTER GDEM v2 over the Altiplano watershed using ICESat / GLAS data. Int. J. Remote Sens., 36, 465–488, doi:10.1080/01431161.2014.999166.

Scheel, M. L. M., M. Rohrer, C. Huggel, D. Santos Villar, E. Silvestre, and G. J. Huffman, 2011: Evaluation of TRMM Multi-satellite Precipitation Analysis (TMPA) performance in the Central Andes region and its dependency on spatial and temporal resolution. Hydrol. Earth Syst. Sci., 15, 2649–2663, doi:10.5194/hess-15-2649-2011. http://www.hydrol-earth-syst-sci.net/15/2649/2011/ (Accessed March 7, 2013).

Shen, Y., A. Xiong, Y. Wang, and P. Xie, 2010: Performance of high-resolution satellite precipitation products over China. J. Geophys. Res., 115, D02114, doi:10.1029/2009JD012097. http://www.agu.org/pubs/crossref/2010/2009JD012097.shtml (Accessed March 12, 2013).

Shige, S., Yamamoto, T., Tsukiyama, T., Kida, S., Ashiwake, H., Kubota, T., Seto, S., Aonashi, K., Okamoto, K., 2009. The GSMaP precipitation retrieval algorithm for microwave sounderspart i: Over-ocean algorithm. IEEE Trans. Geosci. Remote Sens. 47, 3084–3097. doi:10.1109/TGRS.2009.2019954

Sorooshian, S., K.-L. Hsu, X. Gao, H. V. Gupta, B. Imam, and D. Braithwaite, 2000: Evaluation of PERSIANN System Satellite–Based Estimates of Tropical Rainfall. Bull. Am. Meteorol. Soc., 81, 2035–2046, doi:10.1175/1520-0477(2000)081<2035:EOPSSE>2.3.CO;2. http://journals.ametsoc.org/doi/abs/10.1175/1520-0477(2000)081%3C2035:EOPSSE%3E2.3.CO;2 (Accessed October 21, 2014).

Su, F., Y. Hong, and D. P. Lettenmaier, 2008: Evaluation of TRMM Multisatellite Precipitation Analysis (TMPA) and Its Utility in Hydrologic Prediction in the La Plata Basin. J. Hydrometeorol., 9, 622–640, doi:10.1175/2007JHM944.1. http://journals.ametsoc.org/doi/abs/10.1175/2007JHM944.1 (Accessed October 22, 2014).

Thiemig, V., R. Rojas, M. Zambrano-Bigiarini, V. Levizzani, and A. De roo, 2012: Validation of Satellite-Based Precipitation Products over Sparsely Gauged African River Basins. J. Hydrometeorol., 13, 1760–1783, doi:10.1175/JHM-D-12-032.1. http://journals.ametsoc.org/doi/abs/10.1175/JHM-D-12-032.1 (Accessed March 20, 2013).

Thiemig, V., R. Rojas, M. Zambrano-Bigiarini, and A. De Roo, 2013: Hydrological evaluation of satellite-based rainfall estimates over the Volta and Baro-Akobo Basin. J. Hydrol., 499, 324–338, doi:10.1016/j.jhydrol.2013.07.012. http://linkinghub.elsevier.com/retrieve/pii/S0022169413005295 (Accessed October 22, 2014).

Tian, Y., C. D. Peters-Lidard, B. J. Choudhury, and M. Garcia, 2007: Multitemporal Analysis of TRMM-Based Satellite Precipitation Products for Land Data Assimilation Applications. J. Hydrometeorol., 8, 1165–1183, doi:10.1175/2007JHM859.1. http://journals.ametsoc.org/doi/abs/10.1175/2007JHM859.1 (Accessed March 12, 2013).

Tian, Y., and Coauthors, 2009: Component analysis of errors in satellite-based precipitation estimates. J. Geophys. Res., 114, D24101, doi:10.1029/2009JD011949. http://doi.wiley.com/10.1029/2009JD011949 (Accessed November 3, 2014).

Tian, Y., Peters-Lidard, C.D., Adler, R.F., Kubota, T., Ushio, T., 2010. Evaluation of GSMaP Precipitation Estimates over the Contiguous United States. J. Hydrometeorol. 11, 566–574. doi:10.1175/2009JHM1190.1

Vauchel, P. 2005. Hydraccess: Software for Management and processing of Hydro – meteorological data software. Free download http://www.ore-hybam.org/index.php/Software/Hydraccess

Vila, D. a., L. G. G. de Goncalves, D. L. Toll, and J. R. Rozante, 2009: Statistical Evaluation of Combined Daily Gauge Observations and Rainfall Satellite Estimates over Continental South America. J. Hydrometeorol., 10, 533–543, doi:10.1175/2008JHM1048.1. http://journals.ametsoc.org/doi/abs/10.1175/2008JHM1048.1 (Accessed August 3, 2012).

Villar, J. C. E., and Coauthors, 2009: Spatio-temporal rainfall variability in the Amazon basin countries (Brazil, Peru, Bolivia, Colombia, and Ecuador). Int. J. Climatol., 29, 1574–1594, doi:10.1002/joc.1791.

Vuille, M., 1999: Atmospheric circulation over the Bolivian Altiplano during dry and wet periods and extreme phases of the Southern Oscillation. Int. J. Climatol., 19, 1579–1600, doi:10.1002/(SICI)1097-0088(19991130)19:14<1579::AID-JOC441>3.0.CO;2-N. http://doi.wiley.com/10.1002/%28SICI%291097-0088%2819991130%2919%3A14%3C1579%3A%3AAID-JOC441%3E3.0.CO%3B2-N.

Vuille, M., D. R. Hardy, B. Braun, F. Keimig, and R. S. Bradley, 1998: Atmospheric circulation anomalies associated with 1996/1997 summer precipitation events on Sajama Ice Cap, Bolivia. J. Geophys. Res., 103, 191–204, doi:10.1029/98JD00681.

Xie, P., S. Yoo, R. Joyce, and Y. Yarosh, 2011: Bias-Corrected CMORPH: A 13-Year Analysis of High-Resolution Global Precipitation. Geophys. Res. Abstr., 13, 2011.

Yang, Y., and Y. Luo, 2014: Evaluating the performance of remote sensing precipitation products CMORPH, PERSIANN, and TMPA, in the arid region of northwest China. Theor. Appl. Climatol., doi:10.1007/s00704-013-1072-0. http://link.springer.com/10.1007/s00704-013-1072-0 (Accessed November 3, 2014).

Zolá, R. P., and L. Bengtsson, 2010: Long-term and extreme water level variations of the shallow Lake Poopó , Bolivia Long-term and extreme water level variations of the shallow Lake Poopó , Bolivia. Hydrol. Sci. J., 37–41.

Zulkafli, Z., W. Buytaert, C. Onof, B. Manz, E. Tarnavsky, W. Lavado, and J.-L. Guyot, 2014: A Comparative Performance Analysis of TRMM 3B42 (TMPA) Versions 6 and 7 for Hydrological Applications over Andean–Amazon River Basins. J. Hydrometeorol., 15, 581–592, doi:10.1175/JHM-D-13-094.1. http://journals.ametsoc.org/doi/abs/10.1175/JHM-D-13-094.1

V. Capítulo 3

Uso Integrado dos Dados de Sensoriamento Remoto: Caso do lago Poopó

Em dezembro de 2015, o segundo maior lago da Bolívia, o lago Poopó, secou completamente, provocando uma crise ambiental sem precedentes no país (figura 11). Um estado de emergência nacional foi lançado para entender e proteger o ecossistema do Altiplano. As mudanças climáticas, o aumento do uso de água na região para consumo doméstico, agrícola e atividades mineiras são identificados como os principais fatores responsáveis pelo desaparecimento do lago Poopó. Porém, devido à falta de dados *in situ,* é difícil identificar e quantificar claramente o papel de cada um dos fatores. As conclusões atuais feitas em relação a seca do lago Poopó são baseadas em observações visuais de mudanças climáticas e de uso do recurso, mas, não são comprovadas com base em resultados de estudos científicos. Nesse contexto, a seca do lago Poopó representa um estudo de caso perfeito para avaliar o potencial do banco de dados espacial desenvolvido no âmbito deste doutorado. Nesse quadro, os objetivos deste estudo são de caracterizar e quantificar separadamente o papel das atividades humanas dos efeitos das mudanças climáticas.

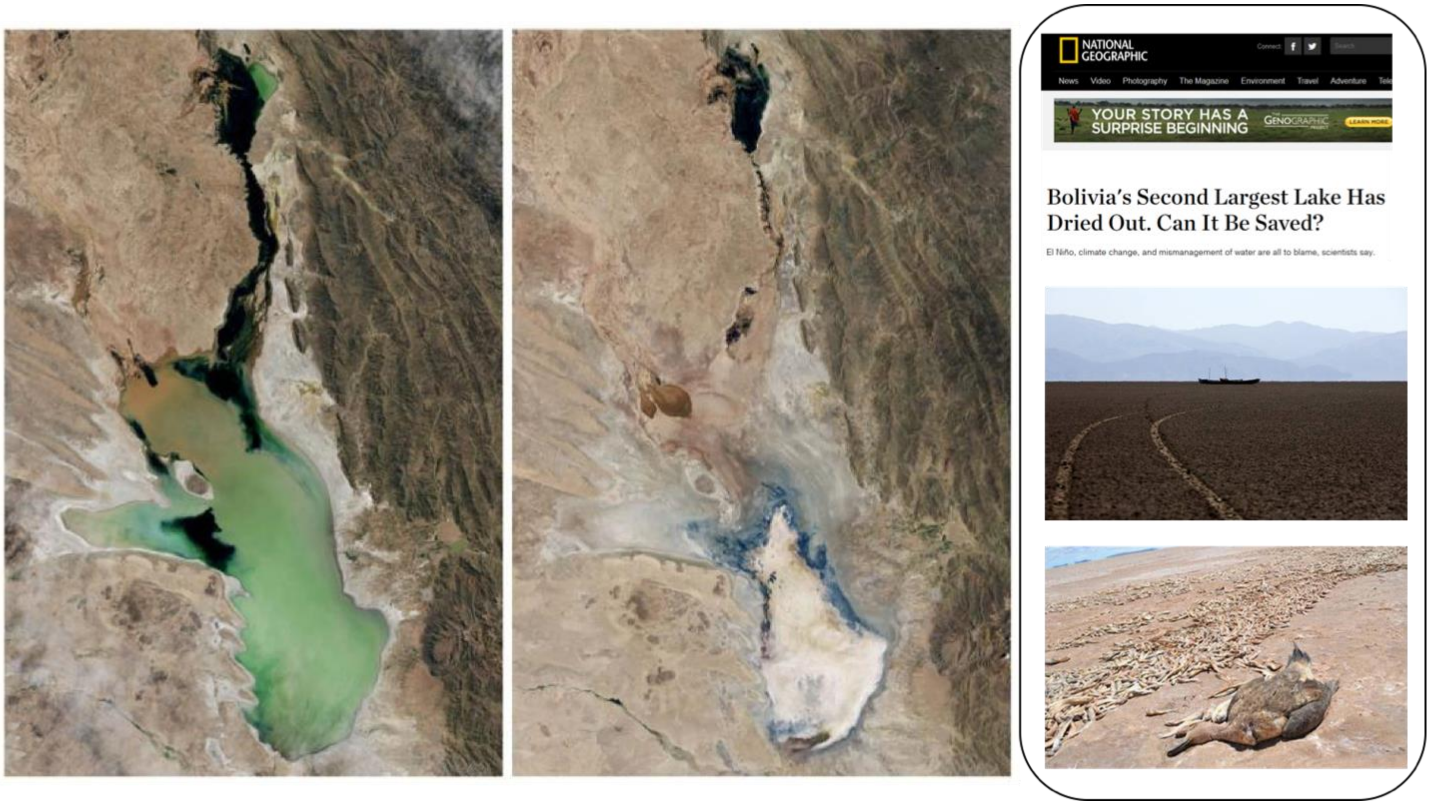

Bolivia's Second Largest Lake Has Dried Out. Can It Be Saved?

El Niño, climate change, and mismanagement of water are all to blame, scientists say.

Figura 11. Lago Poopó o dia 12/04/2013 (esquerda) e o dia 15/01/2016 (direta)

Sendo o lago Poopó o ponto terminal da bacia do Altiplano, as variações de superfície do lago podem ser usadas como estação de controle do estado da bacia similarmente à medição de vazão em saída de bacia hidrológica clássica. As imagens Landsat foram utilizadas para medir a superfície do lago Poopó ao longo do período entre 1990 e 2015, após as estações secas e chuvosas. As imagens do visível, como a imagem do sensor TM/Landsat, estão sujeitas a efeitos atmosféricos. Os efeitos atmosféricos variam ao longo do tempo, modificando as observações derivadas das imagens. Para homogeneizar as observações ao longo do tempo, é necessário corrigir os valores de refletâncias das imagens dos efeitos atmosféricos. Nesse contexto, dois modelos de correções atmosféricas foram testados nas imagens Landsat. Os valores de refletância obtidos antes e depois das correções atmosféricas foram comparados com medições de refletância feitas em campo, na mesma data da imagem (campanha de campo realizada em setembro de 2014).

A separação corpo de água/solo, a partir da imagem no visível, pode ser feita a partir de diferentes índices envolvendo diferentes relações de bandas. Para efetuar a escolha é primordial definir o índice que leva à melhor delimitação da superfície do lago Poopó. Sete índices foram calculados: o *Normalized Difference Water Index* (NDWI), o *Modified* NDWI (MNDWI), o *Water Ratio Index* (WRI), o *Normalized Difference Vegetation Index* (NDVI), o *Automated Water Extraction Index* (AWEI), o *Normalized Burn Ratio* (NBR) e o *Land Surface Water Index* (LSWI). Os valores obtidos a partir de cada índice foram comparados às observações visuais feitas em campo para avaliar a potencialidade de cada índice.

Os produtos TMPA-Adj v7 e IMERG, previamente validados na região no passo de tempo mensal, poderiam ter sido usados neste trabalho. No entanto, não cobrem todo o período de 1990 a 2015. Outros SREs medem as precipitações no período de interesse. É o caso do PERSIANN *Climate Data Record* (PERSIANN-CDR) e do *Multi-Source Weighted-Ensemble Precipitation* (MSWEP). A acurácia do PERSIANN-CDR e MSWEP foi avaliada em um passo de tempo mensal na bacia do lago Poopó por comparações com os valores do TMPA-Adj v7 (Figura 12). A delimitação da bacia do lago Poopó foi feita com base no MDE mais acurado na região, i.e. o SRTM-GL1.

No contexto da região sul do Altiplano, a evapotranspiração regional constitui o segundo maior parâmetro de saída de água do balanço hídrico. O produto MODIS *Global Evapotranspiration Project* (MOD16) da NASA, que mede tanto evapotranspiração real (ETr) quanto potencial (ETp), foi selecionado para estimar a evapotranspiração na bacia de 2000 a 2014. Devido à ausência de sensores adequados para medir a ETr no campo, a avaliação do produto MOD16 foi feita com base nas medições de ETp. As medições de ETp feitas pelo MOD16 foram comparadas às medições feitas em 11 estações meteorológicas da bacia usando a equação do Penman-Monteith (Allen et al., 1998). As comparações foram feitas em um passo de tempo mensal (Figura 12).

$$ETp = \frac{0.408\Delta(Rn - G) + \gamma * \left(\frac{900}{T+273}\right) * U_2 * (E_s - E_a)}{\Delta + \gamma * (1 + 0.34 * U_2)} \quad \text{(Eq. 1)}$$

Onde ETp é a evapotranspiração potencial (mm·dia^{-1}), Rn a "*net radiation*" na superfície (MJ·m^{-2}·dia^{-1}), G a densidade de fluxo de calor no solo (MJ·m^{-2}·dia^{-1}), T temperatura média diária do ar a 2 metros de altura (°C), U$_2$ velocidade do vento a 2 metros de altura (m·s^{-1}), Es a pressão de vapor de saturação (kPa), Ea a pressão de vapor real (kPa), Δ curva de pressão de vapor de inclinação (kPa·°C^{-1}), and γ a constante psychrometric (kPa·°C^{-1}).

Por fim, as superfícies máxima e mínima do lago, de cada ano do período entre 1990 e 2015, foram calculadas usando a correção atmosférica e o índice identificado como sendo o mais adequado na região. A precipitação regional anual no mesmo período (1990-2015) foi calculada com base no SREs avaliados/validados na região e comparada às variações de superfície do lago Poopó (Figura 12).

Em uma segunda etapa, as tendências evolutivas da precipitação, ETr e ETp foram calculadas para o período de 2000 a 2014. Por definição, a ETp é a quantidade de água capaz de ser perdida por evapotranspiração, por um meio contínuo de vegetação ou solo em condição de capacidade de campo ou acima desta. Enquanto que a ETr é a quantidade de água perdida por evapotranspiração de acordo a quantidade realmente disponível no solo. Portanto, considerou-se que as variações de ETp só podem ser explicadas por mudanças climáticas gerais enquanto as variações de ETr podem ser explicadas tanto por variações climáticas gerais quanto pelo aumento da quantidade de água disponível para o processo de evaporação (mudança de uso e ocupação de solo). Desta maneira, a ETp pode ser considerada a integração dos diferentes parâmetros climatológicos (vento, temperatura, pressão atmosférica, radiação solar) em uma única variável (i.e. ETp - Eq.1). Assim usando valores de ETp, ETr e precipitações é possível observar independentemente a variabilidade climática (ETp, precipitação) e de usos antrópicos (ETr).

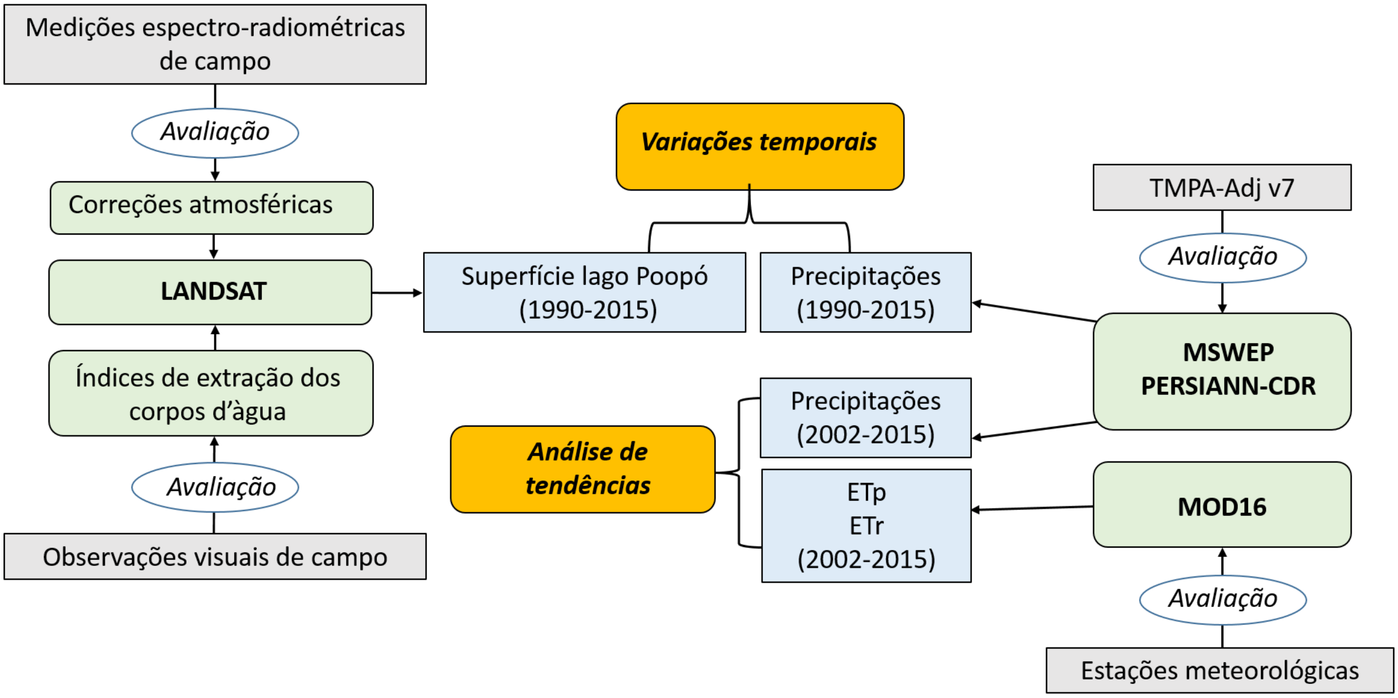

Figura 12. Quadro esquemático que sintetiza o trabalho apresentado neste capítulo no quadro desta tese de doutorado.

O trabalho levou à publicação do artigo, *"Role of climate variability and human activity on Poopó lake droughts between 1990 and 2015 assessed using remote sensing data"* na revista internacional "Remote Sensing" (Satgé et al., 2017a). O estudo permite observar que não é a primeira vez que o lago Poopó seca completamente no período considerado. O lago já secou em 1994 e 1995. As secas de 1994 e 1995 foram associadas a fortes anomalias negativas de precipitação enquanto uma forte anomalia positiva de precipitação ocorreu em 2015. Desta forma, os novos resultados sugerem fortemente que a seca do lago Poopó de 2015 não pode ser explicada por fatores climáticos. A análise das tendências de precipitações ETp e ETr, no período entre 2000 e 2014, mostra uma tendência significativa de aumento da ETr, enquanto não existem tendências significativas nos padrões de ETp, nem de precipitações. Portanto, esta tendência de crescimento da ETr não pode ser relacionada à variabilidade climática no período considerado. Uma espacialização deste fenômeno evidenciou três zonas onde a tendência no aumento da ETr é significativa. Estas zonas são conhecidas como as maiores zonas agrícolas da região. Assim, este estudo evidenciou o papel das atividades agrícolas de irrigação no aumento da ETr e estimou que aumentou em aproximadamente 12,8% no período entre 2000 e 2014. Uma análise de regressão linear múltipla mostrou uma relação significativa entre o aumento de ETr e as variações de superfície do lago, confirmando o importante papel das atividades agrícolas no déficit hídrico regional observado e por consequência na seca do lago Poopó.

De maneira geral, este estudo de caso evidencia a grande potencialidade dos dados de sensoriamento remoto nas zonas isoladas e áridas. A metodologia desenvolvida nesse trabalho usa dados disponíveis em escala global, permitindo a sua fácil transposição da região do Altiplano para qualquer outra região do mundo. Tais dados oferecem grande perspectivas no monitoramento hidroclimático regional em frente às mudanças de uso antrópicos e climatológicos atuais. Um artigo é apresentado para ilustrar o capítulo.

Role of climate variability and human activity on Poopó lake droughts between 1990 and 2015 assessed using remote sensing

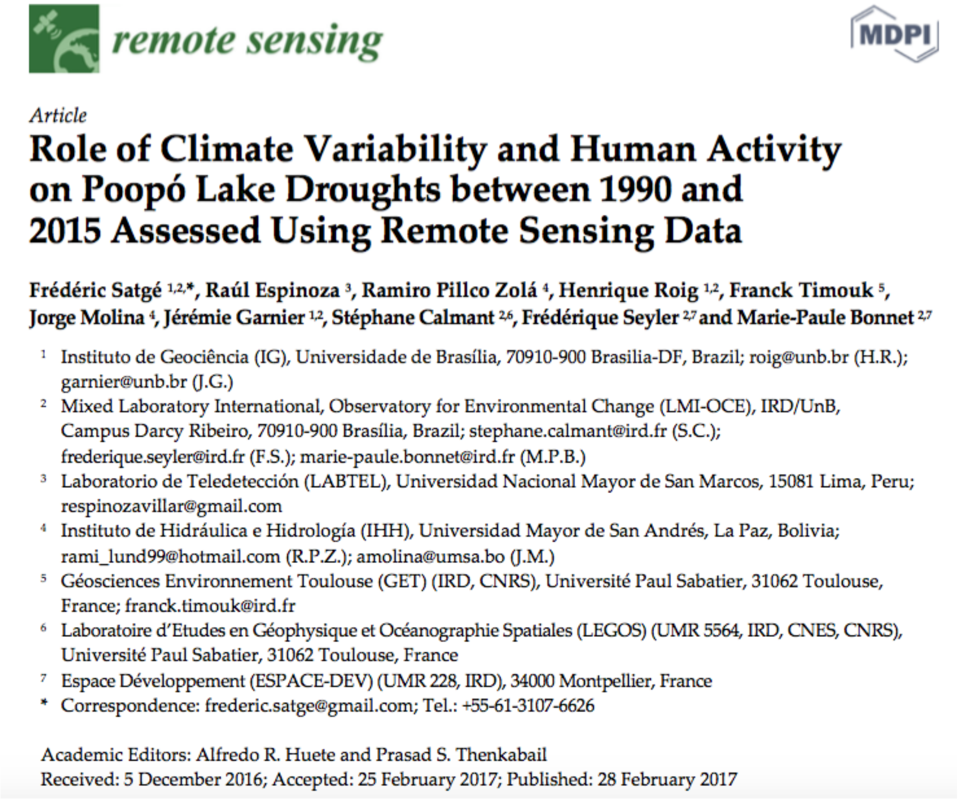

remote sensing

MDPI

Article

Role of Climate Variability and Human Activity on Poopó Lake Droughts between 1990 and 2015 Assessed Using Remote Sensing Data

Frédéric Satgé [1,2,*], Raúl Espinoza [3], Ramiro Pillco Zolá [4], Henrique Roig [1,2], Franck Timouk [5], Jorge Molina [4], Jérémie Garnier [1,2], Stéphane Calmant [2,6], Frédérique Seyler [2,7] and Marie-Paule Bonnet [2,7]

[1] Instituto de Geociência (IG), Universidade de Brasília, 70910-900 Brasilia-DF, Brazil; roig@unb.br (H.R.); garnier@unb.br (J.G.)
[2] Mixed Laboratory International, Observatory for Environmental Change (LMI-OCE), IRD/UnB, Campus Darcy Ribeiro, 70910-900 Brasília, Brazil; stephane.calmant@ird.fr (S.C.); frederique.seyler@ird.fr (F.S.); marie-paule.bonnet@ird.fr (M.P.B.)
[3] Laboratorio de Teledetección (LABTEL), Universidad Nacional Mayor de San Marcos, 15081 Lima, Peru; respinozavillar@gmail.com
[4] Instituto de Hidráulica e Hidrología (IHH), Universidad Mayor de San Andrés, La Paz, Bolivia; rami_lund99@hotmail.com (R.P.Z.); amolina@umsa.bo (J.M.)
[5] Géosciences Environnement Toulouse (GET) (IRD, CNRS), Université Paul Sabatier, 31062 Toulouse, France; franck.timouk@ird.fr
[6] Laboratoire d'Etudes en Géophysique et Océanographie Spatiales (LEGOS) (UMR 5564, IRD, CNES, CNRS), Université Paul Sabatier, 31062 Toulouse, France
[7] Espace Développement (ESPACE-DEV) (UMR 228, IRD), 34000 Montpellier, France
[*] Correspondence: frederic.satge@gmail.com; Tel.: +55-61-3107-6626

Academic Editors: Alfredo R. Huete and Prasad S. Thenkabail
Received: 5 December 2016; Accepted: 25 February 2017; Published: 28 February 2017

Abstract

In 2015, an emergency state was declared in Bolivia when Poopó Lake dried up. Climate variability and the increasing need for water are potential factors responsible for this situation. Because field data are missing over the region, no statements are possible about the influence of mentioned factors. This study is a preliminary step toward the understanding of Poopó Lake drought using remote sensing data. First, atmospheric corrections for Landsat (FLAASH and L8SR), seven satellite derived indexes for extracting water bodies, MOD16 evapotranspiration, PERSIANN-CDR and MSWEP rainfall products potentiality was assessed. Then, the fluctuations of Poopó Lake extent over the last 26 years are presented for the first time jointly, with the mean regional annual rainfall. Three main droughts are highlighted between 1990 and 2015: two are associated with negative annual rainfall anomalies in 1994 and 1995 and one associated with positive annual rainfall anomaly in 2015. This suggests that other factors than rainfall influenced the recent disappearance of the lake. The regional evapotranspiration increased by 12.8% between 2000 and 2014. Evapotranspiration increase is not homogeneous over the watershed but limited over the main agriculture regions. Agriculture activity is one of the major factors contributing to the regional desertification and recent disappearance of Poopó Lake.

Keywords: Poopó Lake; drought; Landsat; Atmospheric correction; MOD16; PERSIANN-CDR; MSWEP

1. Introduction

The recent drought at Poopó Lake, the second largest water body in Bolivia, is of major socio-environmental concern as it condemned local population dependent on fishing activities jointly with local endemic species. Moreover, the sediments contaminated by intense regional mining activities trapped in the lake bottom were exposed to wind erosion, threatening the Altiplano region with contamination. Thus, there is the necessity of providing efficient and consistent surface water monitoring tools for anticipating such crises and giving support for more sustainable use of water resource in this region. Two main factors can be pointed out to explain the recent lake total drought: global warming and water consumption increase. Actually, the region suffers from continuously increasing air temperatures of 0.15 to 0.25 °C over the last decades [1,2] from 1965 to 2012. This temperature increase has had a slight impact on evapotranspiration but has accelerated glacier melting [3]. Some glaciers already disappeared. For example, the Chacaltaya Glacier, which was one of the largest glaciers in the region, entirely melted in 2010 [4]. The shrinkage and disappearance of glaciers obviously reduces the replenishment of water resources (surficial and subterranean), especially during the dry season [5]. In addition to climatic factors, some anthropic factors may directly affect Poopó Lake. Water extraction to sustain increasing mining activity, human populations (for consumption) and agriculture kept rising over the last decades. Actually, the area of quinoa culture in Bolivia increased from 38,800 to 70,000 ha from 1990 to 2012 [6] in response to the world's demands for quinoa and its increasing price. Progressively, the replacement of native vegetation by quinoa has accelerated the desertification process across the region [7,8]. As the outlet of its own watershed, the Poopó Lake extent fluctuation is sensitive to climate change and increasing anthropic water demands along the watershed. With more than 25 years of land observations using different spectral bands and considering replicates of 16 days, Landsat imagery collection is very suitable for monitoring variations in lake surface and for support decision for more sustainable use of water resources in the future. However, the electromagnetic radiation signals collected by satellites in the solar spectrum are modified because they are scattered and absorbed by gazes and aerosols as they travel from the earth's surface to the sensor. Atmospheric correction is arguably the most important step in pre-processing Landsat data to monitor change detection when considering multitemporal time series images [9–11] but not when working on single date [11]. Today, the United States Geological Survey (USGS) service provides an atmospherically corrected version of each LandSat scene: the Landsat Surface Reflectance (LSR) product. Here, we used field spectral measurement to quickly assess LSR estimates for the Landsat-8 OLI products for the first time over the Altiplano. The Surface Reflectances (SRs) obtained after applying the fast line-of-sight atmospheric analysis of spectral hypercubes (FLAASH) atmospheric correction were also considered for comparisons.

The method used to build a time series of the fluctuations of lake extent is based on detecting changes in the pixel's state from one Landsat scene to another. In the literature, several satellite derived indexes (SDIs) are proposed to separate water and land pixels. Depending on the region, one SDI can be more suitable than another for delineating water bodies, and an SDI should be chosen carefully to produce realistic results [12,13]. However, in most studies, choosing the SDI remains arbitrary or is based on the results of studies conducted in supposedly similar regions [14–17]. Here, we compared the results obtained from the Normalized Difference Water Index (NDWI), Modified NDWI (MNDWI), Water Ratio Index (WRI), Normalized Difference Moisture Index (NDVI), Automated Water Extraction Index (AWEI), Normalized Burn Ratio (NBR) and Land Surface Water Index (LSWI) with field observations to provide general guidelines for potential users over the Altiplano region.

Finally, based on the most efficient Atmospheric model correction and SDI, a 26-year temporal series from 1990 to the 2015 disappearance of the lake is presented for the first time. After validation, the MOD16 evapotranspiration (ET) products, the Precipitation Estimation from Remotely Sensed Information Using Artificial Neural Networks–Climate Data Record (PERSIANN-CDR) and Multi-Source Weighted-Ensemble Precipitation (MSWEP) reanalysis rainfall products are confronted to the Poopó Lake extent fluctuations. Rainfall and ET general trends are used to understand the potential influence of the climatic variability and increasing irrigated quinoa culture over the watershed during the last decades. This study provides a preliminary analysis of the hydrological behavior of Poopó Lake over the last decades and could be used as a guideline by national authority to consider more sustainable use of water resources over the region.

2. Materials and Methods

2.1 Study Area

Poopó Lake is located on the southern part of the Andean Plateau in Bolivia between latitudes 17°S and 20°S and longitudes 66°W and 68°W and with a mean elevation of 3686 m (Figure 1a). Poopó Lake is the second largest lake in Bolivia, covering an area of 500 to 3000 km^2 at its lowest and highest levels, respectively [17]. The extent of Poopó Lake drastically changes between wet and dry seasons because the region where the lake is located is very flat [18]. The only outflow of the lake is through the Lakajawuira River on the southern end of the lake, which rarely flows towards the Coipasa Salar. In the last 50 years, this river only flooded once in 1986 [17]. Thus, Poopó Lake is considered a terminal point of the endorheic Altiplano system [17]. The Poopó Lake region is arid, with a mean annual precipitation of approximately 400 mm over the lake [19] and a high evapotranspiration rate [20]. According to pan evaporation measurement, the potential evaporation was estimated at 1700 $mm.year^{-1}$ [17] and resulted in extremely saline water. Regarding the local population, the lake is of primordial importance because people depend on it for fishing and agricultural activities [7,8]. In December 2015, a national emergency alert was launched by the national authority in Bolivia after the lake totally dried up. This situation directly impacted the ecosystem and the population living around the lake.

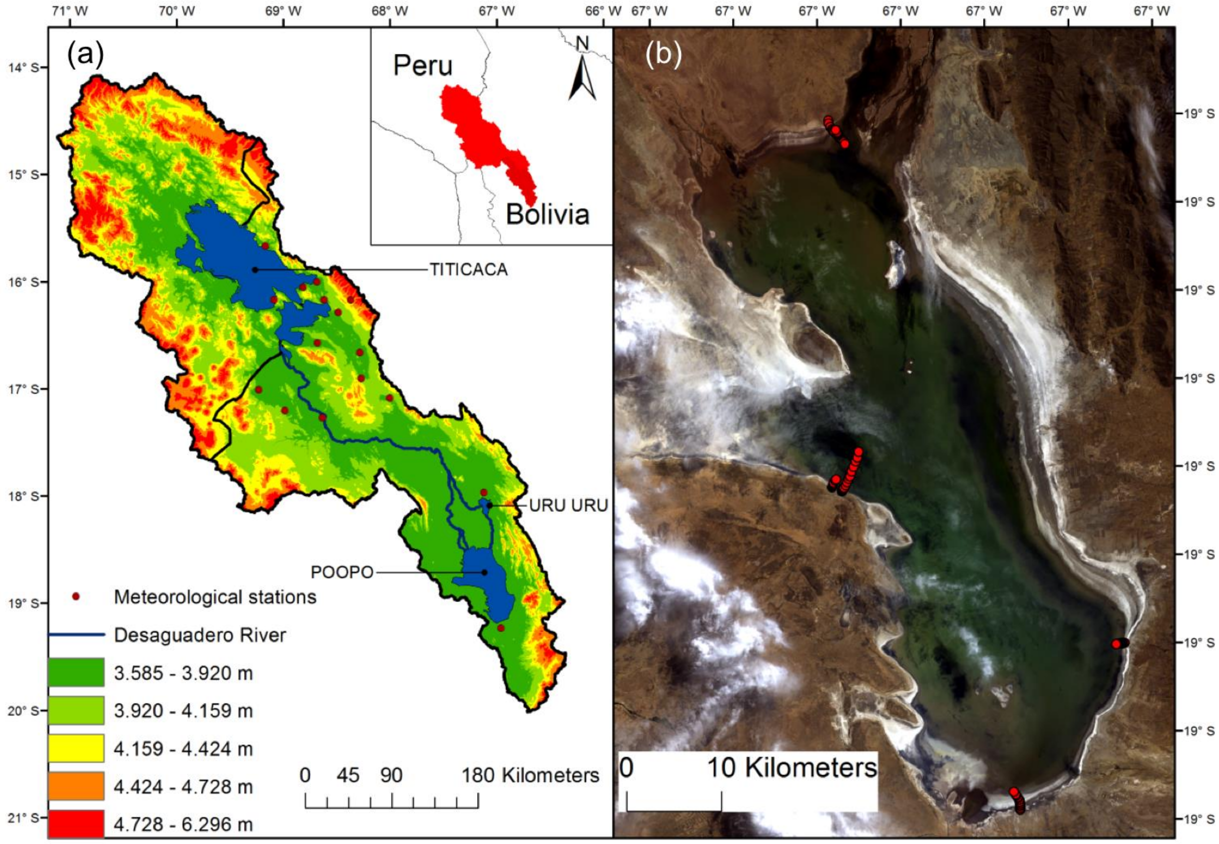

Figure 1. Study area of the watershed (a) and Landsat-8 OLI scene from 6 September 2014, with the ground control points (GCPs) locations (b).

2.2 Data Used

2.2.1 Field Spectral Measurements

Spectral radiometric measurements were acquired from the field, using TriOS RAMSES Sensors on 6 September 2014. A total of 69 points from 5 transects located on the north, east, south and west lakeshores and in the shallow part of the lake were analyzed (Figure 1b). At each point, the lake depth and SR in the spectral domain between 450 and 950 nm were registered. These data were acquired using the methodology established by [21]. Hereafter, we refer to Ground Control Points (GCPs) when referring to the in situ measurements. Spectral radiometric and Landsat measurement differ in term of spatial resolution (point vs. Pixel). This is an important feature to be considered to avoid inconsistent comparison. To account for this, spectral radiometric measurements were done on homogeneous area in term of water depth and water–soil representation to avoid mixed pixel. As Poopó region is a very flat region, and Landsat pixel length is of approximately 30 m, it was easy to find homogeneous areas all around the lake. Recorded values were resampled to match Landsat OLI 8 blue, green, red and near infra-red (NIR) bands. The Landsat Quality Assessment (QA) band provides the bit-packed values of the surface, atmosphere and sensor conditions that can affect the reflectance measured at each pixel of the considered scene. According to the QA band, 13 points were dismissed because of clouds or cirrus cover and 56 points were available for comparisons. Landsat reflectance measurements are given per unit area, while TriOS RAMSES measurements provide reflectance values per unit solid angle (Steradian). Thus, field spectral measurements were multiplied by the π value to match the Landsat reflectance value.

2.2.2 Landsat Imagery

The Landsat-8 satellite was launched in February 2013 with OLI and Thermal Infra-Red Sensor (TIRS) instruments on board. OLI, ETM+, ETM and TM sensors have different bandwidths that could compromise their compatibility. Regarding the OLI and ETM+, good radiometric compatibility was found between their respective bands [22] and can be used as complementary data [23]. OLI was found to largely inherit the band-pass characteristics of ETM+ and achieve continuity of Landsat data [24]. On the other hand, TM and ETM + were found to exhibit excellent data continuity [25], and the measurements of SR obtained by these sensors could be combined with minimal error without sacrificing product accuracy [26–28]. Based on these observations, it is possible to use OLI, ETM+ and TM jointly to retrieve long temporal series or series with increased observation frequencies. Each Landsat scene is available in an atmospherically corrected format called the LSR product and freely available from the USGS. For the Landsat TM, ETM and ETM+, the specialized Landsat Ecosystem Disturbance Adaptive Processing System (LEDAPS) software [29] and the specialized L8SR software [30] are used to retrieve the SR for Landsat TM, ETM and ETM+ and Landsat-8 OLI, respectively.

2.2.3 Satellite Rainfall Estimates

Two reanalysis rainfall products named PERSIANN-CDR [31] and MSWEP [32] were considered to cover the whole 1990–2016 period. PERSIANN-CDR was released in 2014 by the National Climatic Data Center (NCDC) Climate Data Record (CDR) program of the National Oceanic and Atmospheric Administration (NOAA). PERSIANN-CDR covers the 1983 to 2015 period providing daily rainfall estimate on a 0.25° spatial resolution. MSWEP was released in 2016 [32] and covers the 1979–2015 period with daily rainfall data on a 0.25° spatial resolution. MSWEP estimates are based on the Climate Hazards Group Precipitation Climatology (CHPclim) dataset (0.05°) [33]. Additionally, precipitation anomalies from gauge observation, satellite rainfall estimates and atmospheric model reanalysis are used to fix MSWEP estimates temporal variability.

2.2.4 MOD16 Global Evapotranspiration

MOD16 global evapotranspiration is a product of NASA. Estimates are made according to an algorithm based on Penman–Monteith equation [34,35]. NASA's MERRA GMAO (GEOS-5) daily meteorological reanalysis data are used to retrieve radiation, air pressure, temperature and humidity. MODIS products are used to retrieve complementary data on an 8 days temporal scale. MOD12Q1 collection 4 is used for the land cover classification [36], MOD15A2 collection 5 to retrieve Leaf Area Index (LAI) and Fraction of Photosynthetically Active Radiation (FPAR) [37] and MCD43B2/B3 Collection 5 are necessary to get albedo estimates [38]. Four products are available: Potential Evapotranspiration (ETp), Real Evapotranspiration (ETr), Latent Heat Flux (LE) and Potential Latent Heat Flux (PLE). All products are available in a 0.05 grid resolution at 8 days and monthly temporal scale. In this study, we used monthly MOD16 ETp and ETr from January 2002 to December 2014.

2.3 Methods Used

2.3.1 FLAASH Atmospheric Correction

The Landsat-8 OLI scene of 6 September 2015 was used to implement the atmospheric correction process. First, we converted the image from digital numbers to top of atmosphere (TOA) radiance by using pre-processing tools in ENVI v.5.2. Then, the FLAASH model, which is available in ENVI v.5.2, was used to transform the TOA value to land SR. FLAASH used the MODTRAN4 radiation transfer code [39], which was modified to correct errors in the HITRAN-96 water line parameters. Multispectral imagery, such as Landsat imagery, does not include water absorption bands. Instead, a constant amount of water vapor is set for all pixels of the scene according to an atmospheric model. Depending on the water vapor content, different atmospheric models are available. Here, by using MOD_D3_008 (Modis Level 3 Atmospheric products), we observed a vapor content of 2.15 g.cm^{-2} on the date of the Landsat-8 OLI observation. This value corresponds to the water vapor content that is advisable for the Sub-Artic Summer (SAS) atmospheric model [40]. Thus, this model was used to run FLAASH. The rural aerosol model was selected according to the regional context, with an initial visibility of 25 km, which is recommended when moderate haze is observed (Figure 1b). Finally, the elevation of the field was fixed at 3.8 km, which was the approximate value of the elevation observed over Poopó Lake. Hereafter, the atmospheric corrected image is referenced to as FLAASH after the SAS model was applied.

2.3.2 Satellite-Derived Indexes for Water Extraction

Various SDIs exist for separating water bodies from land. Here, the NDWI, MNDWI, WRI, NDVI, AWEI, NBR and LSWR were considered over the Poopó Lake region. The equations and threshold value indexes are reported in Table 1 and are detailed in [12,23].

Table 1. Satellite-derived indexes used for extraction.

Index	Equation	Threshold Value
Normalized Difference Water Index	NDWI = (Green − NIR)/(Green + NIR)	Water > 0
Modified Normalized Difference Water Index	MNDWI = (Green − SWIR1)/(NIR + SWIR1)	Water > 0
Water Ratio Index	WRI = (Green + Red)/(NIR + SWIR1)	Water > 1
Normalized Difference Vegetation Index	NDVI = (NIR − Red)/(NIR + Red)	Water < 0
Automated Water Extraction Index	AWEI = 4 × (Green − SWIR1) − (0.25 × NIR + 2.75 × SWIR2)	Water > 0
Normalized Burn Ratio	NBR = (NIR − SWIR2)/(NIR + SWIR2)	Water > 0
Land Surface Water Index	LSWI = (NIR − SWIR1)/(NIR + SWIR1)	Water > 0

2.4 Assessment of Data and Method

2.4.1 L8SR and FLAASH Assessment

At each GCPs location, field spectral measurement, FLAASH, LSR and Landsat SR value for Blue, Green, Red and NIR were extracted to build the database. Comparisons between field spectral measurement and FLAASH, LSR and Landsat SR were made considering all single band values (red, blue, green and near infra-red) and possible band ratios (green/red, blue/green, red/blue, blue/near infra-red, green/near infra-red, and red/near infra-red) (Table 2). Landsat reflectance value was considered to observe the enhancements of the SR estimations gained through the L8SR and FLAASH processes. The band ratios are considered to observe the relative errors between bands. Indeed, low error in band ratio implies that the trend between the concerned bands is well represented. Considering all GCPs, the Mean Error (ME), Root Mean Square Error (RMSE) and Correlation Coefficient (CC) were computed for all single and band ratios. Different ranges of values were observed for the different bands and band ratios, which complicated the interpretation of the absolute errors. Thus, the ME and RMSE were divided by the average GCP value to obtain the relative statistic error percentage (%ME and %RMSE) (Table 2).

Table 2. %ME, %RMSE and CC for the SR measured by Landsat (uncorrected), FLAASH SAS and LSR in comparison with in situ field measurements.

	ME (%)			RMSE (%)			CC		
	Landsat	FLAASH	LSR	Landsat	FLAASH	LSR	Landsat	FLAASH	LSR
Blue	0.0	−0.9	−0.9	48.4	109.2	110.9	0.92	0.93	0.91
Green	−0.2	−0.9	−0.9	44.0	102.7	103.7	0.91	0.92	0.91
Red	−0.2	−0.9	−0.9	45.2	103.4	104.0	0.91	0.91	0.91
Near IR	−0.1	−0.9	−0.9	57.8	115.1	115.6	0.84	0.84	0.84
Green/Red	0.0	0.0	0.0	13.1	5.0	6.5	0.94	0.98	0.97
Blue/Green	0.4	0.1	0.0	38.6	9.4	12.4	0.47	0.88	0.69
Red/Blue	−0.3	0.0	0.0	41.9	10.9	15.6	0.75	0.96	0.89
Blue/Infra-Red	−0.5	−0.1	−4.0	122.1	46.3	2663.3	0.90	0.93	−0.35
Red/Infra-Red	−0.6	−0.1	−3.8	118.5	45.3	2512.3	0.87	0.92	−0.37
Green/Infra-Red	−0.7	−0.1	−4.4	137.2	50.1	2896.3	0.88	0.93	−0.38

2.4.2 SDI Assessment

Poopó Lake is a very shallow lake. In shallow part, light penetration in water column is very high. Thus, SR is highly influenced by Lake Bottom response complicating water/land separation. To account for this feature, we divided the GCPs into 4 classes corresponding to “water”, “very shallow water”, “interconnected water”, and “soil”. The classes contained 26, 16, 5 and 9 GCPs, respectively. The “Very shallow water” and “water” classes had water depths ranging from 0 to 5 cm and superior to 5 cm, respectively. The “interconnected water” class corresponded to mixed pixels with interconnected water units. At each pixel location, including a GCP, the SDI values from the most accurate scenes in term of the SR estimation were compared with field observations. Two cases are possible: SDI value and field observations agreed or SDI value and field observations disagreed (Table 3). Outlier values were observed when the SDI failed to correctly identify the field observations (Table 3, Figure 2). A large number of outliers mean that the considered SDI was poorly efficient over the region. SDIs potentiality is generally more effective after the threshold value was adjusted. Here, for each considered SDI, we proposed an adjusted threshold to minimize as possible the outlier number. For each SDI, the number of outliers was computed before and after the threshold adjustment (Table 4). Finally, we computed the extent of Poopó Lake based on each SDI using the default and adjusted threshold values (Table 4).

Table 3. Assessment of SDI over Poopó Lake. Water refers to "water" and "very shallow water" classes, and Land refers to "interconnected water" and "soil" classes.

		SDI Observation	
		Water	Land
Field Observation	Water	Ok	Outlier
	Land	Outlier	Ok

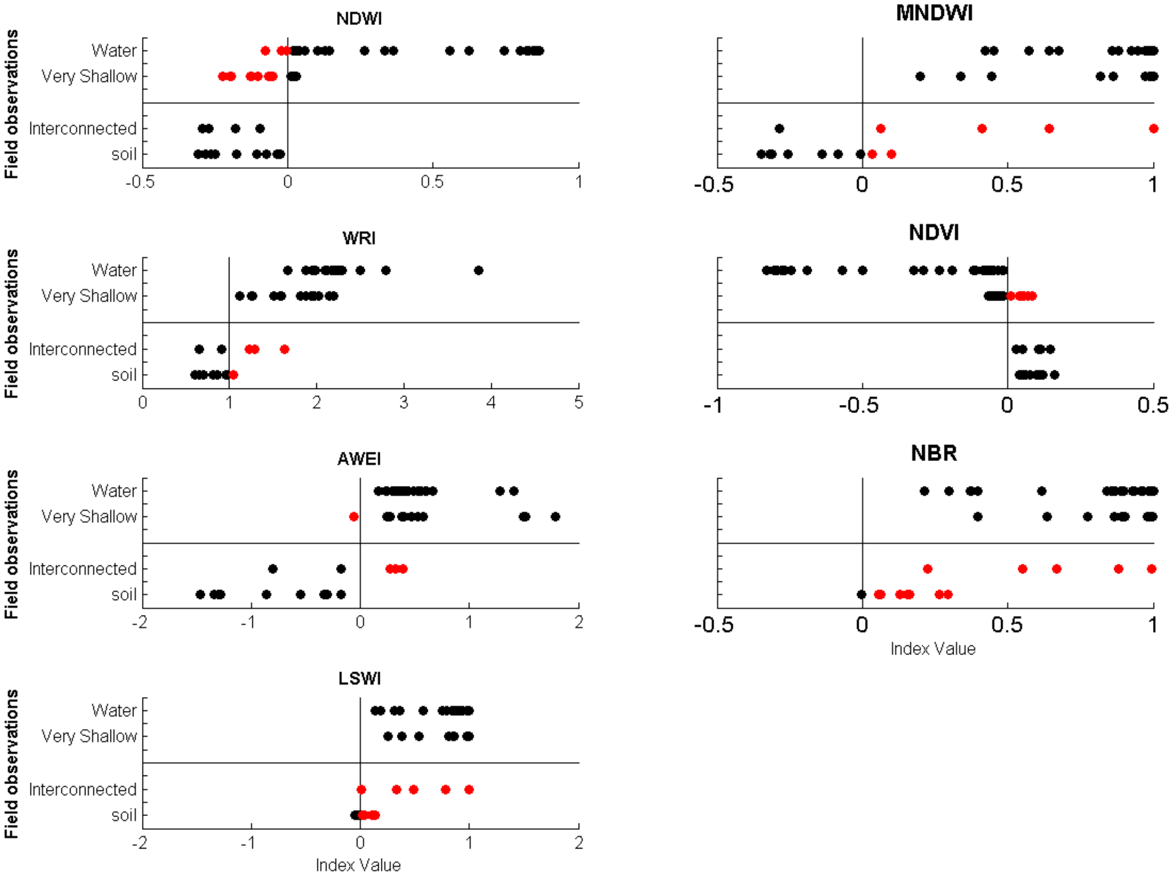

Figure 2. Categorical statistical analysis of SDI. Solid vertical lines represent the advocated thresholds, and the outliers are shown in red.

Table 4. SDI outliers for the default and adjusted threshold values with the corresponding superficial extents of Poopó Lake on 22 September 2014.

SDI	Default Threshold Value	Outlier Number	Superficial (km^2)	Recommended Threshold Value	Outlier Number	Superficial (km^2)
NDWI	0	14	1204	−0.0235	12	1314
MNDWI	0	6	1664	0.15	3	1477
WRI	1	4	1570	1.05	3	1497
NDVI	0	7	1160	0.025	6	1208
AWEI	0	4	1454	−0.1	3	1454
NBR	0	13	2627	0.21	7	1906
LSWI	0	10	2099	0.05	6	1820

2.4.3 Satellite Rainfall and MOD16 Evapotranspiration Estimates Assessment

The mean regional monthly rainfall series was computed for both PERSIANN-CDR and MSWEP for the 1998–2014 period aggregating all pixels included into the watershed. Another mean regional monthly series was computed by meaning PERSIANN-CDR and MSWEP rainfall series (called MERGE hereafter). The three series were compared to a mean reference regional monthly series derived from the Multisatellite Precipitation Analysis 3B42 (TMPA-3B42) v.7 for the same period. TMPA-3B42 v.7 can be used as reference as it was found suitable over the region to describe monthly rainfall events [19]. The accuracy of PERSIANN-CDR, MSWEP and MERGE monthly rainfall estimates were assessed considering Correlation Coefficient (CC) and Bias (Figure 3a).

Real Evapotranspiration (ETr) measurement requires specifics sensor that are not available over the region. Thus, direct comparison between reference and MOD16 ETr are not possible. ETp is easily measurable from meteorological variables. Over the region, ETp derived from Thornthwaite, Hargreaves–Samani and FAO Penman–Monteith equations were compared with ETp derived from lysimiters measurement [20]. According to the authors, Penman–Monteith equations can be used to represent ETp. Following FAO Penman-Monteith equation (Equation (1)) we computed monthly ETp at the location of 16 meteorological stations (Figure 1a) for the period 2002–2010. The equation uses standard climatological records of solar radiation, air temperature, humidity and wind speed.

$$ETp = \frac{0.408\,\Delta(Rn - G) + \gamma \times \left(\frac{900}{T+273}\right) \times U_2 \times (E_s - E_a)}{\Delta + \gamma \times (1 + 0.34 \times U_2)} \tag{1}$$

where ETp is the reference evapotranspiration (mm·day^{-1}), Rn is the net radiation at the crop surface (MJ·m^{-2}·day^{-1}), G is the soil heat flux density (MJ·m^{-2}·day^{-1}), T is the mean daily air temperature at 2 m height (°C), U_2 is the wind speed at 2 m height (m·s^{-1}), Es is the saturation vapor pressure (kPa), Ea is the actual vapor pressure (kPa), Δ is the slope vapour pressure curve (kPa·°C^{-1}), and γ is the psychrometric constant (kPa·°C^{-1}).

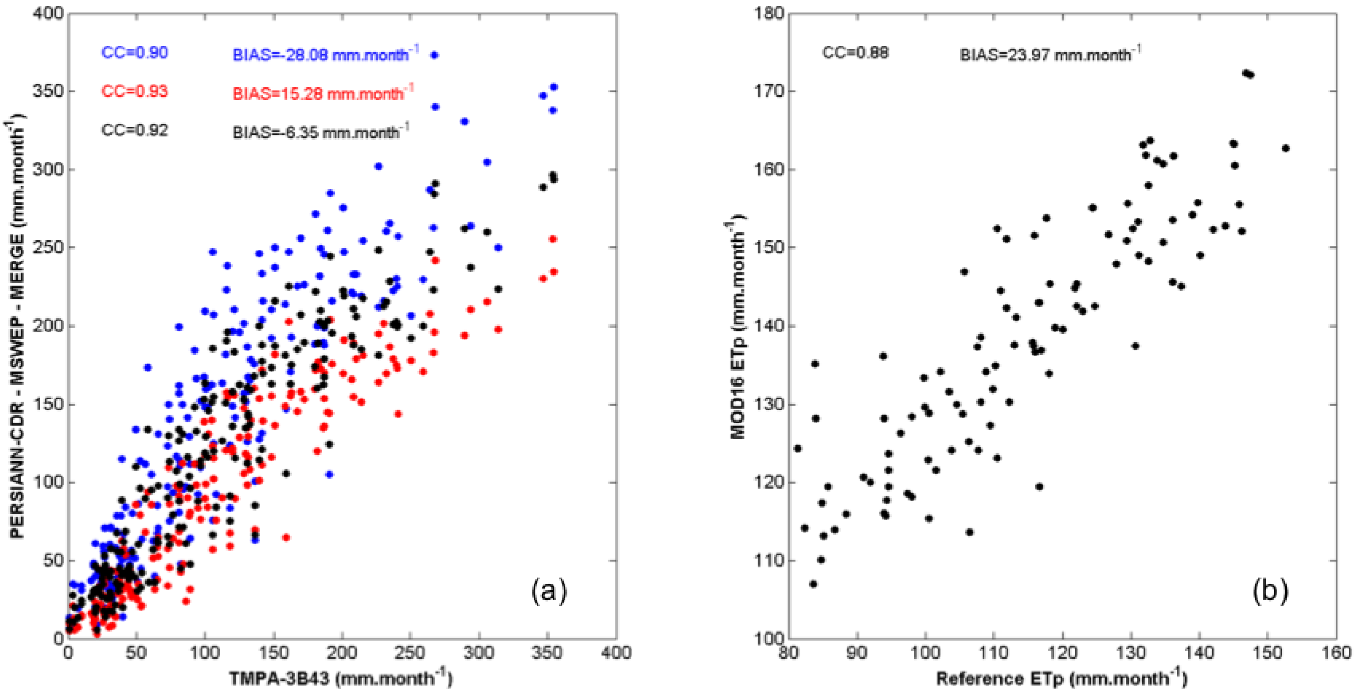

Figure 3. Scatter plot of assessed rainfall products versus TMPA-3B43 with PERSIANN-CDR, MSWEP and MERGE represented in blue, red and black, respectively (a); and scatter plot of assessed MOD16 ETp versus reference ETp (b).

At each of the 16 stations location, the monthly ETp was derived from both the meteorological station and the corresponding MOD16 pixel. Finally, two mean monthly ETp series were derived by aggregating values obtained from the 16 meteorological stations and corresponding MOD16 pixels, respectively. ETp derived from meteorological station is considered as reference ETp (denoted RETp, hereafter). MOD16 ETp and RETp mean monthly series were compared considering CC and Bias (Figure 3b). Finally, MOD16 ETr accuracy is assumed to be similar to MOD16 ETp accuracy.

2.5 Temporal Analysis

2.5.1 Rain versus Superficial Lake Area

From January 1990 to December 2015, the annual highest and lowest lake extents were derived for each year from Landsat imagery by using the most efficient previously identified atmospheric correction processes and SDI. Attention was paid to only select almost cloud free Landsat TM, ETM or OLI scenes. Overall, 48 Landsat scenes were selected and used. From 2012, only Landsat ETM+ scenes are available. Over Poopó Lake, the Landsat ETM+ scenes are strongly impacted by the SLC failure that occurred on 31 May 2003. Thus, these data are not suitable for use in the study. Therefore 2 MODIS scenes were used to fill the gap. Using the MODIS scene to derive the extent of Poopó Lake is acceptable because a strong correlation was previously found between the extents of Poopó Lake derived from MODIS and Landsat data [14]. MODIS scenes are already atmospheric corrected and thus SDI can be directly applied. The fluctuation of the lake extent was compared with the mean regional annual rainfall evolution (Figure 4a). The mean rainfall was computed based on a hydrological year (November to October) and using MERGE rainfall product (Figure 4a). Additionally, the mean seasonal rainfall anomalies and lake extent anomalies for both dry and wet seasons were computed and compared (Figure 4b).

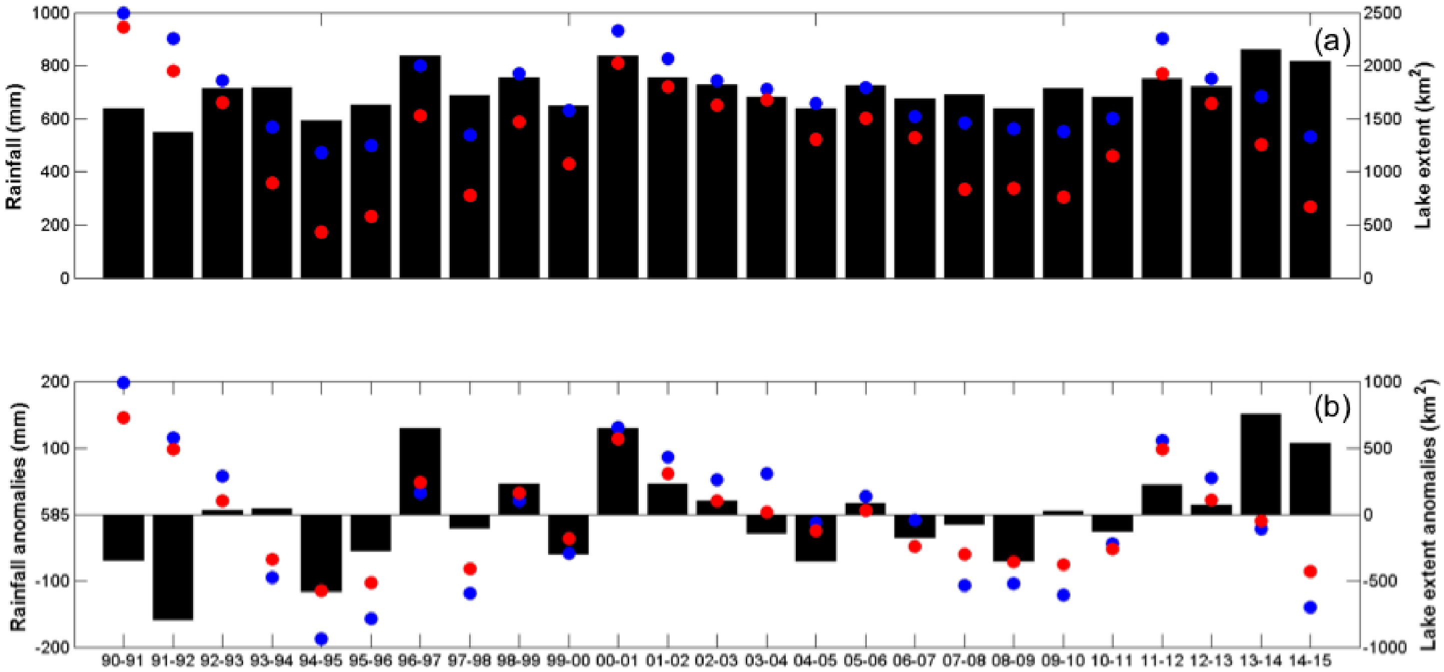

Figure 4. Extent of Poopó Lake (km^2) and the variations of the MERGE seasonal amount of rainfall (mm) between 1990 and 2015 (a); and rainfall and lake extent anomalies (b). The maximum and minimum extents are plotted in blue and red, respectively.

2.5.2 ETr, ETp and Rainfall Tendency over the Last 15 Years

The monthly rainfall, ETp and ETr over Poopó Lake watershed for the period 2000–2014 are presented jointly with their global trend (Figure 5). The global trend is obtained from a simple linear regression of the mean monthly series. The Mann-Kendall (MK) test [41,42] was used to statistically verified if the monotonic trend in the mean monthly rainfall, ETp and ETr over the 2000–2014 period were significant. A MK P-value inferior to 0.05 corresponds to significant monotonic trend. Finally, to observe the ETr dynamic in space along the whole watershed, the mean monthly ETr series were computed at each MOD16 pixel location and its linear regression was used to compute the ETr changing rate from 2000–2014 (Equation (2)). Results are presented in Figure 6. Additionally, the MK P-value was computed at each MOD16 pixel according to the corresponding ETr series. Results are presented in Figure 6.

$$Changing\ Rate = \frac{(ETr_{2014} - ETr_{2000}) \times 100}{ETr_{2000}} \tag{2}$$

where ETr2014 and ETr2000 are the ETr computed from the linear regression of the considered MOD16 pixel for the years 2014 and 2000, respectively.

Finally, a multiple linear regression was used to check the relative influence of rain, ETp and ETr on the lake fluctuations for the 2000–2014 period. The annual lake extent during the dry season was considered as dependent variable while corresponding mean regional annual precipitation, ETp and ETr were considered as independent variables (predictors). The mean annual precipitation, ETp and ETr were computed for the corresponding season between May and March. It is noteworthy that we only considered lake extent fluctuation during the dry season. Actually, the lake extent during the wet season is controlled at 65% by Desaguadero River input and the rest by local Poopó Lake watershed input [17]. Thus, at the regional scale, the influences of rain, ETp and ETr are expected to be more significant during the dry season than during the wet season as Desaguadero River input is much smaller.

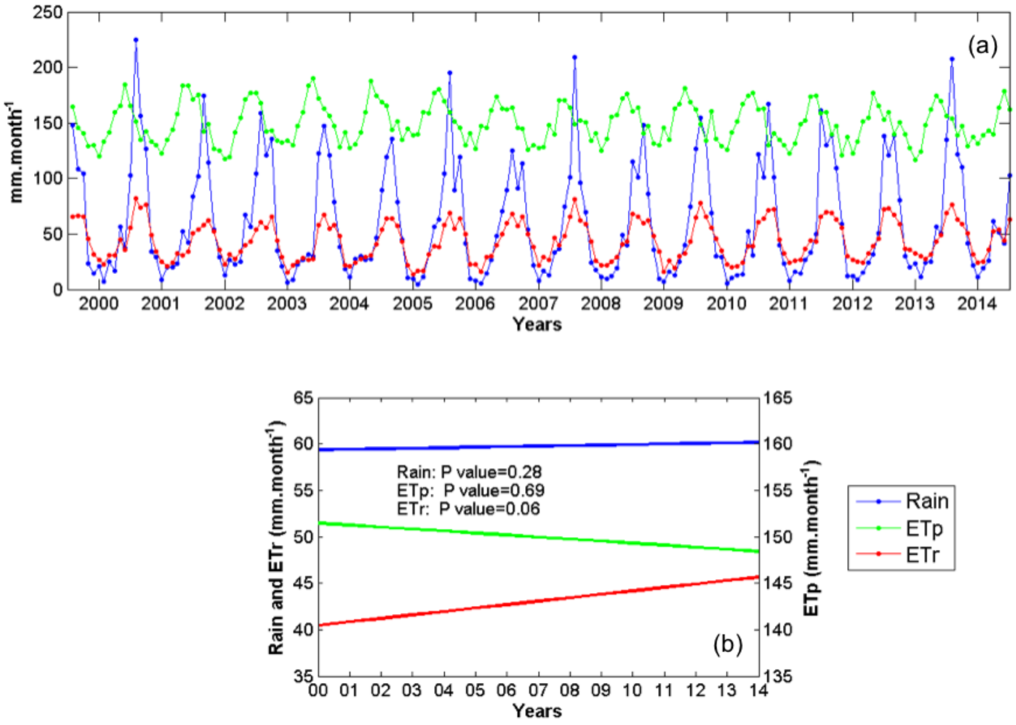

Figure 5. Monthly rain, ETp and ETr derived from MERGE and MOD16 for the 2000–2014 period (a); and their general trend over the same period with the Man Kendal P-value (b).

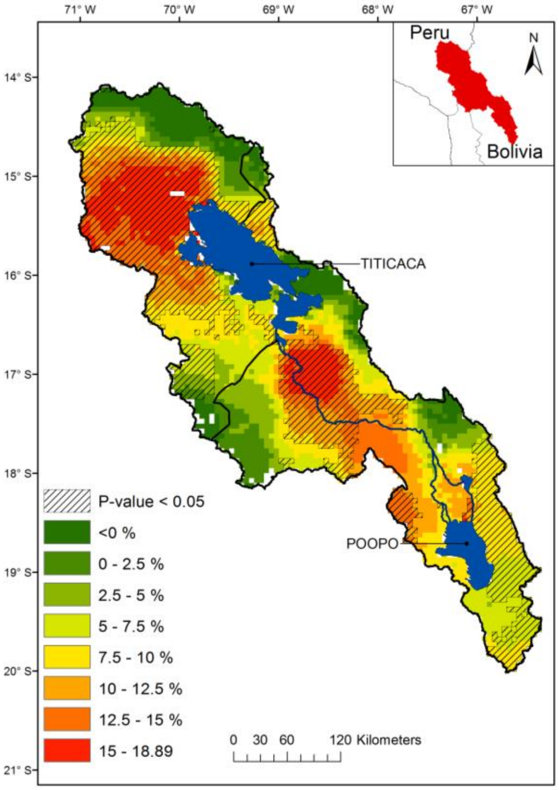

Figure 6. ETr increase rate for the 2000–2014 period and corresponding MK P-value.

3. Results and Discussion

3.1 Effects of Atmospheric Correction

Using a single band approach and for all considered bands, the Landsat SR estimate was generally closer to the field SR measurements than the LSR and FLAASH SR with %ME and %RMSE close to 0. FLAASH and LSR resulted in underestimations of SR with negative bias values. When considering the band ratio, the FLAASH and LSR SR estimations were closer to the field SR than the Landsat SR estimates with %ME closer to 0 and lower RMSE value. The corrected LSR and FLAASH data tended to result in more homogeneous relative trends between the bands than the uncorrected data. Indeed, for all band ratios, the error distribution was closer to 0 for the LSR and FLAASH scenes than for the Landsat scene, which presented greater error distributions.

The NIR band is the most affected by atmospheric absorption and scattering. This band presented lower CCs and higher %RMSEs and %MEs. Consequently, all band ratios including the NIR band presented highest %RMSE values (Table 2). In the case of FLAASH correction, the %RMSE was 5–10 times higher than that of the other ratio (Table 2). This difference was even greater when considering the LSR products with very high %RMSEs for the band ratios including the NIR band. This difference results from the strong underestimation of the NIR with some negative value observed. This LSR inconsistency seems to reoccur because negative values in NIR bands were also observed in the LSR scenes from 21 August and 22 September 2014 as well as over Brazilian water bodies at different date. Although FLAASH also underestimates the NIR SR value, it had a lower impact because no negative value was observed.

Using the single band approach, atmospheric correction degraded the SR estimation because lower %ME and %RMSE values were found before atmospheric correction was applied. However, the opposite trend was observed when considering the band ratios. FLAASH Atmospheric correction enhanced the relative error between the bands, with %RMSE reduction by a factor of 3, higher CCs and lower %MEs for all of the considered band ratios. Thus, over Poopó Lake, FLAASH correction is more suitable than the L8SR algorithm. SDIs are based on band combination and thus their efficiency highly relies on relative band error. As the study aimed to use SDI to retrieve lake extent, we used the FLAASH correction to build the Landsat scene database for the 1990–2015 period.

3.2 SDI Assessment

SDIs were computed for the Landsat-8 OLI scene of 6 September 2015 after the FLAASH correction was applied because it provided better SR estimations. Among the considered indexes, NDWI, NBR and LSWI were the least suitable SDIs for the region, with 14, 13 and 10 outliers, respectively (Figure 2; Table 4). The NDVI, MNDWI, AWEI, and WRI were the most efficient indexes, with only 7, 6, 4, and 4 outliers, respectively. To provide more insights from our results, we considered that outliers located in a dry soil or water pixel were more “problematic” than the outliers located in interconnected water pixels. Indeed, it is difficult to assess the performances of SDIs when considering mixed pixels as the SDI estimates are clearly dependent on the water: soil ratio, and the pixels should be classified based on the dominant component, water or soil. The NDVI, MNDWI, AWEI, and WRI have 7, 2, 1 and 1 “problematic” outliers, respectively (Figure 2). Before any threshold adjustment, the AWEI and WRI are the most efficient SDIs over Poopó Lake. The NDVI and NDWI are not very accurate over the very shallow lake regions, which are misclassified as soil (Figure 2). Thus, using NDVI or NDWI would considerably underestimate the extent of Poopó Lake which is confirmed by the lower extent of Poopó Lake derived from the

NDVI and NDWI (Table 4). NBR and, to a lesser extent, LSWI provided the highest extents (Table 4) because they tended to classify all the GCPs as water. The MNDWI, AWEI and WRI provided similar estimations of the extent of Poopó Lake.

According to Figure 2, it is possible to adjust the recommended threshold to enhance the performances of the SDIs. The adapted threshold values for each SDI are shown in Table 4 with the corresponding numbers of outliers. The threshold adjustment decreased the number of outliers for all the SDIs leading to closer lake extent estimate between them. Finally, the MNDWI, AWEI and WRI perform equally, with similar estimated water extents and should be chosen to estimate Poopó Lake extent. For comparison, in a similar context, over the hyper saline Lake Urmia of Iran, the NDWI was the most suitable SDI for retrieving the spatiotemporal extent of the lake [12]. The different observed results show the relevance of such assessments for selecting the most suitable SDIs over a considered region.

3.3 Satellite Rainfall and MOD16 Evapotranspiration Estimates

Among PERSIANN-CDR, MSWEP and MERGE rainfall estimates, and for the 1998–2014 period MERGE have the lowest Bias and close to highest CC (Figure 3a). MERGE product achieved to represent monthly rainfall over the study area and was selected for the study. A good agreement was found between MOD16 ETp and reference ETp estimates with a CC value of 0.88 and a mean Bias value of 23.97 $\text{mm}\cdot\text{month}^{-1}$ (Figure 3b). As all involved meteorological factors to retrieve ETp are also involved in ETr computation, MOD16 ETp accuracy is highly representative of MOD16 ETr accuracy. Here, we consider MOD16 ETr suitable to describe ETr fluctuation over the region for the period 2000–2014.

3.4 Rainfall versus the Superficial Extent of the Lake

To verify the fluctuations of lake extent with time, we visually compared the fluctuations against the annual amounts of rainfall derived from the MERGE product from January 1990 to December 2015. This comparison included a preliminary approach for understanding the possible factors that affected the drought in Poopó Lake in December 2015.

Maximum lake extents of 2492 km^2, 2333 km^2 and 2256 km^2 were retrieved from multispectral scenes obtained on 31 March 1991, 3 April 2001, and 6 April 2012, respectively. The minimum extents of the lake of 432, 581 and 669 km^2 were observed for 20 October 1995, 22 October 1996, and 14 December 2015, respectively. However, the local population and press indicated that the lake totally dried up in December 2015 (National Geographic, 2016; Earth Observatory, 2016). Thus, according to our results, Poopó Lake should be considered as dried up when its extent is less than 700 km2 because it becomes too shallow to sustain fish life. Thus, during 1990–2015 Poopó Lake dried up three times, in 1994, 1995 and 2015.

Very low extents of 776, 836 and 846 km^2 were also observed on 15 December 1998, 11 October 2008, and 13 December 2009, respectively. For comparison, the lake was observed to dry up in 2009 in a previous study and to nearly dry up in 2008 and 2010 [14]. However, according to local populations, the lake did not completely dry up on these dates. This might be due to the water masked approach used. This study used different methods that were partially based on the NDWI, which is one of the less accurate SDIs according to our results underestimating the superficial extent of Poopó Lake. One interesting feature of our analysis is the presence of a “critical” threshold value of approximately 1500 km2. Each time the lake passed below this extent during the wet season, the extent of the lake decreased drastically during the following dry season and reached a very critical level, which occurred in 1995, 1996, 1998, 2008, 2009, 2010 and 2015 (Figure 4a). The annual variation between the extents of the lake during high and low water periods was much more defined during these years than the others (Figure 4a). This result could be helpful for anticipating when the lake will dry up during periods of low water.

From 1990 to 1996, the Lake extent during the wet and dry seasons steadily decreased in response to low rainfall amount with strong rainfall negative anomalies in 1991 and 1994 years. From 1996 to 2001, the Lake extent globally increased alternating increase and decrease period associated to positive and negative rainfall anomalies (Figure 4b). From 2001 to 2010, the Lake extent during the wet and dry seasons steadily decreased while the recorded annual rainfall steadily decreased from 2001 to 2004 to remain lower than or close to the mean from 2006 to 2010 (Figure 4b). During the last studied period of 2011 to 2015, the Lake extent during the wet and dry seasons dramatically decreased although the amount of annual rainfall was superior to the mean. For the first time, high positive rainfall anomalies (2013–2014 and 2014–2015) were observed in association with negative Lake extent anomalies (Figure 4b). Thus, during the last decades, our results suggest that the amount of water entering the lake from other water sources, mainly groundwater and the Desaguadero River, decreased. Actually, the Desaguadero discharge decreased 42–54% between the periods of 1960–1990 and 1990–2008 [43]. This discharge reduction potentially had an obvious impact because the river is known to contribute 65% of the total water that enters Poopó Lake (Pillco and Bengtsson, 2010). Some anthropic and climatic factors may have non-negligible impacts.

3.5 ETp, ETr and Rainfall Analysis

Figure 5a presents ETp, ETr and rain monthly series for the 2000–2014 period. The seasonal cycle is observed with highest ETp, ETr and rain during the wet season. With rainfall superior to ETr, wet seasons refill hydric resources (Figure 5a). On the contrary, during dry seasons, ETr is superior to rainfall corresponding to a hydric stress period. The annual rainfall amount estimated as 715 mm·month−1hardly compensates for the annual ETr amount estimated at 520 mm/year for the period of 2000–2014. Therefore, Poopó Lake is particularly sensitive to any upstream changes in precipitation and ETr conditions.

At the watershed scale, ETr increased from 43.8 to 48.3 mm·month^{-1} between 2000 and 2014 with a mean increase rate of 12.8%. The MK P-value of 0.06 is slightly superior to the significant threshold value fixed to 0.05 (Figure 5b). This is related to the non-homogenous ETr increase along the watershed (Figure 6). Two hotspot regions with ETr increase rate superior to 15% were observed in the northern and southern part of Lake Titicaca, respectively (Figure 6). The increase rates observed in those regions are significant with MK P-value inferior to 0.05 (Figure 6). Those two regions correspond to intensive agriculture regions. A third region with significant ETr increase trend from 5% to 10% (MK P-value < 0.05) was observed on the eastern part of Poopó Lake (Figure 6). This region is also concerned by an increase in Quinoa crop. The regions where ETr is the most significant correspond to the main agriculture spots. It confirms the desertification processes previously suggested by [7,8] in relation to the replacement of native vegetation by crop (especially Quinoa).

However, climate variability should have participated to ETr increase as well. For example, the temperature increased by 0.15 to 0.25°C·decades^{-1} over the 1965 to 2012 period [1]. ETp and ETr involved the same climatological factor for their estimation. Thus, if climatologic variability played a role in the ETr increase, ETp should have increase as well. However, over the 2000–2014 period and considering the whole watershed, no significant trend was observed on the mean monthly ETp with a MK p-value of 0.69 (Figure 5b). Additionally, no significant trend was found for mean monthly precipitation either, with a MK P-value of 0.28 (Figure 5b). Therefore, the observed ETr increase is more related to the agriculture activities than to climate variability. The replacement of traditional manual cultivation by mechanized system, the reduction of fallow period and the use of irrigation processes facilitate water availability for ETr processes. In the last several decades, new irrigation projects were set up along the Desaguadero River; however, no information regarding the amount of water extracted for irrigation is available. Peruvian and Bolivian Government should consider more reasonable agricultural methods to avoid the desertification process of the region. Currently, such scenario should considerably decrease agriculture yield leading to an economic disaster over the region.

Finally, the respective influences of ETp, ETr and precipitation trends on Poopó extent fluctuation and the recent drought were assessed by multiple linear regression. The results show a significant P-value of 0.048 for ETr while both ETp and Rainfall presented insignificant P-value > 0.05. Thus, the recent decrease of Poopó Lake extent observed during the last 14 years appears to be more related to ETr increase than to precipitation and climate fluctuation (ETp). However, this observation has to be considered with caution due to the small number of points used (14). Therefore, more consistent analyses based on longer temporal series have to be considered in future studies to definitively state the role of ETr on the Poopó Lake drought.

4. Conclusions

In this study, a guideline to monitor Poopó Lake extent variation in time from remote sensing data is presented to understand its recent disappearance. Landsat imagery was used to retrieve Poopó Lake extent and PERSIANN-CDR, MSWEP and MOD16 data were used to understand Poopó Lake extent variation in time at seasonal and annual scales in relation to climate variability and agricultural activities.

The first step consisted of a quick assessment of atmospheric correction, SDIs to retrieve Poopó Lake extent, reanalysis satellite rainfall products (PERSIANN-CDR and MSWEP) and MOD16 ET products at a monthly scale. Despite the scarcity of the ground reference, some consistent features emerged from the analysis:

(1) More accurate SR values are obtained after the FLAASH correction was applied on the Landsat scene than from the already atmospheric corrected LSR scene. One positive effect of both atmospheric correction methods is the decrease of the relative error

between the bands. This effect is even more pronounced when considering SR derived from the FLAASH correction with lower %RMSE, %ME values and higher CC values for all the considered band ratios. Thus, FLAASH is recommended to pre-process Landsat imagery rather than the use of LSR product.

(2) The AWEI, WRI and MNDWI were the most accurate SDIs over the region and only failed to classify mixed water and soil pixels. The NDVI and NDWI classified the shallower lake region as soil, which considerably underestimated the extent of Poopó Lake. The proposed threshold adjusted values enhance all SDIs efficiencies.

(3) The two rainfall reanalysis products, PERSIANN-CDR and MSWEP, are accurate enough to represent regional monthly rainfall amount. Thus, using PERSIANN-CDR with MSWEP, the proposed MERGE monthly rainfall amount is even more suitable with a very low mean monthly bias value.

(4) The low bias and high CC observed comparing MOD16 and reference ETp suggest that MOD16 ETr is accurate enough to represent regional monthly ETr.

Secondly, thanks to 26 years of common data acquisition of Landsat and MERGE rainfall data, preliminary insights regarding the fluctuations of Poopó Lake during the last decades are discussed. The extent of the lake passed by three maximum extents in 1991, 2001 and 2012 with lake extent of 2492 km2, 2333 km2 and 2256 km2, respectively. Considering the recent dry extent of December 2015, it appears that Poopó Lake already dried up in 1994 and 1995, which are associated with strong negative rainfall anomalies. However, in 2014 and 2015, two high positive rainfalls are observed while lake extent drastically decreased until the lake dried up in December 2015. This observation suggests that outside factors influenced the recent disappearance of the lake. Various hypotheses can be made regarding the effects of global warming, which has resulted in the shrinkage and disappearance of some glaciers in the region. In addition, the increase of quinoa culture, mining activity and population water consumption potentially played roles in the disappearance of the lake. Consequently, a discharge decrease of 50% over the last 50 years is observed on the Desaguadero River which contribute 65% of the total water to Poopó Lake [17].

The analysis of ETr reveals an increase of approximately 12.8% at the watershed scale for the 2000–2014 period. The increase of ETr is not homogeneous over the region but located over the three main agricultural regions around Lake Titicaca and Poopó Lake. In those regions, the surface dedicated to quinoa crop kept rising over the last decades in response to a world demand and irrigation processes are involved to improve yield. Consequently, the local ETr over those regions drastically increased at a rate superior to 15% over the 2000–2014 period. Therefore, the agricultural activity and irrigation project from the Desaguadero River must be rigorously controlled before the total desertification of the region. In this line, according to this study, a minimum water extent of 1500 km^2 at the end of the rainy season is recommended to avoid allowing the drying up of the lake during the following dry season. National authorities should consider this threshold as an objective agreement to preserve the region from desertification while maintaining quinoa culture and the economic benefit it generates.

Acknowledgments

This work was supported by the Centre National d’Etudes Spatiales (CNES) in the framework of the HASM project (Hydrology of Altiplano: from Spatial to Modeling). The first author is grateful to the IRD (Institut de Recherche pour le Développement) and CAPES (Coordenação de Aperfeiçoamentode Pessoal de Nível Superior) Brazil for their financial support.

References

1. López-Moreno, J.I.; Morán-Tejeda, E.; Vicente-Serrano, S.M.; Bazo, J.; Azorin-Molina, C.; Revuelto, J.; Sánchez-Lorenzo, A.; Navarro-Serrano, F.; Aguilar, E.; Chura, O. Recent temperature variability and change in the Altiplano of Bolivia and Peru. Int. J. Clim. 2015, doi:10.1002/joc.4459.
2. Seiler, C.; Hutjes, R.W. A.; Kabat, P. Climate variability and trends in Bolivia. J. Appl. Meteorol. Climatol. 2013, 52, 130–146.
3. Bradley, R.S.; Vuille, M.; Díaz, H.F.; Vergara, W. Threats to water supplies in the tropical Andes. Science. 2006, 312, 1755–1756.
4. Rabatel, A.; Francou, B.; Soruco, A.; Gomez, J.; Cceres, B.; Ceballos, J.L.; Basantes, R.; Vuille, M.; Sicart, J.E.; Huggel, C.; et al. Current state of glaciers in the tropical Andes: A multi-century perspective on glacier evolution and climate change. Cryosphere 2013, 7, 81–102.
5. Juen, I.; Kaser, G.; Georges, C. Modelling observed and future runoff from a glacierized tropical catchment (Cordillera Blanca, Perú). Glob. Planet. Chang. 2007, 59, 37–48.
6. Cusicanqui, J.; Dillen, K.; Garcia, M.; Geerts, S.; Raes, D.; Mathijs, E. Economic assessment at farm level of the implementation of deficit irrigation for quinoa production in the Southern Bolivian Altiplano. Span. J. Agric. Res. 2013, 11, 894.
7. Jacobsen, S.E. What is wrong with the sustainability of Quinoa production in Southern Bolivia—A reply to Winkel et al. (2012). J. Agron. Crop. Sci. 2012, 198, 320–323.
8. Jacobsen, S.-E. The situation for Quinoa and its production in Southern Bolivia: From

economic success to environmental disaster. J. Agron. Crop. Sci. 2011, 197, 390–399.

9. Hadjimitsis, D.G.; Papadavid, G.; Agapiou, A.; Themistocleous, K.; Hadjimitsis, M.G.; Retalis, A.; Michaelides, S.; Chrysoulakis, N.; Toulios, L.; Clayton, C.R.I. Atmospheric correction for satellite remotely sensed data intended for agricultural applications: impact on vegetation indices. Nat. Hazards Earth Syst. Sci. 2010, 10, 89–95.
10. Agapiou, A.; Hadjimitsis, D.G.; Papoutsa, C.; Alexakis, D.D.; Papadavid, G. The Importance of accounting for atmospheric effects in the application of NDVI and interpretation of satellite imagery supporting archaeological research: The case studies of Palaepaphos and Nea Paphos sites in Cyprus. Remote Sens. 2011, 3, 2605–2629.
11. Song, C.; Woodcock, C.; Seto, K.C.; Lenney, M.P.; Macomber, S.A. Classification and change detection using Landsat TM Data—When and how to correct atmospheric effects? Remote Sens. Environ. 2001, 75, 230–244.
12. Rokni, K.; Ahmad, A.; Selamat, A.; Hazini, S. Water feature extraction and change detection using multitemporal landsat imagery. Remote Sens. 2014, 6, 4173–4189.
13. Zhai, K.; Wu, X.; Qin, Y.; Du, P. Comparison of surface water extraction performances of different classic water indices using OLI and TM imageries in different situations. Geo-Spat. Inf. Sci. 2015, 18, 32–42.
14. Arsen, A.; Crétaux, J.F.; Berge-Nguyen, M.; del Rio, R.A. Remote sensing-derived bathymetry of Poopó. Remote Sens. 2013, 6, 407–420.
15. Feyisa, G.L.; Meilby, H.; Fensholt, R.; Proud, S.R. Automated water extraction index: A new technique for surface water mapping using Landsat imagery. Remote Sens. Environ. 2014, 140, 23–35.
16. Fisher, A.; Flood, N.; Danaher, T. Remote Sensing of Environment Comparing Landsat water index methods for automated water classi fi cation in eastern Australia. Remote Sens. Environ. 2016, 175, 167–182.
17. Pillco, R.; Bengtsson, L. Long-term and extreme water level variations of the shallow Poopó , Bolivia Long-term and extreme water level variations of the shallow Poopó , Bolivia. Hydrol. Sci. J. 2006, 51, 98–114.
18. Satgé, F.; Bonnet, M.P.; Timouk, F.; Calmant, S.; Pillco, R.; Molina, J.; Lavado-Casimiro, W.; Arsen, A.; Crétaux, J.F.; Garnier, J. Accuracy assessment of SRTM v4 and ASTER GDEM v2 over the Altiplano watershed using ICESat/GLAS data. Int. J. Remote Sens. 2015, 36, 465–488.
19. Satgé, F.; Bonnet, M.-P.; Gosset, M.; Molina, J.; Hernan Yuque Lima, W.; Pillco Zolá, R.; Timouk, F.; Garnier, J. Assessment of satellite rainfall products over the Andean plateau. Atmos. Res. 2016, 167, 1–14.
20. Garcia, M.; Raes, D.; Allen, R.; Herbas, C. Dynamics of reference evapotranspiration in the Bolivian highlands (Altiplano). Agric. For. Meteorol. 2004, 125, 67–82.
21. Mobley, C.D. Estimation of the remote-sensing reflectance from above-surface measurements. Appl. Opt. 1999, 38, 7442–7445.
22. Mishra, N.; Haque, M.O.; Leigh, L.; Aaron, D.; Helder, D.; Markham, B. Radiometric cross calibration of landsat 8 Operational Land Imager (OLI) and landsat 7 enhanced thematic

mapper plus (ETM+). Remote Sens. 2014, 6, 12619–12638.

23. Li, P.; Jiang, L.; Feng, Z. Cross-comparison of vegetation indices derived from landsat-7 enhanced thematic mapper plus (ETM+) and landsat-8 operational land imager (OLI) sensors. Remote Sens. 2013, 6, 310–329.
24. She, X.; Zhang, L.; Cen, Y.; Wu, T.; Huang, C.; Baig, M.H. A. Comparison of the continuity of vegetation indices derived from Landsat 8 OLI and Landsat 7 ETM+ data among different vegetation types. Remote Sens. 2015, 7, 13485–13506.
25. Bryant, R.; Moran, M.S.; McElroy, S.; Holifield, C.; Thome, K.; Miura, T. Data continuity of Landsat-4 TM, Landsat-5 TM, Landsat-7 ETM+, and Advanced Land Imager (ALI) sensors. IEEE Int. Geosci. Remote Sens. Symp. 2002, 1, 584–586.
26. Holifield, C.D.; McElroy, S.; Moran, M.S.; Bryant, R.; Miura, T.; Emmerich, W.E. Temporal and spatial changes in grassland transpiration detected using Landsat TM and ETM+ imagery. Can. J. Remote Sens. 2003, 29, 259–270.
27. Moran, M.; Bryant, R.; Thome, K.; Ni, W.; Nouvellon, Y.; Gonzalez-Dugo, M.; Qi, J.; Clarke, T. A refined empirical line approach for reflectance factor retrieval from Landsat-5 TM and Landsat-7 ETM+. Remote Sens. Environ. 2001, 78, 71–82.
28. Vogelmann, J.E.; Helder, D.; Morfitt, R.; Choate, M.J.; Merchant, J.W.; Bulley, H. Effects of Landsat 5 thematic mapper and Landsat 7 enhanced thematic mapper plus radiometric and geometric calibrations and corrections on landscape characterization. Remote Sens. Environ. 2001, 78, 55–70.
29. Masek, J.G.; Vermote, E.F.; Saleous, N.E.; Wolfe, R.; Hall, F.G.; Huemmrich, K.F.; Gao, F.; Kutler, J.; Lim, T.K. A landsat surface reflectance dataset for North America, 1990–2000. IEEE Geosci. Remote Sens. Lett. 2006, 3, 68–72.
30. Geological Survey: Provisionla Landsat 8 Surface Reflectance Code (LaSRC) Product. Available online: https://landsat.usgs.gov/sites/default/files/documents/provisional_lasrc_product_guide.pdf (accessed on 26 February 2017).
31. Ashouri, H.; Hsu, K.L.; Sorooshian, S.; Braithwaite, D.K.; Knapp, K.R.; Cecil, L.D.; Nelson, B.R.; Prat, O.P. PERSIANN-CDR: Daily precipitation climate data record from multisatellite observations for hydrological and climate studies. Bull. Am. Meteorol. Soc. 2015, 96, 69–83.
32. Beck, H.E.; van Dijk, A.I. J.M.; Levizzani, V.; Schellekens, J.; Miralles, D.G.; Martens, B.; de Roo, A. MSWEP: 3-hourly 0.25° global gridded precipitation (1979–2015) by merging gauge, satellite, and reanalysis data. Hydrol. Earth Syst. Sci. Discuss. 2016, 2016, 1–38.
33. Funk, C.; Verdin, A.; Michaelsen, J.; Peterson, P.; Pedreros, P.; Husak, G. A global satellite-assisted precipitation climatology. Earth Syst. Sci. Data 2016, 7, 275–287.
34. Mu, Q.; Zhao, M.; Running, S.W. Improvements to a MODIS global terrestrial evapotranspiration algorithm. Remote Sens. Environ. 2011, 115, 1781–1800.
35. Mu, Q.; Heinsch, F.A.; Zhao, M.; Running, S.W. Development of a global evapotranspiration algorithm based on MODIS and global meteorology data. Remote Sens. Environ. 2007, 111, 519–536.

36. Friedl, M.A.; McIver, D.K.; Hodges, J.C.F.; Zhang, X.Y.; Muchoney, D.; Strahler, A.H.; Woodcock, C.E.; Gopal, S.; Schneider, A.; Cooper, A.; et al. Global land cover mapping from MODIS: Algorithms and early results. Remote Sens. Environ. 2002, 83, 287–302.
37. Myneni, R.B.; Hoffman, S.; Knyazikhin, Y.; Privette, J.L.; Glassy, J.; Tian, Y.; Wang, Y.; Song, X.; Zhang, Y.; Smith, G.R.; et al. Global products of vegetation leaf area and fraction absorbed PAR from year one of MODIS data. Remote Sens. Environ. 2002, 83, 214–231.
38. Jin, Y.; Schaaf, C.B.; Woodcock, C.E.; Gao, F.; Li, X.; Strahler, A.H.; Lucht, W.; Liang, S. Consistency of MODIS surface bidirectional reflectance distribution function and albedo retrievals: 2. Validation. J. Geophys. Res. 2003, 108, 4159.
39. Adler-Golden, S.M.; Matthew, M.W.; Bernstein, L.S.; Levine, R.Y.; Berk, A.; Richtsmeier, S.C.; Acharya, P.K.; Anderson, G.P.; Felde, J.W.; Gardner, J.A.; et al. Atmospheric correction for shortwave spectral imagery based on MODTRAN4. Imaging Spectrom. 1999, 3753, 61–69.
40. Atmospheric Correction Module: QUAC and FLAASH User’s Guide; Harris Geospatial: Boulder, CO, USA, 2009.
41. Mann, H.B. Nonparametric tests against trend. Econometrica 1945, 13, 163–171.
42. Burn, D.H.; Hag Elnur, M.A. Detection of hydrologic trends and variability. J. Hydrol. 2002, 255, 107–122.
43. Molina Carpio, J.; Satgé, F.; Pillco Zola, R. Water resources in the TDPS system. Available online: https://portals.iucn.org/library/sites/library/files/documents/2014-015.pdf (accessed on 26 February 2017).

VI. Conclusões e perspectivas

Durante a primeira etapa do doutorado, dedicada à elaboração do banco de dados de sensoriamento remoto na região do Altiplano, as maiores contribuições do trabalho são (i) o desenvolvimento e uso de metodologia de avaliação de erro dos produtos novos e originais, complementando as metodologias previamente utilizadas até hoje e (ii) dar um primeiro retorno do potencial dos dados de sensoriamento remoto para seguir os processos hidrológicos na região do Altiplano.

De maneira geral, os estudos prévios de avaliação de erro dos produtos de sensoriamento remoto não levaram em consideração o uso previsto para esses dados. Por isso, as metodologias utilizadas na avaliação do potencial dos dados não permitem ter uma visão representativa do potencial real dos dados dentro de um contexto de aplicação definido.

Nesse contexto, neste trabalho houve um empenho em entender os diferentes componentes dos erros dos produtos de sensoriamento remoto para poder identificar qual componentes do erro tem a maior influência no uso previsto no âmbito do doutorado. Dessa forma, o trabalho levou ao desenvolvimento de novos índices e metodologia original para responder a essas perguntas dando um passo mais a frente na consideração do erro completo dos produtos para efetuar a escolha do produto mais adequado para o contexto regional, bem como, para os objetivos de trabalho. A título de exemplo, os estudos sobre os MDEs permitiram evidenciar o grande papel do erro relativo dos MDEs. Porém, até hoje nenhum estudo referenciava o erro relativo dos MDEs. Assim, uma nova e primeira metodologia foi desenvolvido no meu trabalho de doutorado. Os resultados mostram que o erro vertical considerado pelos diferentes autores até hoje não é suficiente para poder concluir sobre o potencial dos MDEs. De fato, como demostrado no capítulo 1, os erros vertical e relativo podem ter comportamentos diferentes e a consideração única de um ou outro erro (i.e. vertical – relativo) leva a conclusões diferentes sobre o potencial dos MDEs. Da mesma forma, a avaliação da eficiência das correções atmosféricas desenvolvida no capítulo 3 levou a uma conclusão similar. Para ilustrar o caso, em geociências aplicadas, o maior uso das imagens multiespectrais é feito considerando a razão de bandas na classificação das imagens (i.e. separação água-solo, delimitação dos diferentes tipos de uso, qualidade de água, ...). Porém, na literatura de maneira geral, a avaliação do potencial das correções atmosféricas é feita baseada na análise de sensibilidade das correções atmosféricas, considerando as bandas individuais. Essa abordagem é um primeiro passo útil, mas insuficiente por não considerar o erro relativo entre as bandas e que eles controlam a eficiência dos índices feitos a partir de razão de bandas. O trabalho realizado no doutorado mostra a importância de considerar a razão de bandas nas análises de sensibilidade das correções atmosféricas. De fato, como mostrado no capítulo 3, a interpretação das análises de sensibilidade das correções atmosféricas com base na banda individuais ou de razão de bandas são diferentes. Finalmente, o trabalho de comparação dos diferentes SREs de primeira e segunda geração e o trabalho de reanálise permitiu mostrar o grande potencial dos SREs na região, assim como suas principais limitações. De fato, como mostrado no capítulo 2, existe uma forte influência das anomalias de emissividade e temperatura ocorrendo acima do lago Titicaca assim como na zona de montanha. O trabalho realizado no doutorado permitiu evidenciar essas limitações e dessa forma pôde contribuir com a melhoria das estimativas dos futuros SREs por dar maior ênfase a esses fenômenos nos algoritmos futuros. Adicionalmente, trabalhos futuros podem utilizar os resultados para propor uma metodologia adequada à diminuição dos erros em zonas específicas. A primeira fase deste doutorado desenvolveu um banco de dados de sensoriamento remoto sem precedentes no Altiplano, incluindo MDEs, dados de precipitação e evapotranspiração e uma metodologia de monitoramento da dinâmica espaço-temporal da superfície de água com base em imagens multiespectrais Landsat. O banco de dados gerado esta disponível para as autoridades responsáveis e a elaboração do banco de dados online está em discussão para facilitar o acesso a qualquer usuário na região. O banco de dados é composto por estações chamadas de estações virtuais por incluir as variáveis obtidas unicamente a partir dos dados de sensoriamento remoto. A longo prazo, para os países com poucos recursos financeiros e as regiões fronteiriças, o sensoriamento remoto oferece a possibilidade de autonomia completa no monitoramento hidrometeorológico regional. Por isso, os resultados obtidos durante este doutorado demostram o interesse de acoplar a rede de estação *in situ* com uma rede orientada por sensoriamento remoto. Desta maneira se espera uma melhorada da qualidade do monitoramento tomando conta da variabilidade hidro-climática espacial e temporal do altiplano. A utilização da rede orientada por sensoriamento remoto poderia também permitir redistribuir algumas estações para melhorar a calibração dos produtos de sensoriamento de acordo com as fontes de erro potencial devido ao relevo e corpo de água (emissividade e temperatura).

A segunda etapa do doutorado consistiu na utilização do banco de dados estabelecido para a questão socioambiental de maior importância para a região do Altiplano: a seca desde dezembro de 2015 do segundo maior lago da Bolívia, o lago Poopó. Devido à falta de dados *in* *situ,* nenhum estudo informava sobre os potenciais fatores responsáveis pela situação (i.e. fatores climatológicos e de uso antrópico). Portanto, a mudança climática era designada como o principal fator da seca do lago Poopó. Este trabalho conseguiu mostrar que o papel da atividade agrícola representa um fator adicional muito importante para a desertificação regional observada nas últimas décadas. As mudanças de cobertura, juntamente com processos de irrigação, contribuíram para o aumento da ETr em aproximadamente 12.8% em escala regional. Devido ao contexto árido, com taxas evaporativas e de precipitação muito próximas, e ao aumento considerável no desequilíbrio do balanço hídrico, as precipitações não são mais suficientes para manter as atividades agrícolas e o ecossistema regional (lago Poopó). De fato, devido à entrada da quinoa no mercado internacional, as populações se dedicaram ao cultivo desse cereal para melhorar suas condições econômicas. Por falta de informação, controle e monitoramento das atividades nessa região, as superfícies dedicadas a esses cultivos subiram exponencialmente e foram acompanhadas de processos mecanizados e de irrigação que contribuíram com o processo de desertificação (Figura 13). Atualmente, o Altiplano está frente à situação crítica potencial na qual as populações podem estar ameaçadas de crises econômicas por não poder mais manter as atividades agrícolas e a economia que delas resultam. As mudanças climáticas, as tensões geopolíticas decorrentes do recurso hídrico e as atividades mineiras, contribuíram também para aumentar esta ameaça, pois diminuíram a quantidade de água disponível (Figura 13).

Além disso, o processo de desertificação pode ter um efeito sobre os fenômenos de tempestade de areia. De maneira geral, se espera um aumento destes fenômenos devido a (i) ao aumento da erosão eólica causado pela supressão da vegetação nativa em favor do cultivo e (ii) à diminuição da umidade do ar, causada pela redução geral da superfície do lago Poopó, o qual tem um papel de retenção da umidade local. Dependendo da intensidade e da época, as tempestades de areia poderiam cobrir os cultivos que acabaram de germinar e impedir assim, o crescimento deles, o que resultaria em uma importante perda de rendimento, ameaçando economicamente as populações. Esses fenômenos de tempestade de areia foram observados em campo (Figura 13) e até capturados nas imagens MODIS o qual abre a possibilidade de monitoramento e estudo baseado no sensoriamento remoto a grande escala.

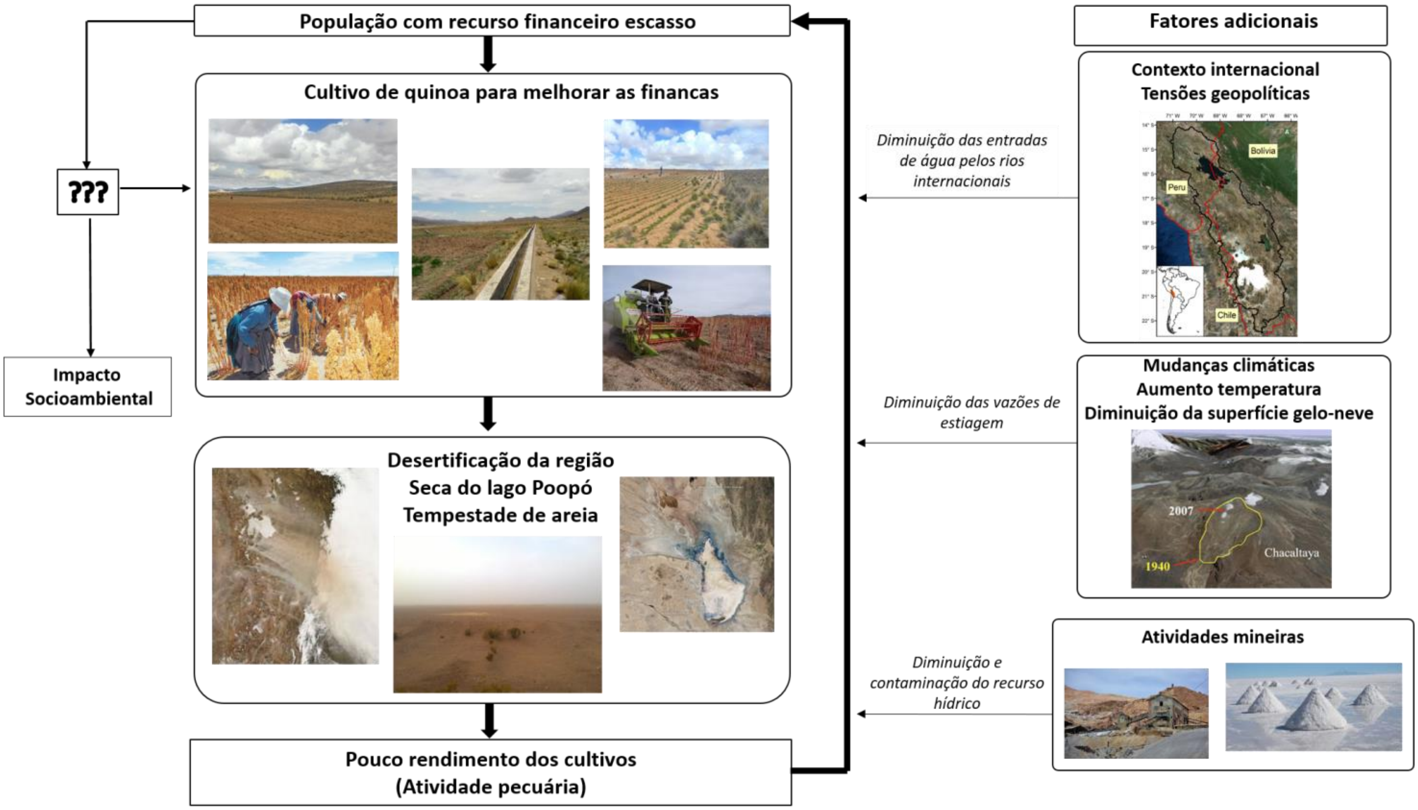

Figura 13. Esquema da situação socioambiental atual no Altiplano em relação às diferentes pressões humanas e climáticas existentes.

Este trabalho mostra a grande potencialidade do sensoriamento remoto para regiões isoladas, desde o monitoramento hidrometeorológico, até constituir dados adicionais para tomada de decisão em decorrência da preservação conjunta do meio ambiente e das atividades econômicas. De fato, a partir dos resultados obtidos, podemos sugerir um valor limiar mínimo de superfície do lago Poopó de 1.500 km^2 a ser utilizado como referencia de superfície após a estação chuvosa para evitar que o lago seque durante a estação seca seguinte.

O trabalho realizado sugere a contribuição significativa das atividades agrícolas no processo de desertificação progressivo nos últimos anos, que culminou com a seca completa do lago Poopó, em dezembro 2015. Ao mesmo tempo, os resultados mostram que a variabilidade climática não contribuiu para o aumento da ETr observado nas zonas agrícolas. Este aumento poderia ser atribuído à mudança de cobertura do solo e ao processo de irrigação. Além disso, como ilustrado na introdução, a região está enfrentando mudanças climáticas com o aumento da temperatura. Essas mudanças são responsáveis pela redução global dos glaciares, na ordem de 43% entre 1981 e 2014. Nesse contexto é importante seguir estudando o comportamento hidroclimatológico regional. Uma atenção particular deve ser dada à bacia do lago Titicaca.

Devido a sua localização na parte norte da bacia, em que o escoamento ocorre de norte para sul e a sua característica morfológica (8.400 km^2, 107 m de profundidade média), esse lago tem o papel de reservatório de água do sistema TDPS. Ao mesmo tempo, a parte à montante das bacias que contribuem com o aporte de água no lago estão ocupados por uma cobertura importante de neve/gelo. A bacia está então sujeita aos efeitos das variações climáticas através da diminuição da cobertura de neve/gelo e pelo aumento potencial da evaporação do lago Titicaca. Trabalhos futuros poderiam focar no potencial dos dados de sensoriamento remoto para representar a dinâmica espaço-temporal da cobertura de neve/gelo nessa região e a sua influência na reposta hidrológica na saída das bacias do lago Titicaca. Modelos empíricos para representação da cobertura de gelo/neve poderiam ser avaliados na região (Clark et al., 2009; Hublart et al., 2015) e utilizados como entrada adicional para modelos hidrológicos. Tais modelos permitiriam testar novos produtos de sensoriamento remoto, úteis na representação da dinâmica neve/gelo e avaliar os dados do sensoriamento remoto considerados no doutorado em um contexto de modelagem hidrológica. Esta abordagem permitirá validar de maneira mais robusta a representação da variabilidade espaço-temporal feita a partir dos dados e observar a influência da variabilidade climática no reservatório neve/gelo. Por fim, a evaporação do lago constitui a principal saída de água do lago. A radiação nesta região é muito importante devido à altura média do lago, localizado a uma elevação média de 4.000m. Uma linha de trabalho poderia focar na estimativa da radiação no lago para calcular de maneira mais precisa a sua evaporação. Estudos recentes mostram que tal trabalho pode ser realizado a partir de produtos de sensoriamento remoto (emissividade, temperatura de superfície e ar, radiação de onda curta e larga, albedo, imagens multiespectrais) com resultados satisfatórios (de Oliveira et al., 2016; Moukomla and Blanken, 2016). Por fim, conforme ilustrado no capítulo 3, uma região agrícola, na qual foi registrado um aumento significativo da ETr, está localizada na bacia do lago Titicaca e poderia ser utilizado para confirmar o papel das atividades agrícolas na região.

Para finalizar, uma segunda linha de pesquisa poderá focar no reservatório de água subterrânea, o qual não foi considerado no doutorado. Por isso, os diferentes produtos e algoritmos que permitiram fazer uma estimativa da umidade do solo deveriam ser avaliados na região. Esses produtos podem ser usados com aos dados de anomalia gravimétrica *Gravity Recovery And Climate Experiment* (GRACE) para determinar as variações do estoque de água subterrâneo (Voss et al., 2013; Forootan et al., 2014;). Ao mesmo tempo, um estudo recém publicado demostra o grande potencial dos dados de umidade do solo na estimativa das precipitações de acordo com o algoritmo *bottom-up SM2RAIN* (Brocca et al., 2013, 2014), permitindo estimar a precipitação com alta precisão. Nessa linha de pesquisa, estudos recentes mostram a possibilidade de identificar as zonas irrigadas e quantificar a água utilizada no processo de irrigação (Kumar et al., 2015; Brocca et al., 2017) . Primeiro, esta metodologia identifica as zonas agrícolas irrigadas por anomalia nos valores de umidade do solo. Segundo, a quantidade de água usada no processo de irrigação é estimada pela diferença entre a estimativa de chuva clássica (por sensoriamento remoto ou não) com as derivadas do algoritmo *bottom-up SM2RAIN*. Essa abordagem se baseia no fato que os valores de umidade do solo usados nas estimativas de chuva derivada do *bottom-up SM2RAIN* são influenciados pelas precipitações e irrigações enquanto as precipitações clássicas não. Nas regiões isoladas, como o Altiplano, essa metodologia oferece grande perspectiva no controle das diferentes atividades agrícolas. No altiplano, sendo uma região descoberta com vegetação muito rasa, os produtos de sensoriamento remoto de umidade poderiam ser suficientemente acurados por não ser influenciados pelos efeitos da vegetação nas estimativas. Nesse contexto, esses dados oferecem grande perspectiva no monitoramento do uso agrícola da água e no monitoramento do reservatório subterrâneo (em conjunto com os dados GRACE).

Assim, a partir de dados de sensoriamento remoto, pode-se avaliar o ciclo hidrológico regional, considerando tanto as águas superficiais quantos as subterrâneas. Esse abordagem permitirá uma representação mais robusta e consistente do ciclo e assim permitirá melhorar as análises das reservas hídricas e assim como, as medidas de preservação do meio ambiente do Altiplano Sul-Americano.

VII. Referências

Alanoca, L., Guédron, S., Amouroux, D., Audry, S., Monperrus, M., Tessier, E., Goix, S., Acha, D., Seyler, P., Point, D., 2016. Synergistic effects of mining and urban effluents on the level and distribution of methylmercury in a shallow aquatic ecosystem of the Bolivian Altiplano. Environ. Sci. Process. Impacts 18, 1550–1560. doi:10.1039/C6EM00547K

Allen, R.G., Pereira, L.S., Raes, D., Smith, M., Ab, W., 1998. Crop evapotranspiration - Guidelines for computing crop water requirements - FAO Irrigation and drainage paper 5.

Argollo, J., Mourguiart, P., 2000. Late Quaternary climate history of the Bolivian Altiplano. Quat. Int. 72, 37–51.

Bicheron, P., Defourny, P., Brockmann, C., Schouten, L., Vancutsem, C., Huc, M., Bontemps, S., Leroy, M., Achard, F., Herold, M., Ranera, F., Arino, O., 2008. GLOBCOVER Products Report Description.

Boulange, B., Aquize Jaen, E., 1981. Morphologie, hydrographie et climatologie du lac Titicaca et de son bassin versant. Hydrobiol. trop. 14, 269–287.

Bradley, R.S., Vuille, M., Díaz, H.F., Vergara, W., 2006. Threats to water supplies in the tropical Andes. Science (80-.). 312, 1755–1756.

Brocca, L., Ciabatta, L., Massari, C., Camici, S., Tarpanelli, A., 2017. Soil Moisture for Hydrological Applications: Open Questions and New Opportunities. Water 9, 140. doi:10.3390/w9020140

Brocca, L., Ciabatta, L., Massari, C., Moramarco, T., Hahn, S., Hasenauer, S., Kidd, R., Dorigo, W., Wagner, W., Levizzani, V., 2014. Soil as a natural rain gauge: Estimating global rainfall from satellite soil moisture data. J. Geophys. Res. Atmos. 119, 5128–5141. doi:10.1002/2014JD021489

Brocca, L., Moramarco, T., Melone, F., Wagner, W., 2013. A new method for rainfall estimation through soil moisture observations. Geophys. Res. Lett. 40, 853–858. doi:10.1002/grl.50173

Canedo, C., Pillco Zolá, R., Berndtsson, R., 2016. Role of Hydrological Studies for the Development of the TDPS System. Water 8, 144. doi:10.3390/w8040144

Carmouze, J., Aquize, E., 1981. La régulation hydrique du lac Titicaca et l'hydrologie de ses tributaires. Hydrobiol. trop. 14, 311–328.

Carmouze, J., Arce, C., Quintanilla, J., 1977. LA REGULATION HYDRIQUE DES LACS TITICACA ET POOPO. Cah. O.R.ST.O.M., Sér. Hydrobiol 11, 269–283.

Clark, M.P., Hreinsson, E., Martinez, G.F., Tait, A., Slater, A., Hendrikx, J., Owens, I., Gupta, H. V., Schmidt, J., Woods, R., 2009. Simulations of seasonal snow for the South Island, New Zealand 48, 41–58.

Cook, S.J., Kougkoulos, I., Edwards, L.A., Dortch, J., Hoffmann, D., 2016. Glacier change and glacial lake outburst flood risk in the Bolivian Andes. Cryosphere 10, 2399–2413. doi:10.5194/tc-10-2399-2016

Countries, D., Processes, H., 2011. Global Water Sustainability 7.

Cusicanqui, J., Dillen, K., Garcia, M., Geerts, S., Raes, D., Mathijs, E., 2013. Economic assessment at farm level of the implementation of deficit irrigation for quinoa production in the Southern Bolivian Altiplano, in: Spanish Journal of Agricultural Research. p. 894. doi:10.5424/sjar/2013114-4097

de Oliveira, G., Brunsell, N.A., Moraes, E.C., Bertani, G., dos Santos, T. V., Shimabukuro, Y.E., Aragao, L.E.O.C., 2016. Use of MODIS sensor images combined with reanalysis products to retrieve net radiation in Amazonia. Sensors (Switzerland) 16. doi:10.3390/s16070956

Forootan, E., Rietbroek, R., Kusche, J., Sharifi, M.A., Awange, J.L., Schmidt, M., Omondi, P., Famiglietti, J., 2014. Separation of large scale water storage patterns over Iran using GRACE, altimetry and hydrological data. Remote Sens. Environ. 140, 580–595.

doi:10.1016/j.rse.2013.09.025

Frans, C., Istanbulluoglu, E., Lettenmaier, D.P., Naz, B.S., Clarke, G.K.C., Condom, T., Burns, P., Nolin, A.W., 2015. Predicting glacio-hydrologic change in the headwaters of the Zongo River, Cordillera Real, Bolivia. Water Resour. Res. 51, 9029–9052. doi:10.1002/2014WR016728

Fritz, S.C., Baker, P.A., Lowenstein, T.K., Seltzer, G.O., Rigsby, C.A., Dwyer, G.S., Tapia, P.M., Arnold, K.K., Ku, T.L., Luo, S., 2004. Hydrologic variation during the last 170,000 years in the southern hemisphere tropics of South America. Quat. Res. 61, 95–104. doi:10.1016/j.yqres.2003.08.007

Garreaud, R., Vuille, M., Clement, A.C., 2003. The climate of the Altiplano: observed current conditions and mechanisms of past changes. Palaeogeogr. Palaeoclimatol. Palaeoecol. 194, 5–22. doi:10.1016/S0031-0182(03)00269-4

Giordano, M., 2009. Global Groundwater? Issues and Solutions. Annu. Rev. Environ. Resour. 34, 153–178. doi:10.1146/annurev.environ.030308.100251

Gleeson, T., Wada, Y., Bierkens, M.F.P., van Beek, L.P.H., 2012. Water balance of global aquifers revealed by groundwater footprint. Nature 488, 197–200. doi:10.1038/nature11295

Guyot, J.-L., Gumiel, D., 1990. Premières données sur l’hydrogéologie et l´hydrogéochimie du Nord de lÁltiplaneau bolivien. Hydrogéologie 3, 159–164.

Hanasaki, N., Fujimori, S., Yamamoto, T., Yoshikawa, S., Masaki, Y., Hijioka, Y., Kainuma, M., Kanamori, Y., Masui, T., Takahashi, K., Kanae, S., 2013a. A global water scarcity assessment under Shared Socio-economic Pathways - Part 1: Water use. Hydrol. Earth Syst. Sci. 17, 2375–2391. doi:10.5194/hess-17-2375-2013

Hanasaki, N., Fujimori, S., Yamamoto, T., Yoshikawa, S., Masaki, Y., Hijioka, Y., Kainuma, M., Kanamori, Y., Masui, T., Takahashi, K., Kanae, S., 2013b. A global water scarcity assessment under Shared Socio-economic Pathways - Part 2: Water availability and scarcity. Hydrol. Earth Syst. Sci. 17, 2393–2413. doi:10.5194/hess-17-2393-2013

Hublart, P., Ruelland, D., Dezetter, A., Jourde, H., 2015. Reducing structural uncertainty in conceptual hydrological modelling in the semi-arid Andes. Hydrol. Earth Syst. Sci. 19, 2295–2314. doi:10.5194/hess-19-2295-2015

Huss, M., Farinotti, D., Bauder, A., Funk, M., 2009. Modelling runoff from highly glacierized drainage basins in a changing climate. Mitteilungen der Versuchsanstalt fur Wasserbau, Hydrol. und Glaziologie an der Eidgenoss. Tech. Hochschule Zurich 123–146. doi:10.1002/hyp.7055

IPCC, 2014. Climate Change 2014 Synthesis Report Summary Chapter for Policymakers. Ipcc 31. doi:10.1017/CBO9781107415324

Jacobsen, S.-E., 2011. The Situation for Quinoa and Its Production in Southern Bolivia: From Economic Success to Environmental Disaster. J. Agron. Crop Sci. 197, 390–399. doi:10.1111/j.1439-037X.2011.00475.x

Jacobsen, S.E., 2012. What is Wrong With the Sustainability of Quinoa Production in Southern Bolivia - A Reply to Winkel et al. (2012). J. Agron. Crop Sci. 198, 320–323. doi:10.1111/j.1439-037X.2012.00511.x

Jorge, Q., Daza Pelaez, C., 2014. CONTAMINACIÓN EN METALES PESADOS EN EL SISTEMA TDP, in: Línea Base de Conocimientos Sobre Los Recursos Hidrológicos En El Sistema TDPS Con Enfoque En La Cuenca Del Lago Titicaca. pp. 252–263.

Kessler, A., Monheim, F., 1966. El balance hidrologico del lago Titicaca, una contribución al aprovechamiento de sus aguas, in: Conferencia Regional Latinoamericana / Union Geografica Internacional. pp. 412–422.

Koos Dijkshoorn; Jan Huting;, Tempel, P., 2005. Update of the 1 : 5 million Soil and Terrain Database for Latin America and the Caribbean (SOTERLAC). ISRIC Rep. 2005/01 1, 25.

Kumar, S. V., Peters-Lidard, C.D., Santanello, J.A., Reichle, R.H., Draper, C.S., Koster, R.D., Nearing, G., Jasinski, M.F., 2015. Evaluating the utility of satellite soil moisture retrievals over irrigated areas and the ability of land data assimilation methods to correct for unmodeled processes. Hydrol. Earth Syst. Sci. 19, 4463–4478. doi:10.5194/hess-19-4463-2015

Lambrecht, A., Mayer, C., 2009. Temporal variability of the non-steady contribution from glaciers to water discharge in western Austria. J. Hydrol. 376, 353–361. doi:10.1016/j.jhydrol.2009.07.045

Lemoalle, J., Bader, J.C., Leblanc, M., Sedick, A., 2012. Recent changes in Lake Chad: Observations, simulations and management options (1973-2011). Glob. Planet. Change 80–81, 247–254. doi:10.1016/j.gloplacha.2011.07.004

Long, D., Chen, X., Scanlon, B.R., Wada, Y., Hong, Y., Singh, V.P., Chen, Y., Wang, C., Han, Z., Yang, W., 2016. Have GRACE satellites overestimated groundwater depletion in the Northwest India Aquifer? Sci. Rep. 6, 24398. doi:10.1038/srep24398

López-Moreno, J.I., Fontaneda, S., Bazo, J., Revuelto, J., Azorin-Molina, C., Valero-Garcés, B., Morán-Tejeda, E., Vicente-Serrano, S.M., Zubieta, R., Alejo-Cochachín, J., 2014. Recent glacier retreat and climate trends in Cordillera Huaytapallana, Peru. Glob. Planet. Change 112, 1–11. doi:10.1016/j.gloplacha.2013.10.010

López-Moreno, J.I., Morán-Tejeda, E., Vicente-Serrano, S.M., Bazo, J., Azorin-Molina, C., Revuelto, J., Sánchez-Lorenzo, A., Navarro-Serrano, F., Aguilar, E., Chura, O., 2015. Recent temperature variability and change in the Altiplano of Bolivia and Peru. Int. J. Climatol. n/a-n/a. doi:10.1002/joc.4459

Lozada, G., 1985. BALANCE HIDRICO DE LA CUENCA DEL LAGO TITICACA.

Mark, B.G., Mckenzie, J.M., 2007. Tracing increasing tropical Andean glacier melt with stable isotopes in water. Environ. Sci. Technol. 41, 6955–6960. doi:10.1021/es071099d

Mark, B.G., McKenzie, J.M., Gómez, J., 2005. Hydrochemical evaluation of changing glacier meltwater contribution to stream discharge: Callejon de Huaylas, Peru / Evaluation hydrochimique de la contribution évolutive de la fonte glaciaire à l'écoulement fluvial: Callejon de Huaylas, Pérou. Hydrol. Sci. J. 50, 975–988. doi:10.1623/hysj.2005.50.6.975

Molina Carpio, J., Cruz, R., Alurralde, J.C., 2012. Impactos transfronterizos de proyectos de trasvase: El caso de la cuenca del rio Mauri, in: XXV CONGRESO LATINOAMERICANO DE HIDRÁULICA SAN JOSÉ, COSTA RICA.

Moore, I.D., Grayson, R.B., Ladson, A.R., 1991. Digital terrain modelling: A review of hydrological, geomorphological, and biological applications. Hydrol. Process. 5, 3–30. doi:10.1002/hyp.3360050103

Moore, R.D., Fleming, S.W., Menounos, B., Wheate, R., Fountain, A., Stahl, K., Holm, K., Jakob, M., 2009. Glacier change in western North America: Influences on hydrology, geomorphic hazards and water quality. Hydrol. Process. doi:10.1002/hyp.7162

Moran, R.E., 2009. Mining Water: The San Cristobal Mine, Bolivia, in: Minando El Agua: San Cristobal, Bolivia. CGIAB (Comisión de Gestión Integral de Aguas de Bolivia, Commission for the Integrated Management of Bolivian Waters) and FRUTCAS (Federación Regional Única de los Trabajadores Campesinos del Altiplano Sud-- Regional Farmers Federation of the Southern Alt, pp. 7–37.

Moukomla, S., Blanken, P.D., 2016. Estimating the Great Lakes net radiation using satellite remote sensing and MERRA reanalysis. Int. J. Digit. Earth 0, 1–21.

doi:10.1080/17538947.2016.1252432

Ndehedehe, C.E., Agutu, N.O., Okwuashi, O., Ferreira, V.G., 2016. Spatio-temporal variability of droughts and terrestrial water storage over Lake Chad Basin using independent component analysis. J. Hydrol. 540, 106–128. doi:10.1016/j.jhydrol.2016.05.068

Painter, J., 2007. Human Development Report 2007 / 2008 Deglaciation in the Andean Region.

Pillco, R., Bengtsson, L., 2010. Long-term and extreme water level variations of the shallow Lake Poopó , Bolivia Long-term and extreme water level variations of the shallow Lake Poopó , Bolivia. Hydrol. Sci. J. 37–41.

Pillco, R., Uvo, C.B., Bengtsson, L., 2007. Precipitation variability and regionalization over the Southern Altiplano , Bolivia. Int. J. Climatol. 149–164.

Precoda, N., 1991. Requiem for the Aral Sea. Ambio 20, 109–114.

Rabatel, A., Francou, B., Soruco, A., Gomez, J., Caceres, B., Ceballos, J.L., Basantes, R., Vuille, M., Sicart, J.E., Huggel, C., Scheel, M., Lejeune, Y., Arnaud, Y., Collet, M., Condom, T., Consoli, G., Favier, V., Jomelli, V., Galarraga, R., Ginot, P., Maisincho, L., Mendoza, J., Ménégoz, M., Ramirez, E., Ribstein, P., Suarez, W., Villacis, M., Wagnon, P., 2013. Current state of glaciers in the tropical Andes: A multi-century perspective on glacier evolution and climate change. Cryosphere 7, 81–102. doi:10.5194/tc-7-81-2013

Rangecroft, S., Harrison, S., Anderson, K., Magrath, J., Castel, A.P., Pacheco, P., 2013. Climate change and water resources in arid mountains: An example from the bolivian andes. Ambio. doi:10.1007/s13280-013-0430-6

Richerson, P.J., 1977. THE LIMNOLOGY OF LAKE TITICACA (PERU-BOLIVIA), A Large, High Altitude Tropical Lake. Inst. Ecol. Publ.

Roche, M.A., Bourges, J., Cortes, J., Mattos, R., 1992. Climatología e hidrología de la cuenca del lago Titicaca. Springer Netherlands, Boston. doi:10.1007/978-94-011-2406-5_4

Rodell, M., Velicogna, I., Famiglietti, J.S., 2009. Satellite-based estimates of groundwater depletion in India. Nature 460, 999–1002. doi:10.1038/nature08238

Rokni, K., Ahmad, A., Selamat, A., Hazini, S., 2014. Water feature extraction and change detection using multitemporal landsat imagery. Remote Sens. 6, 4173–4189. doi:10.3390/rs6054173

Rutllant, J., Ulriksen, P., 1979. ARID DYNAMICS PART OF THE EXTREMELY OF CHILE : The Antofagasta Field Experiment. Bound. Layer Meteorol. 17, 41–55. doi:10.1007/BF00121936

Satgé, F., Bonnet, M.-P., Gosset, M., Molina, J., Hernan Yuque Lima, W., Pillco Zolá, R., Timouk, F., Garnier, J., 2016a. Assessment of satellite rainfall products over the Andean plateau. Atmos. Res. 167, 1–14. doi:10.1016/j.atmosres.2015.07.012

Satgé, F., Bonnet, M.P., Timouk, F., Calmant, S., Pillco, R., Molina, J., Lavado-Casimiro, W., Arsen, A., Crétaux, J.F., Garnier, J., 2015. Accuracy assessment of SRTM v4 and ASTER GDEM v2 over the Altiplano watershed using ICESat/GLAS data. Int. J. Remote Sens. 36, 465–488. doi:10.1080/01431161.2014.999166

Satgé, F., Denezine, M., Pillco, R., Timouk, F., Pinel, S., Molina, J., Garnier, J., Seyler, F., Bonnet, M.-P., 2016b. Absolute and relative height-pixel accuracy of SRTM-GL1 over the South American Andean Plateau. ISPRS J. Photogramm. Remote Sens. 121. doi:10.1016/j.isprsjprs.2016.09.003

Satgé, F., Espinoza, R., Zolá, R., Roig, H., Timouk, F., Molina, J., Garnier, J., Calmant, S., Seyler, F., Bonnet, M.-P., 2017a. Role of Climate Variability and Human Activity on Poopó Lake Droughts between 1990 and 2015 Assessed Using Remote Sensing Data. Remote Sens. 9, 218. doi:10.3390/rs9030218

Satgé, F., Xavier, A., Zolá, R.P., Hussain, Y., Timouk, F., Garnier, J., Bonnet, M.-P., 2017b. Comparative Assessments of the Latest GPM Mission's Spatially Enhanced Satellite Rainfall Products over the Main Bolivian Watersheds. Remote Sens. 9, 369. doi:10.3390/rs9040369

Scanlon, B.R., Faunt, C.C., Longuevergne, L., Reedy, R.C., Alley, W.M., McGuire, V.L., McMahon, P.B., 2012. Groundwater depletion and sustainability of irrigation in the US High Plains and Central Valley. Proc. Natl. Acad. Sci. 109, 9320–9325. doi:10.1073/pnas.1200311109

Seiler, C., Hutjes, R.W.A., Kabat, P., 2013. Likely ranges of climate change in Bolivia. J. Appl. Meteorol. Climatol. 52, 1303–1317. doi:10.1175/JAMC-D-12-0224.1

Seth, A., Thibeault, J., Garcia, M., Valdivia, C., 2010. Making Sense of Twenty-First-Century Climate Change in the Altiplano: Observed Trends and CMIP3 Projections. Ann. Assoc. Am. Geogr. 100, 835–847. doi:10.1080/00045608.2010.500193

Siebert, S., Burke, J., Faures, J.M., Frenken, K., Hoogeveen, J., Döll, P., Portmann, F.T., 2010. Groundwater use for irrigation - A global inventory. Hydrol. Earth Syst. Sci. 14, 1863–1880. doi:10.5194/hess-14-1863-2010

Small, I., Van Der Meer, J., Upshur, R.E.G., 2001. Acting on an environmental health disaster: The case of the Aral Sea. Environ. Health Perspect. 109, 547–549. doi:10.1289/ehp.01109547

Soruco, A., Vincent, C., Rabatel, A., Francou, B., Thibert, E., Sicart, J.E., Condom, T., 2015. Contribution of glacier runoff to water resources of La Paz city, Bolivia (16° S). Ann. Glaciol. 56, 147–154. doi:10.3189/2015AoG70A001

Trenberth, K.E., 2011. Changes in precipitation with climate change. Clim. Res. 47, 123–138. doi:10.3354/cr00953

Urquidi Barrau, F., 2012. Diagnóstico del agua en las américas.

Vacher, J.J., 1998. Responses of two main Andean crops, quinoa (Chenopodium quinoa Willd) and papa amarga (Solanum juzepczukii Buk.) to drought on the Bolivian Altiplano: Significance of local adaptation. Agric. Ecosyst. Environ. 68, 99–108. doi:10.1016/S0167-8809(97)00140-0

Valdivia, C., Seth, A., Gilles, J.L., García, M., Jiménez, E., Cusicanqui, J., Navia, F., Yucra, E., 2010. Adapting to climate change in Andean ecosystems: Landscapes, capitals, and perceptions shaping rural livelihood strategies and linking knowledge systems. Ann. Assoc. Am. Geogr. 100, 818–834. doi:10.1080/00045608.2010.500198

Valdivia, C., Thibeault, J., Gilles, J.L., García, M., Seth, A., 2013. Climate trends and projections for the Andean Altiplano and strategies for adaptation. Adv. Geosci. 33, 66–77. doi:10.5194/adgeo-33-69-2013

van Steenbergen, F., Kaisarani, A.B., Khan, N.U., Gohar, M.S., 2015. A case of groundwater depletion in Balochistan, Pakistan: Enter into the void. J. Hydrol. Reg. Stud. 4, 36–47. doi:10.1016/j.ejrh.2014.11.003

Vicente-Serrano, S.M., Chura, O., López-Moreno, J.I., Azorin-Molina, C., Sanchez-Lorenzo, A., Aguilar, E., Moran-Tejeda, E., Trujillo, F., Martínez, R., Nieto, J.J., 2015. Spatio-temporal variability of droughts in Bolivia: 1955-2012. Int. J. Climatol. 35, 3024–3040. doi:10.1002/joc.4190

Voss, K.A., Famiglietti, J.S., Lo, M., De Linage, C., Rodell, M., Swenson, S.C., 2013. Groundwater depletion in the Middle East from GRACE with implications for transboundary water management in the Tigris-Euphrates-Western Iran region. Water Resour. Res. 49, 904–914. doi:10.1002/wrcr.20078

Vuille, M., 1999. Atmospheric circulation over the Bolivian Altiplano during dry and wet periods and extreme phases of the Southern Oscillation. Int. J. Climatol. 19, 1579–1600. doi:10.1002/(SICI)1097-0088(19991130)19:14<1579::AID-JOC441>3.0.CO;2-N

Vuille, M., Hardy, D.R., Braun, B., Keimig, F., Bradley, R.S., 1998. Atmospheric circulation anomalies associated with 1996/1997 summer precipitation events on Sajama Ice Cap, Bolivia. J. Geophys. Res. 103, 191–204. doi:10.1029/98JD00681

Wheater, H.S., Gober, P., 2015. Water security and the science agenda. Water Resour. Res. 51, 5406–5424. doi:10.1002/2015WR016892

ANEXO 1

Accuracy assessment of SRTM v4 and ASTER GDEM v2 over the Altiplano watershed using ICESat/GLAS data

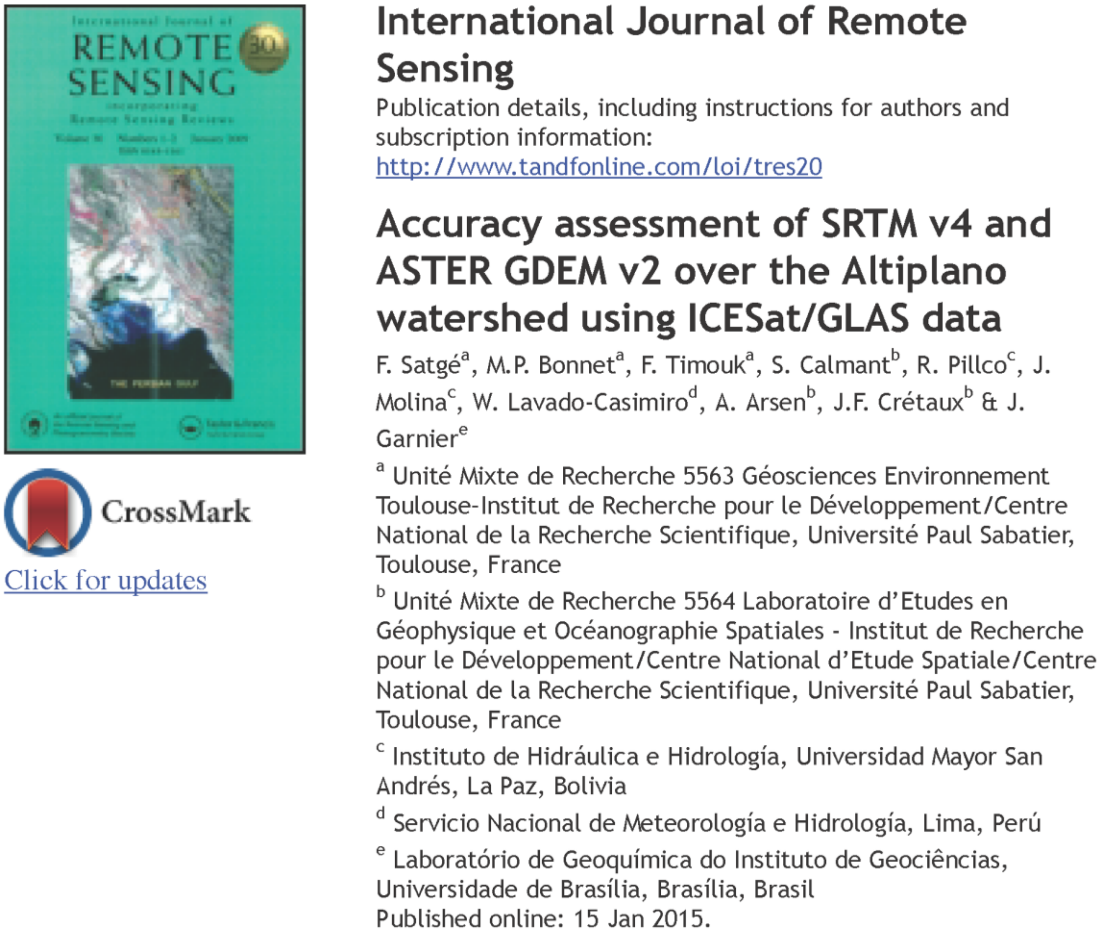

International Journal of Remote Sensing

Publication details, including instructions for authors and subscription information:
http://www.tandfonline.com/loi/tres20

Click for updates

Accuracy assessment of SRTM v4 and ASTER GDEM v2 over the Altiplano watershed using ICESat/GLAS data

F. Satgé[a], M.P. Bonnet[a], F. Timouk[a], S. Calmant[b], R. Pillco[c], J. Molina[c], W. Lavado-Casimiro[d], A. Arsen[b], J.F. Crétaux[b] & J. Garnier[e]

[a] Unité Mixte de Recherche 5563 Géosciences Environnement Toulouse-Institut de Recherche pour le Développement/Centre National de la Recherche Scientifique, Université Paul Sabatier, Toulouse, France

[b] Unité Mixte de Recherche 5564 Laboratoire d'Etudes en Géophysique et Océanographie Spatiales - Institut de Recherche pour le Développement/Centre National d'Etude Spatiale/Centre National de la Recherche Scientifique, Université Paul Sabatier, Toulouse, France

[c] Instituto de Hidráulica e Hidrología, Universidad Mayor San Andrés, La Paz, Bolivia

[d] Servicio Nacional de Meteorología e Hidrología, Lima, Perú

[e] Laboratório de Geoquímica do Instituto de Geociências, Universidade de Brasília, Brasília, Brasil

International Journal of Remote Sensing, 2015
Vol. 36, No. 2, 465–488, http://dx.doi.org/10.1080/01431161.2014.999166

Taylor & Francis
Taylor & Francis Group

Accuracy assessment of SRTM v4 and ASTER GDEM v2 over the Altiplano watershed using ICESat/GLAS data

F. Satgé[a]*, M.P. Bonnet[a], F. Timouk[a], S. Calmant[b], R. Pillco[c], J. Molina[c], W. Lavado-Casimiro[d], A. Arsen[b], J.F. Crétaux[b], and J. Garnier[e]

[a]*Unité Mixte de Recherche 5563 Géosciences Environnement Toulouse–Institut de Recherche pour le Développement/Centre National de la Recherche Scientifique, Université Paul Sabatier, Toulouse, France;* [b]*Unité Mixte de Recherche 5564 Laboratoire d'Etudes en Géophysique et Océanographie Spatiales - Institut de Recherche pour le Développement/Centre National d'Etude Spatiale/Centre National de la Recherche Scientifique, Université Paul Sabatier, Toulouse, France;* [c]*Instituto de Hidráulica e Hidrología, Universidad Mayor San Andrés, La Paz, Bolivia;* [d]*Servicio Nacional de Meteorología e Hidrología, Lima, Perú;* [e]*Laboratório de Geoquímica do Instituto de Geociências, Universidade de Brasília, Brasília, Brasil*

(*Received 7 May 2013; accepted 5 November 2014*)

The new Global Digital Elevation Model (GDEM v2) has been available since 17 October 2011. With a resolution of approximately 30 m, this model should provide more accurate information than the latest version of Shuttle Radar Topographic Mission (SRTM v4) with a resolution of 90 m outside of the USA. The accuracies of these two recently released digital elevation models (DEMs) were assessed over the Altiplano watershed in South America using ICESat/GLAS data (Ice, Cloud and Land Elevation Satellite/Geoscience Laser Altimeter System). On the global scale, GDEM v2 is more accurate than SRTM v4, which presents a negative bias of approximately 8.8 m. Strong correlations between the DEMs' accuracies and mean slope values occurred. Regarding land cover, SRTM v4 could be more accurate or easier to correct on a smaller scale than GDEM v2. Finally, a merged and corrected DEM that considers all of these observations was built to provide more accurate information for this region. The new model featured lower absolute mean errors, standard deviations, and root mean square errors relative to SRTM v4 or GDEM v2.

1. Introduction

Digital elevation models (DEMs) are widely used in geological, glaciological, and hydrological studies. In hydrological studies, DEMs are used to extract watershed and drainage systems using numerical methods (Jenson and Domingue 1988; Mackay and Band 1998; Martz and Garbrecht 1999; O'callaghan and Mark 1984; Planchon and Darboux 2002 among others) that rely on cell-to-cell slope to retrieve the flow direction.

In large and poorly monitored areas, the topography may be extracted from DEMs based on remotely sensed observations, such as SRTM Shuttle Radar Topography Mission) (Farr et al. 2007) and GDEM (Global Digital Elevation Model) (ASTER GDEM Validation Team 2009), which offer nearly global coverage. Spaceborne interferometric synthetic aperture radar (SAR) technology was used to acquire the SRTM elevation data. In addition, InSAR equipment obtained a nearly global

---

*Corresponding author. Email: frederic.satge@gmail.com

elevation dataset [60° N to 56°S] with a spatial resolution of 30 m × 30 m and a global vertical precision of 16 m. However, several studies have reported errors, particularly related to vegetation (Sun et al. 2003). Stereo-pair images obtained in the visible and near-infrared (VNIR) bands collected by the ASTER instrument were used to generate a GDEM elevation dataset [83° N to 83° S]. One of the drawbacks of this technology is its sensitivity to clouds and the presence of bump and pit artefacts (Arefi and Reinartz 2011).

In case of an inaccurate DEM, numerical algorithms may fail or lead to erroneous flow direction; as a result, unrealistic hydrological analysis may occur (Tsanis et al. 2013). DEM accuracy is particularly crucial in flat regions (Getirana et al. 2009).

Elevation datasets for specific regions around the world have been analysed in numerous studies. One commonly used method is to compare the DEM with high-quality ground control points (GCPs). The GCPs can be obtained using global positioning system (GPS) measurements (Hirt, Filmer, and Featherstone 2010; Zhao et al. 2011), topographic maps (Zhao et al. 2011), or high-quality radar altimetry data, such as ICESat/GLAS (Billemont 2010; Carabajal et al. 2011; Ensle, Heinzel, and Koch 2012; Zhao, Xue, and Ling 2010). Alternatively, remotely sensed DEMs can be compared with high-quality DEMs (Forkuor and Maathuis 2012; Sertel 2010). Based on one of these two methodologies, several studies have already addressed the evaluation of the first version of GDEM (v1) and various SRTM products in different regions of the world, including Turkey (Sertel 2010), China (G. Zhao, Xue, and Ling 2010; Zhao et al. 2011), Australia (Hirt, Filmer, and Featherstone 2010), and Ghana (Forkuor and Maathuis 2012) (Table 1). In these studies, good agreement was generally observed between the remotely sensed DEMs and the ground truth data.

Since October 2011, a new GDEM version (GDEM v2) has been freely available to the public (https://reverb.echo.nasa.gov). Apart from the studies led by the GDEM v2 team on a global scale (Carabajal 2011) and across the USA (Gesch et al. 2011), only a few studies have addressed the accuracy of GDEM v2. Assessments have been conducted in Germany (Ensle, Heinzel, and Koch 2012), China (Li et al. 2012), and Indonesia (Suwandana et al. 2012) (Table 1). Based on these studies, GDEM v2 is generally more suitable than GDEM v1. However, this suitability is not evident based on comparisons with SRTM products. More suitable DEMs depend on the region and final purpose. Thus, the accuracy of GDEM v2 is still debated, and its evaluation in different regions of the world remains of interest to the scientific community.

As reported in many previous studies, a DEM's horizontal accuracy may range from a few metres to hundreds of metres (Table 2). The horizontal accuracy is important for understanding and interpreting the vertical accuracy (Nikolakopoulos, Kamaratakis, and Chrysoulakis 2006). Horizontal accuracy assessments have been provided for various GDEM and SRTM versions in different regions of the world.

Generally, the horizontal offset between DEMs is represented by a sub-pixel length and could be absent (Hirt, Filmer, and Featherstone 2010). The high values found by Nikolakopoulos, Kamaratakis, and Chrysoulakis (2006) could be linked to the old version of the ASTER-derived DEM that was assessed in this study. In the event of horizontal bias, a DEM could provide good elevation data that are associated with the wrong locations; thus, the DEM is inaccurate. Based on this hypothesis, the horizontal shift estimation represents a primordial step in the evaluation of DEM accuracy.

Table 1. Summary of previous studies focused on GDEM v1, GDEM v2, and various SRTM products' horizontal accuracy.

Authors	DEMs assessed	GCPs used	Results
Zhao et al. (2011)	GDEM v1/SRTM v4	Derived from topographic Map	In Loess plateau, GDEM v1 and SRTM v4 accuracies are similar whereas in North China Plain SRTM v4 is more accurate than GDEM v1.
Sertel (2010)	GDEM v1	DEM generated from topographic maps	GDEM v1 is found suitable to characterize topography in Turkey.
Hirt, Filmer, and Featherstone (2010)	GDEM v1/SRTM v4/GEODATA DEM-9S ver3	GPS	Better accuracy for SRTM v4 and GEODATA DEM-9S ver3. GDEM v1 should be improved as was done for the SRTM previous version.
Zhao, Xue, and Ling (2010)	GDEM v1	ICESat/GLAS/SRTM v2/SRTM v4	GDEM v1 performs better in flat regions than in mountainous areas. GDEM v1 presents fewer voids than SRTM v2 but presents many artefacts.
Forkuor and Maathuis (2012)	GDEM v1/SRTM v4	DEM generated from topographic maps	Better vertical accuracy is found for SRTM v4, which tends to overestimate elevation while GDEM v1 underestimates it. SRTM v4 is found more suitable for hydrological applications.
Billemont (2010)	GDEM v1/GDEM v2	ICESat/GLAS	GDEM v1 accuracy is very good in flat regions and decreases with increasing mean slope. The presence of artefacts alters GDEM v1 accuracy.
Carabajal et al. (2011)	GDEM v2/SRTM v2	ICESat/GLAS	Regarding global statistics, over South America, SRTM v2 and GDEM v2 seem to be in pretty good agreement.
Li et al. (2012)	GDEM v2/GDEM v1/SRTM v4	GPS/SRTM v4	Lower values of both RMS and mean difference are found for GDEM v2 than for GDEM v1 and SRTM v4.
Ensle, Heinzel, and Koch (2012)	GDEM v2/SRTM v4/SRTM 25	ICESat/GLAS	The better DEM for mountainous areas is the GDEM v2 whereas SRTM products are more suitable for flat areas.
Suwandana et al. (2012)	GDEM v2/SRTM v4	GPS/ DEM generated from topographic maps	SRTM v4 is more accurate in terms of elevation but GDEM v2 remains more suitable for inundation area delimitation.
Gesch et al. (2011)	GDEM v1/ GDEM v2 /SRTM 1/NED	GPS	GDEM v2 shows a global enhancement in comparison with GDEM v1. NED is the more accurate DEM following SRTM.

Table 2. Summary of previous studies focused on horizontal offset estimation between DEMs.

Authors	Regions	DEMs assessed	Absolute mean west/east shift	Absolute mean north/south shift
Nikolakopoulos, Kamaratakis, and Chrysoulakis (2006)	Greece	DEM derived from ASTER/ SRTM 3	6.66″ (200 m)	13.33″ (400 m)
Reuter, Nelson, and Jarvis (2007)	4 GDEM v1 tiles over the world: N05W02, N40E023, N14W087, N45E008 and S02W079	GDEM v1/ SRTM 3	<1″ (<30 m)	<1″ (<30 m)
Hirt, Filmer, and Featherstone (2010)	Australia	GDEM v1/ SRTM v4	0″ (0 m)	0″ (0 m)
Tachikawa et al. (2011)	Japan	GDEM v2/GSI (Geographical Survey Institute) DEM	0.13″ (3.9 m)	0.19″ (5.7 m)
NGA (National Geospatial-Intelligence Agency)	284 GDEM v2 tiles over 20 sites over the world	SRTM DTED2/ GDEM v2	0.104″ (3.12 m)	0.175″ (5.25 m)

In the present study, we have evaluated SRTM v4 and GDEM v2 for the Altiplano watershed region in South America. This region includes emblematic ecosystems, such as Lake Titicaca and Poopó Lake. The water resources in this region are under increasing anthropic pressure with several conflicting uses by the international boundary watershed countries (Molina Carpio, Cruz, and Alurralde 2012; Urquidi Barrau 2012) and mining areas (Moran 2009; Molina Carpio 2007). The regional topography is very flat, but the areas are surrounded by the two highest mountain ranges (cordilleras) in South America. The best available topographic information for the Altiplano region consists of topographic maps (1:50 000) from the IGMB (Instituto Geográfico Militar Bolivia). The Altiplano watershed includes three countries (Bolivia, Peru, and Chile) with their own topographic information sources. These information sources may not be consistent with each other due to their different information processing methods, resolutions, and formats. Consequently, the compilation of topographic data is a difficult task that can be easily bypassed using a DEM.

Thus, a quality assessment of the available DEMs is crucial before considering regional hydrological modelling. Our methodology is based on using the ICESat/GLAS data as GCPs for comparison purposes at the basin scale. In addition, our method considers different ranges of slope and land cover, and provides a general framework for DEM quality assessments in large and remote regions.

2. Materials

2.1. Study area

The Altiplano watershed is an endorheic system located between latitudes of 22° S and 14° S and longitudes of 71° W and 66° W, with a total area of approximately 192,390 km^2. The Altiplano watershed is shared by three countries, Bolivia (70%), Peru (26%), and Chile (4%). The climate of this region is semi-arid with low precipitation, and the total amount varies strongly between the north (approximately 750 mm year^{-1}) and south (160 mm year^{-1}) (Condom et al. 2004). The elevation dataset was generated using 33 GDEM v2 tiles for the GDEM version and 5 SRTM v4 tiles for the SRTM version. The elevations of the region varied between 3500 and 6500 m, with a mean elevation of 4700 m. The region includes the TDPS system, which is composed of Lake Titicaca, the Desaguadero River, Poopó Lake, and the Coipasa Salt Pan (or Salar) Basin. The lowest elevations are mainly located in the southern portion of the region and in the floodplain of the Desaguadero River. This river serves as a surficial connection between Lake Titicaca in the north and Uru-Uru and Poopó lakes in the central portion of the basin. The Altiplano Plateau is a very flat region with a mean slope value of approximately 2°. High reliefs are found in two cordilleras (Occidental and Royal) that form the western and eastern borders, respectively, of the watershed. In addition, our study area includes Uyuni Salar, which is located south of the TDPS system but is not part of the same watershed (Figure 1).

2.2. SRTM version 4

The SRTM is a joint product of the National Geospatial-Intelligence Agency (NGA) and the National Aeronautics and Space Administration (NASA). Data were collected over 11 days in February 2000 using dual spaceborne imaging radar (SIR-C) and dual X-band synthetic aperture radar (X-SAR). From these data, a near-global DEM was generated that spanned 60° N to 56° S. The SRTM DEM data featured two different resolutions. One dataset featured a resolution of 1 arc-second (30 m near the equator) (SRTM1) and was only available for the USA, and the other featured a resolution of 3 arc-seconds (90 m near the equator) (SRTM3). These products were released in 2003 by the United States Geological Survey (USGS) and have been freely available to the public since September 2003.

Since their release, the quality of SRTM3 has progressively improved. The SRTM research team made several improvements to the first version by correcting spurious points, such as spikes and wells, and has aimed to better represent waterbodies and coastlines. A second version was released in 2006 that is still freely available on the USGS website (USGS 2014). The absolute vertical error is 12.6 m in South America for SRTM3 (Rodríguez, Morris, and Belz 2006). More recently, the Consortium for Spatial Information (CSI) of the Consultative Group of International Agricultural Research (CGIAR) released the last official version of SRTM3, which includes several additional improvements (Jarvis et al. 2008). Particularly, the interpolation method described by Reuter, Nelson, and Jarvis (2007), in combination with an auxiliary DEM, allowed the remaining data gaps to be filled. The definition of the waterbodies and coastlines was clarified using the Shorelines and Water Bodies Database (SWBD) produced by the USGS (2003). The final product (SRTM v4) was released in August 2008 and is freely available on the USGS website (CGIAR 2014). The data are delivered in tiles of 5° by 5° that are referenced to the WGS84 ellipsoid and the

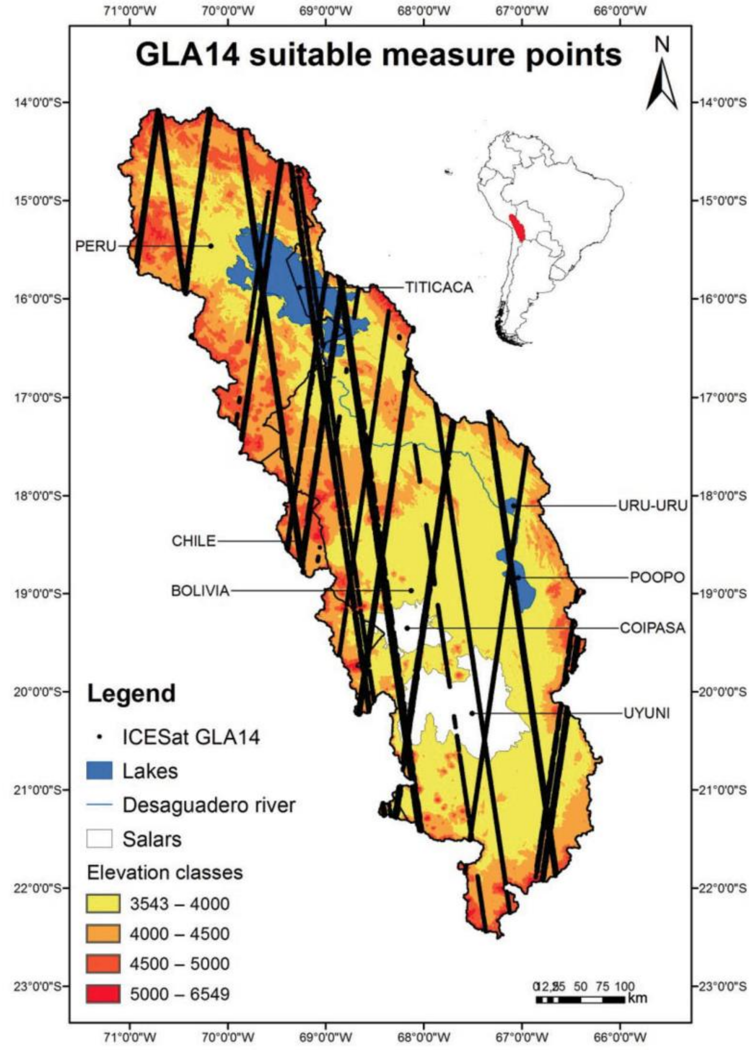

Figure 1. Study area.

EGM96 geoid. Because this version is the last result of a long enhancement process that began with the release of the first SRTM3 version in 2003, SRTM v4 was chosen for this study.

2.3. *ASTER GDEM version 2*

The ASTER GDEM was jointly developed by the Ministry of Economy, Trade, and Industry (METI) of Japan and NASA. Approximately 1,200,000 scenes of stereoscopic data were collected by the advanced spaceborne thermal emission and reflection radiometer (ASTER) aboard the NASA Terra spacecraft. These data were used to develop a DEM known as GDEM version 1 (GDEM v1). This freely available version was released in June 2009 with a horizontal resolution of 1 arc-second (30 m near the equator) and covered land between 83° N and 83° S. However, according to the ASTER validation team, GDEM v1 should be considered at the research level (ASTER Global DEM Validation 2009), and methodologies have been developed to improve its quality (Arefi and Reinartz 2011). A second version (GDEM v2) was developed by the ASTER GDEM research team. This version relies on a larger number of stereoscopic scenes than the first version (260,000 more scenes have been used). Zhao, Xue, and Ling (2010) showed that the accuracy of GDEM v1 was better for areas where more scenes were used for its production. Consequently, we could expect an accuracy enhancement in this new version. In addition, this practice led to a significant decrease in the number of anomalies and artefacts, such as residual clouds, bumps, and pits occurring in GDEM v1. In some areas, the artefacts were entirely eliminated (Tachikawa et al. 2011). In addition to the higher number of scenes, a smaller correlation kernel was used (5 × 5 vs. 9 × 9 pixels) to yield higher spatial resolution. An improved water mask enabled a more accurate definition of the water surface. Finally, the negative overall bias that was estimated by Zhao et al. (2011) and the ASTER GDEM team to equal approximately 5 m was removed. Overall accuracy shifted from 20 to 17 m at 95% confidence level (ASTER GDEM Validation Team: USGS/EROS METI/ERSDAC NASA/LPDAAC 2009). The GDEM v2 was released on 17 October 2011 and is freely available on the NASA website (NASA 2014b). The data are delivered in tiles of 1° by 1° that are referenced to the WGS84 ellipsoid and EGM96 geoid.

2.4. ICESat/GLAS

The ICESat/GLAS data were produced by NASA. The data were collected between 12 January 2003 and 11 October 2009 by the geoscience laser altimeter system (GLAS) aboard the Ice Cloud and Land Elevation Satellite (ICESat). The footprint size is approximately 70 m, and the inter-track spacing is 30 km (near the equator). The elevation was calculated every 172 m for each track. The altimeter measures the two-way travel time of a pulse that is reflected by the ground. The height is determined by considering the actual velocity of the signal due to propagation in the atmosphere. The ICESat/GLAS mission was initially launched for monitoring the icecaps. This mission had a nearly global coverage, and many studies have considered its capability for monitoring other types of land cover. For example, in Bolivia, Fricker et al. (2005) assessed the performance of the ICESat/GLAS over the Uyuni Salar. The data were compared to a local DEM that was derived from kinematic GPS measurements. The absolute vertical accuracy was within 2 cm over the salar. Baghdadi et al. (2011) demonstrated the satellite's ability for monitoring a French lake with a vertical accuracy of 5 cm relative to automatic *in situ* water-level measurements. Zwally et al. (2002) showed that the vertical accuracy was approximately 15 cm under good conditions at the global scale. Regarding the absolute height error of 12.6 m in South America for SRTM3 and an overall accuracy of 17 m at the 95% confidence level for GDEM v2, the accuracy of ICESat/GLAS can be used as GCPs data. The data are referenced to the TOPEX/Poseidon ellipsoid and EGM96 geoid and can be downloaded through the NASA website (NASA 2014b). The National Snow and Ice Data Centre (NSIDC) provides an IDL routine for reading ICESat/GLAS data and for extracting information in an easy array format with the latitude, longitude, elevation and geoid of each measured point. Thus, this script was used in this study.

Various ICESat/GLAS products are available. These products are referenced from GLA01 to GLA15, and each one is more suitable for a specific task. For this study, we used the latest release (v33) of the GLA14 Global Land-Surface Altimeter data, which is specifically for land-surface elevations (referred to as GLA14 hereafter).

2.5. GlobCover Land Cover

With a spatial resolution of 1 km at the equator, the Vegetation Map of Latin America over South America (Eva et al. 2002) was the first accurate description for land cover over this area. Recently, the European Space Agency (ESA) with the help of the Joint Research Center, European Environmental Agency, Food and Agriculture Organization of the United Nations (FAO), United Nations Environment Programme (UNEP), Global Observation for Forest Cover and Land Dynamics, and International Geosphere–Biosphere Programme developed the GlobCover Land Cover (GCLC). This product is the result of an interpretation of data collected by the ENVISAT Medium Resolution Imaging Spectrometer (ENVISAT-MERIS) between 1 December 2004 and 30 June 2006. With a spatial resolution of 300 m, the GCLC presents the most accurate description of land cover ever released. The classification was performed according to the Land Cover Classification System (LCCS) and was developed jointly by the FAO and the UNEP. Overall, 22 different classes are described. Over South America, a more detailed classification based on accurate regional observations is also available. The number of descriptions increases from 22 classes to 52 (Bicheron et al. 2008). The data are freely available on the ESA website (ESA 2014) and are referenced to the GRS80 ellipsoid of WGS84. Due to its greater accuracy, this dataset was used in this study. The study area counts with 22 classes from the 52 defined for South America.

The three most represented classes are bare areas (31%), closed to open shrubland (17%), and sparse vegetation (16%). These classes represent 64% of the entire coverage. According to the GCLC class distribution, the Altiplano can be described as a desert region with only a few urbanized areas (0.1%), and waterbodies and salt areas account for considerable percentages (3.5% and 5.3%, respectively) of the entire surface area.

3. Data processing

3.1. Preprocessing of DEM data and GPCs selection

The first step consisted of referencing all elevation data to the same ellipsoid and geoid systems. The SRTM v4 and GDEM v2 data are referenced to the same ellipsoid (GRS80 of WGS84) and geoid (EGM96). However, the ICESat/GLAS dataset is referenced to the T/P ellipsoid. To make the references coherent between the three elevation products, we used the NSIDC-provided IDL tool called 'IDL Ellipsoid Conversion', which enables the conversion of the GLA14 array of latitude and elevation from T/P to WGS84 (NSDIC 2014). At each ICESat/GLAS measurement location, the EGM96 was computed using the interpolation program available on the NGA website (NGA 2014) and subtracted from the GLA14 elevation to obtain the GLA14 value referenced to the same system (WGS84/EGM96) as GDEM v2 and SRTM v4. Using a two-dimensional linear interpolation tool available in Matlab software, the elevation of each DEM was computed for all GLA14 points.

Overall, 381,289 GLA014 points are available in the study region. The NSIDC provides quality control based on several flags from which we selected four as follows:

I_elvuseFlg: indicates whether the value should be used or not. Only the data with this flag set 'on' were selected.

I_FRir_gaFlg: indicates the presence of clouds. Only the data with this flag set 'off' were selected.

I_rng_UQF: indicates the quality of the flags. Only the data with good flag quality were selected.

I_satCorrFlg: indicates whether saturation phenomenon occurred during the acquisition and if it was corrected. Only the non-saturated data were selected.

Approximately 50% of the points were unreliable based on the quality control results provided by NSIDC, demonstrating that the quality control is necessary. Thus, 183,713 data points were kept. Another flag called '*i_DEM_hires_elv*' was used by Ensle, Heinzel, and Koch (2012) to remove the ICESat/GLAS data with absolute differences of more than 100 m with respect to a high-quality DEM. Following a similar approach, we computed the absolute difference between GLA14 for both SRTM v4 and GDEM v2 data. Overall, the 116 GCPs had an absolute difference of 100 m or more in comparison to the two DEMs, and 654 GCPs had an absolute difference of 50 m. Considering the small proportions of these data points, we kept the 50 m threshold to ensure a very-high-quality GCP database. The repetitive cycle of ICESat can lead to numerous measurements at the same location. Only one measurement based on location was kept for the database. Because the precision of ICESat is approximately 15 cm and the precisions of GDEM v2 and SRTM v4 are approximately 17 m and 12.6 m, respectively, such a selection will not affect this comparison. According to these criteria, we recorded a data decrease from 183,059 to 157,254 points. The GCLC class was extracted, and the mean slope was computed using the ArcGIS Spatial Analyst tool for each GCP location. Ultimately, the constructed database contained the latitude and longitude, the GLA14, GDEM v2, and SRTM v4 elevations, and the GCLC class and mean slope values for each selected GLA14 point.

3.2. Horizontal accuracy assessment

Our study area includes 33 GDEM v2 tiles and five SRTM v4 tiles. In some of these tiles, only a few square kilometres were included in the TDPS watershed. The horizontal accuracy assessment was applied to only 21 GDEM v2 tiles with at least 50% of their area within the Altiplano watershed. The total considered area included 210,000 km^2 and covered 84% of the study area. First, we set the two DEMs to the same spatial resolution. The 3″ resolution of SRTM v4 was kept, and we aggregated the GDEM v2 pixels from the original 1″ resolution to the 3″ resolution by computing the mean value of the nine original cells. For each GDEM v2 tile and SRTM v4 tile, we extracted six elevation profiles, three east–west profiles, and three north–south profiles (Figure 2).

Second, assuming that the elevation between two successive DEM points follows a linear equation, the variation in the horizontal position of an elevation increment of 1 m was computed for both DEMs (Figure 3) along each profile. Then, along each profile, the same elevation for both DEMs was detected and the mean horizontal shift was computed. Finally, a mean horizontal shift was computed for both directions by considering all profiles.

ICESat does not present continuous measurements along its footprint; the measurement points are spaced 175 m apart, and some of them are missing due to the quality assessment.

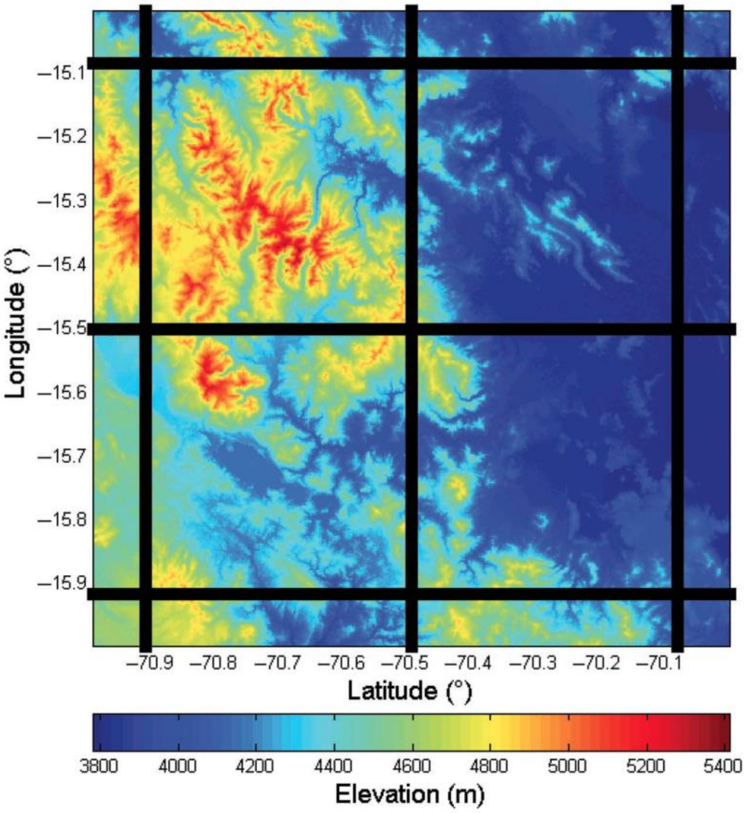

Figure 2. Aggregated GDEM v2 tile with transect locations.

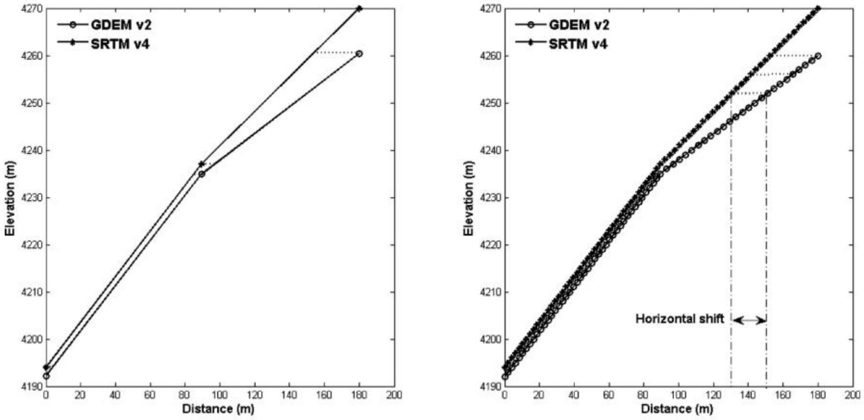

Figure 3. Original elevation profile on the left and elevation profile with increment computation of 1 m to the right.

To assess the DEMs' horizontal shift compared to the GCPs, we extracted eight elevation profiles from an area where the ICESat data were the most homogeneous, with four profiles oriented northwest–southeast and four oriented northeast–southwest.

3.3. Vertical accuracy assessment

To assess the DEMs' qualities, we computed different statistical parameters, including the absolute mean error (AME), standard deviation (STD), and root mean square error (RMSE) (Equations (1)–(3)).

$$\mathrm{STD} = \sqrt{\frac{1}{n-1}\sum_{i=1}^{n}\left[(x_i - y_i) - (\overline{x-y})\right]^2}, \tag{1}$$

$$AME = \sum_{1}^{n}\left|(x_i - y_i)\right|, \tag{2}$$

$$RMSE = \sqrt{\frac{\sum_{i=1}^{n}\left[(x_i - y_i)^2\right]}{n}}, \tag{3}$$

where n is the number of values; x is the GLA14 value in metres; and y is the DEM value in metres.

This assessment was first performed at a regional scale and considered all available comparison points. However, a global assessment cannot indicate the limitations of DEMs due to their acquisition mode. In rugged regions, the SAR interferometry used to construct the SRTM DEM may fail because the radar backscatter is disrupted in mountainous areas. Because the elevation calculation is based on the delay between emissions and reception, we could expect DEM inconsistencies in such regions. In addition, problems can occur with the GDEM v2 data during the interpretation step of the scenes used for DEM construction due to, for example, shading effects. Consequently, the slope and land use could represent potential influence factors on DEM quality. Therefore, we assessed the DEMs' accuracy with regard to the mean slope value and land cover.

The Altiplano is a very flat region, where 67% of the measured points have a slope value less than or equal to 5°, but there are also areas with rough relief.

To assess the DEMs' accuracy as a function of the mean slope, we developed a frequency histogram based on the mean slope value (Table 3). The first and second intervals account for approximately 55% and 16%, respectively, of the entire dataset. The third and fourth intervals account for approximately 14% and 13%, respectively, of the dataset. The fifth interval accounts for only 2% of the dataset.

To assess the DEMs' quality as a function of the land cover, we selected the six most representative land-cover classes (bare areas, sparse vegetation, closed to open shrubland, mosaic grassland/forest-shrubland, mosaic forest-shrubland/grassland, and waterbodies) and two additional classes (salt hardpans and permanent snow and ice) for their physical particularities. A field investigation showed inconsistencies in the GCLC classifications for these two last classes. Below an altitude of 4500 m, many salt areas were defined as permanent snow and ice instead of as salt hardpans. No permanent snow or ice was found at this elevation in this region. To remain near the ground truth data, we merged these two classes into a single class, salt hardpans, below 4500 m. First, we accounted for all of the GCPs to compute the

Table 3. Computed AME, STD, and RMSE value for GDEM V2 and STMV4 in function of slope ranges.

			AME (m)			STD (m)			RMSE (m)		
Classes (°)	Number of points	Area (%)	GDEM v2	SRTM v4	MERGE DEM	GDEM v2	SRTM v4	MERGE DEM	GDEM v2	SRTM v4	MERGE DEM
0–2	86,595	55	5.2	7.2	3.7	6.6	4.1	5.3	6.6	8.1	5.3
2–5	24,583	16	6.0	8.5	6.0	8.0	6.8	8.0	8.0	10.2	8.0
5–10	22,143	14	7.8	9.9	7.8	10.2	10.5	10.2	10.2	12.6	10.2
10–20	20,144	13	10.8	13.4	10.8	13.8	15.6	13.8	13.9	16.9	13.9
>20	3789	2	14.6	17.0	14.6	18.0	20.7	18.0	18.2	21.1	18.2
TOTAL	1,57,254	100	**6.6**	**8.8**	**5.8**	**9.0**	**8.6**	**8.5**	**9.0**	**11.1**	**8.6**

AME, STD, and RMSE for these eight classes. Then, to avoid any influences of the mean slope values, the STD and RMSE were computed for the GCPs with mean slope values between 0° and 2° and for the GCPs with mean slope values of between 10° and 15°. For this second step, the classes were ordered as follows according to the GCLC classification system from the sparser and lower classes to the denser and higher classes: bare areas, sparse vegetation, mosaic grassland/forest shrubland, closed to open shrubland, and mosaic forest-shrubland/grassland. These categories are numbered 1 to 5 in Figure 9. Because of their particularities, salt hardpans and waterbodies were not considered (Table 4).

4. Results and discussion

4.1. Horizontal accuracy

From a visual perspective, no significant horizontal shift was observed between the DEMs. Regarding the bias computation from the elevation profiles with respect to SRTM v4, GDEM v2 shifted by an average of 13.3 m (0.44′) east–west and 2.5 m (0.08′) north–south. For example, a GDEM v2 shift of 0.104′ (east–west) and 0.175′ (north–south) was observed relative to SRTM DTED2 (Tachikawa et al. 2011). This difference could be linked to the use of a different DEM as the reference and due to the use of a homogenous region when comparing the 20 sites around the world studied by Tachikawa et al. (2011).

As described in Section 3, the horizontal shift with respect to the GCPs was computed along 8 profiles. We computed mean average shifts of 5.1 and 2.8 m for GDEM v2 and 3.7 and −7.3 m for SRTM v4 in the northeast–southwest and northwest–southeast directions, respectively.

The shift values between the two DEMs and the DEMs with respect to the GCPs remained lower than the DEM resolutions and consequently should not have a significant effect on the vertical assessment of this study.

4.2. Regional Altiplano scale

Overall, 157,254 GLA14 points are available to assess the DEMs' quality in the study area. A significant negative bias was found when comparing the GLA14 and SRTM V4 elevations, with approximately 140,000 negative differences between the two series (Figure 4). The differences are better distributed around zero when comparing with the GDEM v2 and GLA14 elevation series.

The statistics of the comparisons are reported in Table 3. The AME values between the DEM and GCP elevations were 6.7 and 9.6 m for the GDEM v2 and SRTM V4 products, respectively. The STD is approximately similar for both DEMs, whereas the RMSE is lower for GDEM v2 than for SRTM v4. In previous studies, the RMSE values found for the GDEM v2 products relative to the ICESat data were 6.3 m for Germany (Ensle, Heinzel, and Koch 2012) and 8.8 m for the entirety of South America (Carabajal 2011). A RMSE value of 8.68 m for GDEM v2 was found for the USA in comparison with the GPS benchmark (Gesch et al. 2011). The RMSE computed in this study was similar to the values computed for South America, Germany, and the USA and was lower than the values reported when using GDEM v1. For example, the reported values were 13.1 m (using GPS points as GCPs) and 17.3 m (using ICESat as GCPs) for China and Australia, respectively (Hirt, Filmer, and Featherstone 2010; Zhao, Xue, and Ling 2010). In this case, the GDEM v2 STD was equivalent to the STD of 8.5 m that was computed for South America by Carabajal (2011).

Table 4. Computed AME, STD, and RMSE values for GDEM V2 and STMV4 in function of GCLC classes.

				AME (m)			STD (m)			RMSE (m)		
Classes	Number of points	Area (%)	Mean slope (°)	GDEM v2	SRTM v4	MERGE DEM	GDEM v2	SRTM v4	MERGE DEM	GDEM v2	SRTM v4	MERGE DEM
Bare areas	58,265	31	0.34	5.0	7.6	5.0	7.1	6.1	6.1	7.1	8.9	7.1
Sparse vegetation	22,383	16	7.5	8.1	10.6	8.1	10.9	11.3	11.3	10.9	13.6	10.9
Closed to open shrubland	22,504	17	3.7	7.1	10.7	7.1	9.7	10.1	10.1	9.7	12.9	9.7
Mosaic grassland/ Forest-shrubland	7643	5.7	3.5	6.2	11.6	6.2	8.7	8.6	8.6	8.7	13.3	8.7
Mosaic forest-shrubland/ grassland	7269	4.3	6.0	7.8	10.7	7.8	10.5	10.5	10.5	10.5	13.2	10.5
Salt hardpans	9243	5.3	0.6	5.8	4.8	2.1	8.0	2.5	2.5	8.2	5.3	3.0
Waterbodies	12,363	3.5	0.03	8.5	3.7	0.9	2.4	1.8	1.8	8.8	4.1	2.3

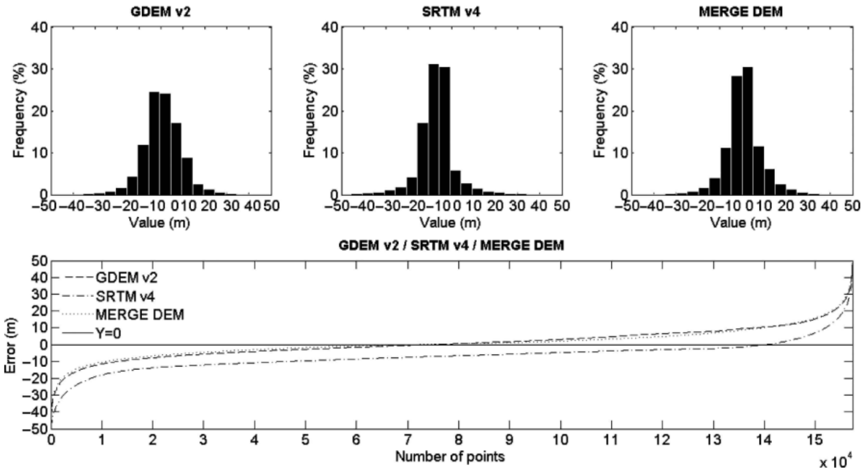

Figure 4. Error distribution of GDEM v2 (top left) and SRTM v4 (top middle) and MERGE DEM (top right) and error distribution of GDEM v2, SRTM v4, and MERGE DEM (bottom).

The good performance of GDEM v2 can be explained by the large number of scenes used in its construction for the Altiplano region. As presented in Carabajal (2011), the study region includes a large number of scenes (between 20 and 60 scenes). Previous studies on the GDEM v1 show that the GDEM v1 quality increases with the number of scenes used (Billemont 2010; Zhao, Xue, and Ling 2010). This result partly explains the good results obtained for GDEM v2.

4.3. Mean slope

As reported in Table 3, the AME increases from 5.2 to 14.6 m for GDEM v2 and from 7.2 to 17.0 m for SRTM v4 but remains lower for GDEM v2. The STD value increased from 6.6 to 18.0 m for GDEM v2 and from 4.1 to 20.7 m for SRTM v4. The regions with gentle relief present a lower STD for SRTM v4. The RMSE values increased from 6.6 to 18.2 m for GDEM v2 and from 8.1 to 21.1 m for SRTM v4. For both DEMs, the AME, STD, and RMSE increased with the mean slope value. The accuracies of the DEMs were clearly linked to the mean slope values (Figure 5).

Regions with low mean slopes presented lower STD and higher RMSE values for SRTM v4. These results are consistent with those obtained for different GCLC classes. The low mean slope areas are primarily bare areas, closed to open shrubland, mosaic grassland/forest-shrubland, salt hardpans, and waterbodies (Table 4). For all of these classes, the STD values were lower for SRTM v4 than for GDEM v2, or the values were very similar for both DEMs. Higher RMSE values were observed for SRTM v4 and for all land-cover classes, except for salt hardpans and waterbodies, which are less representative of the studied regions. Consequently, a lower mean STD and a higher RMSE were observed for the low mean slopes for SRTM v4.

The negative bias of 8.8 m occurred for all classes when comparing the entire GCPs dataset with the SRTM v4 elevations. Because of the small STD and RMSE values of the first two classes, the negative SRTM v4 bias is clearly identifiable in these classes (Figure 6).

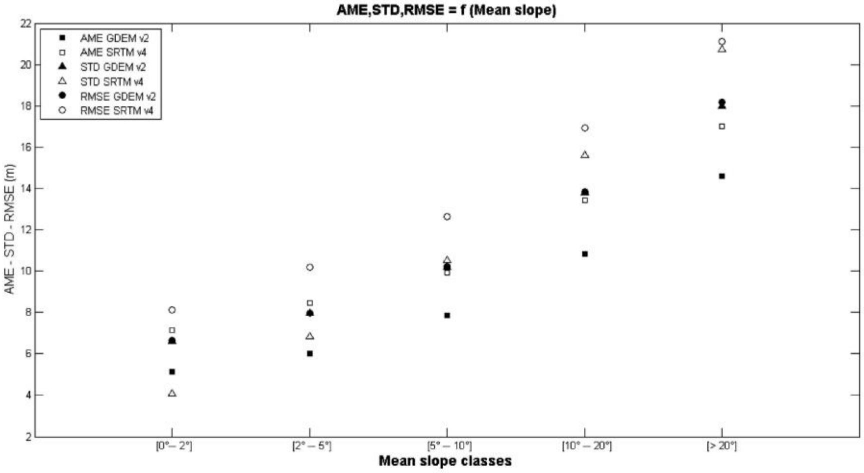

Figure 5. STD (top) and RMSE (bottom) distribution in function of the slope range for SRTM v4 and GDEM v2 DEMs.

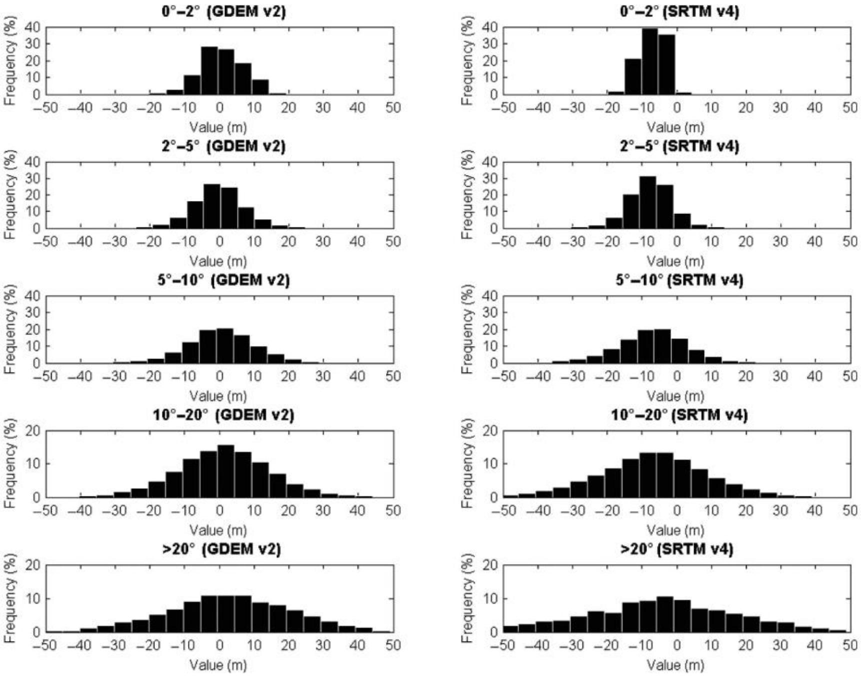

Figure 6. Error distribution for GDEM v2 (left) and SRTM v4 (right) for increasing slope range (from top to bottom).

4.4. Land cover

The negative bias observed for SRTM v4 at the regional scale is confirmed in every type of cover. For salt hardpans and waterbodies classes, the negative bias was very noticeable (Figure 7 and 8).

The AME and RMSE values were lower for GDEM v2 than for SRTM v4, except for the salt hardpans and waterbodies classes. The STD values were lower for SRTM v4, except for sparse vegetation and closed to open shrubland, but the values were very similar to those of GDEM v2 (Table 4).

The bare areas class exhibits lower STD and RMSE values in both DEMs. These results agree with the values computed for the same class in GDEM v2 by Carabajal (2011) through the use of ICESat/GLAS data over South America. Carabajal (2011) observed STD and RMSE values of 7.9 and 8 m, respectively. Slightly better scores were observed in our study (STD and RMSE values of 7.1 m) due to the low mean slope value of this class (approximately 0.34°). As previously shown, the qualities of the DEMs increased as the mean slope values decreased.

For low mean slope values and the GDEM v2 data, no significant correlations were observed between the STD and RMSE values and the GCLC classes. Although more variations were highlighted for the SRTM v4 data for both low and high mean slope values, no correlation was found with the cover type. In both cases, for both DEMs and for all of the land-cover classes, the STD and RMSE values increase

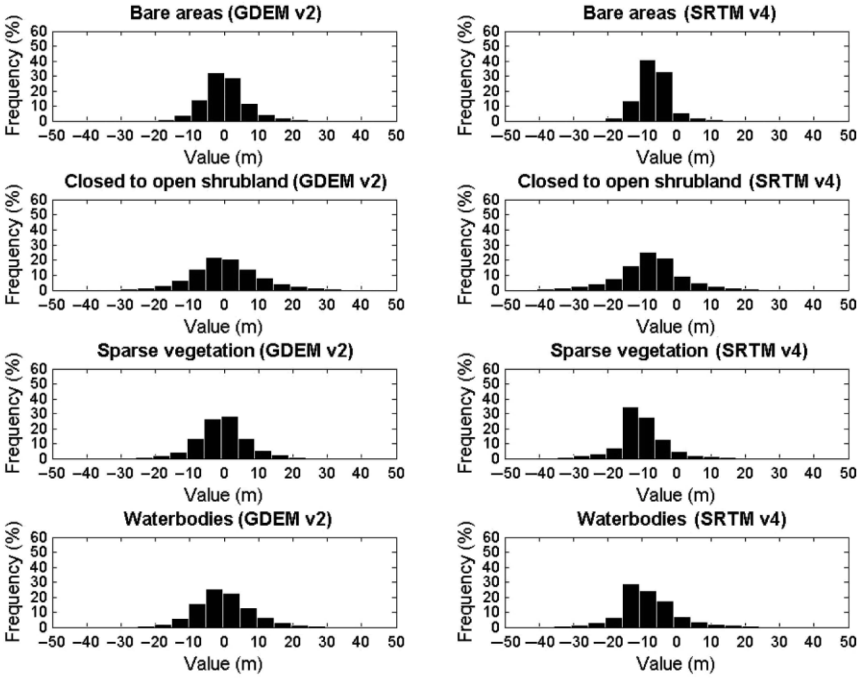

Figure 7. Error distribution for GDEM v2 (left) and SRTM v4 (right) for different land occupation classes (from top to bottom).

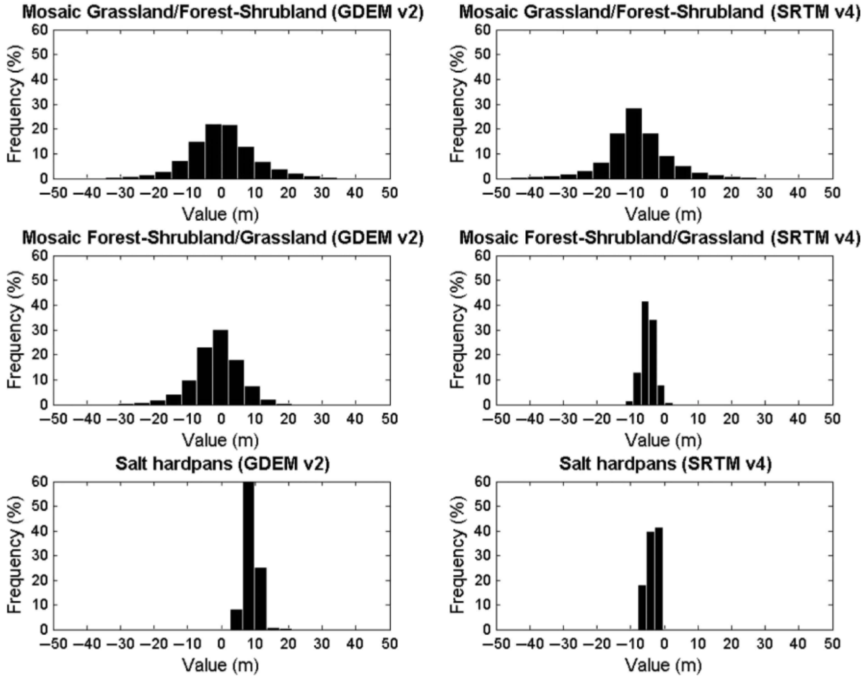

Figure 8. Error distribution for GDEM v2 (left) and SRTM v4 (right) for different land occupation classes (from top to bottom).

considerably as the mean slope values increase (Figure 9). Finally, in the Altiplano region, the DEMs' quality is clearly related to the mean slope value and not to land cover. These results are consistent with the significant homogeneity in land cover that was observed during the field investigation. The entire region could be characterized as a bare to shrub area.

5. Enhancement of SRTM v4 accuracy in specific areas

For SRTM v4, the salt hardpans and waterbodies classes exhibited very small STD values (< 3) and small RMSE values (< 6) (Table 4). Removing the negative bias can enhance the SRTM v4 accuracy for this particular land cover without resulting in additional errors in the data. Due to the hydrological context within this region and the very low slope, these specific areas feature a significant tidal effect. The lake water levels can vary by up to 2 m depending on the season, and the salars can be flooded periodically to a depth of approximately 1 m. The SRTM v4 data were acquired in February 2000, which corresponds to the wet season in this region. Consequently, the high lake water levels were measured, which resulted in negative bias for the lakes and salars. To compute the SRTM v4 bias for these surfaces, we only used the GLA14 data for the dry period to record the low water levels. The dry season occurs between April and October. Unfortunately, the ICESat sensor did not work continuously during this period because of technical problems (NASA 2014a). The data used to compute

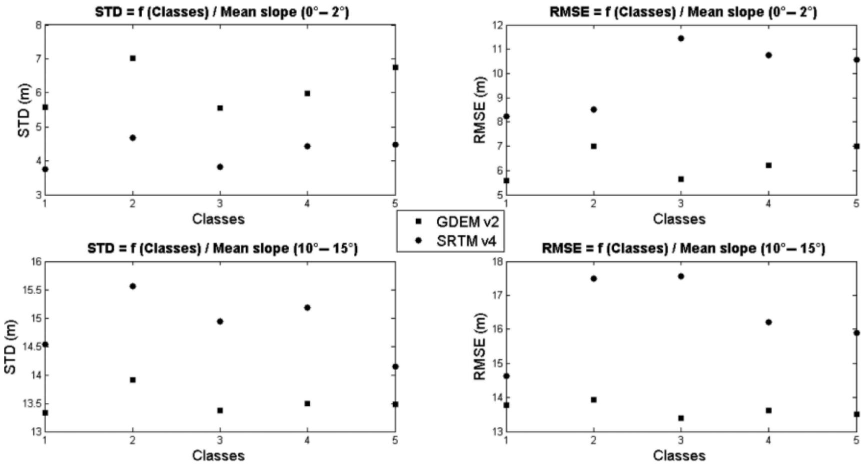

Figure 9. STD (left) and RMSE (right) distribution in function of vegetation height and density for low mean slope value (top) and high mean slope value (bottom) for SRTM v4 and GDEM v2.

the bias on Lake Titicaca, Lake Poopó, and the Uyuni and Coipasa Salars were from the operational periods in May and June.

We removed the computed bias in the SRTM v4 for these specific areas. The resulting 'SRTM v4 corrected' was used for the Titicaca, Poopó, Coipasa, and Uyuni areas, whereas the GDEM v2 was used to characterize all of the other areas. A new DEM (termed MERGE DEM hereafter) was obtained by merging these different areas together. Overall, the GDEM v2 accounted for 90% of the MERGE DEM, whereas the corrected SRTM v4 only represented 10%. To assess the quality of this new DEM, the same statistical approach used for the GDEM v2 and SRTM v4 was used. The results are summarized in Tables 3 and 4.

The AME values were significantly reduced and were well distributed around 0 (Figure 4). In addition, the RMSE and STD values were reduced, and the correction resulted in a considerable improvement. This MERGE DEM appears to be a more accurate product for characterizing the topography of the Altiplano watershed.

The corrected areas were defined by using the GCLC data, which were not very robust. In addition, the GCLC does not represent Lake Uru-Uru as a continuous surface waterbody. Only a few, unconnected pixels were identified as water areas. Consequently, this lake was not considered in this study. Previously, we observed that problems could also occur in the delineation of salt areas. To enhance the definition of the lake and salt areas, high-resolution satellite imagery is more appropriate.

The differences between the MERGE DEM and the GDEM v2 and SRTM v4 varied between −573.5 and 390.5 m (Figure 10). This large variation range could be explained by the presence of artefacts, such as clouds, bumps, and pits, which were also detected in the GDEM v1 (ASTER GDEM Validation Team: USGS/EROS METI/ERSDAC NASA/LPDAAC 2009; Arefi and Reinartz 2011; Jarvis et al. 2008; Hirt, Filmer, and Featherstone 2010) and were not totally removed in the processing method of the GDEM v2 (Tachikawa et al. 2011). Because SRTM v4 does not represent the ground truth data, these differences cannot be attributed in their totality to GDEM v2 deficiencies.

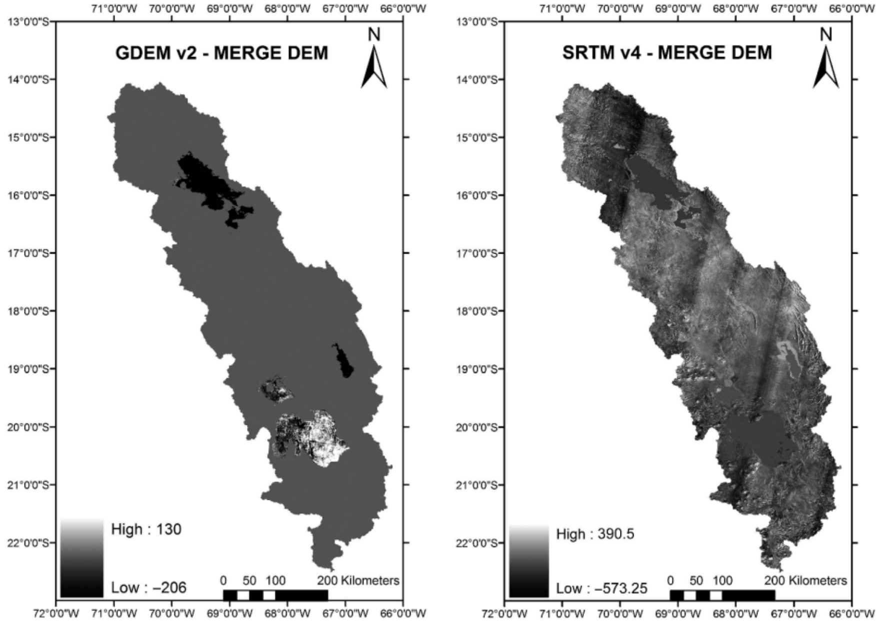

Figure 10. Elevation differences between GDEM v2 and MERGE DEM (left) and between SRTM v4 and MERGE DEM (right).

Due to their small-scale impacts (one to a few pixels), these differences are hardly evidenced through the use of GCPs that consist of point measurements that often do not match these specific areas. Using a high-quality, global-scale dataset, such as a reference DEM, would allow for the characterization of these deficiencies. The method developed by Arefi and Reinartz (2011) to enhance GDEM v1 should be applied to enhance the DEM quality for those specific areas.

6. Conclusions

The quality of the two most commonly used DEMs (SRTM v4 and GDEM v2) was assessed for the Altiplano watershed by using the ICESat/GLAS data as GCPs. A database of approximately 150,000 high-quality GCPs was used. We conducted a quality assessment for each land-cover type encountered in the study area and for different types of relief. A global assessment showed a significantly negative bias in the SRTM v4 data of 8.8 m, whereas the GDEM v2 was well distributed around zero with an AME of 6.6 m. The STD and RMSE values were 9.0 and 9.0 m, respectively; for GDEM v2 and 8.6 and 11.1 m, respectively, for SRTM v4. Although some artefacts were not completely removed from the GDEM v1, the GDEM v2 better represented the topography in this area. A significant correlation occurred between the quality and slope values of the DEMs. The quality decreased when the slope value increased. Considering the techniques that were used in their development, the SRTM v4 should provide information regarding the ground elevation independently of the cover, whereas the GDEM v2 should provide the ground elevation while considering its cover. However, for the Altiplano region, the vegetation did not impact the accuracies of the DEMs. Finally, we demonstrated that correcting the SRTM v4 for negative bias in specific areas (lakes and salars) and merging it with the GDEM v2 values can be an efficient method for better representing the topography of this region.

From a more general perspective, this study highlights the usefulness of the ICESat/GLAS data for evaluating DEMs for use in remote regions. Due to their accuracy and dense spatial coverage, the ICESat/GLAS data are very well suited for this type of assessment because they provide a large dataset of GCPs. As shown here, this large dataset allows users to split the dataset and combine it with land-cover products to investigate the accuracy of the DEM over several ranges of slope and land-cover type while maintaining a sufficiently large dataset for statistical evaluation.

However, this study is the first step in assessing two commonly used DEMs. The study focuses on horizontal and vertical accuracy using point comparisons. Based on the performance of GDEM v2 and the new MERGE DEM, these DEMs better represent the topography of the TDPS. However, users must remember that this study focused on a point-to-point comparison and does not consider relationships between neighbouring pixels. If an elevation pixel is greater than or lower than the surrounding elevation pixels while the truth data are the opposite, an incorrect topographic shape will result. Hydrological applications are based on mean slope calculations, which involve global topography computations. Even if certain local corrections are possible, errors could remain and result in poor hydrological network extraction and incorrect watershed delimitation. The performances of DEMs in a hydrological application are not linked to the mean elevation error but to the good relative elevation between the pixels. Future DEM studies should focus on this point. However, reference data for the Altiplano are currently missing, which would make such a study difficult. High-quality DEMs, a hydrological network, or watershed delimitation could be used as reference data to compare and assess the results obtained from remotely sensed DEMs.

Acknowledgements

This work was supported by the Centre National d'Etudes Spatiales (CNES) in the framework of the HASM project (Hydrology of Altiplano: from Spatial to Modeling). The work presented here is based on observations with the GLAS instrument aboard the ICESat mission. The first author is grateful to the IRD (Institut de Recherche pour le Développement) and the CAPES (Coordenação de Aperfeiçoamento de Pessoal de Nível Superior) Brazil for their financial support. Note that the three DEMs (SRTM v4, GDEM v2 and MERGE) are freely available to the scientific community upon request.

References

Arefi, H., and P. Reinartz. 2011. "Accuracy Enhancement of ASTER Global Digital Elevation Models Using ICESat Data." *Remote Sensing* 3 (7): 1323–1343. doi:10.3390/rs3071323.

ASTER GDEM Validation Team: USGS/EROS METI/ERSDAC NASA/LPDAAC. 2009. "ASTER Global DEM Validation Summary Report." https://lpdaac.usgs.gov/sites/default/files/public/aster/docs/ASTER_GDEM_Validation_Summary_Report.pdf

Baghdadi, N., N. Lemarquand, H. Abdallah, and J. S. Bailly. 2011. "The Relevance of GLAS/ICESat Elevation Data for the Monitoring of River Networks." *Remote Sensing* 3 (12): 708–720. doi:10.3390/rs3040708.

Bicheron, P., P. Defourny, C. Brockmann, L. Schouten, C. Vancutsem, M. Huc, S. Bontemps, M. Leroy, F. Achard, M. Herold, F. Ranera, and O. Arino. 2008. "GLOBCOVER Products Report Description and Validation Report." http://due.esrin.esa.int/globcover/LandCover_V2.2/GLOBCOVER_Products_Description_Validation_Report_I2.1.pdf

Billemont, S. 2010. “Validation of ASTER GDEM over Tibet.” *Rapport de recherché*, Delft University of Technology.

Carabajal, C. C. 2011. “ASTER Global DEM Version 2 0 Evaluation using ICESat Geodetic Ground Control.” Report to the ASTER GDEM Version 2 Validation Team. http://www.jspacesystems.or.jp/ersdac/GDEM/ver2 Validation/Appendix_D_ICESat_GDEM2_validation_report.pdf

Carabajal, C. C., D. J. Hardingb, J.-P. Boyc, J. J. Danielson, D. Geschd, and V. P. Suchdeo. 2011. “Evaluation of the Global Multi-Resolution Terrain Elevation Data 2010 (GMTED2010) Using ICESat Geodetic Control.” International Symposium on Lidar and Radar Mapping: Technologies and Applications (LIDAR & RADAR 2011), Nanjing, October 24. doi:10.1117/12.912776.

CGIAR. 2014. “CGIAR.” http://srtm.csi.cgiar.org/

Condom, T., A. Coudrain, A. Dezetter, D. Brunstein, F. Delclaux, and J. E. Sicart. 2004. “Transient Modelling of Lacustrine Regressions: Two Case Studies from the Andean Altiplano.” *Hydrological Processes* 18 (13): 2395–2408. doi:10.1002/hyp.1470.

Ensle, F., J. Heinzel, and B. Koch. 2012. “Evaluating Height Differences between Global Digital Surface Models and ICESat Heights at Footprint Geolocation.” In *GIS Ostrava 2012: Surface Models for Geosciences*, edited by J. Ruzika and K. Ruzickova, January 23–25, 37–48. Ostrava: VŠB Technical University of Ostrava. ISBN 978-80-248-2667-7.

ESA. 2014. http://www.esa.int/Our_Activities/Observing_the_Earth/Space_for_our_climate/ESA_global_land_cover_map_available_online

Eva, H. D., E. E. De Miranda, C. M. Di Bella, V. Gond, O. Huber, M. Sgrenzaroli, S. Jones, A. Coutinho, A. Dorado, M. Guimarães, C. Elvidge, F. Achard, A. S. Belward, E. Bartholome, A. Baraldi, G. De Grandi, P. Vogt, S. Fritz, and A. Hartley. 2002. “A Vegetation Map of South America. Publications of the European Commission.” http://www.cobveget.cnpm.embrapa.br/resulta/relat/vegetation.pdf

Farr, T. G., P. A. Rosen, E. Caro, R. Crippen, R. Duren, S. Hensley, M. Kobrick, M. Paller., E. Rodriguez, L. Roth, D. Seal, S. Shaffer, J. Shimada, and J. Umland. 2007. “The Shuttle Radar Topography Mission.” *Reviews of Geophysics* 45 (2): 1–43. doi:10.1029/2005RG000183.

Forkuor, G., and B. M. Maathuis. 2012. “Comparison of SRTM and ASTER Derived Digital Elevation Models over Two Regions in Ghana: Implications for Hydrological and Environmental Modeling.” In *Studies on Environmental and Applied Geomorphology*, edited by T. Piacentini and E. Miccadei, 219–240. InTech. doi:10.5772/28951. ISBN 978-953-51-0361-5.

Fricker, H. A., A. Borsa, B. Minster, C. Carabajal, K. Quinn, and B. Bills. 2005. “Assessment of Icesat Performance at the Salar De Uyuni, Bolivia.” *Geophysical Research Letters* 32 (21): 3–7. doi:10.1029/2005GL023423.

Gesch, D., M. Oimoen, Z. Zhang, J. Danielson, and D. Meyer. 2011. “Validation of the ASTER Global Digital Elevation Model (GDEM) Version 2 over the Conterminous United States.” Report to the ASTER GDEM Version 2 Validation Team. http://www.jspacesystems.or.jp/ersdac/GDEM/ver2 Validation/Appendix_B_CONUS%20_GDEMv2_validation_report.pdf

Getirana, A. C. V., M.-P. Bonnet, O. C. Rotunno Filho, and W. J. Mansur. 2009. “Improving Hydrological Information Acquisition from DEM Processing in Floodplains.” *Hydrological Processes* 23 (3): 502–514. doi:10.1002/hyp.7167.

Hirt, C., M. S. Filmer, and W. E. Featherstone. 2010. “Comparison and Validation of the Recent Freely Available ASTER-GDEM Ver1, SRTM Ver4.1 and GEODATA DEM-9S Ver3 Digital Elevation Models over Australia.” *Australian Journal of Earth Sciences* 57 (3): 337–347. doi:10.1080/08120091003677553.

Jarvis, A., H. I. Reuter, A. Nelson, and E. Guevara. 2008. “Hole-Filled SRTM for the Globe Version 4, Available from the CGIAR-CSI SRTM 90 m Database.” http://srtm.csi.cgiar.org

Jenson, S. K., and J. O. Domingue. 1988. “Extracting Topographic Structure from Digital Elevation Data for Geographic Information System Analysis.” *Photogrammetric Engineering and Remote Sensing* 54 (11): 1593–1600.

Li, P., C. Shi, Z. Li, J.-P. Muller, J. Drummond, X. Li, T. Li, Y. Li, and J. Liu. 2012. “Evaluation of ASTER GDEM Ver2 Using GPS Measurements and SRTM Ver4.1 in China.” *XXII Congress of International Society of Photogrammetry, Remote Sensing and Spatial Information Sciences* 1 (4): 181–186. doi:10.5194/isprsannals-I-4-181-2012.

Mackay, D. S., and L. E. Band. 1998. “Extraction and Representation of Nested Catchment Areas from Digital Elevation Models in Lake-Dominated Topography.” *Water Resources Research* 34 (4): 897–901. doi:10.1029/98WR00094.

Martz, L. W., and J. Garbrecht. 1999. "An Outlet Breaching Algorithm for the Treatment of Closed Depressions in a Raster DEM." *Computers & Geosciences* 25 (7): 835–844. doi:10.1016/S0098-3004(99)00018-7.

Molina Carpio, J. 2007. "Agua y recurso hídrico en el Sudoeste de Potosí." *Foro Boliviano sobre Medio Ambiente y Desarrollo*, Foro Boliviano sobre Medio Ambiente y Desarrollo.

Molina Carpio, J., R. Cruz, and J. C. Alurralde. 2012. "Impactos transfronterizos de proyectos de trasvase: El caso de la cuenca del rio Mauri." XXV Congreso Latinoamericano de Hidráulica, San José, Septiembre 9–12.

Moran, R. E. 2009. "Mining Water: The San Cristobal Mine, Bolivia." In *Minando el agua: San Cristobal, Bolivia*, edited by I. Peñaranda, 7–37. CGIAB (Comisión de Gestión Integral de Aguas de Bolivias), FRUTCAS (Federación Regional Única de los Trabajadores Campesinos del Altiplano Sud-) and CGIAB (Comision para la Gestion Integral del Agua en Bolivia). http://www.google.fr/url?sa=t&rct=j&q=&esrc=s&source=web&cd=1&cad=rja&uact=8&ved=0CCQQFjAA&url=http%3A%2F%2Fwww.bivica.org%2Fupload%2Fminando-agua.pdf&ei=6G-hVLmXAor5apKugMAI&usg=AFQjCNHx6BtnMnAyLLUmZJdJocM66MT89w&sig2=D9pVBuZHr3esXyy7YV4rqQ

NASA. 2014a. "NASA." http://icesat.gsfc.nasa.gov/icesat/missionevents.php

NASA. 2014b. "NASA." http://reverb.echo.nasa.gov/reverb/#utf8=%E2%9C%93&spatial_map=satellite&spatial_type=rectangle

NGA. 2014. "NGA." http://earth-info.nga.mil/GandG/wgs84/gravitymod/egm96/egm96.html

Nikolakopoulos, K. G., E. K. Kamaratakis, and N. Chrysoulakis. 2006. "SRTM vs ASTER Elevation Products. Comparison for Two Regions in Crete, Greece." *International Journal of Remote Sensing* 27 (21): 4819–4838. doi:10.1080/01431160600835853.

NSDIC. 2014. "NSDIC." http://nsidc.org/data/icesat/tools.html

O'callaghan, J. F., and D. M. Mark. 1984. "The Extraction of Drainage Networks from Digital Elevation Data." *Computer Vision, Graphics, and Image Processing* 28: 323–344. doi:10.1016/S0734-189X(84)80011-0.

Planchon, O., and F. Darboux. 2002. "A Fast, Simple and Versatile Algorithm to Fill the Depressions of Digital Elevation Models." *Catena* 46: 159–176. doi:10.1016/S0341-8162(01)00164-3.

Reuter, H. I., A. Nelson, and A. Jarvis. 2007. "An Evaluation of Void Filling Interpolation Methods for SRTM Data." *International Journal of Geographical Information Science* 21 (9): 983–1008. doi:10.1080/13658810601169899.

Rodríguez, E., C. S. Morris, and E. Belz. 2006. "A Global Assessment of the SRTM Performance." *Photogrammetric Engineering & Remote Sensing* 72 (3): 249–260. doi:10.14358/PERS.72.3.249.

Sertel, E. 2010. "Accuracy Assessment of Aster Global Dem over Turkey." Special Joint Symposium of ISPRS Technical Commission IV & AutoCarto in Conjunction with ASPRS/CaGIS 2010 Fall Specialty, Orlando, FL, November 15–19.

Sun, G., K. J. Ranson, V. I. Kharuk, and K. Kovacs. 2003. "Validation of Surface Height from Shuttle Radar Topography Mission Using Shuttle Laser Altimeter." *Remote Sensing of Environment* 88 (4): 401–411. doi:10.1016/j.rse.2003.09.001.

Suwandana, E., K. Kawamura, Y. Sakuno, E. Kustiyanto, and B. Raharjo. 2012. "Evaluation of ASTER GDEM2 in Comparison with GDEM1, SRTM DEM and Topographic-Map-Derived DEM Using Inundation Area Analysis and RTK-dGPS Data." *Remote Sensing* 4: 2419–2431. doi:10.3390/rs4082419.

Tachikawa, T., M. Kaku, A. Iwasaki, D. Gesch, M. Oimoen, Z. Zhang, J. Danielson, T. Krieger, B. Curtis, J. Haase, M. Abrams, R. Crippen, and C. Carabajal. 2011. "ASTER Global Digital Elevation Model Version 2 – Summary of Validation Results." http://www.jspacesystems.or.jp/ersdac/GDEM/ver2 Validation/Summary_GDEM2_validation_report_final.pdf

Tsanis, I. K., K. D. Seiradakis, I. N. Daliakopoulos, M. G. Grillakis, and A. G. Koutroulis. 2013. "Assessment of GeoEye-1 Stereo-Pair-Generated DEM in Flood Mapping of an Ungauged Basin." http://www.iwaponline.com/jh/up/jh2013197.htm

Urquidi Barrau, F. 2012. "Un punto de vista estratégico sobre la problemática de las aguas transfronterizas." In *Diagnóstico Del Agua En Las Américas (Diagnosis of Water in the Americas)*, edited by J.-P. Laclette and P. Zúñiga, 75–95. Distrito Federal: Foro Consultivo Científico y Tecnológico. ISBN 978-607-9217-04-4.

USGS. 2003. "USGS." http://dds.cr.usgs.gov/srtm/version2_1/SWBD/

USGS. 2014. "USGS." http://dds.cr.usgs.gov/srtm/version2_1/SRTM3/

Zhao, G., H. Xue, and F. Ling. 2010. “Assessment of ASTER GDEM Performance by Comparing with SRTM and ICESat /GLAS Data in Central China.” Proceedings of the 18th International Conference on Geoinformatics, Beijing, June 18–20. doi:10.1109/GEOINFORMATICS.2010.5567970. ISBN 9781424473021.

Zhao, S., W. Cheng, C. Zhou, X. Chen, S. Zhang, Z. Zhou, H. Liu, and H. Chai. 2011. “Accuracy Assessment of the ASTER GDEM and SRTM3 DEM: An Example in the Loess Plateau and North China Plain of China.” *International Journal of Remote Sensing* 32 (23): 8081–8093. doi:10.1080/01431161.2010.532176.

Zwally, H. J., B. Schutz, W. Abdalati, J. Abshire, C. Bentley, A. Brenner, J. Bufton, J. Dezio, D. Hancock, D. Harding, T. Herring, B. Minster, K. Quinn, S. Palm, J. Spinhirne, and R. Thomas. 2002. “Icesat’s Laser Measurements of Polar Ice, Atmosphere, Ocean, and Land.” *Journal of Geodynamics* 34: 405–445. doi:10.1016/S0264-3707(02)00042-X.

ANEXO 2

ALOS World 3D-30m absolute and relative height pixel accuracy over a barren region and hydrological conditioning potential

ALOS World 3D-30m absolute vertical and relative height pixel accuracy over a barren region and hydrological conditioning potential.

F.Satgé[1,3] ; A. X.Ferreira[1,3]; S.Pinel[2,3]; R.Pillco[4]; J.Molina[4]; F.Timouk[5]; J.Garnier[1,3]; M-P. Bonnet[3,5].

[1] *Institute of Geosciences (LAGEQ), University of Brasília (UnB), Campus Darcy Ribeiro, 70910-900 Brasília, Brazil; frederic.satge@gmail.com ;garnier@unb.br; alvaroxavier.f@gmail.com.*
[2] *RHASA/ State of Amazonas University (UEA), Av. Darcy Vargas, 1200, Parque 10, 69050-020 Manaus, Brazil; jsdsilva@uea.edu.br; sebpinel@gmail.com of Manaus, Manaus, Brazil; sebpinel@gmail.com.*
[3] *Mixed Laboratory International, Observatory for Environmental Change (LMI-OCE), Institute of Research for Development (IRD)/University of Brasilia (UnB), Campus Darcy Ribeiro, 70910-900 Brasília, Brazil; marie-paule.bonnet@ird.fr (M.-P.B.).*
[4] *Institute of hydrology and Hydraulic, University Mayor of San Andres, La Paz, Bolivia;* rami_lund99@hotmail.com*;* amolina@umsa.bo*; franck.timouk@ird.fr.*
[5] *UMR 228 ESPACE-DEV - Institut de Recherche pour le Développement/Université de la Guyane – Maison de la télédétection, Montpellier, France.*

In Revision (Journal of Hydrology)

Abstract

The ALOS World 3D-30m (AW3D30) Digital Elevation Model (DEM) at 1 arc-second mesh size was released for free in May 2016. AW3D30 accuracy is assessed for the first time over the barren Andean plateau. A total of 124,000 ICESat/GLAS (Ice, Cloud and Land Elevation Satellite/Geoscience Laser Altimeter System) data are used as ground reference measurements to assess AW3D30 elevation estimates at the global scale and for different slope classes. Complementary to the vertical error, the relative error is assessed using the new False Slope Ratio (FSR) index jointly with quantitative statistics on base to approximately 475,000 reference slope values derived from ICESat/GLAS points pairs. Additionally, the hydrological network derived from the DEM is compared with a reference one to assess DEM hydrological potential. The evaluations are done at both 1 and 3 arc-seconds mesh size and after applying a simple hydrological conditioning to observe the influence of both aggregation and hydrological conditioning processes on DEM accuracy. For comparison, the SRTM-GL1 DEM is also considered in this study. Over the region, AW3D3O and SRTM-GL1 are as accurate in term of elevation estimates while AW3D30 is much more accurate in term of relative height-pixel accuracy. This result confirmed the necessity of considering both vertical and relative error to have a full insight into DEMs accuracy. Before the hydrological conditioning, AW3D30 is the most suited DEMs to extract the regional hydrological network with a higher value of FM and CR confirming it lowest relative height pixel error. The hydrological conditioning clearly enhanced DEMs ability to extract the regional hydrological network. However, it considerably decreased both vertical and relative accuracy and therefore should be used with cautions in studies using slope as a constraint parameter or requiring accurate elevation estimates.

1. Introduction

Remote sensed Digital Elevation Models (DEMs) are of valuable information in remote regions to describe regional and local topographic features where ground information is missing. DEMs are of primary importance in hydrological and geomorphological studies as topographic features are used to drive flows and/or prevent potential geomorphological risks. In this context, many studies assessed available DEMs accuracy over different regions to provide a general guideline for potential users. Ground Control Points (GCPs) are used as references elevation data to assess DEMs elevation accuracy. GCPs are generally derived from high accuracy GPS and/or altimetric data (Athmania and Achour, 2014; Carabajal, 2011; Enble et al., 2012; Satgé et al., 2016, 2015; Zhao et al., 2010). Comparing DEMs and GCPs elevations provides information on DEMs elevation accuracy. When the GCPs database is large enough, some corrections are possible to enhance DEMs vertical accuracy (Arefi and Reinartz, 2009; Pinel et al., 2015; Satgé et al., 2015; Zhao et al., 2011). Most of the authors limited the assessment to the elevation accuracy, which is not enough to definitely statute on DEMs potentiality for hydrological or geomorphological process studies. Indeed, a DEM can be accurate in term of elevation while poorly describing the Earth Superficial Shape (ESS) (El Hage et al., 2012; Satgé et al., 2016). ESS is defined by the elevation relation between pixels. Each pixel can be higher or lower than its neighbors while the opposite trend is observed on field. As a result, false ESSs are retrieved from the DEMs. To assess DEMs capacity in ESS retrieving, authors compared hydrological features (i.e. rivers network and watershed shape) derived from DEMs with reference ones (Bothale et al., 2013; El Hage et al., 2012; Le Coz et al., 2009; Li and Wong, 2010; Metz et al., 2011; Paz and Collischonn, 2007; Rahman et al., 2010; Satgé et al., 2016; Vogt et al., 2003). As hydrological features strongly rely on the ESS, authors assumed that the closer are the derived and reference considered features, the better is the ESS representation. However, such approach only provides a qualitative overview of the DEMs potentiality in term of global slope orientation, as it only permits to assess ESS at the regional scale but not at the very local scale. Indeed, Satgé et al. (2016) showed that such type of assessment is not enough as the ESS can be well represented in term of slope orientation while high discrepancies in local slope values remained. Remaining slope errors may have strong consequences for hydrological and geomorphological studies as slope value is used as a constraining parameter in various processes such as erosive processes for example. In this context, Satgé et al., (2016) proposed a new method to assess the ESS derived from the DEMs both quantitatively and qualitatively at the local scale. Slope values are computed between GCPs and compared with slope value derived from DEMs. A categorical statistic is used to assess the ESS in term of slope orientation using the new False Slope Ratio index (FSR). Quantitative statistics are used to compare slope values derived from the DEMs and from GCPs to verify if the ESS is correctly quantified. Authors concluded that both statistical analyses are complementary as the ESS can be satisfactory in term of slope orientation but not well quantified.

In May 2016, the ALOS World 3D-30m (AW3D30), was made available for free at a 30 m resolution. AW3D30 accuracy was assessed in the Philippines in term of vertical elevation accuracy over different land cover type (Santillan and Makinano-Santillan, 2016). AW3D30 provided more accurate elevation information than the Shuttle Radar Topographic Mission – Global 1 (SRTM-GL1) and ASTER Global DEM Version 2 (GDEM v2) in term of Root Mean Square Error (RMSE). To date, apart from AWD30 team developers studies (Tadono et al., 2014; Takaku et al., 2014), this is the only study reporting information on AW3D30 accuracy. Authors focused on vertical elevation accuracy using few GCPs and did not consider the relative accuracy. As both vertical and relative height-pixel accuracy are complementary (El Hage et al., 2012; Satgé et al., 2016) additional studies are still needed to provide insights on AW3D30 accuracy. Here, we assess for the first time, the AW3D30 DEM accuracy over the high barren South American Andean plateau in term of both vertical and relative height-pixel accuracy using ICESat/GLAS altimetry. A reference river network is compared with the river network extracted from the DEM to assess the DEM ESS representation at the regional scale and its hydrological potentiality. Additionally, AW3D30 is aggregated from 30 to 90 m mesh size to observe the potential increase in DEM accuracy introduced through the aggregation process. Finally, a simple hydrological conditioning is applied to observe its potentiality over the study area. The SRTM-GL1 is considered for comparison as it provided the most accurate elevation information to date over the region (Satgé et al., 2016).

2. Materials

2.1 Study area

The Altiplano basin is an endorheic system located between latitudes 22°S and 14°S and longitudes of 71°W and 66°W. The river basin covers a total area of approximately 192,390 km^2 and is shared by three countries: Bolivia (70 %), Peru (26%) and Chile (4%). It is semi-arid with low precipitation occurring for 82.7% during the 5 rainy months, with the total amounts decreasing from the north (approximately 715mm.year^{-1}) to the south (170mm.year^{-1}) (Satgé et al., 2016).The Altiplano can be considered as a barren region where urban areas, water bodies and salt areas represent 0.1%, 3.5% and 5.3% of the area respectively (Satgé et al., 2015). The elevation of the region varies between 3500 and 6500 m, with an average elevation of 4000 m and a mean slope value of approximately 5°. The region comprises the Titicaca Desaguadero Poopó Salar system (TDPS), composed of Lake Titicaca, Desaguadero River, Poopó Lake and Coipasa Salt desert (Salar) (Figure 1).

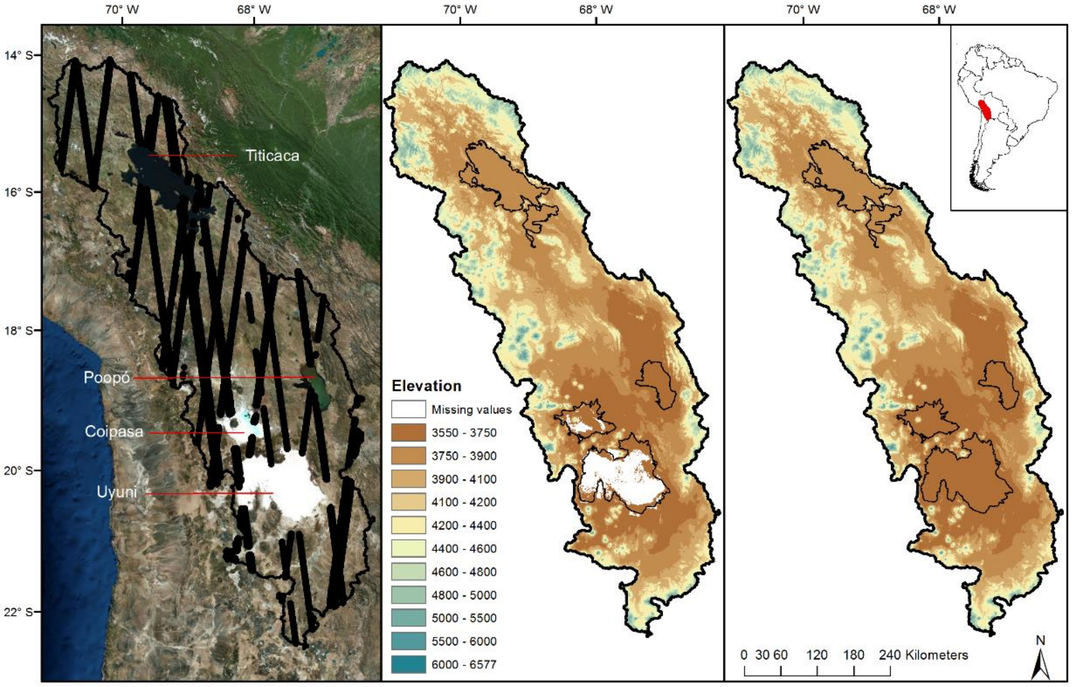

Figure 1. (a) Study area with GCPs locations (b) AW3D30 DEM (c) SRTM-GL1 DEM

2.2 Digital Elevation Models

This study focused on the newly released AW3D30 DEM product of The Japan Aerospace Exploration Agency (JAXA). Stereoscopic images were acquired from 2006 to 2011 by the Panchromatic Remote-sensing Instrument for Stereo Mapping (PRISM) onboard the Advanced Land Observing Satellite (ALOS). Stereoscopic images are generated by three independent panchromatic radiometers of the PRISM viewing forward, nadir and backwards in 2.5 m spatial resolution (Tadono et al., 2014; Takaku et al., 2014). A total of approximately one million of stereoscopic images, each covering 35 km^2, were used to generate the DEM at the global scale. A specific software, described in (Takaku et al., 2014), first processed the stereoscopic images at their original size (35*35 km^2) and then mosaicked the results into a 1°x1° tiles with a 0.15 arc-second mesh size (5 m near the equator). Finally, an automatic quality check of the data was run using ICESat and SRTM data as reference jointly with a complementary verification by human operators. The generated DEM at 5 m mesh size is available but users have to pay to get access to the data. In May 2016, the JAXA resampled the 5-meter mesh version into a 30 m mesh version to produce the AW3D30 DEM. AW3D30 DEM is freely available and spans 82°N-82°S. Data are delivered as 1° by 1° tiles referenced to the World Geodetic System 84 (WGS84) ellipsoid and Earth Gravitational Model 1996 (EGM96) geoid. In this study, we only consider the AW3D30 version. It is noteworthy that some data are missing over the region. This occurs over white land covers such as the salt desert of Uyuni and Coipasa and some permanently snow-covered mountain (Figure 1). A blending approach using over DEMs to fill the gaps should be considered to overcome this issue (Yue et al., 2017).

The SRTM-GL1 is a joint product of the National Geospatial-Intelligence Agency (NGA) and the National Aeronautics and Space Administration (NASA). Data were collected during 11 days in February 2000 using dual spaceborne imaging radar (SIR-C) and dual X-band synthetic aperture radar (X-SAR). The SRTM-GL1 data features a resolution of 1 arc-second (30 m near the equator) and spans 60°N–56°S. Previously, the native 1 arc-second version (SRTM-GL1) was available for free over the CONUS, while the mesh size was limited to 3 arc-second outside CONUS. The SRTM-GL1 data have been freely released in November 2014. They can be downloaded at NASA's Earth Observing System Data and Information System (EOSDIS) website (http://reverb.echo.nasa.gov/). Data are delivered as 1° by 1°tiles referenced to the World Geodetic System 84 (WGS84) ellipsoid and Earth Gravitational Model 1996 (EGM96) geoid.

2.3 ICESat Altimetry

The ICESat/GLAS data were produced by NASA. The data were collected between 12 January 2003 and 11 October 2009 by the geoscience laser altimeter system (GLAS) aboard the Ice Cloud and Land Elevation Satellite (ICESat). The footprint size is approximately 70 m, with one elevation measurement every 172 m and inter-track spacing of 30 km (near the equator). The altimeter measures the two-way travel time of a pulse that is reflected by the ground. GLA14 v33 Global Land-Surface Altimeter data were used, as they are specifically suited for land-surface elevation studies. The data are referenced to the TOPEX/Poseidon ellipsoid and EGM96 geoid and can be downloaded from the NASA website. The National Snow and Ice Data Center (NSIDC) provides an IDL routine for reading ICESat/GLAS data and for extracting information in a readable array format with the latitude, longitude, elevation and geoid of each measured point. Thus, this script was used in this study. The ICESat/GLAS vertical accuracy at the global scale is approximately 15 cm (Zwally et al., 2002) and of 5 cm over the Uyuni salt desert (Fricker et al., 2005). The AW3D30 accuracy is of 5 m STD according to producers and of 3.66 m STD over the Philippines (Santillan and Makinano-Santillan, 2016). ICESat/GLAS data are accurate enough to be used as GCPs for assessing AW3D30.

3. Methods

3.1 DEM data and GCP preprocessing

AW3D30 and SRTM-GL1 use the same ellipsoid/geoid system (WGS84/EGM96). However, the ICESat/GLAS dataset is referenced to the T/P ellipsoid. To allow comparison between DEMs and ICESat/GLAS measurements, we used the NSIDC-provided IDL tool called 'IDL Ellipsoid Conversion' to convert ICESat/GLAS measurement from T/P to WGS84. The EGM96 was computed and subtracted at each ICESat/GLAS measurement using the interpolation program available on the NGA website (Satgé et al., 2016, 2015). Several flags provided by NSDIC were used to select accurate ICESat/GLAS measurements over the study area (Satgé et al., 2015). GCPs located over lake Poopó and Titicaca were not considered as these regions are subject to seasonal water level fluctuation which can degrade GCPs quality. Similarly, GCPs located over the Coipasa and Uyuni salt desert were not considered as they are periodically flooded. A total of 124,061 GCPs were available for this study. Finally, at each GCPs location, the AW3D30 data elevation and the slopes values were computed using the ArcGIS Spatial Analyst tool. For each pixel including GCPs, the maximum slope with its neighbors was computed and kept in our database.

3.2 Hydrological conditioning

We used the Topo to Raster tool (TR) available in ARCGis 10. TR provides an interpolation method specifically designed for the creation of meaningful DEMS for hydrological purposes. TR is based on the ANUDEM v5.3 algorithm developed by Michael Hutchinson (Hutchinson et al., 2011; Hutchinson, 2000, 1989). The algorithm is based on the water erosive force which determines the general ESS to interpolate elevation values and ensure a well-connected drainage structure with a correct representation of ridges and stream. To run TR, a shape point files providing DEM elevation values and a shape line file corresponding to the Reference Hydrological Network (RHN) are required. Therefore, we converted the raster grids into a shape point file using the parameter “raster to point” tool in ArcGis 10. The RHN was digitized from Google-Earth (GE) which was previously found accurate enough over the region to extract the river network (Satgé et al., 2016). An additional shape polygon file was used as a mask to limit the TR computation outside the lakes (Titicaca and Poopó) and desert salts (Uyuni and Coipasa). The TR tool also allows considering others input data to enhance the computation process in regions where known sinks, cliffs or coastlines have to be considered. Such cases are not observed over the region and thus are not considered. Different parameters are available to adjust the TR computation according to the studied area features. We do not change the default recommended values except for the parameter “vertical standard error” which was fixed to the standard deviation error of the DEMs estimated to 8 m using ICESat/GLAS data as GCPs. According to the size of the study area, to limit computation time and avoid the needs of splitting the area into overlapped subset regions, TR was run on both AW3D30 and SRTM-GL1 at the 3 arc-second mesh size. We used AW3D30_HC and SRTM-GL1_HC names to refer to the AW3D30 and SRTM-GL1 after applied the TR hydrological conditioning.

3.3 Vertical Accuracy

We assessed AW3D30 vertical accuracy by comparing its elevation with the GCP elevation considering Mean Error (ME) and Root Mean Square Error (RMSE) (Equation 1 and 2).

$$(1)\ ME = \frac{\sum_{i=1}^{i=n}(x_i - y_i)}{n}$$

$$(2)\ RMSE = \sqrt{\frac{\sum_{i=1}^{i=n}[(x_i - y_i)^2]}{n}}$$

$$(3)\ MAE = \frac{\sum_{i=1}^{i=n}(|x_i - y_i|)}{n}$$

where n is the number of values, x is the GCP value (m), y is the DEM value (m).

Those statistical parameters were computed at regional scale considering all GCPs and for different slope classes. The 0-2°, 2–5°, 5–10°, 10–20° and >20° corresponding to 44%, 19%, 18%, 16% and 3% of the GCP data set, respectively, are considered to allow comparison with previous results obtained for GDEM-v2 and SRTM-v4 over the same region (Satgé et al., 2016; Satgé et al., 2015). The region was previously described as a bare region with no vegetation influence on DEMs accuracy. Thus, we do not consider land cover in our analysis. The assessment is done at the native 1arc-second and aggregated 3arc-second mesh size and after having applied the previously described hydrological conditioning. The 3 arc-second value were obtained by averaging the 9 1 arc-second pixel values included in the corresponding 3 arc-second pixels.

3.4 Relative Accuracy

We used the recent method described by (Satgé et al., 2016) to assess AW3D30 relative accuracy. In this study, relative accuracy is defined as how well DEMs represent the relation from point to point elevation. To describe the relation from point to point (i.e. relative accuracy), the slope values between the considered points are used. Close slope values between DEMs and GCPs mean good relative accuracy while far slope values mean low relative accuracy.

Here, slopes between GCPs are computed for all point pairs in the region using all DEMs and GCPs. Only the slopes computed between points separated by at least 100 m are considered to take into account the maximum DEMs mesh size of 90 m (3 arc-second). A maximum distance threshold value between point pairs was arbitrarily fixed at 500 m. Indeed, above this threshold, the slopes are more representative of ESS than of DEM’s relative accuracy (Satgé et al., 2016). To account for the global absolute vertical accuracy of ICESat/GLASS (15 cm), we only considered slopes retrieved from GCPs with elevation differences greater than or equal to 1 m (Satgé et al., 2016). In summary, only GCPs point pairs horizontally distant from 100 to 500 m with an absolute elevation difference superior to 1 m were considered. According to this selection procedure, a data set of 475,943 slope values was used to compare DEMs and GCPs. The slopes are not expected to be only positive. Thus, the ME is expected to be insignificant, with values close to 0. In this context, MAE (Eq. 3) was preferred to ME for quantifying the relative DEM accuracy. % MAE and % RMSE were computed by dividing MAE and RMSE by reference mean absolute values obtained from GCPs. A total of 241,117, 111,355, 76,359, 41,431 and 5681 slope measurements were available for the 0–2°, 2–5°, 5–10°, 10–20° and >20° classes, respectively. Finally, we used a statistical analysis based on the False Slope Ratio (FSR) (eq. 4) described in

(Satgé et al., 2016) to evaluate DEM's relative accuracy. The slope is considered as a discrete value with only two options: positive or negative value. Two outcomes are possible: (a) DEMs and GCPs report the same slope trend or (b) DEMs and GCPs report different slope trends (Fig. 2).

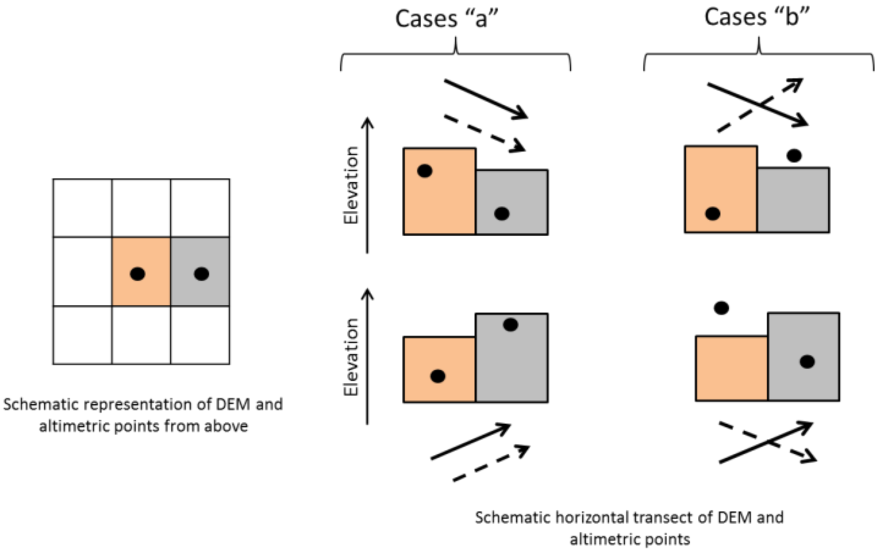

Figure 2. Categorical statistic approach. Black points represent GCPs, black and dotted arrows represent the slope orientation from DEM and GCPs, respectively (source: Satgé et al.2016)

$$FSR = \frac{B}{A+B} \times 100 \qquad (4)$$

3.5 Hydrological potentiality

The regional ESS derived from DEM is controlled by the point-to-point elevation relationship. Thus, assessing DEMs derived ESS is a way to indirectly assess DEMs relative accuracy on the regional scale. As ESS controls rivers location, it is possible to indirectly assess the ESS derived from DEMs by evaluating the hydrological networks derived from the DEM (DHNs). DHNs were computed from all DEMs using the Arc Hydro tool in ArcGIS 10.2 (Maidment, 2002). This tool is based on the D8 algorithm (Jenson and Domingue, 1988). All sinks were first filled using the 'fill sink' function to ensure flow continuity across the study area. To account for the endorheic regional context, lakes, salt areas and the associated floodplains were masked in each DEM. Using the filled DEMs, the 'flow direction' function was applied to define the direction of the steepest descent in each cell. The result is used by the 'flow accumulation' function, which defines the number of accumulated upstream cells for each cell. Finally, the hydrological network was extracted using the 'stream definition' function, which defines rivers based on a threshold value for the contributing area. The number of extracted rivers varies with the threshold value. Thus, a larger threshold reduces the number of small streams, while a smaller threshold may create some stream features that do not actually exist. To ensure significant comparisons, artifacts rivers in DHNs were used in the analysis and the length of each river extracted from the GE and DEM data sets was limited to the maximum length of the corresponding river among all DHNs. The DHNs and RHN were converted to grids to compute correctness (Cr) and figure of merit (FM) indices (Eqs. (5) and (6)) to assess the similarity between the RHN and DHNs (Li and Wong, 2010; Pontius et al., 2008; Satgé et al., 2016). A pixel size of 100 m was used to account for the 90 m mesh size of the AW3D30_90, SRTM-GL1_90, AW3D30_HC and SRTM-GL1_HC data and the global positioning accuracy of GE, which is approximately 10 m according to the literature (Satgé et al., 2016). Cr indicates the proportion of RHN correctly represented by the DHNs. FM indicates how well the DHNs can replicate the RHN. Both Cr and FM have a perfect score value of 1.

$$(5)\ C_r = \frac{N_{A\cap B}}{N_B}$$

$$(6)\ FM = \frac{N_{A\cap B}}{N_{A\cup B}}$$

where N_B is the number of cells representing the RHN, $N_{A\cap B}$ is the number of DHN cells overlapping RHN cells and $N_{A\cup B}$ is the sum of all DHN and RHN cells.

4. Results and discussion

4.1 Vertical Accuracy

Table 1 presents the results for the vertical accuracy for AW3D30 and SRTM-GL1 at the 1 and 3 arc-second mesh size and after the hydrological conditioning. At the global scale, both DEMs over-estimated elevation as negative ME was observed. The hydrological conditioning slightly decreased the negative bias but considerably increased the RMSE and thus decreased the elevation estimated accuracy of both DEMs. Considering slope classes, AW3D30 elevation accuracy decreased when slope values increased. Indeed, RMSE increased by a factor close to 2 from regions with slope value inferior to 2° to regions with slope value superior to 20°. This tendency was slightly more marked for SRTM-GL1. Very close ME and RMSE values were observed for all considered classes and for both AW3D30 and AW3D30_90. Thus, the spatial resolution aggregation did not enhance the vertical accuracy. The hydrological conditioning decreased AW3D30 vertical accuracy as RMSE increased for all slope classes. For slope classes superior to 5°, an increase of up to 6 m in RMSE was observed after applying the hydrological conditioning. In high slope value regions (slope >5°), elevations and slopes were highly variable at local scale from point to point. The hydrological conditioning smoothes the topography to inforce flow towards rivers network. Therefore, the hydrological conditioned DEMs did not represent this high elevation and slope variability which is traduced by the decrease of vertical accuracy in those regions.

		SRTM-GL1		**AW3D30**		**SRTM-GL1_90**		**AW3D30_90**		**SRTM-GL1_HC**		**AW3D30_HC**	
Slope	Numbers of GCPs	*ME*	*RMSE*	*ME*	*RMSE*	*ME*	*RMSE*	*ME*	*RMSE*	*ME*	*RMSE*	*ME*	*RMSE*
0-2	54853	-8.4	9.3	-8.1	9.0	-8.4	9.3	-8.1	9.0	-7.9	11.1	-7.8	10.8
2-5	23650	-7.6	9.4	-7.5	9.4	-7.6	9.4	-7.6	9.3	-7.3	13.7	-7.3	13.6
5-10	21861	-7.2	10.4	-7.3	10.5	-7.3	10.4	-7.3	10.3	-7.2	15.2	-7.1	16.0
10-20	19929	-6.7	12.5	-6.9	12.6	-6.7	12.5	-6.8	12.4	-6.1	18.8	-6.1	18.3
>20	3768	-6.0	16.2	-5.8	15.8	-5.9	16.2	-5.6	15.6	-4.1	26.0	-3.5	23.9
Total	124061	-7.7	10.4	-7.6	10.2	-7.7	10.3	-7.6	10.1	-7.3	14.4	-7.2	14.2

Table 1. Computed ME and RMSE values (m) for AW3D30 and SRTM-GL1 at both 1 and 3 arc-second mesh size and after the hydrological conditioning based on an absolute vertical accuracy assessment considering different slope classes.

4.2 Relative Accuracy

Figure 2 shows FSR values obtained for both DEMs at their original and aggregate mesh size before and after hydrological conditioning. At the regional scale, AW3D30 presented lowest FSR value than SRTM-GL1. The differences between SRTM-GL1 and AW3D30 FSR values were much marked over very flat regions where slope values are inferior to 2°. Indeed, FSR values of approximately 14% and 9% were obtained for SRTM-GL1 and AW3D30, respectively. Additionally, both DEMs are poorly accurate with %AME and %RMSE very high (Table 2). It is noteworthy that slightly lowest %AME and %RMSE were observed for AW3D30 in comparison with SRTM-GL1. For slope values superior to 2°, SRTM-GL1 and AW3D30 performed similarly with very close FSR, %AME and %RMSE values (Figure 2 and Table 2). For the region of mean slope value superior to 5°, both DEMs correctly represented the local ESS with FSR inferior to 2% and %AME and %RMSE values of approximately 26% and 37%. The aggregation process did not bring significant improvements on DEMs relative accuracy in term of FSR with very close FSR values before and after the aggregation process and for all considered classes. However, it slightly decreased %AME and %RMSE over low mean slope regions (inferior to 2°) enhancing the local ESS quantification. At the regional scale, hydrological conditioning decreased DEMs potentiality in term of FSR. It is more marked for AW3D30 as FSR increased from 6% to 9% (50%). Over very flat regions (slope<2°), hydrological conditioning only decreased AW3D30 potentiality as no significant change was observed in SRTM-GL1 FSR values. However, for slope values superior to 2°, the hydrological conditioning increased both SRTM-GL1 and AW3D30 FSR values by a factor close to 100%. The hydrological conditioning objective is to enhance the regional ESS by forcing local slope to ensure flow directions towards the hydrological networks. As a result, slopes variation at finer scale are altered decreasing DEMs relative accuracy and thus the local ESS representation with an increase of FSR, %AME and %RMSE (Figure 2, Table 2). Therefore, these results show that hydrological conditioning cannot be used to increase DEMs relative accuracy.

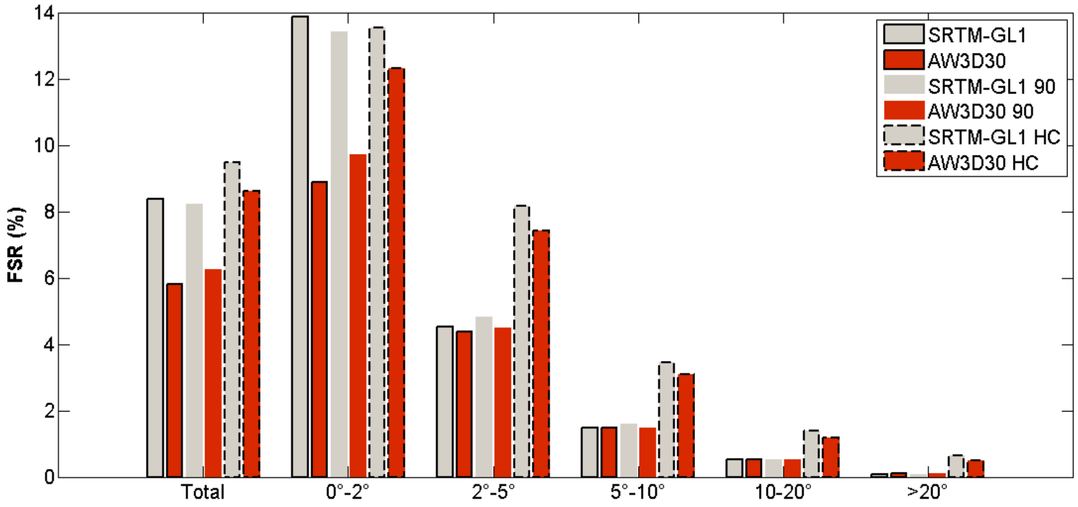

Figure 3. FSR values for AW3D30 and SRTM-GL1 at both 1 and 3 arc-second mesh size and after the hydrological conditioning on a global scale and for different slope classes.

		AME (%)						RMSE (%)					
Classes	Numbers of measurements	SRTM-GL1	AW3D30	GL1_90	AW3D30_90	SRTM-GL1_HC	AW3D30_HC	SRTM-GL1	AW3D30	GL1_90	AW3D30_90	GL1_HC	AW3D30_ HC
0-2	241117	80.8	68.9	69.9	62.3	81.4	77.7	139.5	135.5	128.3	124.4	168.0	167.1
2-5	111355	40.1	39.9	38.6	37.6	48.1	46.5	61.0	62.0	58.2	57.4	72.5	72.1
5-10	76359	26.0	26.0	26.1	25.3	34.6	33.1	37.2	37.7	36.7	35.9	47.3	45.7
10-20	41431	19.3	19.0	20.5	19.5	31.1	29.4	27.0	26.8	28.0	26.9	40.2	38.4
>20	5681	22.4	20.8	25.4	23.8	40.5	38.6	28.5	26.7	31.5	29.6	47.1	45.2
Total	475943	32.5	31.0	31.7	30.0	41.7	39.8	55.7	55.3	55.6	53.9	75.4	73.1

Table 2. Computed AME and RMSE values for AW3D30 and SRTM-GL1 at 1 and 3 arc-second mesh size and after Hydrological Conditioning based on a relative accuracy assessment considering different slope classes.

4.3 Hydrological Potentiality

Table 3 presents FM and CR values for AW3D30 and SRTM-GL1 at the 1 and 3 arc-second mesh size and after hydrological conditioning. Before hydrological conditioning, AW3D30 presented higher value of FM and CR than SRTM-GL1. Therefore, AW3D30 is more suited to describe the regional ESS. Hydrological conditioning increased FM and CR by a factor 2 enhancing the regional ESS representation. As discussed in the relative accuracy section, hydrological conditioning only enhanced the global ESS to turn it hydrologically coherent. However, it considerably decreased the local ESS and thus has to be carefully used. As an example, such hydrological conditioning should introduce uncertainty in runoff erosive process computation as slope orientation and quantification are highly biased (Table 2, Figure 2).

	AW3D30	SRTM-GL1	AW3D30_90	SRTM-GL1_90	AW3D30_HC	SRTM-GL1_90_HC
FM	0.24	0.17	0.24	0.17	0.47	0.49
CR	0.34	0.26	0.34	0.26	0.57	0.58

Table 3. FM and CR values for AW3D30 and SRTM-GL1 at both 1 and 3 arc-second mesh size and after hydrological conditioning.

5. Conclusion

For the first time, the newly released AW3D30 DEM was assessed in term of vertical and relative accuracy over a barren region. AW3D30 and SRTM-GL1 estimates are very close in term of ME and RMSE and both overestimated elevations by 8.1 m and 8.4 m, respectively. In term of relative accuracy, AW3D30 is more accurate than SRTM-GL1 with considerably lower FSR values, %AME and %RMSE in comparison to SRTM-GL1. Over the region, AW3D30 reasonably represents the ESS (low FSR), but still failed to quantify it (high %AME and %RMSE). Based on elevation accuracy, AW3D30 and SRTM-GL1 would have been considered similarly accurate while the relative accuracy assessment shows that AW3D30 is the most accurate DEM over the region. Thus, in future studies, DEMs have to be assessed in term of both vertical and relative accuracy to produce more consistent results. The comparison between DHN and RHNs confirmed the relative accuracy assessment. Indeed, a more realistic hydrological network is derived from AW3D30 than from SRTM-GL1. The aggregation from 1 to 3 arc-second mesh size does not significantly enhance both vertical and relative DEMs accuracy over the region. Finally, the hydrological conditioning method used in this study enhances DEMs potentiality to describe the regional hydrological network. However, it is noteworthy that it drastically decreases vertical and relative DEMs accuracy. In term of elevation accuracy and at the global scale, an increase of approximately 40 % in RMSE is observed for both AW3D30 and SRTM-GL1. In term of relative accuracy, FSR, AME and RMSE increased by factors close to 50%, 30% and 35%, respectively for both AW3D3O and SRTM-GL1. These results show that hydrological conditioning should be used with caution as it considerably modified the ESS at the local scale and thus should introduce significant errors in studies using slope value as constraining parameter. On a more general point of view, this study shows the usefulness of the reference data set used. ICESat/GLAS data can be used to effectively assess vertical accuracies as shown in this study, which utilized a large data set (124,000 points). The methodology used to assess the relative error benefits a large number of ICESat/GLAS data from which close to 475,000 local slope values was derived in view of the analysis. Comparisons were conducted over a large slope range, making this study the most comprehensive AW3D30 vertical and relative error assessment to date. In Barren regions, such as the Andean plateau studies requiring accurate ESS descriptions, such as hydrological and geomorphological analyses, should utilize AW3D30 instead of SRTM-GL1 as it presents the best vertical and relative height-pixel accuracies among the freely available DEMs.

Acknowledgments

This work was supported by the *Centre National d'Etudes Spatiales* (CNES) in the framework of the HASM project (Hydrology of Altiplano: from Spatial to Modeling). The first author thanks the IRD (*Institut de Recherche pour le Développement*) and CAPES (*Coordenação de Aperfeiçoamento de Pessoal de Nível Superior*) Brazil for their financial support.

References

Arefi, H., Reinartz, P., 2009. ELIMINATION OF THE OUTLIERS FROM ASTER GDEM DATA.

Athmania, D., Achour, H., 2014. External validation of the ASTER GDEM2, GMTED2010 and CGIAR-CSI- SRTM v4.1 free access digital elevation models (DEMs) in Tunisia and Algeria. Remote Sens. 6, 4600–4620. doi:10.3390/rs6054600

Bothale, R.V., Joshi, A.K., Krishnamurthy, Y.V.N., 2013. Cartosat-1 derived DEM (CartoDEM) towards Parameter Estimation of Microwatersheds and Comparison with ALTM DEM. J Indian Soc Remote Sens 41, 487–495. doi:10.1007/s12524-012-0258-8

Carabajal, C.C., 2011. ASTER GLOBAL DEM VERSION 2.0 EVALUATION USING ICESat GEODETIC GROUND CONTROL.

El Hage, M., Simonetto, E., Faour, G., Polidori, L., 2012. EVALUATION OF ELEVATION, SLOPE AND STREAM NETWORK QUALITY OF SPOT DEMS, in: ISPRS Annals of Photogrammetry, Remote Sensing and Spatial Information Sciences. pp. 63–67. doi:10.5194/isprsannals-I-2-63-2012

Enble, F., Heinzel, J., Koch, B., 2012. EVALUATING HEIGHT DIFFERENCES BETWEEN GLOBAL DIGITAL SURFACE MODELS AND ICESAT HEIGHTS AT FOOTPRINT GEOLOCATION, in: GIS Ostrava 2012 - Surface Models for Geosciences.

Fricker, H.A., Borsa, A., Minster, B., Carabajal, C., Quinn, K., Bills, B., 2005. Assessment of ICESat performance at the salar de Uyuni, Bolivia. Geophys. Res. Lett. 32, 3–7. doi:10.1029/2005GL023423

Jenson, S.K., Domingue, J.O., 1988. Extracting Topographic Structure from Digital Elevation Data for Geographic Information System Analysis. Photogramm. Eng. Remote Sensing 54, 1593–1600.

Le Coz, M., Delclaux, F., Genthon, P., Favreau, G., 2009. Assessment of Digital Elevation Model (DEM) aggregation methods for hydrological modeling: Lake Chad basin, Africa. Comput. Geosci. 35, 1661–1670. doi:10.1016/j.cageo.2008.07.009

Li, J., Wong, D.W.S., 2010. Computers , Environment and Urban Systems Effects of DEM sources on hydrologic applications. Comput. Environ. Urban Syst. 34, 251–261. doi:10.1016/j.compenvurbsys.2009.11.002

Maidment, D.R., 2002. Arc Hydro: GIS for Water Resources, Volume 1.

Metz, M., Mitasova, H., Harmon, R.S., 2011. Efficient extraction of drainage networks from massive , radar-based elevation models with least cost path search. Hydrol. Earth Syst. Sci. 667–678. doi:10.5194/hess-15-667-2011

Paz, A.R., Collischonn, W., 2007. River reach length and slope estimates for large-scale hydrological models based on a relatively high-resolution digital elevation model. J. Hydrol. 343, 127–139. doi:10.1016/j.jhydrol.2007.06.006

Pinel, S., Bonnet, M.-P., Santos Da Silva, J., Moreira, D., Calmant, S., Satgé, F., Seyler, F., 2015. Correction of Interferometric and Vegetation Biases in the SRTMGL1 Spaceborne DEM with Hydrological Conditioning towards Improved Hydrodynamics Modeling in the Amazon Basin. Remote Sens. Remote Sens 7, 16108–16130. doi:10.3390/rs71215822

Pontius, R.G., Boersma, W., Castella, J.C., Clarke, K., Nijs, T., Dietzel, C., Duan, Z., Fotsing, E., Goldstein, N., Kok, K., Koomen, E., Lippitt, C.D., McConnell, W., Mohd Sood, A., Pijanowski, B., Pithadia, S., Sweeney, S., Trung, T.N., Veldkamp, a. T., Verburg, P.H., 2008. Comparing the input, output, and validation maps for several models of land change. Ann. Reg. Sci. 42, 11–37. doi:10.1007/s00168-007-0138-2

Rahman, M.M., Arya, D.S., Goel, N.K., 2010. Limitation of 90 m SRTM DEM in drainage network delineation using D8 method-a case study in flat terrain of Bangladesh. Appl. Geomatics 2, 49–58. doi:10.1007/s12518-010-0020-2

Santillan, J.R., Makinano-Santillan, M., 2016. Vertical accuracy assessment of 30-M resolution ALOS, ASTER, and SRTM global DEMS over Northeastern Mindanao, Philippines. Int. Arch. Photogramm. Remote Sens. Spat. Inf. Sci. - ISPRS Arch. 41, 149–156. doi:10.5194/isprsarchives-XLI-B4-149-2016

Satgé, F., Bonnet, M.-P., Gosset, M., Molina, J., Hernan Yuque Lima, W., Pillco Zolá, R., Timouk, F., Garnier, J., 2016a. Assessment of satellite rainfall products over the Andean plateau. Atmos. Res. 167, 1–14. doi:10.1016/j.atmosres.2015.07.012

Satgé, F., Bonnet, M.P., Timouk, F., Calmant, S., Pillco, R., Molina, J., Lavado-Casimiro, W., Arsen, A., Crétaux, J.F., Garnier, J., 2015. Accuracy assessment of SRTM v4 and ASTER GDEM v2 over the Altiplano watershed using ICESat/GLAS data. Int. J. Remote Sens. 36, 465–488. doi:10.1080/01431161.2014.999166

Satgé, F., Denezine, M., Pillco, R., Timouk, F., Pinel, S., Molina, J., Garnier, J., Seyler, F., Bonnet, M.-P., 2016. Absolute and relative height-pixel accuracy of SRTM-GL1 over the South American Andean Plateau. ISPRS J. Photogramm. Remote Sens. 121. doi:10.1016/j.isprsjprs.2016.09.003

Tadono, T., Ishida, H., Oda, F., Naito, S., Minakawa, K., Iwamoto, H., 2014. Precise Global DEM Generation by ALOS PRISM. ISPRS Ann. Photogramm. Remote Sens. Spat. Inf. Sci. II-4, 71–76. doi:10.5194/isprsannals-II-4-71-2014

Takaku, J., Tadono, T., Tsutsui, K., 2014. Generation of high resolution global DSM from ALOS PRISM. Int. Arch. Photogramm. Remote Sens. Spat. Inf. Sci. - ISPRS Arch. 40, 243–248. doi:10.5194/isprsarchives-XL-4-243-2014

Vogt, J. V., Colombo, R., Bertolo, F., 2003. Deriving drainage networks and catchment boundaries : a new methodology combining digital elevation data and environmental characteristics. Geomorphology 53, 281–298. doi:10.1016/S0169-555X(02)00319-7

Yue, L., Shen, H., Zhang, L., Zheng, X., Zhang, F., Yuan, Q., 2017. High-quality seamless DEM generation blending SRTM-1, ASTER GDEM v2 and ICESat/GLAS observations. ISPRS J.

Photogramm. Remote Sens. 123, 20–34. doi:10.1016/j.isprsjprs.2016.11.002

Zhao, G., Xue, H., Ling, F., 2010. Assessment of ASTER GDEM Performance by Comparing with SRTM and ICESat / GLAS Data in Central China, in: 18th International Conference on Geoinformatics. Beijing. doi:10.1109/GEOINFORMATICS.2010.5567970

Zhao, S., Cheng, W., Zhou, C., Chen, X., Zhang, S., Zhou, Z., Liu, H., Chai, H., 2011. Accuracy assessment of the ASTER GDEM and SRTM3 DEM: an example in the Loess Plateau and North China Plain of China. Int. J. Remote Sens. 32, 8081–8093. doi:10.1080/01431161.2010.532176

Zwally, H.J., Schutz, B., Abdalati, W., Abshire, J., Bentley, C., Brenner, A., Bufton, J., Dezio, J., Hancock, D., Harding, D., Herring, T., Minster, B., Quinn, K., Palm, S., Spinhirne, J., Thomas, R., 2002. ICESat's laser measurements of polar ice, atmosphere, ocean, and land. J. Geodyn. 34, 405–445. doi:10.1016/S0264-3707(02)00042-X

ANEXO 3

Comparative Assessments of the Latest GPM Mission’s Spatially Enhanced Satellite Rainfall Products over the Main BolivianWatersheds

remote sensing

MDPI

Article

Comparative Assessments of the Latest GPM Mission's Spatially Enhanced Satellite Rainfall Products over the Main Bolivian Watersheds

Frédéric Satgé [1,2,*], Alvaro Xavier [1], Ramiro Pillco Zolá [3], Yawar Hussain [4], Franck Timouk [5], Jérémie Garnier [1,2] and Marie-Paule Bonnet [2,6]

[1] Instituto de Geociência (IG), Universidade de Brasília, 70910-900 Brasília-DF, Brasil; alvaroxavier.f@gmail.com (A.X.); garnier@unb.br (J.G.)
[2] Mixed Laboratory International, Observatory for Environmental Change (LMI-OCE), IRD/UnB, Campus Darcy Ribeiro, 70910-900 Brasília-DF, Brasil; marie-paule.bonnet@ird.fr
[3] Instituto de Hidráulica e Hidrología (IHH), Universidad Mayor de San Andrés, La Paz, Bolivia; rami_lund99@hotmail.com
[4] Departamento de Engenharia Civil e Ambiental, Universidade de Brasilia, 70910-900 Brasília-DF, Brasil; yawar.pgn@gmail.com
[5] Géosciences Environnement Toulouse (GET) (UMR 5563, IRD, CNRS), Université Paul Sabatier, 31062 Toulouse, France; franck.timouk@ird.fr
[6] Espace Développement (ESPACE-DEV) (UMR 228, IRD), 34093 Montpellier, France
* Correspondence: frederic.satge@gmail.com

Academic Editors: Magaly Koch and Prasad S. Thenkabail
Received: 7 February 2017; Accepted: 9 April 2017; Published: 13 April 2017

Abstract: The new IMERG and GSMaP-v6 satellite rainfall estimation (SRE) products from the Global Precipitation Monitoring (GPM) mission have been available since January 2015. With a finer grid box of 0.1°, these products should provide more detailed information than their latest widely-adapted (relatively coarser spatial scale, 0.25°) counterpart. Integrated Multi-satellitE Retrievals for GPM (IMERG) and Global Satellite Mapping of Precipitation version 6 (GSMaP-v6) assessment is done by comparing their rainfall estimations with 247 rainfall gauges from 2014 to 2016 in Bolivia. The comparisons were done on annual, monthly and daily temporal scales over the three main national watersheds (Amazon, La Plata and TDPS), for both wet and dry seasons to assess the seasonal variability and according to different slope classes to assess the topographic influence on SREs. To observe the potential enhancement in rainfall estimates brought by these two recently released products, the widely-used TRMM Multi-satellite Precipitation Analysis (TMPA) product is also considered in the analysis. The performances of all the products increase during the wet season. Slightly less accurate than TMPA, IMERG can almost achieve its main objective, which is to ensure TMPA rainfall measurements, while enhancing the discretization of rainy and non-rainy days. It also provides the most accurate estimates among all products over the Altiplano arid region. GSMaP-v6 is the least accurate product over the region and tends to underestimate rainfall over the Amazon and La Plata regions. Over the Amazon and La Plata region, SRE potentiality is related to topographic features with the highest bias observed over high slope regions. Over the TDPS watershed, the high rainfall spatial variability with marked wet and arid regions is the main factor influencing SREs.

Keywords: IMERG; GSMaP; TMPA; Bolivia; assessment; GPM

1. Introduction

Accurate rainfall estimation is crucial to monitor long- and short-term hydro-climatologic variations. Drought and flood scenarios can be predicted or understood from the rainfall analysis, protecting the local environment and increasing population security. In remote regions, few meteorological stations are available and are unevenly distributed due to difficulties of access for installation and maintenance. Over the last few decades, numerous Satellite Rainfall Estimates (SREs) were made available from different organizations allowing a high quality of rainfall monitoring over the same periods. Nowadays, a new generation of SREs is being made available to ensure continuity in rainfall monitoring, addressing previous SREs' deficiencies related to aging sensors. Two SRE groups, which are derived from the Global Precipitation Monitoring (GPM) mission launched on 27 February 2014, are now available. They are the Integrated Multi-satellitE Retrievals for GPM (IMERG) and the GPM Global Satellite Mapping of Precipitation (GSMaP-v6). Available at a 0.1° and half-hourly and hourly temporal scales, respectively, they offer the opportunity of capturing finer local rainfall variations in space and time. Data is available from March 2014 to present. However, IMERG and GSMaP-v6 products were released in early January 2015 and, thus, few studies have assessed their potentiality yet. A study compared IMERG, with TRMM Multisatellite Precipitation Analysis (TMPA) on a global scale at a monthly temporal step [1]. Differences between IMERG and TMPA estimates were related to surfaces type and precipitation rates with a tendency for IMERG to better capture major heavy precipitation regions. Over India, on a daily scale and using rain gauges as a reference, IMERG is more suitable to represent monsoon rainfall than GSMaP-v6 and TMPA gauges adjusted versions while GSMaP-v6 slightly outperformed IMERG and TMPA over low rainfall Indian regions [2]. Over Iran, in comparison with gauges measurements, IMERG daily estimates are more accurate than TMPA considering categorical and quantitative statistical analysis [3]. Over China, in comparison with rain gauge estimates, IMERG monthly estimates are more accurate than TMPA [4] with the same observations made at daily and sub-daily scales [5]. Due to the small number of publications about GPM-derived SREs, there is still a need for more assessment studies in other regions of the globe. This is even true when considering GSMaP-v6 as there is only one study reported on its accuracy assessment [2]. In this context, we assessed for the first time IMERG and GSMaP-v6 over Bolivia, using 247 rain gauges as a reference. Bolivia is a very interesting region for such studies, as it includes very wet, wet, and semi-arid to arid regions corresponding to the Amazon, La Plata and Altiplano watersheds, respectively. Therefore, the SREs can be assessed for both heavy and low rainfall amounts as well as intensity. These regions are separated by the Andean Cordillera resulting in high elevation variation ranging over the country from few hundred meters to more than 6000 m. Thus, variable rainfall processes are observable and the SREs ability can be evidenced in relation to dominant rainfall processes. Here, IMERG and GSMaP-v6 are assessed for the very first time in Bolivia at annual, monthly and daily scales over the three main hydrological watersheds (Altiplano, Amazon and La Plata) separately for both wet and dry seasons. Topography is a well-known factor influencing SREs and, generally, SREs are more biased over mountainous regions than over relative flat regions [6–8]. Therefore, a complementary analysis regarding the topographic influence is done by assessing SREs' potentiality over different slope classes for each national watershed separately. In previous studies [9,10], TMPA was found to provide the most accurate SREs over the country, in comparison to Climate prediction center MORPHing (CMORPH), Precipitation Estimation from remotely Sensed Information using Artificial Neural Networks (PERSIANN), GSMaP-v5, Climate Forecast System Reanalysis and Reforecast (CFSR) and Modern-Era Retrospective Analysis for Research and Application (MERRA) products considering annual, monthly and daily rainfall amount. Thus, TMPA is considered to observe the potential enhancement brought by IMERG and GSMaP-v6 products.

2. Materials and Methods

2.1. Study Area

Bolivia is located in central South America with an extent close to 1,100,000 km^2. Elevation ranges between 75 and 6549 m following an increasing east-west pattern from the Amazon to the Altiplano region. Bolivia can be divided into three main watersheds: The Titicaca, Poopó, Desaguadero and

Salar system (TDPS), La Plata and Amazon with a superficial extent of approximately 149,000, 226,000 and 716,000 km^2, respectively (Figure 1a). The Altiplano region is trapped between the occidental and oriental cordillera at a mean elevation of 4000 m with mean slope value of 4.7° [11,12]. The climate throughout the region is semi-arid with mean rainfall of 350 mm (1998–2015). According to SRTM and TMPA data [9,12], the Amazon region is located at a mean elevation of 680 m with a mean slope value of 5.3° and a mean annual rainfall of 1550 mm (1998–2015). Finally, the La Plata watershed presents a mean elevation of 1350 m for a mean slope value of 7° and a mean annual rainfall of 850 mm (1998–2015).

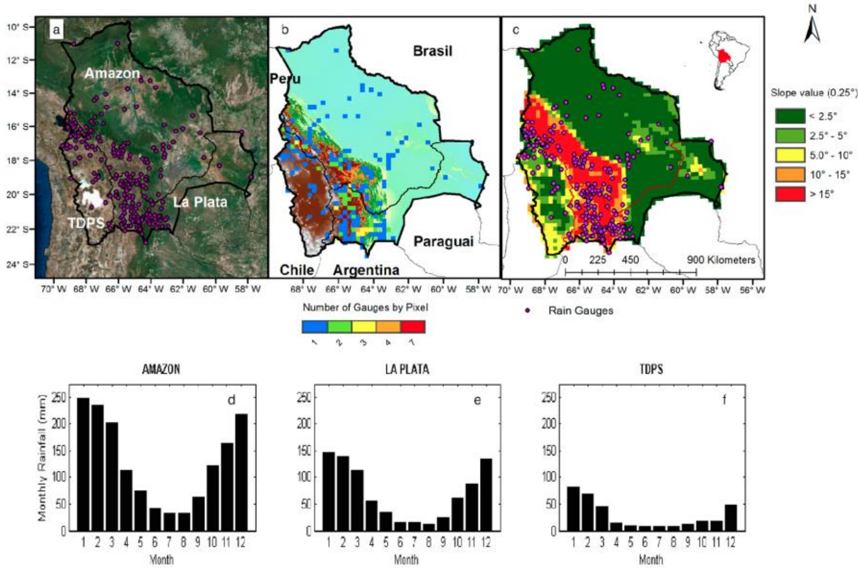

Figure 1. The study area (**a**) with the number of rain gauges included in studied 0.25° SREs pixels (**b**) 0.25° mean slope pixel derived from SRTM-GL1 (**c**) and mean monthly rainfall amounts derived from TMPA for the 1998–2015 period for each considered regions (**d**–**f**).

2.2. Datasets

IMERG is a product of the National Aeronautics and Space Administration (NASA). Rainfall estimate algorithms involve components from the previous algorithms of TMPA, CMORPH and PERSIANN rainfall estimates. IMERG uses both passive microwave (PMW) and infra-red (IR) sensors available from Low Earth Orbital (LEO) and geostationary satellites, respectively. Firstly, rainfall estimates are derived from PMWs using the Goddard profiling algorithm 2014 (GPROF2014) [13] and IR rainfall estimates provided by the Climate Prediction Center (CPC). Then, the CMORPH–Kalman filter Lagrangian time interpolation is used to produce half-hourly estimates from PMW and IR estimates. Finally, an adjustment of rainfall estimates is made by using the Global Precipitation Climatology Centre's (GPCC) figures for monthly precipitation. Three stage levels of IMERG rainfall estimates are available, and are called Early-, Late- and Final Run, respectively. The Early- and Late Run only use PMW and IR data while the Final Run includes a GPCC adjustment. All the products are delivered at half-hourly, daily and monthly scales on at 0.1° grid box. In this study, we used the IMERG Final Run (called IMERG hereafter).

GSMaP-v6 is a product of the Japan Science and Technology (JST) agency under the Core Research for Evolutional Science and Technology (CREST). GSMaP-v6 uses a combination of PMW and IR data from CPC. The algorithms used to retrieve the rainfall rate from PMWs utilize brightness temperature. IR data from CPC merged at 4 km are used to increase the temporal and spatial resolutions. To do so, a Kalman filter refined PMW rainfall estimation propagation by using the atmospheric moving vector derived from two successive IR images [14]. In comparison to the previous GSMaP-v5, GSMaP-v6 includes new algorithms to enhance rainfall estimates over land and ocean [15]. GSMaP-v6 is available in the form of near-to-real-time and post-adjusted versions. In this study, we used the post-adjusted version of the GSMaP-v6 gauge, which is gauge-adjusted by using daily CPC global rain gauge data set.

TMPA is a product of NASA in collaboration with the Japan Aerospace Exploration Agency (JAXA). It provides rainfall estimates at a 0.25° spatial resolution over 50°N to 50°S at a 3-hourly temporal scale. Passive microwave (PMW) radiometers on board LEO satellites are used to estimate rainfall rates. IR data from the CPC of the National Weather Service/NOAA (CPC-IR here-after), from the Meteorological Operational satellite program (MetOp) and from the 0.07° Grisat-B1 are used to fill the gaps between PMW measurements [16]. There is a Real Time version (TMPA-RT v7) based only on PMW and IR data, and an adjusted version (TMPA-Adj v7) using gauge-based data from GPCC and Climate Assessment and Monitoring System (CAMS). In this study, we used the TMPA-Adj v7 (called TMPA hereafter).

The Servicio Nacional de Hidrología y Meteorología (SENAMHI) of Bolivia is in charge of the national hydro-meteorological network stations. For this study, SENAMHI provided the daily rainfall data of 247 stations over the regions for the 2014–2016 period. TDPS, La Plata and Amazon regions count with 37, 111 and 99 rain gauges, respectively (Figure 1a). The stations are distributed on 233 SRE 0.1° and 187 SRE 0.25° spatial resolution pixels.

2.3. Method Used

2.3.1. Pre-Process

For the inter-comparison with TMPA, GSMaP-v6 and IMERG were resampled to the 0.25° grid box [4]. To do so, GSMaP-v6 and IMERG were first sampled from 0.1° to 0.05°, then the rainfall at the 0.25° was obtained by taking the mean rainfall value of the 5 pixels (0.05°) included into the 0.25° pixel. At each rain gauge location, daily and monthly rainfall series were derived from the gauges and the corresponding TMPA, IMERG and GSMaP-v6 pixels. GSMaP-v6 and IMERG were cumulated from hourly and 30 min, respectively, to derive daily and monthly temporal series at 0.25° and 0.1° resolution. TMPA was cumulated from 3-hourly to derive daily and monthly temporal series at 0.25° resolution. When various gauges were available on a single pixel (Figure 1b), the mean rainfall value of all gauges included in the corresponding pixel was computed.

Finally, the digital elevation model SRTM-GL1 [12] was used to derive the mean slope value in the 0.25° grid box (Figure 1c). Slope values were computed at the native 1 arc second SRTM-GL1 mesh-size and resampled to the 0.25° grid box by meaning the slope value corresponding to each 0.25° grid box.

2.3.2. Comparison Methodology

First, annual rainfall maps were generated from IMERG and GSMaP-v6 at both 0.1° and 0.25° scales and from TMPA at 0.25° resolution to highlight the SREs' ability to represent regional patterns (Figure 2). For comparison, a rainfall map was derived from the 247 available gauges at the 0.25° using the Inverse Distance Weight (IDW) interpolation. Additionally, comparisons between gauges and SREs were done at the national scale and for each watershed separately, considering Coefficient Correlation (CC), Root Mean Square Error (RMSE) in percent and Bias in percent at both 0.1° and 0.25° grid box (Table 1).

Secondly, SREs were assessed at the monthly scale by comparing monthly SREs and gauge estimates. Comparisons between gauges and SREs were done at the national scale and for each watershed separately. At each considered spatial scale, CC, RMSE, Bias and Standard Deviation (STD) were computed considering all months and for dry and wet seasons, separately, to observe the seasonal variability in the SREs' ability. Wet and dry seasons extend from November to March and from April to October, respectively (Figure 1d–f). For IMERG and GSMaP-v6, statistical scores were computed at both 0.1° and 0.25° scales to observe the potential enhancement introduced by the finer 0.1° resolution. To facilitate the interpretation of CC, RMSE and STD, the results are presented in form of Taylor diagram [17] (Figure 3). The Taylor diagrams allow a direct comparison between SREs by offering the opportunity to consider STD, CC and RMSE as a whole. RMSE and STD values were normalized to allow comparison between watersheds as rainfall amounts differ from one to another watershed (Figure 1d–f). The normalization process was made by dividing the SREs RMSE and STD values by the STD of the reference. As a result, in the Taylor diagrams, the reference is represented by the dot black point in which, the STD, RMSE and CC values are equal to 1, 0 and 1, respectively. Therefore, the lower the distance between the SREs and reference, the closer the SREs and reference rainfall estimates are. Additionally, Bias values are presented in Table 2 to observe the potential over/under estimation of each considered SRE. RMSE in percent and CC are also presented in Table 2 to complete the Taylor diagram analysis. To observe the topographic influence on monthly SREs from TMPA, IMERG and GSMaP-v6, a supplementary analysis was performed. For each national watershed (Amazon, La Plata and TDPS) the mean slope value at each 0.25° pixel derived from SRTM-GL1 (Figure 1c) was used to separate the 187 0.25° grid box pixels in 5 slope classes. The five considered slope classes are 0°–2.5°, 2.5°–5°, 5°–10°, 10°–15° and >15°. Each class gathered, respectively, 23, 5, 7, 22 and 26 pixels for the Amazon region, 8, 1, 12, 32 and 19 pixels for the La Plata region and 8, 10, 11, 2 and 0 pixels for the TDPS region. For each region and classes, CC, RMSE and Absolute Bias (AB) were computed considering all months (Figure 4 and Table 3). The seasonal assessment of this study shows high variation in Bias values oscillating between positive and negative value according to the considered season. Thus, to avoid seasonal effects on the interpretation of result, we preferred the use of the AB value instead of bias value. The assessment was not done at the national scale as topographic effects are expected to vary in function to the regional rainfall pattern. Therefore, topographic effects would be different from one region to another and difficult to observe at the national scale. The analysis was only performed at the 0.25° grid box size as close to similar accuracy in IMERG and GSMaP-v6 are observed for 0.1° and 0.25° grid box size.

Finally, a daily analysis using categorical statistical analysis was done considering both all days and wet and dry seasons, separately. Rainfall amounts were considered as discrete values with only two observable cases: rainy day or not. A rainy day is considered when the precipitation amount is greater than or equal to a prescribed threshold (mm day^{-1}). For pixels including more than one rain gauge, the mean daily rainfall from all rain gauges was considered. It is noteworthy that some authors consider a pixel to be rainy when any of the gauges observed a rainfall amount greater or equal to the prescribed threshold. This consideration allows the consideration of the rainfall variability at the pixel scale [6]. However, such consideration requires the availability of various gauges into the considered pixel. In this study, only a few pixels count for more than one rain gauge and are mainly located over the La Plata region. Therefore, to get a homogeneous assessment over the entire study area, we did not use such a methodology. Here, we fixed the threshold value to 1 mm day^{-1}, as used by [18]. Four cases are possible: both SRE and rain gauge report a rain event (a), only SRE reports a rain event (b), only rain gauge reports a rain event (c) or neither SRE nor rain gauge report a rain event (d).

According to this characterization, several statistical parameters can be computed: the Probability of Detection (POD), the False Alarm Ratio (FAR), the Critical Success Index (CSI) and the Bias (B) (Equations (1)–(4)) [9,18–23].

$$\mathrm{POD} = \frac{\mathrm{a}}{(\mathrm{a}+\mathrm{c})} \tag{1}$$

$$\mathrm{FAR} = \frac{\mathrm{b}}{(\mathrm{a}+\mathrm{b})} \tag{2}$$

$$\mathrm{CSI} = \frac{\mathrm{a}}{(\mathrm{a}+\mathrm{b}+\mathrm{c})} \quad (3)$$

$$\mathrm{B} = \frac{(\mathrm{a}+\mathrm{b})}{(\mathrm{a}+\mathrm{c})} \quad (4)$$

POD is an indicator of the SRE's ability to correctly forecasts rain events. Values vary from 0 to 1, with 1 as a perfect score.

FAR is an indicator of how often SREs detect a rain event when, actually, it does not occur. Values vary from 0 to 1, with 0 as a perfect score. FAR is also represented in form of the Success Ratio (SR = 1 − FAR).

CSI is the ratio between the number of a rain events correctly detected by the SRE and the number of all rain events registered by the gauge and the SRE data. Values vary between 0 and 1 with a perfect score of 1.

B is the ratio of satellite rain estimates to actual precipitation events. A B value above or below 1.0 implicates that the SRE overestimates or underestimates the number of rain events in a considered period.

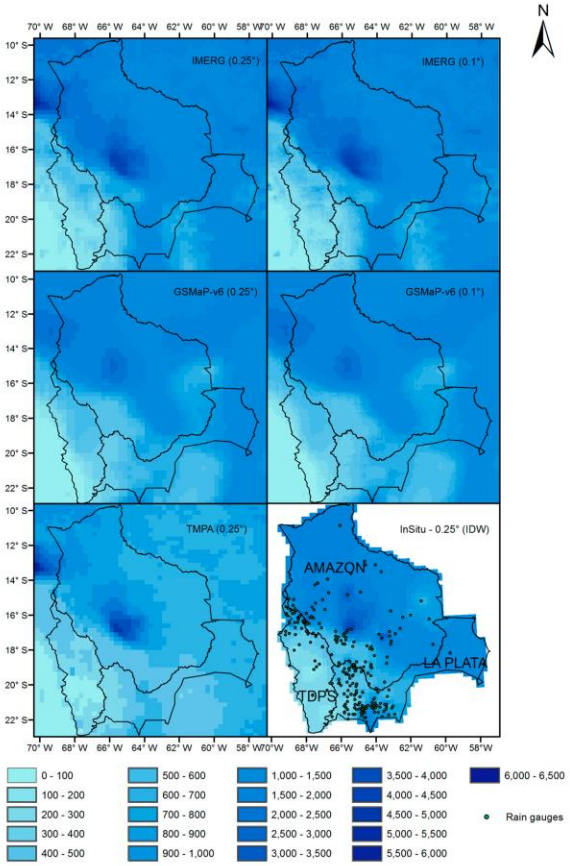

Figure 2. Annual rainfall pattern for all SREs. Rainfall amounts are in mm.

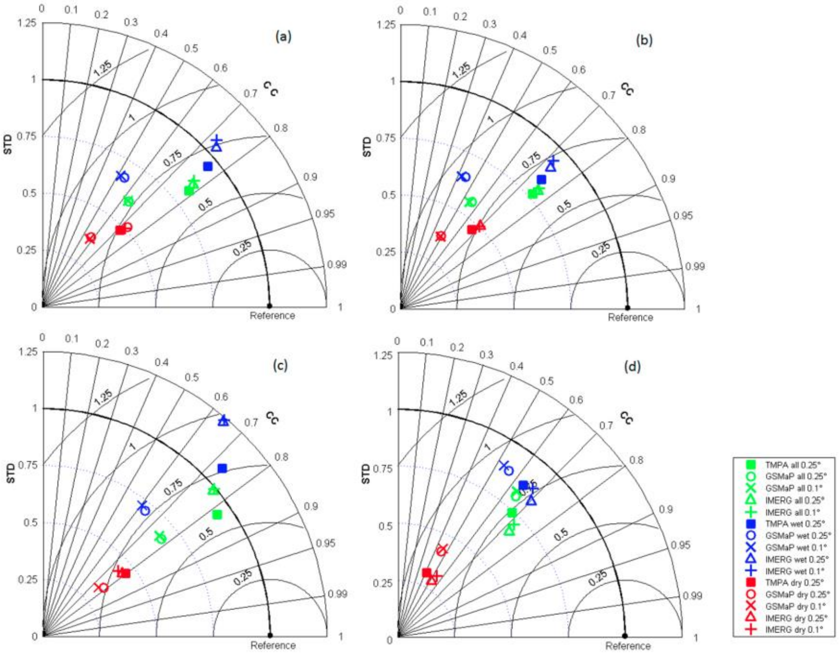

Figure 3. Taylor diagram for monthly rainfall considering the whole Bolivia (**a**), Amazon (**b**), La Plata (**c**) and TDPS (**d**) regions separately. The continuous curved lines represent RMSE values.

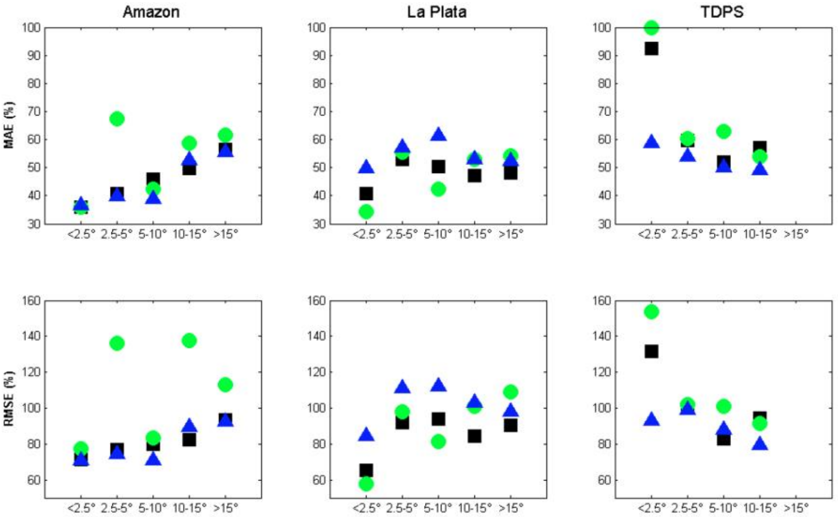

Figure 4. Absolute Bias (%) and RMSE (%) for different slope classes. Black squares, blue tringle and green point represent TMPA, IMERG and GSMaP-v6, respectively.

In the same way as for the monthly analysis, the results are presented in form of a synthesis diagram to consider POD, FAR, CSI and B as a whole in order to facilitate SREs' inter-comparison. The performance diagram [24] is used in this study as it was previously used for daily rainfall analysis over the Brazilian Amazon region [18]. The geometric relationship between SR, POD, B and the CSI is used to construct the performance diagram. Thus, the perfect forecast is lying in the upper right region of the diagram (Figure 5). Additionally, POD, FAR, CSI and B values are presented in Table 4 to complete the Performance diagram analysis. To complete the assessment, SREs' potentiality at the daily scale was also assessed, considering the mean slope classes used at the monthly scale. For each watershed, POD and FAR were computed for TMPA, IMERG and GSMaP-v6 for all considered classes (Figure 6). The topographic analysis was only performed at the 0.25° grid box size as close to similar accuracy in IMERG and GSMaP-v6 are observed for 0.1° and 0.25° grid box size.

3. Results and Discussion

3.1. Annual Scale

Figure 2 represents the annual rainfall maps for IMERG, GSMaP-v6 and TMPA for the 2014–2015 hydrological year. Over the region, with regard to annual maximum a great discrepancy is observed between SREs. A maximum value close to 3000, 5000 and 6400 mm year^{-1} is observed for GSMaP-v6, TMPA and IMERG. These high annual rainfall amount values are related to the especially strong ENSO anomaly which occurred that year, causing historical flooding in the Amazon watershed [25]. TMPA and IMERG seem more sensitive to extreme rainfall than GSMaP-v6 with higher rainfall amount observed which are closer to the maximum observed from gauge measurements (Figure 2). Similar CC, RMSE and Bias value from both IMERG and TMPA were obtained while GSMaP-v6 considerably underestimated rainfall amount by 30% (Table 1).

In the Amazon region, the two previously-evidenced rainfall hotspots [26] in the north-west corner and central amazon region are well detected by all SREs. In a general sense, GSMaP-v6 rainfall pattern is smoother than IMERG and TMPA. For example, over the TDPS, GSMaP-v6 has better captured the typical north-south decreasing rainfall patterns. However, the rainfall amount was poorly retrieved from GSMaP-v6 with the lowest CC and highest Bias and RMSE value among considered SREs and for all considered regions (Table 1).

TMPA and IMERG rainfall patterns are very close as they include very similar sensors and algorithm to retrieve rainfall. It is noteworthy that TMPA presents some spurious pixels with anomalous rainfall amounts relative to their neighboring pixels. This is clearly observable over the TDPS southern western parts. These pixels were well removed from IMERG estimates. This feature was already observed in China [4]. Here and in China, this occurs over regions with low rainfall amounts, showing TMPA difficulty over arid regions and the enhancements brought by the new IMERG over TMPA. In the actual context of climate variability and increased water usage for agriculture purpose over the TDPS region [27], IMERG offers great potential for regional monitoring and protection.

Indeed, IMERG presents a slightly better statistical score than TMPA over the TDPS region (Table 1). The finer 0.1° grid box size did not provide more accurate SREs, with similar statistical scores being observed for IMERG and GSMaP-v6 for all considered regions.

Table 1. Annual Bias (%), RMSE (%) and CC for TMPA, IMERG and GSMaP-v6.

	TMPA			**IMERG**						**GSMaP-v6**					
	Bias	**RMSE**	**CC**	**Bias**		**RMSE**		**CC**		**Bias**		**RMSE**		**CC**	
	0.25°	**0.25°**	**0.25°**	**0.1°**	**0.25°**	**0.1°**	**0.25°**	**0.1°**	**0.25°**	**0.1°**	**0.25°**	**0.1°**	**0.25°**	**0.1°**	**0.25°**
Bolivia	3.6	55.4	0.8	4.1	3.4	55.6	55.9	0.79	0.79	−25.1	−25.1	81.1	81.2	0.52	0.53
Amazon	1.8	53.4	0.76	3.1	3.5	52.8	52.3	0.78	0.77	−31.5	−30.7	83.5	81.3	0.38	0.38
La Plata	6.2	45.1	0.7	8.3	5.7	51.6	52.8	0.6	0.59	−19.7	−19.4	53.8	54.5	0.6	0.6
TDPS	7.9	54	0.63	−6.1	−5.6	49	51.5	0.68	0.67	−4.1	−2.8	55.9	56.8	0.53	0.54

3.2. Monthly Scale

Figure 3 presents the Taylor diagram for monthly rainfall for all the considered regions. Generally, all SREs performed better during the wet season than during the dry season. During dry seasons, rainfall amounts are lower and shorter in time, making their detection complicated by PMWs sensors [28,29]. During wet seasons for all considered regions, TMPA presents CC higher than 0.7, RMSE close to 50% and Bias values into the −10%–10% intervals (Table 2; Figure 3). These specific values were previously defined as objective values to ensure the good performance of SREs at monthly scale [9,10,19,30]. Results over the TDPS and for TMPA are in line with a previous study of the 2005–2007 period [9] with similar CC, RMSE and Bias values. Thus, the change in calibration procedure due to the end of TRMM Precipitation Radar estimates in October 2014 did not have a significant impact on TMPA rainfall estimates over Bolivia.

Regarding IMERG, at the 0.25° mesh size and global scale, statistical results are very close to TMPA and thus IMERG keeps on measuring rainfall at the same accuracy level as TMPA (Figure 3, Table 2). However, during the wet season, TMPA is slightly more suitable than IMERG due to its closer relative position to the dot-pointed reference (Figure 3); and IMERG is slightly more accurate than TMPA during the dry season, with lower Bias and RMSE and higher CC (Figure 3 and Table 2).

Some discrepancies are observed along the considered regions. Over the Amazon region, IMERG and TMPA performances are very similar (Figure 3), with close Bias, CC and RMSE values (Table 2). As for the global scale (Bolivia), TMPA slightly outperforms IMERG during the wet season and the opposite case is observed during the dry season (Figure 3, Table 2). Over the TDPS region, IMERG outperforms TMPA for all the considered seasons (Figure 3). This confirms the annual observation, with some pixels anomalously biased in relation to their neighboring pixels in both this study and that conducted over a similar region in China [4]. However, IMERG still slightly underestimates monthly rainfall amounts, as a negative bias of −18.2% is observed (Table 2). A higher discrepancy between IMERG and TMPA is observed over the La Plata river watershed. In this region, TMPA highly outperforms IMERG during the wet season with lower RMSE and higher CC (Figure 3; Table 2). Over this region, reference rainfall amounts are lower than in the Amazon (Figure 1d,e), and gauges are located over high, rough relief regions (Figure 1c). Indeed, the mean regional slope is estimated at 7°, according to SRTM-GL1 measurements, which have remained higher than the values of 4.7° and 5.3° registered for the TDPS and Amazon region, respectively. Thus, IMERG estimates are more affected by local relief and rainfall intensities than TMPA. These differences are characterized by lower CC and a RMSE increase of 18%. The future improvements brought to IMERG algorithms should focus on those specific features (rainfall amount and relief), to at least continue measuring rainfall estimates with the same accuracy trend as TMPA.

Passing from 0.1° to 0.25° grid box did not have a significant influence on rainfall estimate accuracy with quite similar CC, RMSE and Bias values at both 0.1° and 0.25° grid box for all regions and seasons (Figure 3; Table 2). For comparison, the spatial aggregation of SREs grid box was already found to be insignificant over the Altiplano (TDPS) considering TMPA estimates [21].

GSMaP-v6 is the least accurate considered SREs over the whole Bolivia with very high RMSE value higher to 100%, Bias values lower to −20% and low CC value lower to 0.7 (Table 2; Figure 3). None of the considered parameters fit the previously defined quality thresholds. The lower annual rainfall estimates observed for GSMaP-v6 in comparison to TMPA, IMERG and rain gauges (Figure 2) is confirmed by negative bias value at both 0.1° and 0.25° scales. GSMaP-v6 underestimates monthly rainfall at global scale and over the Amazon and La Plata regions at seasonal scale and for both dry and wet periods. GSMaP-v6 bias is lower over arid TDPS region with positive bias value. This shows the slight enhancement of GSMaP-v6 estimate over the TDPS arid region, and is in line with results observed over low-rainfall regions in India [2].

As observed for IMERG, the resampling step from 0.1° to 0.25° mesh size did not affect GSMaP-v6 estimates with very close relative position of both GSMaP-v6 at 0.25° and 0.1° in the Taylor diagrams (Figure 3) and close statistical score (Table 2).

Regarding the topographic assessment, very different patterns are observed from one region to another. Over the Amazon region, and for all SREs, the AB and RMSE values tend to increase with slope value while the opposite is observed over the TDPS region with a decrease of AB and RMSE values when mean slope value increase. Topography is known to affect SREs, and so do the rainfall amounts. Indeed, higher biases are generally observed over mountainous regions, and SREs are less accurate over arid regions in comparison to wet regions [6,8,9]. As a humid region, the Amazon region is well suited to observing topographic effects, because SREs' accuracy is not affected by low rainfall amounts (arid regions). Thus, the only factor altering SREs' accuracy in space is the topography. Actually, from lowlands to mountainous regions, AB and RMSE increased by approximately 20% for both IMERG and TMPA, and by approximately 30% for GSMaP-v6 (Figure 4 and Table 3). Over the TDPS region, the rainfall pattern follows a marked north-south gradient with rainfall amount decreasing from north to south. This typical rainfall pattern controls SREs' potentiality with SREs being more accurate in the northern, humid part than over the southern, more arid, part [9]. In this study, pixels with higher slope values are located in the northern part (high rainfall amount) while pixels with low slope value are located in the southern part (low rainfall amount) (Figure 1c). As a result, AB and RMSE values decreased by close to 10%, 20% and 50% for IMERG, TMPA and GSMaP-v6 from low to high slope region (Figure 4 and Table 3). Therefore, over the TDPS region the climatological context is the predominant factor influencing SREs' accuracy in space, rather than topographic effects. It is noteworthy that for all considered slope classes, IMERG presents close to the lowest AB and RMSE values, and higher CC values, confirming the higher performance previously observed over the same region for the annual and monthly seasonal comparisons (Figure 3, Tables 1 and 2). Over the La Plata region, no 'linear' relation is observed between topographic effect (slope value) and the SREs' accuracy. However, topographic influence is still observed with lower AB and RMSE values over the flat regions (slope <2.5°). Between the first class (<2.5°) and second class (2.5°–5°), all SREs present a positive gap in AB and RMSE values remaining high and relatively constant for all next classes (Figure 4 and Table 3). The observed AB increase between flat region class (slope <2.5°) and the rest of the considered classes is of approximately 10% for both IMERG and TMPA and close to 20% for GSMaP-v6. This non-linear trend between SRE accuracy and slope value should be related to the rain gauges' distribution. Indeed, most of the gauges with slope values higher than 2.5° are located and trapped in high-slope regions (Figure 1c). As a result, for those pixels there is a high discrepancy between neighboring slope values, which is not observed for the pixels with slope value lower than 2.5° (Figure 1c). Therefore, pixels with slope values above 2.5° are under a homogeneous topographic effect, expected to be similar among all classes that could explain the tendency observed in Figure 4.

In a general sense, IMERG keeps providing rainfall estimates as accurate as TMPA over the Amazon region, while offering the possibility to observe more local scale variation thanks to its lower grid box size. The main enhancement is observed over the TDPS arid region, where a slight increase in rainfall estimates is obtained from IMERG. However, over the mountain-dominated region of the La Plata head watershed, TMPA provides more accurate rainfall estimates than the new IMERG. The results evidence a relation between SRE accuracy and both seasonal and topographic contexts. SREs are generally more accurate during the wet season as rainfall amounts are higher than during the dry season. In the same way, SREs are more accurate over the low slope region as topographic effects are less important. In this context, it is noteworthy that the gauges' distribution influenced the observed results and conclusion. SREs' lower suitability observed over the La Plata region is partially explained by the distribution of the gauges. Actually, most of the gauges are located over the mountainous region where high slope values influence SREs (Figure 4). Different conclusions would have been dressed if the gauges were located over the low lands where slopes are lower and SREs would appear more efficient. In a similar way, over the TDPS region, most of the gauges are located on the northern wet part where SREs are known to be more accurate than over the southern arid region [9]. Different conclusions would have been achieved if the gauges were located on the southern arid region. The potential intercomparison of SREs between the Amazon, La Plata and TDPS should be made with caution as different conclusions should be make from different rain gauge distribution.

Table 2. Monthly Bias (%), RMSE (%), and CC for TMPA, IMERG and GSMaP-v6 for both wet and dry seasons.

		TMPA 3B43			**IMERG-FR (0.1°–0.25°)**						**GSMaP-v6 (0.1°–0.25°)**					
		Bias	**CC**	**RMSE**	**Bias (%)**		**CC**		**RMSE**		**Bias**		**CC**		**RMSE**	
		0.25°	**0.25°**	**0.25°**	**0.1°**	**0.25°**	**0.1°**	**0.25°**	**0.1°**	**0.25°**	**0.1°**	**0.25°**	**0.1°**	**0.25°**	**0.1°**	**0.25°**
Bolivia	All	1.2	0.78	90.7	−2.3	−1.4	0.77	0.78	95.2	92.7	−22.6	−22.4	0.63	0.63	116.8	115.1
	Wet	5.7	0.76	64.2	−0.1	0.7	0.72	0.74	70.4	68.2	−20.9	−20.7	0.51	0.54	87	85.7
	Dry	−7.2	0.71	135.9	−6.5	−5.3	0.73	0.73	134.6	131.5	−25.9	−25.6	0.57	0.57	162.9	160.1
Amazon	All	0.5	0.75	82.7	−1.2	0.8	0.76	0.76	84.6	82	−30.1	−29.1	0.54	0.56	112	108.7
	Wet	6.2	0.74	59.7	1.9	3.3	0.72	0.73	63.5	60.7	−28.9	−28	0.42	0.44	87.9	84.5
	Dry	−8.5	0.67	117	−6.2	−3.2	0.69	0.7	114.7	112.8	−32	−30.7	0.49	0.49	142.4	140.1
La Plata	All	1.4	0.82	86.1	−10	−1.4	0.76	0.76	102.1	100.8	−17	−16.5	0.76	0.77	98.8	96.1
	Wet	4.9	0.73	63.3	−17	0.7	0.64	0.65	76	76.5	−16.4	−15.4	0.6	0.63	72.3	71.4
	Dry	−8.5	0.8	120.5	10.2	−7.2	0.76	0.79	132.8	122.6	−18.8	−19.7	0.75	0.78	135.6	129.2
TDPS	All	6.1	0.68	105.4	−17.4	−18.2	0.72	0.73	74.1	80.6	9.4	10.2	0.64	0.64	142.8	145.4
	Wet	4.9	0.64	58.6	−16.2	−16.8	0.67	0.7	41.6	44.8	11.2	11.6	0.53	0.56	80.2	80.8
	Dry	8.9	0.41	207.3	−20	−21.2	0.54	0.52	143.2	158.6	5.4	7.3	0.46	0.45	275.8	286.1

Table 3. Monthly AB (%), RMSE (%) and CC for TMPA, IMERG and GSMaP-v6 for different slope classes.

	Classes	**TMPA**			**IMERG**			**GSMaP-v6**		
		AB	**RMSE**	**CC**	**AB**	**RMSE**	**CC**	**AB**	**RMSE**	**CC**
Amazon	0°–2.5°	35.9	71.4	0.71	36.7	70.7	0.71	35.8	77.5	0.66
	2.5°–5°	40.8	76.8	0.80	39.9	74.1	0.81	67.3	136.3	0.16
	5°–10°	45.8	80.0	0.87	38.7	70.8	0.90	42.3	83.5	0.86
	10°–15°	49.8	82.2	0.85	52.8	89.5	0.82	58.7	137.7	0.41
	>15°	56.6	93.6	0.64	55.6	92.2	0.66	61.5	113.1	0.47
La Plata	0°–2.5°	40.8	65.3	0.87	49.6	84.6	0.75	34.4	57.9	0.86
	2.5°–5°	53.0	91.9	0.89	57.2	111.0	0.89	55.6	97.9	0.86
	5°–10°	50.5	94.0	0.81	61.3	111.8	0.79	42.3	81.5	0.83
	10°–15°	47.2	84.3	0.85	52.8	102.8	0.79	52.9	101.0	0.77
	>15°	48.0	90.6	0.79	52.3	97.8	0.75	54.2	108.8	0.71
TDPS	0°–2.5°	92.6	131.8	0.71	58.8	93.2	0.83	100.0	153.9	0.69
	2.5°–5°	59.8	99.8	0.56	53.8	99.0	0.61	60.4	101.9	0.56
	5°–10°	52.0	83.1	0.81	50.2	87.8	0.77	63.0	100.8	0.72
	10°–15°	57.1	94.5	0.84	49.0	79.5	0.90	53.9	91.2	0.79

3.3. Daily Scale

Figure 5 presents the POD, SR, CSI and B values for all SREs and all the considered regions in the form of a performance diagram. At the national scale and for all regions, all SREs better detect rainfall events during the wet season than during the dry season. As observed at the monthly scale, in the Amazon region, the ability of IMERG and TMPA to forecast daily rainfall are very similar (Figure 5). In the TDPS region, IMERG outperforms TMPA at both wet and dry season as its relative position to zero in Figure 5 is further than the relative TMPA position. This confirms the slightly better estimation observed at the monthly scale for IMERG in comparison to TMPA over the same region. With regard to the La Plata region, the ability of IMERG to detect daily rainfall is better than that of TMPA. However, TMPA remains more accurate at the monthly scale. Therefore, the relatively poor accuracy for monthly estimates observed for IMERG in comparison to TMPA over the same region seems to be linked to inaccuracy in daily rainfall amount estimates, rather than to their detection. Indeed, IMERG seems to underestimate daily rainfall amount as a negative monthly bias is observed (Table 2).

As noted for the monthly scale, the aggregation process from 0.1° to 0.25° does not change the ability of IMERG, according to the daily analysis. Indeed, both the 0.1° and 0.25° versions are very close into the performance diagram for the Amazon and TDPS regions (Figure 5). Interestingly, over the La Plata region, the 0.1° grid box version of IMERG is slightly less suitable for discretizing rainy and non-rainy days. This confirms the general deficiency of IMERG at capturing the spatial variability of local rainfall induced by topographic features in this specific region. Passing from a 0.1° to a 0.25° grid box smoothed the rainfall spatial variability and should explain the slightly better ability of the 0.25° grid box version at the daily scale.

Regarding the topographic assessment, over the Amazon and La Plata regions, SREs' ability in differentiating rainy from non-rainy days decreases with the increase of slope value. For the Amazon region, POD and FAR respectively decrease and increase from flat- to high-slope regions. For the La Plata region POD decreases while the FAR remains relatively constant along the considered classes. Therefore, those observations agreed with monthly topographic assessment (Figure 6). Over the TDPS region, FAR decreased from flat- to high-slope regions, while no clear tendency is observed for the POD value along the considered classes. These results agreed with the monthly analyses, with the rainfall pattern as the main factor controlling SRE potential.

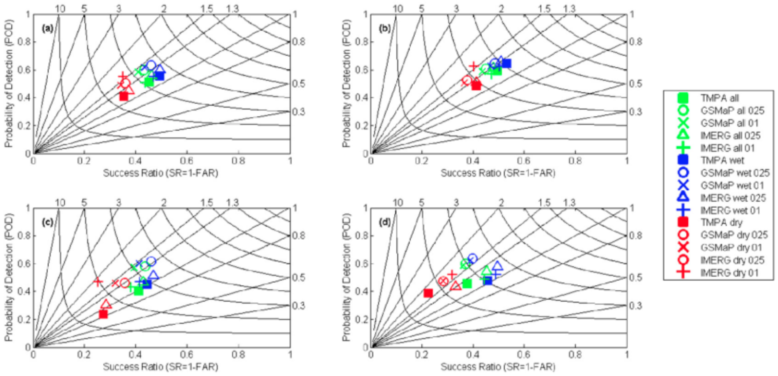

Figure 5. Performance diagram for the whole Bolivia (**a**), Amazon (**b**), La Plata (**c**) and TDPS (**d**) regions. Straight and curved lines represent the B and CSI values, respectively.

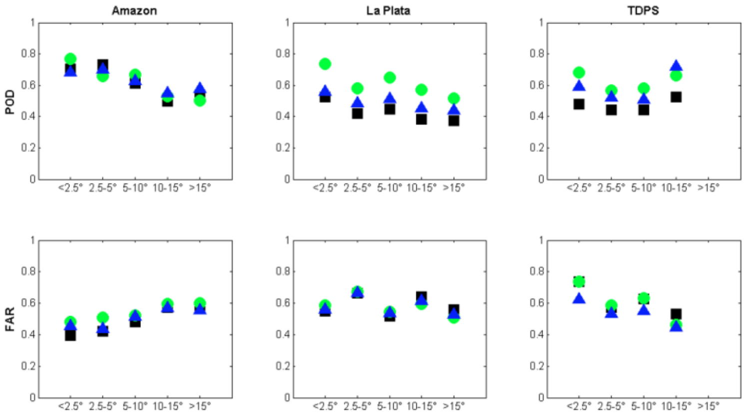

Figure 6. POD and FAR for different slope classes. Black squares, blue tringle and green point represent TMPA, IMERG and GSMaP-v6, respectively.

Table 4. POD, FAR, BIAS and CSI for TMPA, IMERG and GSMaP-v6 for both wet and dry season.

		TMPA				**IMERG**								**GSMaP-v6**							
		POD	**FAR**	**BIAS**	**CSI**	**POD**		**FAR**		**BIAS**		**CSI**		**POD**		**FAR**		**BIAS**		**CSI**	
		0.25°	**0.25°**	**0.25°**	**0.25°**	**0.1°**	**0.25°**	**0.1°**	**0.25°**	**0.1°**	**0.25°**	**0.1°**	**0.25°**	**0.1°**	**0.25°**	**0.1°**	**0.25°**	**0.1°**	**0.25°**	**0.1°**	**0.25°**
Bolivia	All	0.51	0.55	1.13	0.32	0.51	0.56	0.56	0.54	1.16	1.2	0.31	0.34	0.58	0.6	0.59	0.57	1.42	1.38	0.32	0.34
	Wet	0.55	0.51	1.12	0.35	0.55	0.6	0.53	0.5	1.17	1.2	0.34	0.37	0.62	0.63	0.57	0.54	1.42	1.37	0.34	0.36
	Dry	0.41	0.65	1.16	0.23	0.4	0.45	0.65	0.63	1.14	1.2	0.23	0.26	0.49	0.5	0.66	0.64	1.43	1.4	0.25	0.27
Amazon	All	0.59	0.51	1.2	0.37	0.57	0.61	0.53	0.55	1.21	1.27	0.35	0.37	0.59	0.61	0.56	0.52	1.35	1.35	0.33	0.35
	Wet	0.65	0.47	1.22	0.41	0.62	0.66	0.5	0.52	1.24	1.29	0.39	0.4	0.63	0.65	0.53	0.49	1.34	1.33	0.37	0.38
	Dry	0.49	0.59	1.18	0.29	0.46	0.51	0.6	0.62	1.13	1.23	0.27	0.3	0.51	0.53	0.63	0.59	1.38	1.39	0.27	0.28
La Plata	All	0.4	0.59	0.99	0.26	0.43	0.47	0.62	0.57	1.13	1.09	0.25	0.33	0.57	0.58	0.61	0.56	1.45	1.33	0.3	0.29
	Wet	0.45	0.56	1.02	0.29	0.47	0.51	0.58	0.53	1.13	1.09	0.28	0.36	0.6	0.62	0.59	0.54	1.45	1.34	0.32	0.32
	Dry	0.24	0.73	0.87	0.14	0.28	0.3	0.75	0.72	1.12	1.07	0.15	0.25	0.46	0.46	0.68	0.64	1.43	1.29	0.23	0.17
TDPS	All	0.46	0.62	1.21	0.26	0.49	0.54	0.55	0.55	1.1	1.61	0.3	0.33	0.59	0.6	0.64	0.63	1.62	1.2	0.29	0.3
	Wet	0.48	0.54	1.05	0.3	0.52	0.58	0.51	0.5	1.07	1.6	0.34	0.36	0.62	0.64	0.61	0.6	1.6	1.16	0.32	0.32
	Dry	0.39	0.78	1.72	0.17	0.38	0.44	0.68	0.67	1.2	1.66	0.21	0.23	0.48	0.47	0.72	0.72	1.68	1.31	0.22	0.22

4. Conclusions

The new GPM rainfall products were assessed for the first time in Bolivia at the annual, monthly and daily scales. The analysis was done at the national scale and for the three main watersheds (Amazon, La Plata and TDPS), separately, at both wet and dry seasons and for different slope classes. Generally, IMERG achieved its main objective of continuing to measure rainfall with the same accuracy as its predecessor, TMPA. However, some discrepancies are observed when considering different rainfall features over the regions. Over the wet Amazon region, at the annual and monthly scale, in comparison to gauge estimates, IMERG performs similarly to TMPA while TMPA is slightly more accurate than IMERG over the La Plata watersheds. This should be linked to the mountainous context that interferes on IMERG measurements quantification as IMERG was found to better discretize rainfall events occurrence. Over the TDPS arid region, IMERG better quantifies monthly rainfall in both wet and dry seasons. The enhancement of rainfall estimates over arid regions is very valuable for future hydro-climatic studies, as little changes in rainfall patterns have a strong impact on local water budgets. An interesting observed enhancement brought by IMERG in comparison to TMPA is its better ability to discretize rainy and non-rainy days for all considered regions and seasons. Therefore, it brings good perspective for future studies using the ratio of rainy to non-rainy days as a constraining factor in agriculture and drought monitoring. GSMaP-v6 is the least accurate SRE in Bolivia and for all considered regions and seasons. It underestimates monthly rainfall amounts over the Amazon and La Plata regions and overestimates rainfall over the arid TDPS region.

The study also showed a clear topography influence on the SREs' potentiality. SREs are most biased over mountainous region in relation to high slope values. This is clearly evidenced over the Amazon and La Plata region. However, such observation is not possible over the TDPS watershed, due to the rain gauges' distribution in relation to slope variability and the typical regional rainfall pattern. Over the TDPS, the rainfall pattern represents the main factor controlling SREs' potentiality. Along these lines, the study shows the importance of gauges' distribution in the assessment and the conclusions made, especially regarding the SREs' potential to compare different geomorphological climatic regions (Amazon, La Plata and TDPS). Indeed, different results and conclusions should be obtained from a different rain gauges' distribution giving more or less weight to slope and rainfall effects on SREs. Therefore, future study should base on a gauge network distribution, defined to represent topographic and rainfall patterns as well as possible.

In a general sense, the main advantage of IMERG and GSMaP-v6 is the higher spatial resolution of 0.1° that offers the opportunity to observe small local rainfall pattern variations. Therefore, GPM rainfall estimates open the opportunity to transfer SRE-based study from hydrological, drought, agriculture monitoring, initially used on a regional scale, to more local, unmonitored scales. Even if these two new SREs took advantage of a larger PMWs and IR sensors for their respective rainfall estimates, they do not always provide the most accurate estimates. Thus, we hope this timely study will be proven helpful in the near future for the enhancement of current algorithms used in IMERG and GSMaP-v6. Finally, the SREs' dependency on topographic effects should be used as guidelines for future SRE-related study over the region, in order to try and minimize topographic effects on SREs.

Acknowledgments: This work was supported by the Centre National d'Etudes Spatiales (CNES) in the framework of the HASM project (Hydrology of Altiplano: from Spatial to Modeling). The first author is grateful to the IRD (Institut de Recherche pour le Développement) and CAPES (Coordenação de Aperfeiçoamento de Pessoal de Nível Superior) Brazil for the financial support and to the SENAMHI-Bolivia for the rain gauge data.

Author Contributions: Frédéric Satgé, Alvaro Xavier and Marie-Paule Bonnet conceived the experiments and analyzed the data. Jérémie Garnier, Ramiro Pillco Zolá, Yawar Hussain and Franck Timouk contributed in resolving problems during the data processing and interpretation. Frédéric Satgé and Marie-Paule Bonnet wrote the paper.

Conflicts of Interest: The authors declare no conflict of interest.

References

1. Liu, Z. Comparison of Integrated Multisatellite Retrievals for GPM (IMERG) and TRMM Multisatellite Precipitation Analysis (TMPA) Monthly Precipitation Products: Initial Results. *J. Hydrometeorol.* **2016**, *17*, 777–790. [CrossRef]
2. Prakash, S.; Mitra, A.K.; AghaKouchak, A.; Liu, Z.; Norouzi, H.; Pai, D.S. A preliminary assessment of GPM-based multi-satellite precipitation estimates over a monsoon dominated region. *J. Hydrol.* **2016**. [CrossRef]
3. Sharifi, E.; Steinacker, R.; Saghafian, B. Assessment of GPM-IMERG and Other Precipitation Products against Gauge Data under Different Topographic and Climatic Conditions in Iran: Preliminary Results. *Remote Sens.* **2016**, *8*, 135. [CrossRef]
4. Chen, F.; Li, X. Evaluation of IMERG and TRMM 3B43 Monthly Precipitation Products over Mainland China. *Remote Sens.* **2016**, *8*, 472. [CrossRef]
5. Tang, B.H.; Shao, K.; Li, Z.L.; Wu, H.; Nerry, F.; Zhou, G. Estimation and validation of land surface temperatures from chinese second-generation polar-orbit FY-3A VIRR data. *Remote Sens.* **2015**, *7*, 3250–3273. [CrossRef]
6. Müller, M.F.; Thompson, S.E. Bias adjustment of satellite rainfall data through stochastic modeling: Methods development and application to Nepal. *Adv. Water Resour.* **2013**, *60*, 121–134. [CrossRef]
7. Amani, M.; Parsian, S.; MirMazloumi, S.M.; Aieneh, O. Two new soil moisture indices based on the NIR-red triangle space of Landsat-8 data. *Int. J. Appl. Earth Obs. Geoinf.* **2016**, *50*, 176–186. [CrossRef]
8. Condom, T.; Rau, P.; Espinoza, J.C. Correction of TRMM 3B43 monthly precipitation data over the mountainous areas of Peru during the period 1998–2007. *Hydrol. Process.* **2010**, *25*, 1924–1933. [CrossRef]
9. Satgé, F.; Bonnet, M.-P.; Gosset, M.; Molina, J.; Hernan Yuque Lima, W.; Pillco Zolá, R.; Timouk, F.; Garnier, J. Assessment of satellite rainfall products over the Andean plateau. *Atmos. Res.* **2016**, *167*, 1–14. [CrossRef]
10. Blacutt, L.A.; Herdies, D.L.; de Gonçalves, L.G.G.; Vila, D.A.; Andrade, M. Precipitation comparison for the CFSR, MERRA, TRMM3B42 and Combined Scheme datasets in Bolivia. *Atmos. Res.* **2015**, *163*, 117–131. [CrossRef]
11. Satgé, F.; Bonnet, M.P.; Timouk, F.; Calmant, S.; Pillco, R.; Molina, J.; Lavado-Casimiro, W.; Arsen, A.; Crétaux, J.F.; Garnier, J. Accuracy assessment of SRTM v4 and ASTER GDEM v2 over the Altiplano watershed using ICESat/GLAS data. *Int. J. Remote Sens.* **2015**, *36*, 465–488. [CrossRef]
12. Satge, F.; Denezine, M.; Pillco, R.; Timouk, F.; Pinel, S.; Molina, J.; Garnier, J.; Seyler, F.; Bonnet, M.-P. Absolute and relative height-pixel accuracy of SRTM-GL1 over the South American Andean Plateau. *ISPRS J. Photogramm. Remote Sens.* **2016**, *121*, 157–166. [CrossRef]
13. Kummerow, C.D.; Randel, D.L.; Kulie, M.; Wang, N.Y.; Ferraro, R.; Joseph Munchak, S.; Petkovic, V. The evolution of the goddard profiling algorithm to a fully parametric scheme. *J. Atmos. Ocean. Technol.* **2015**, *32*, 2265–2280. [CrossRef]
14. Ushio, T.; Sasashige, K.; Kubota, T.; Shige, S.; Okamoto, K.; Aonashi, K.; Inoue, T.; Takahashi, N.; Iguchi, T.; Kachi, M.; et al. A Kalman Filter Approach to the Global Satellite Mapping of Precipitation (GSMaP) from Combined Passive Microwave and Infrared Radiometric Data. *J. Meteorol. Soc. Jpn.* **2009**, *87*, 137–151. [CrossRef]
15. Yamamoto, M.K.; Shige, S. Implementation of an orographic/nonorographic rainfall classification scheme in the GSMaP algorithm for microwave radiometers. *Atmos. Res.* **2014**, *163*, 36–47. [CrossRef]
16. Huffman, G.J.; Bolvin, D.T. *TRMM and Other Data Precipitation Data Set Documentation*; NASA/GSFC: Greenbelt, MD, USA, 2014.
17. Taylor, K.E. Summarizing multiple aspects of model performance in a single diagram. *J. Geophys. Res.* **2001**, *106*, 7183–7192. [CrossRef]
18. Oliveira, R.; Maggioni, V.; Vila, D.; Morales, C. Characteristics and Diurnal Cycle of GPM Rainfall Estimates over the Central Amazon Region. *Remote Sens.* **2016**, *8*, 544. [CrossRef]
19. Hussain, Y.; Satge, F. Performance of CMORPH, TMPA and PERSIANN rainfall datasets over plain, mountainous and glacial regions of Pakistan. *Theor. Appl. Climatol.* **2017**, 1–14. [CrossRef]
20. Prakash, S.; Sathiyamoorthy, V.; Mahesh, C.; Gairola, R.M. An evaluation of high-resolution multisatellite rainfall products over the Indian monsoon region. *Int. J. Remote Sens.* **2014**, *35*, 3018–3035. [CrossRef]

21. Scheel, M.L.M.; Rohrer, M.; Huggel, C.; Santos Villar, D.; Silvestre, E.; Huffman, G.J. Evaluation of TRMM Multi-satellite Precipitation Analysis (TMPA) performance in the Central Andes region and its dependency on spatial and temporal resolution. *Hydrol. Earth Syst. Sci.* **2011**, *15*, 2649–2663. [CrossRef]
22. Katiraie-Boroujerdy, P.-S.; Nasrollahi, N.; Hsu, K.; Sorooshian, S. Evaluation of satellite-based precipitation estimation over Iran. *J. Arid Environ.* **2013**, *97*, 205–219. [CrossRef]
23. Ochoa, A.; Pineda, L.; Crespo, P.; Willems, P. Evaluation of TRMM 3B42 precipitation estimates and WRF retrospective precipitation simulation over the Pacific–Andean region of Ecuador and Peru. *Hydrol. Earth Syst. Sci.* **2014**, *18*, 3179–3193. [CrossRef]
24. Roebber, P.J. Visualizing Multiple Measures of Forecast Quality. *Weather Forecast.* **2009**, *24*, 601–608. [CrossRef]
25. Espinoza, J.C.; Marengo, J.A.; Ronchail, J.; Carpio, J.M.; Flores, L.N.; Guyot, J.L. The extreme 2014 flood in south-western Amazon basin: The role of tropical-subtropical South Atlantic SST gradient. *Environ. Res. Lett.* **2014**, *9*, 124007. [CrossRef]
26. Espinoza, J.C.; Chavez, S.; Ronchail, J.; Junquas, C.; Takahashi, K.; Lavado, W. Rainfall hotspots over the southern tropical Andes: Spatial distribution, rainfall intensity, and relations with large-scale atmospheric circulation. *Water Ressour. Res.* **2015**, *51*, 3459–3475. [CrossRef]
27. Satgé, F.; Espinoza, R.; Zolá, R.; Roig, H.; Timouk, F.; Molina, J.; Garnier, J.; Calmant, S.; Seyler, F.; Bonnet, M.-P. Role of Climate Variability and Human Activity on Poopó Lake Droughts between 1990 and 2015 Assessed Using Remote Sensing Data. *Remote Sens.* **2017**, *9*, 218. [CrossRef]
28. Tian, Y.; Peters-Lidard, C.D.; Eylander, J.B.; Joyce, R.J.; Huffman, G.J.; Adler, R.F.; Hsu, K.-L.; Turk, F.J.; Garcia, M.; Zeng, J. Component analysis of errors in satellite-based precipitation estimates. *J. Geophys. Res.* **2009**, *114*, D24101. [CrossRef]
29. Gebregiorgis, A.S.; Hossain, F. Understanding the Dependence of Satellite Rainfall Uncertainty on Topography and Climate for Hydrologic Model Simulation. *IEEE Trans. Geosci. Remote Sens.* **2013**, *51*, 704–718. [CrossRef]
30. Yang, Y.; Luo, Y. Evaluating the performance of remote sensing precipitation products CMORPH, PERSIANN, and TMPA, in the arid region of northwest China. *Theor. Appl. Climatol.* **2014**, *118*, 429–445. [CrossRef]

ANEXO 4

Assessment of satellite rainfall products over the Andean Plateau: Supplementary results (GSMaP)

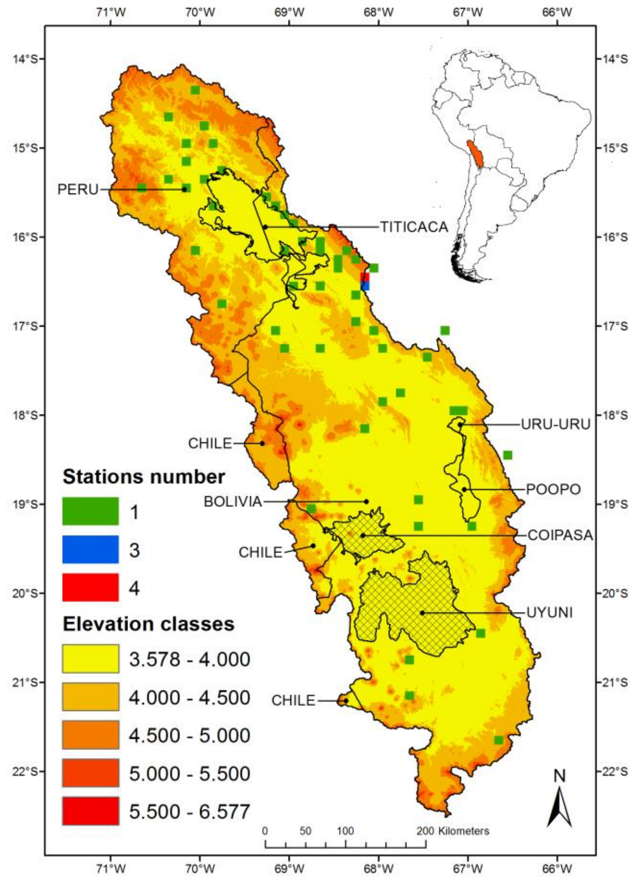

Figure S14. Study area with the number of rain gauges included in studied pixels

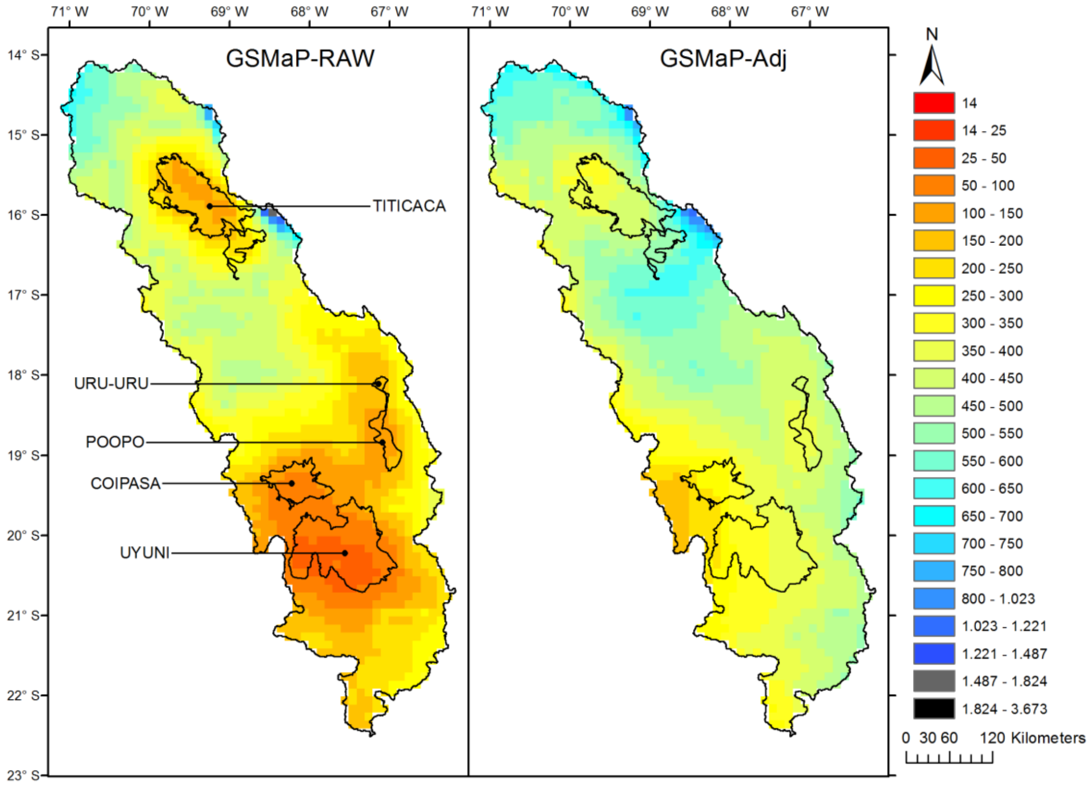

Figure S2. Annual rainfall pattern for GSMaP-RAW and Adj measurements. Rainfall amounts are in mm.

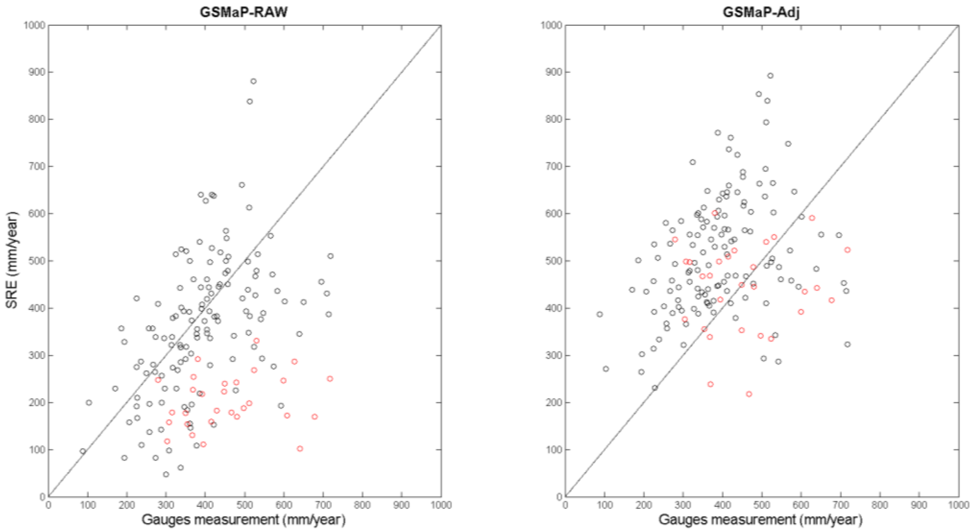

Figure S3. Scatter plots of GSMaPs versus rain gauges, with inland pixel values in black and coastal pixel values in red.

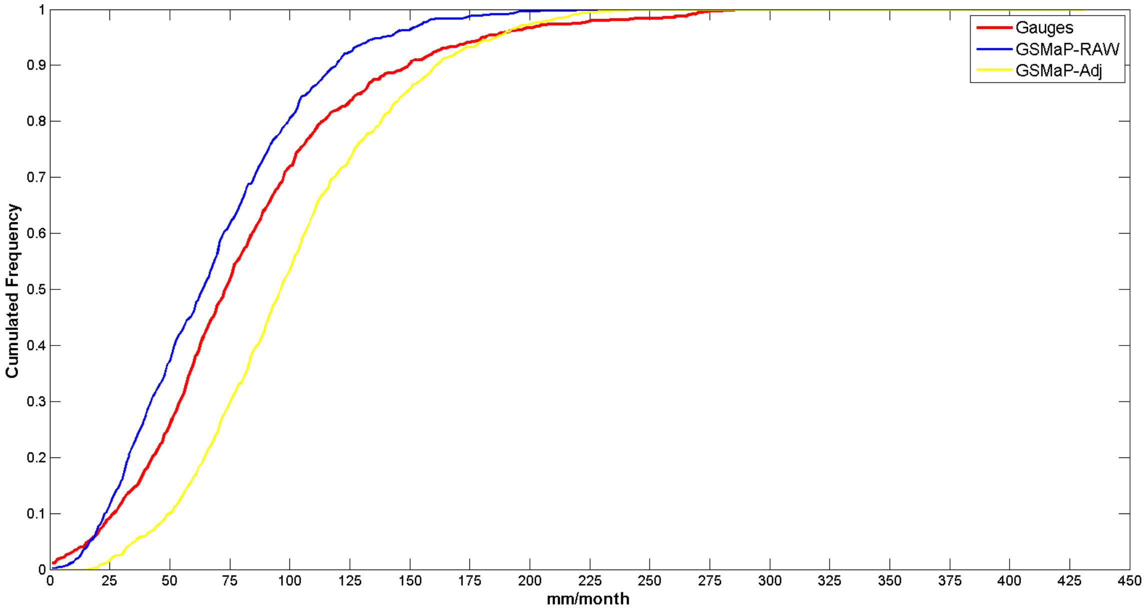

Figure S4. CDF for rain gauges and GSMaPs with a 1 mm.month^{-1} increment.

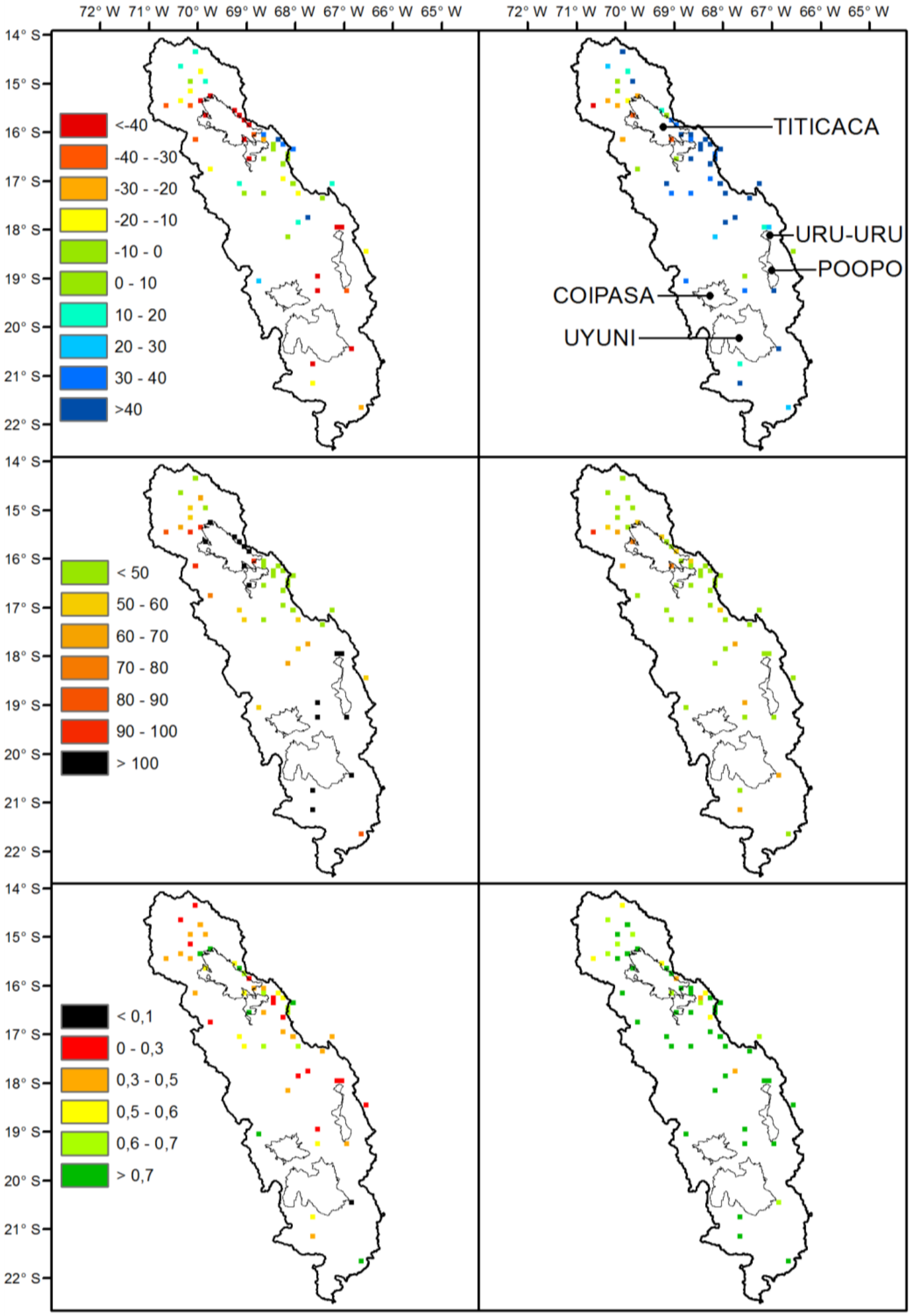

Figure S5. Spatial pattern of Bias (Up), RMSE (middle) and CC (down) between rain gauges and both GSMaP-RAW and Adj monthly precipitation for the 2005-2007 period.

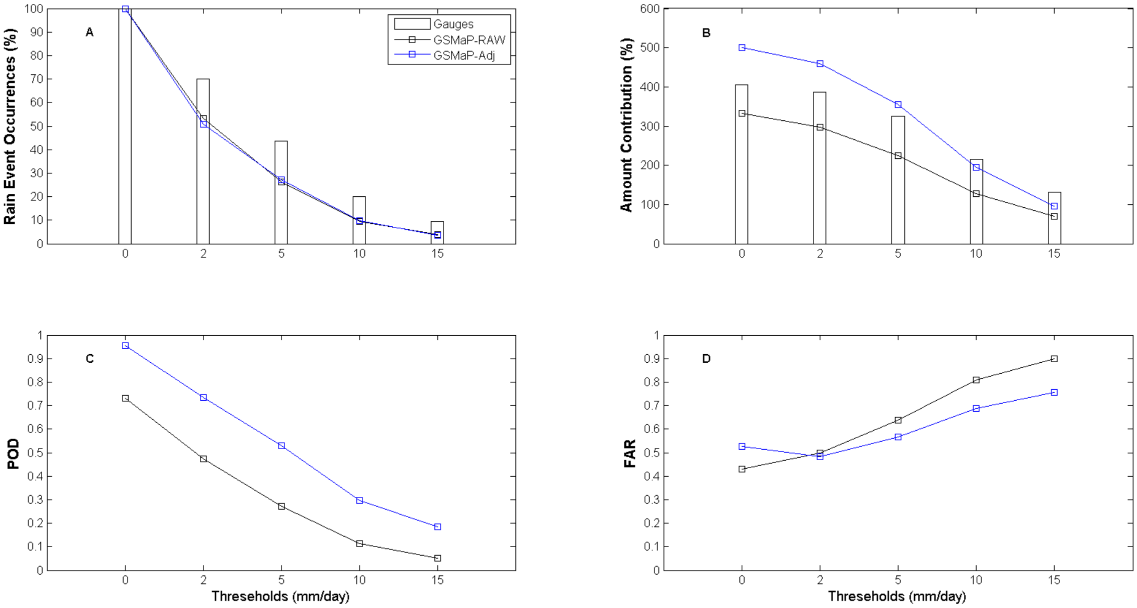

Figure S6. Rain event occurrences (A) and total amount contribution (B) for GSMaP-RAW, Adj and rain gauge measurements for different threshold values and for the entire 2005- 2007 period. Categorical statistics (POD, FAR) for GSMaP-RAW and Adj are based on the same threshold values and period (C,D).